Diss. 2005 - 12
September

Creation and Storage of Long and Flat Bunches in the LHC

Dipl.-Phys. Heiko Damerau

(Dissertation der Technischen Universität Darmstadt)

Gesellschaft für Schwerionenforschung mbH
Planckstraße 1 · D-64291 Darmstadt · Germany
Postfach 11 05 52 · D-64220 Darmstadt · Germany

Creation and Storage of Long and Flat Bunches in the LHC

Vom Fachbereich 18
– Elektrotechnik und Informationstechnik –
der Technischen Universität Darmstadt
genehmigte

Dissertation

zur Erlangung des akademischen Grades eines
Doktor-Ingenieurs (Dr.-Ing.)
von

Dipl.-Phys. Heiko Damerau
geboren am 21. Dezember 1974 in Lünen

Referent:	Prof. Dr.-Ing. Th. Weiland
Korreferent:	Prof. Dr. rer. nat. K. Wille

Tag der Einreichung:	18. Mai 2005
Tag der mündlichen Prüfung:	1. September 2005

D17
Darmstädter Dissertation

Genf, Schweiz, 2005

Abstract

To maximize the luminosity of the Large Hadron Collider (LHC), the collision of particle bunches with a uniform longitudinal particle density is considered for a future upgrade. The benefits of such bunches and their generation by means of special longitudinal beam manipulations are presented in this report.

Three possible options are analyzed with respect to their potential luminosity gain at the beam-beam limit: short rectangular bunches held by radio frequency (RF) harmonics using multiples of the nominal RF frequency of 400.8 MHz, long and flat bunches held by multiples of 40.08 MHz, and so-called superbunches, confined by barrier buckets. The comparison of the three different approaches shows that flat bunches, with an intermediate bunch length of the order of several meters, are capable of producing a comparable luminosity to superbunches, while avoiding most of their inherent disadvantages.

Possible schemes to create the bunches with uniform line density are studied and a longitudinal manipulation to combine a batch of ordinary bunches into a long and flat bunch is proposed. These RF gymnastics are based on well-proven techniques such as batch compression and bunch pair merging. Their advantages and disadvantages, including optimization with respect to degradation of the longitudinal particle density, are discussed in detail. Special attention is paid to the investigation of collective effects due to the large line charge density and the influence of the beam on the RF installation is also studied.

Contents

Chapter 1

Introduction

During the last fifty years, substantial contributions to the understanding of the fundamental principles of nature have been initiated by particles accelerators. These machines accelerate beams of charged particles, like electrons or protons, to high kinetic energies, so that their velocities may approach the speed of light. The particle beams are guided and focused by magnetic elements. The acceleration itself is effectuated by longitudinal electric fields. Large alternating voltages are generated in radio frequency (RF) resonators, so-called cavities. In contrast to linear accelerators, where the particles pass through these accelerating cavities once, the beam is guided through the RF cavities multiple times in circular accelerators. At constant beam energy, it can even be accumulated or stored in a storage ring for many hours.

Cosmic rays represent a natural source of high energetic particles. However, the flux of such particles is low compared to the flux of intense beams generated in modern accelerator and storage ring facilities. Therefore, high energy accelerators represent the only man-made possibility to access the energy range required to produce new matter in a laboratory environment and have lead to decisive discoveries of new particles [1, 2, 3].

The combination of all the experimental data collected so far results in the standard model of particle physics, which has been remarkably successful and is now considered as a well established theory. However, the fundamental mechanism that determines the different masses of the particles remains unexplained. At present, this mechanism is attributed to the so-called Higgs field, which should be detectable in the form of the associated particle. The rest energy of this boson is expected to be in the range of about 100 to 120 GeV. A first glimpse of the Higgs particle might have been detected in the Large Electron Positron Collider (LEP), operated at CERN[1] until 2000 with beam energies up to 105 GeV per beam [4, 5]. As no definitive evidence has been found so far, the discovery of the Higgs particle is a prime motivation for the construction of high energy accelerator facilities such as the Large Hadron Collider (LHC), where the mass region of the Higgs boson is within reach.

The hadron collider principle, where two beams of protons or antiprotons in circular storage rings are brought to collision inside dedicated detectors to analyze the debris, has been proven to be extremely successful [6, 7, 8] since the full kinetic energy of both beams is available for the production of new particles. On the high energy frontier, collisions of proton and antiproton beams with an energy of almost 1 TeV [9, 10] each have been reached, and on the high intensity frontier up to 57.75 A [11] of average proton current has been stored successfully in colliding beam facilities.

Besides its optimum reach in energy, the efficiency of colliding beam facilities is measured

---

[1] Conseil Européen pour la Recherche Nucléaire, European Organization for Nuclear Research

in terms of luminosity, which can be described as the number of particle crossings per unit of transverse area in the interaction region and per second. The actual luminosity record of $\mathcal{L} = 2.2 \cdot 10^{32}\,\mathrm{cm}^{-2}\mathrm{s}^{-1}$ for hadron colliders is held by the now decommissioned Intersecting Storage Rings (ISR) at CERN, but at the moderate energy of 31 GeV per beam.

The Large Hadron Collider (LHC), which will be operational at CERN in 2007, will reach a maximum proton beam energy of 7 TeV, with a nominal luminosity of $10^{34}\,\mathrm{cm}^{-2}\mathrm{s}^{-1}$ [12, 13, 14, 15], almost two orders of magnitude above luminosities obtained so far. Previous high energy hadron accelerators were operated as single ring proton-antiproton colliders, and their beam intensities were limited by the availability of antiprotons, whose production as a brilliant beam is complex and time consuming. This limitation no longer exists in the LHC since it consists of two separate storage rings, one for each beam with opposite polarity so that two counter-rotating intensive proton beams will collide at four interaction points.

The construction of an accelerator such as the LHC, with almost 27 km circumference, represents a considerable investment that must be exploited as efficiently as possible, including the implementation of all feasible means to extend its physics reach as far as possible. After several years of operation with nominal beam and collision parameters, the LHC will have covered the initially foreseen research domain, and several components will have to be replaced because of irradiation. Therefore, various upgrade scenarios, starting with modifications of the beam parameters at the interaction regions up to a replacement of all bending magnets, are being envisaged. In this report, a scenario is proposed and analyzed to upgrade the LHC luminosity by up to an order of magnitude, based on the collision of long and flat bunches.

In the first, nominal stage, the LHC will be operated with 2808 bunches per beam, held by an RF system consisting of eight cavities producing 16 MV per beam at 400.8 MHz. The resulting bunch length (four sigma) in collision is expected to be about 30 cm. These bunches are generated by sophisticated RF manipulations in the upstream injectors, the Proton Synchrotron (PS) and the Super Proton Synchrotron (SPS), delivering a well prepared proton beam at an energy of 450 GeV to the LHC. Finally, the beam is confined as numerous short bunches, while the major fraction of the circumference remains longitudinally unoccupied. The suggestion has recently been made to concentrate the particles in a limited number of long and flat superbunches [16]. Coasting sausage-like beams would be brought to intersect at large crossing angles. Such a scheme is especially interesting with respect to electron cloud effects and undesired electromagnetic crosstalk between both beams in the collision regions. This phenomenon, known as beam-beam interaction, can be partly compensated by homogeneous bunches which are much longer than the luminous region at the intersection points.

Although confining the whole beam to a single superbunch with a length of some 260 m has been considered as an upgrade option for the LHC, no scheme to generate this bunch, with reasonable modifications of the accelerator itself and the injector chain, has been proposed up to now. This report thus suggests a variety of flat bunch options and analyzes their potential benefits for the improvement of the LHC performance. An intermediate solution is proposed, combining batches of 16 or 32 nearly nominal LHC bunches, to form a flat bunch with a length of four to five meters. This offers a peak luminosity comparable to the superbunch option.

In collision mode, these intermediate long and flat bunches are held by multi-harmonic RF systems, operating at multiples of 40.08 MHz. It is shown that even RF systems with three different harmonics are sufficient to form an almost ideal barrier bucket, providing bunches with a long section of quasi-constant line density and comparatively much shorter tails.

The combination scheme, to create the intermediate long and flat bunches, presented in this report is based on well-proven RF manipulations called batch compression and bunch pair merging. Furthermore, the scheme can be performed completely in the LHC itself so that the modifications to the injector chain, apart from a significant intensity increase, remain straightforward.

This report is organized as follows: the subsequent chapter introduces the subject of longitudinal beam dynamics in circular particle accelerators, which describes the interaction of a particle beam with electromagnetic fields generated across longitudinal gaps in the beam pipe. Multiple harmonic RF systems are included, as well as the beam dynamics of barrier RF systems. Besides the so-called single particle dynamics, the behaviour of bunches as a whole is also discussed in the subsequent chapter. Furthermore, a short introduction to the basics of longitudinal particle tracking is given.

While the characteristics of the RF systems are considered to be constant in the second chapter, chapter three is devoted to longitudinal beam manipulations, using special variations of the external RF parameters, such as frequency, phase and amplitude. This chapter gives an overview of the most important bunch manipulation processes: bunch merging and splitting, batch compression and bunch rotation. Additionally, more recent barrier bucket manipulation techniques, like moving barrier bunch compression and fast barrier stacking are described in order to illustrate the possibilities offered by longitudinal beam gymnastics.

The fourth chapter is dedicated to the optimization of the luminosity close to the beam-beam limit. Three possible schemes, i.e. short rectangular bunches, flat bunches of intermediate length and very long superbunches are discussed and classified according to their potential luminosity gain. Formulas, including corrections for the luminosity and beam-beam tune spread of short and long rectangular bunches, are derived and applied to the different LHC scenarios of colliding long and flat bunches. The luminosity loss due to a non-perfect rectangular bunch held by a multiple harmonic RF system is also worked out. Finally, the longitudinal parameters of the two collision options, using flat bunches of intermediate bunch length comprising either 16 or 32 nearly nominal LHC bunches, are defined.

Once the parameters during the collision of long bunches are identified, their generation is discussed in detail in the fifth chapter. Though the process is based on well-known subprocedures, its optimization is essential to conserve the longitudinal beam quality during the long and flat bunch combination scheme. It can be demonstrated that, though tunable in frequency, only two RF systems of reasonable size and performance are sufficient to perform the required complex RF gymnastics. The scheme is finally crosschecked by extensive tracking calculations to particularly analyze the beam quality degradation under various conditions.

A first outlook on collective effects and beam loading during creation and collision of the long and flat bunches is presented in the last chapter, including a comparison with calculations available for the nominal LHC scheme. It turns out that operating the LHC with a 40.08 MHz RF system makes the beam more sensitive to longitudinal instabilities. Possible counter-measures and their potential benefits are discussed.

The report closes with a summary of the work done so far and an outlook on further studies.

It should be mentioned that a machine experiment to study the behaviour of long proton bunches in a large accelerator has been accomplished in the SPS. The experimental results and conclusions for the LHC are described in App. A.

During the study it turned out that the bunch combination scheme proposed for the upgraded LHC could also be applied in the planned heavy ion synchrotron SIS100 at GSI[2]. The detailed proposal is also presented in the appendix.

---

[2] Gesellschaft für Schwerionenforschung mbH, Darmstadt, Germany

Chapter 2

Longitudinal Beam Dynamics

The controlled acceleration of charged particles requires a continuous energy transfer of an external source to the particle beam. In synchrotrons, the particle beam is accelerated by longitudinal electric fields, while the transverse magnetic field of the bending magnets is increased such that the bending radius of the particle orbit stays constant. These longitudinal electric fields are developed across special gaps inside RF resonators, so-called RF cavities. Stable acceleration implies that the frequency of the RF field has to be chosen such that it remains nearly repetitive from one turn to the next. With increasing energy, the particle gets faster and the RF frequency is increased synchronously. The longitudinal particle motion under the effect of electric fields generated by the RF cavities is described by the longitudinal beam dynamics.

As long as the accelerating cavities in a circular accelerator are placed in non-dispersive sections, with negligible dependence of the position of a particle on its energy deviation, it is legitimate to treat the longitudinal and transverse phase space motions separately in first order approximation [17, 18]. This is the case for most modern synchrotrons and storage rings. However, acceleration is not the only use of RF systems in circular accelerators. Of equal importance are the so-called RF gymnastics with which the longitudinal beam charge and bunch distribution is manipulated. They are therefore addressed in a dedicated chapter.

Starting from the general relation between RF frequency and magnetic bending field, the concept of phase stability for individual particles under the influence of a general RF amplitude function will be derived on the basis of the Hamilton formalism. The isolated and barrier bucket technique is introduced in a dedicated section. Following the dynamics of single particles, the behaviour of an ensemble of particles with different distributions and its description in terms of emittance is discussed. Finally, effects like space charge and synchrotron radiation are examined.

2.1 Magnetic cycle

In a synchrotron, the particle beam couples the transverse magnetic field B of the bending magnets to the frequency of a longitudinal electric field generated in RF cavities which is used for acceleration.

2.1.1 RF frequency and bending field

To keep particles on an orbit of constant radius, the centripetal force has to be exactly compensated by the Lorentz force. Considering that the angular revolution frequency of the beam is given by $\omega_0 = \beta c / R_{\text{mean}}$, this relation between both forces leads to the dependence of the revolution frequency on the bending field:

$$\omega_0(B) = \frac{B}{\sqrt{\left(\frac{m_0 c}{e R_{\mathrm{mag}}}\right)^2 + B^2}} \cdot \frac{c}{R_{\mathrm{mean}}} \,. \tag{2.1}$$

the radii R_{mean} and R_{mag} are the average radius of the accelerator and the bending radius of its dipole magnets. The properties of the particle are defined by its rest mass m_0 and charge e; $\beta = v/c$ is the fraction of the beam velocity with respect to the speed of light in vacuum. If the radius R is used without an index, it replaces the average radius of the accelerator so that the circumference is defined as $2\pi R_{\mathrm{mean}} = 2\pi R$.

2.1.2 Energy gain during acceleration

As one acceleration cycle in a synchrotron lasts for some thousands to millions of revolutions, the magnetic bending field varies very slowly compared to the time scale of the longitudinal particle motion, therefore the energy gain per turn is small. The time derivative of the momentum $\dot{p}$ can be approximated by a stepwise momentum increase $\Delta p/\Delta t$ according to[1]

$$\dot{p} = \frac{\Delta p}{\Delta t} = \frac{m_0 c^2 \beta}{2\pi R}(\beta \Delta\gamma + \gamma \Delta\beta) = \frac{\Delta E}{2\pi R} \,. \tag{2.2}$$

The average energy gain ΔE per turn has to be generated by a longitudinal electric field. The relativistic mass factor is given by $\gamma = E/(m_0 c^2)$. As the dependence of the particle momentum on the magnetic field is again defined by the cancellation of Lorentz and centripetal force which gives $p = e R_{\mathrm{mag}} B$, the average energy gain per turn can be written as

$$\Delta E = 2\pi e R_{\mathrm{mag}} R_{\mathrm{mean}} \dot{B} \,. \tag{2.3}$$

It it worth noting that the circulating particle may experience an additional energy loss. This energy loss may be caused by synchrotron radiation ΔE_{rad} (see Sec. 2.8) and small losses induced by the resistive impedance of the beam pipe or other components of the accelerator. In what follows, it is just assumed that the RF system has to compensate a certain average energy gain or loss W_0 being the total of all average energy changes during one turn.

2.2 Single particle dynamics and phase stability

Stable acceleration of a particle in a circular machine requires a longitudinal electric field that is periodic for each turn. This condition leads to the requirement that the possible angular RF frequency ω_{RF} of the acceleration system is restricted to near integer harmonics

$$\omega_{RF} = h\omega_0 \qquad \text{with} \qquad h \in \mathbb{N} \tag{2.4}$$

of the revolution frequency ω_0. The parameter h is the so-called harmonic number and defines the frequency of the RF system. It can range from unity to values up to several ten thousands.

---

[1] A list of symbols and notations used throughout this report is found on pp. 173-175.

2.2.1 Synchronous particle

It is convenient to define a synchronous particle whose energy $E_0(t)$ is arbitrarily chosen to characterize the expected behaviour of the center of the distribution of real particles. The energy gain or loss of the synchronous particle is exactly compensated by the RF systems so that it is always at the reference energy $E_0(t)$. Assuming that there is only one RF frequency with the amplitude U_0 present, the particle has to ride on the RF waveform at the so-called synchronous phase ϕ_0 which fulfills the condition

$$eU_0 \sin\phi_0 = W_0\,. \tag{2.5}$$

All non-synchronous particles move in the longitudinal phase space with respect to the synchronous particle.

2.2.2 Non-synchronous particle

Any particle is characterized by a certain phase and energy deviation with respect to the synchronous particle. It is therefore necessary to define a completely new set of parameters to describe the motion of particles with respect to the synchronous particle as reference of the longitudinal phase space [19, 20]:

Revolution frequency	$\omega = \omega_0 + \Delta\omega$
Phase with respect to the accelerator	$\theta = \theta_0 + \Delta\theta$
Phase with respect to the RF frequency $h\omega$	$\phi = \phi_0 + \Delta\phi$
Mean orbit radius	$R = R_0 + \Delta R$
Particle momentum	$p = p_0 + \Delta p$
Particle energy	$E = E_0 + \Delta E\,.$

The motion of the non-synchronous particle can be determined by comparing its behaviour with the synchronous one. The condition which connects the momentum variation of a particle to the average energy gain per turn has already been given in Eq. (2.2). A simple conversion leads to

$$R\dot{p} = \frac{eU_0}{2\pi} g(\phi)\,, \tag{2.6}$$

where $g(\phi)$ is a generalized RF voltage normalized to unity. The only conditions $g(\phi)$ needs to fulfill are periodicity with the lowest RF harmonic and the absence of a direct current (DC) component:

$$g(\phi) = g(\phi + 2\pi) \qquad \text{and} \qquad \int_0^{2\pi} g(\phi)\,d\phi = 0\,.$$

In Eq. (2.6) the particle parameters, orbit radius and momentum derivative, are condensed on the left side. Comparing Eq. (2.6) to the analogous relation for the synchronous particle becomes

$$R\dot{p} - R_0\dot{p}_0 = \Delta(R\dot{p}) = \frac{eU_0}{2\pi}[g(\phi) - g(\phi_0)]\,. \tag{2.7}$$

The expression $\Delta(R\dot{p})$ on the left can be expanded in first order assuming that the relative radial $\Delta R/R$ and momentum deviations $\Delta p/p$ are negligible [21]:

$$\Delta(R\dot{p}) = R\Delta\dot{p} + \dot{p}\Delta R \simeq R_0\Delta\dot{p} + \dot{p}_0\Delta R\,. \tag{2.8}$$

Furthermore, the second term is replaced by its first order approximation $\dot{p}_0 \Delta R(\Delta p) \simeq (dp/dt)_0 (dR/dp)_0 \Delta p = \dot{R}_0 \Delta p$ and by using the equation (see Eq. 2.2)

$$R_0 \Delta p = R_0 mc \Delta(\beta\gamma) = \frac{\Delta E}{\omega_0} \tag{2.9}$$

one gets the relation

$$\Delta(R\dot{p}) = \frac{d}{dt}(R_0 \Delta p) = \frac{d}{dt}\frac{\Delta E}{\omega_0} . \tag{2.10}$$

Finally, the combination of Eqs. (2.7) and (2.10) leads to the first fundamental equation of the longitudinal beam dynamics:

$$\frac{d}{dt}\frac{\Delta E}{\omega_0} = \frac{eU_0}{2\pi}[g(\phi) - g(\phi_0)] . \tag{2.11}$$

The second fundamental equation can be obtained from the relationship between a radial deviation and a deviation in revolution frequency. The proportional factor is called phase slip factor and defined as[2]

$$\eta = -\frac{\Delta\omega/\omega}{\Delta p/p} = \frac{1}{\gamma_{\mathrm{tr}}^2} - \frac{1}{\gamma^2} = \alpha_c - \frac{1}{\gamma^2} , \tag{2.12}$$

where α_c is the momentum compaction factor $\alpha_c = (\Delta L/L)/(\Delta p/p) = 1/\gamma_{\mathrm{tr}}^2$. The momentum compaction factor is determined by the magnet lattice of the accelerator and is a positive parameter for the common magnet structures in synchrotrons. The energy $\gamma_{\mathrm{tr}} m_0 c^2$ at which the phase slip factor vanishes is called transition energy. At transition energy, all particles rotate with the same revolution frequency which is virtually independent from their energy deviation. As will be shown later, the longitudinally focusing force, keeping the bunches together, vanishes at this energy. However, Eq. (2.12) is only an approximation and higher order terms lead to a non-linear coupling between energy deviation and revolution frequency [23].

The deviation of the revolution frequency can be substituted by the phase position derivative and by transformation to an angle ϕ with reference to the RF phase, resulting in

$$\Delta p = -\frac{p_0}{\eta_0 \omega_0}\Delta\omega = -\frac{p_0}{\eta_0 \omega_0}\frac{d\theta}{dt} = \frac{p_0}{h\eta_0 \omega_0}\frac{d\phi}{dt} . \tag{2.13}$$

The convention of the signs is sketched in Fig. 2.1. Replacing the momentum deviation with

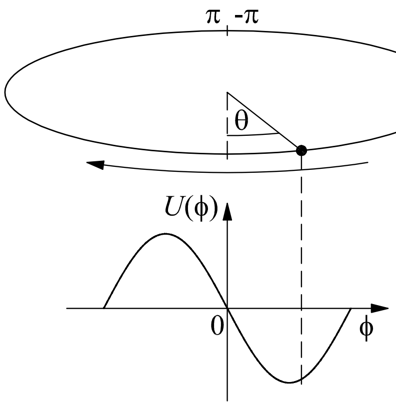

Fig. 2.1: Illustration of the relationship between the phase θ of a particle rotating clockwise in the reference frame of the accelerator and its phase ϕ with reference to an RF system.

---

[2] In the literature the sign of the phase slip factor is sometimes defined differently, see e.g. [22].

the term given by Eq. (2.9) finally gives the second fundamental equation

$$\frac{d\phi}{dt} = \frac{h\eta_0\omega_0}{p_0 R_0}\left(\frac{\Delta E}{\omega_0}\right) \tag{2.14}$$

of the longitudinal beam dynamics.

Both fundamental Eqs. (2.11) and (2.14) together have the structure of Hamilton equations

$$\frac{dq}{dt} = \frac{\partial H}{\partial p} \qquad \text{and} \qquad \frac{dp}{dt} = -\frac{\partial H}{\partial q}\,, \tag{2.15}$$

where the canonical conjugated variables q and p coincide with the physical variables ϕ and $\Delta E/\omega_0$. The set of Hamilton equations for the longitudinal beam dynamics is thus given by [24]

$$\frac{d\phi}{dt} = \frac{h\eta_0\omega_0}{p_0 R_0}\left(\frac{\Delta E}{\omega_0}\right) \tag{2.16}$$

$$\frac{d}{dt}\left(\frac{\Delta E}{\omega_0}\right) = \frac{eU_0}{2\pi}[g(\phi) - g(\phi_0)]\,. \tag{2.17}$$

The choice of the set of variables ϕ and $\Delta E/\omega_0$ is arbitrary and defines only the explicit form of the Hamiltonian. As will be shown later, a different pair of variables can be chosen to get a more compact form of the explicit operator.

It has to be mentioned that the parameters p_0, R_0, η_0 in Eqs. (2.16) and (2.17) have an explicit time dependence during the acceleration cycle. However, as these parameters usually vary very slowly with respect to the period of the synchrotron frequency, this dependence can be neglected. Furthermore, the indices to indicate the parameters of the reference particles are suppressed in the subsequent calculations as the relative deviations from the synchronous particle are negligible, e.g. $(p - p_0)/p_0 \ll 1$.

From the two Hamilton equations it is now possible to extract the full Hamiltonian

$$H\left(\phi, \frac{\Delta E}{\omega_0}\right) = \frac{1}{2}\frac{h\eta\omega_0}{pR}\left(\frac{\Delta E}{\omega_0}\right)^2 + \frac{eU_0}{2\pi}\left[g(\phi_0)\phi - \int g(\phi)\,d\phi\right] \tag{2.18}$$

for the longitudinal single particle motion.

Furthermore, the equation of motion can be extracted from the Hamilton equations by calculating the time derivative of Eq. (2.16) and combining it with Eq. (2.17). The general equation of motion is thus given by

$$\frac{d^2}{dt^2}\phi + \frac{\omega_s^2}{\cos\phi_0}[g(\phi) - g(\phi_0)] = 0 \qquad \text{with} \qquad \omega_s^2 = -\frac{h\eta\omega_0 eU_0\cos\phi_0}{2\pi pR}\,, \tag{2.19}$$

where ω_s is the so-called synchrotron frequency. For small amplitude oscillations one can show that this definition is meaningful because Eq. (2.19) reduces to the differential equation of a harmonic oscillator as will be demonstrated in the next section.

For completeness, the Hamiltonian of the interaction of a particle with only one RF system can be written as

$$H\left(\phi, \frac{\Delta E}{\omega_0}\right) = \frac{1}{2}\frac{h\eta\omega_0}{pR}\left(\frac{\Delta E}{\omega_0}\right)^2 + \frac{eU_0}{2\pi}[\cos\phi - \cos\phi_0 + (\phi - \phi_0)\sin\phi_0]\,. \tag{2.20}$$

It should be noted that the Hamiltonian Eq. (2.20) is normalized so that it vanishes for a synchronous particle, namely $H(\phi = \phi_0, \Delta E = 0) = 0$.

2.2.3 Small amplitude oscillations

In the case of small amplitude motion the phase ϕ of the particle stays closely to the synchronous phase ϕ_0. Approximation of the general voltage function $g(\phi)$ to first order and insertion to Eq. (2.19) gives

$$\frac{d^2}{dt^2}\Delta\phi + \frac{\omega_s^2}{\cos\phi_0}\,\frac{dg(\phi)}{d\phi}\bigg|_{\phi=\phi_0}\Delta\phi = 0\,, \tag{2.21}$$

the differential equation of the harmonic oscillator. The independent phase variable is now $\Delta\phi$, whose first and second time derivatives are equal to the derivatives of ϕ.

Considering a single RF system with a normalized amplitude of $g(\phi) = \sin\phi$, Eq. (2.21) simplifies to

$$\frac{d^2}{dt^2}\Delta\phi + \omega_s^2\Delta\phi = 0\,, \tag{2.22}$$

and it becomes obvious why ω_s is called synchrotron frequency. It is the angular frequency of the ΔE-ϕ-oscillation of non-synchronous particles with respect to the synchronous particle.

However, for stable and closed trajectories the squared synchrotron frequency ω_s needs to be positive corresponding to $\eta\cos\phi_0 < 0$. Two different regions of oscillatory motions can be identified, depending on whether the accelerator is operated below or above the transition energy:

$$\begin{aligned} &\gamma < \gamma_{\mathrm{tr}} \quad \text{and} \quad 0 \le \phi_0 < \pi/2 \\ \text{or} \quad &\gamma > \gamma_{\mathrm{tr}} \quad \text{and} \quad \pi/2 < \phi_0 \le \pi\,. \end{aligned} \tag{2.23}$$

This so-called principle of phase stability [25, 26] assures that ensembles of particles can be accelerated in synchrotrons, even if they are not exactly at the synchronous phase and energy. Such particles just oscillate around the reference particle.

2.2.4 Convenient choice of variables and Hamiltonian

The conversion of the Hamiltonian in Eq. (2.18) leads to a form being more compact and convenient for the subsequent calculations. Following Eq. (2.16), the variable ΔE describing the energy deviation is converted to a phase velocity $\dot\phi$ while the phase variable ϕ remains unchanged. The resulting Hamiltonian reduces to

$$H(\phi,\dot\phi) = \frac{1}{2}\dot\phi^2 + \omega_s^2 W(\phi) \tag{2.24}$$

with the beam potential function

$$W(\phi) = \frac{1}{\cos\phi_0}\left[\int g(\phi)\,d\phi - g(\phi_0)\phi\right]\,; \tag{2.25}$$

the normalization of $H(\phi,\dot\phi)$ is different from Eq. (2.18). The set of variables chosen is again canonically conjugated: with $q = \phi$ and $p = \dot\phi$ the first Hamilton equation (2.16) is trivial and the second one reproduces, as expected, the general equation of motion Eq. (2.19).

2.2.5 Large amplitude oscillations

Even though the equation of motion (2.19) cannot be solved in general, the Hamiltonian allows the full calculation of trajectories in the longitudinal phase space.

To get the trajectory of a particle starting at $\phi = \phi_m$ and $\dot{\phi} = \dot{\phi}_1$, the Hamiltonian (2.24) is equated with its value $H_0 = H(\phi_m, \dot{\phi}_1)$ at the starting point, and the equation of the trajectory can be written as

$$\dot{\phi}(\phi) = \pm\sqrt{2[H_0 - \omega_s^2 W(\phi)]}\,. \tag{2.26}$$

The ensemble of all closed trajectories around the synchronous particle is called an RF bucket. The number of possible buckets in a circular accelerator corresponds to the lowest harmonic number h. Regarding the potential function Eq. (2.25), buckets can be identified by potential valleys and reach from a local potential maximum to the phase where the potential again has the same value as at the local maximum. The trajectories outside the RF buckets are not closed and, with the exception of some special applications [27, 28], they cannot be used for acceleration. Particles on these trajectories are normally lost at the inner part of the beam pipe when the increase of the magnetic bending field starts.

An example for amplitude, potential and longitudinal phase space is illustrated in Fig. 2.2. The synchronous phase was chosen to be $\phi_0 = \pi/6$. In the phase space plot (Fig. 2.2, bottom), the separatrix and inner as well as outer trajectories are shown. The trajectories around the synchronous phase are almost elliptical, and particles thereon oscillate with the synchrotron frequency. Due to non-linearities of the bucket, the synchrotron frequency decreases towards the separatrix as will be calculated in Sec. 2.2.6.

Separatrix

The trajectory which separates open and closed trajectories is called the separatrix. The value of its Hamiltonian can be calculated by taking into account that one limit of the bucket is a local maximum of the potential. It is worth noting that a local potential maximum appears as an unstable fixed point in the longitudinal phase space, while local potential minima generate a stable fixed point equivalent to the center of a bucket. This means that a test particle at the phase of the maximum ϕ_m must have a vanishing energy deviation $\dot{\phi} = 0$, leading to

$$H_{\text{sep}} = H(\phi = \phi_m, \dot{\phi} = 0) = \omega_s^2 W(\phi_m) \tag{2.27}$$

and the general separatrix function can be written as

$$\dot{\phi}(\phi) = \pm\sqrt{2\omega_s^2[W(\phi_m) - W(\phi)]}\,. \tag{2.28}$$

For a single RF system the separatrix can be calculated analytically. The local potential maximum is at $\phi_m = \pi - \phi_0$, and the Hamiltonian of the separatrix reduces to

$$H_{\text{sep}} = H(\phi = \pi - \phi_0, \dot{\phi} = 0) = \frac{\omega_s^2}{\cos\phi_0}(1 + \cos\phi_0 - (\pi - \phi_0)\sin\phi_0)\,.$$

Again, equating with the Hamiltonian Eq. (2.24) leads to the separatrix trajectory

$$\dot{\phi}(\phi) = \pm\sqrt{\frac{2\omega_s^2}{\cos\phi_0}[(\phi + \phi_0 - \pi)\sin\phi_0 + \cos\phi_0 + \cos\phi]} \tag{2.29}$$

in the longitudinal phase space. To calculate the separatrix in real energy units, Eqs. (2.28) and (2.29) have to be multiplied with a scaling factor according to

$$\Delta E(\phi) = \frac{pR}{h\eta}\dot{\phi}(\phi) = \sqrt{\frac{E\beta^2\, eU_0}{2\pi h\eta}} \cdot \frac{\dot{\phi}(\phi)}{\sqrt{\omega_s^2/\cos\phi_0}}\,. \tag{2.30}$$

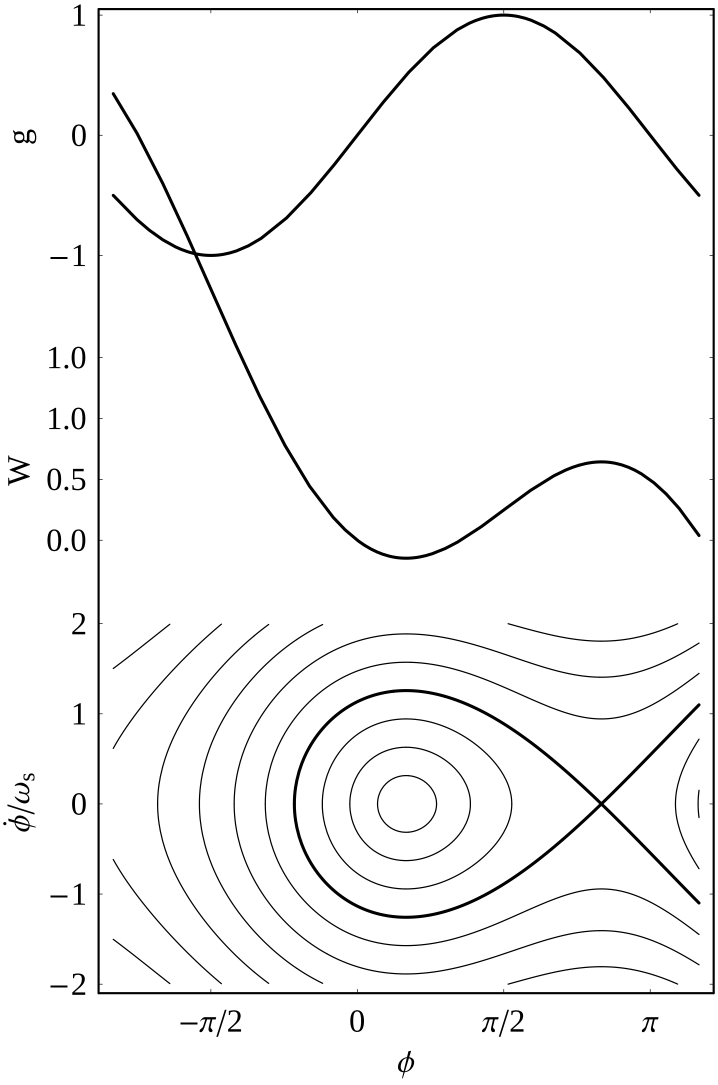

Fig. 2.2: RF Amplitude $g(\phi)$ (top), potential function (center) $W(\phi)$ and longitudinal phase space (bottom) for an arbitrary chosen synchronous phase of $\phi_0 = \pi/6$. Below transition energy, the particles rotate counterclockwise. In fact, the whole diagram could be mirrored around a vertical line at the synchronous phase and one gets the same situation above transition energy with $\phi_0 = \pi - \pi/6 = 5/6\pi$ and particles rotating clockwise.

Bucket length

The length of an RF bucket can only be calculated numerically. The first bucket limit corresponds to the phase position ϕ_m of the unstable fixed point as used in the previous section. The second bucket limit ϕ_n is determined by the phase where the RF potential $W(\phi)$ is equal to $W(\phi_m)$. The bucket length $\phi_n - \phi_m$ is usually given in units of phase or physical length. For the latter convention, $\phi_n - \phi_m$ is to be multiplied by $c/(h\omega_0)$.

Even for a single sinusoidal RF system, the condition $W(\phi) = W(\phi_m)$ becomes a transcendental equation. As can be seen from the numerically calculated curve in Fig. (2.3), the bucket length shrinks rapidly when the synchronous phase slightly differs from the stationary values $\phi_0 = 0$ (below the transition) or π (above transition), but approximates a linear function for larger (below) or smaller (above) synchronous phase angles.

Bucket height

The bucket height is given by the maximum energy deviation of the separatrix function from Eq. (2.28). As the potential $W(\phi)$ has by definition a minimum at the synchronous phase, the

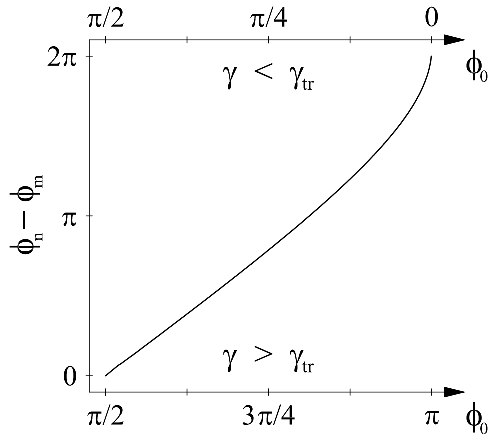

Fig. 2.3: Bucket length $\phi_n - \phi_m$ versus synchronous phase ϕ_0.

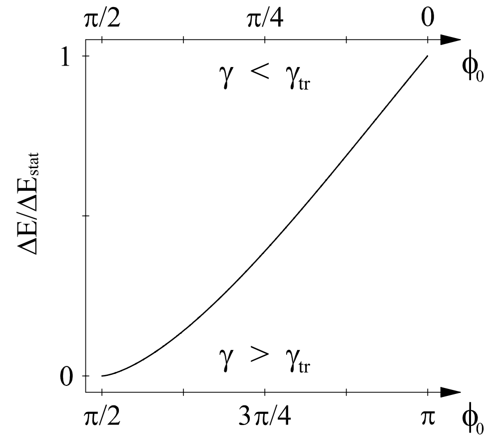

Fig. 2.4: Relative bucket height versus synchronous phase ϕ_0.

energy acceptance simplifies to

$$\hat{\dot{\phi}} = \sqrt{2\omega_s^2[W(\phi_m) - W(\phi_0)]} \quad \text{or} \quad \Delta\hat{E} = \sqrt{\frac{E\beta^2\, eU_0 \cos\phi_0}{\pi h \eta}[W(\phi_m) - W(\phi_0)]}\,. \tag{2.31}$$

For a single RF system, the bucket height calculated from Eq. (2.31) becomes

$$\Delta\hat{E} = \sqrt{\frac{E\beta^2\, eU_0}{\pi h \eta}[(\pi - 2\phi_0)\sin\phi_0 - 2\cos\phi_0]} \tag{2.32}$$

as sketched in Fig. 2.4. Both bucket length and height decrease nearly linearly with the synchronous phase.

Bucket area

The bucket area is the area enclosed by the separatrix trajectory. Generally it is defined by twice the integral

$$A = 2\int_{\phi_m}^{\phi_n} \dot{\phi}(\phi)\, d\phi \tag{2.33}$$

of the separatrix. As in the case of the bucket length, the area of a bucket generated by single sinusoidal RF voltage cannot be calculated analytically. It is proportional to the integral

$$\alpha(\phi_0) = \frac{1}{4\sqrt{2}}\int_{\phi_m}^{\pi-2\phi_0} \sqrt{\cos\phi_0 + \cos\phi - (\pi - \phi_0 - \phi)\sin\phi_0}\, d\phi\,, \tag{2.34}$$

which has to be evaluated numerically. The expression is only valid below transition. Above transition, the limits of the integration need to be changed to $\pi - 2\phi_0$ and ϕ_n, as well as the sign of the argument of the square root (Fig. 2.5). The most common unit for areas in the longitudinal phase space is [time · energy] = eV · s. The conversion from phase space areas in other units can be performed according to

$$A_{\mathrm{eVs}} = \frac{E\beta^2}{h^2\omega_0^2|\eta|}A_{\mathrm{rad^2/s}} \quad \text{or} \quad A_{\mathrm{eVs}} = \frac{1}{h\omega_0}A_{\mathrm{eV\,rad}}\,. \tag{2.35}$$

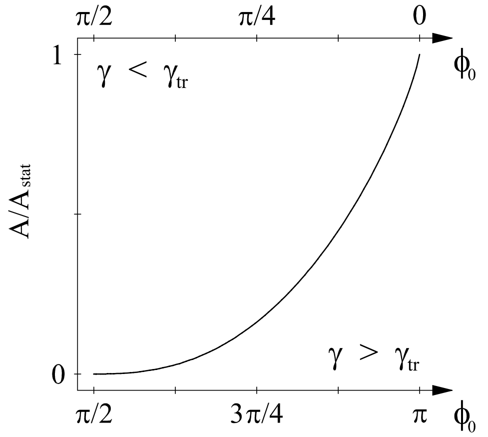

Fig. 2.5: Relative bucket area versus synchronous phase ϕ_0.

From the scaling with the RF amplitude, it could be expected that the bucket area varies in proportion to the square root of the applied voltage. However, this is only true in the absence of acceleration. In the case of an accelerating bucket an additional factor due to dependence of the synchronous phase (see Eq. 2.5) on the RF amplitude contributes to the area diminution. Combining these two factors, the area effectively varies almost linearly with the RF voltage for typical synchronous phases [29] which are in the range of $\phi_0 = 0.35$ to 0.7 rad (20^0 – 40^0).

Stationary bucket

Of special importance is the stationary bucket because most longitudinal beam manipulations are done at constant energy. In such a case the bucket is symmetric around the synchronous phase ϕ_0, which is either zero (below) or π (above transition energy). This approximation is reasonable when the bending field is held constant in the main magnets for all proton accelerators up to an energy of more than 1 TeV. Even in the LHC at its full energy, synchrotron radiation contributes to negligible losses compared to the nominal RF voltage and a stationary bucket is a good approximation.

The parameters of the stationary bucket can be obtained by following the equations in Sec. 2.2.5 and applying $\phi_0 = 0, \pi$. An illustration of the longitudinal phase space of a stationary bucket is represented in Fig. 2.6. Each particle in a stationary bucket behaves like a physical pendulum. The phase ϕ and energy deviation in units of phase deviation $\dot{\phi}$ directly correspond to the deflection angle and the phase velocity of the oscillating mass [30].

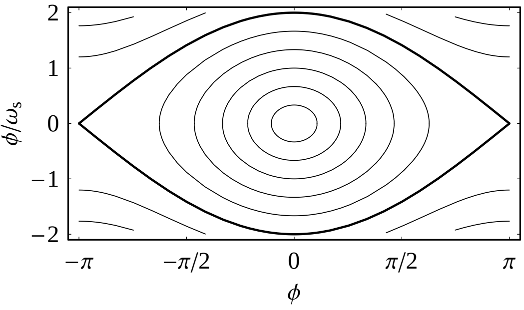

Fig. 2.6: Stationary bucket around the synchronous angle $\phi_0 = 0$ (below transition) or $\phi_0 = \pi$ (above). Particles follow the trajectories clockwise.

Separatrix. The separatrix of the stationary bucket is defined by

$$\dot{\phi}(\phi) = \pm\sqrt{4\omega_s^2(1-\cos\Delta\phi)} = \pm 2\omega_s \sin\frac{\phi}{2}\,. \tag{2.36}$$

Therefore, particles having exactly the reference energy circulate theoretically stable at any arbitrary phase around the accelerator.

Bucket length. As the bucket extends over 2π with respect to ϕ, the bucket length in phase or length units is directly given by $2\pi/h$ (with respect to θ) or $2\pi R/h$.

Bucket height. The bucket height is the maximum value of the separatrix given by Eq. (2.36) at $\Delta\phi = 0$:

$$\hat{\dot{\phi}} = 2\omega_s \qquad \text{or} \qquad \Delta\hat{E} = \sqrt{\frac{2E\beta^2\, eU_0}{\pi h|\eta|}}\,. \tag{2.37}$$

Bucket area. Also the bucket area can be analytically calculated by integration over Eq. (2.36):

$$A = 8\hat{\dot{\phi}} = 16\omega_s \qquad \text{or} \qquad A_{\mathrm{eVs}} = \frac{8\sqrt{2}}{h\omega_0}\sqrt{\frac{E\beta^2\, eU_0}{\pi h|\eta|}}\,, \tag{2.38}$$

where the latter expression was converted using the conversion factor from Eq. (2.35).

2.2.6 Synchrotron frequency distribution

The linear synchrotron frequency ω_s as defined in Eq. (2.19) is only valid for particles which oscillate around the synchronous phase with a small phase and energy deviation. In fact, in a single harmonic RF bucket it decreases with increasing deviation from the bucket center and is approaching zero in the region of the separatrix, because a particle would come to rest at the unstable fixed point.

It can be calculated by making use of so-called action-angle variables, meaning that the Hamiltonian of the motion is transformed to a new set of variables ω and J. The action-angle variable J is defined as [31]

$$J(H) = \frac{1}{2\pi\omega_s}\oint \dot{\phi}(\phi)\, d\phi\,. \tag{2.39}$$

The integration has to be carried out over one full revolution of the trajectory $\dot{\phi}(\phi)$. The characteristic oscillation period of the system is then defined according to the first Hamilton equation for the set of new variables

$$\omega(H) = \frac{dH}{dJ} \qquad \text{or} \qquad T(H) = 2\pi\frac{d}{dH}J\,, \tag{2.40}$$

where $T(H)$ is the oscillation period in dependence of the Hamiltonian of the trajectory. In fact, the action-angle variable J and the characteristic frequency represent a canonically conjugated set of variables. Assuming that the RF bucket is symmetric around the reference energy, the circular integral can be converted to a conventional integration according to

$$T(H) = \frac{\sqrt{2}}{\omega_s}\int_{\phi_l}^{\phi_u} \frac{1}{\sqrt{H/\omega_s^2 - W(\phi)}}\, d\phi\,, \tag{2.41}$$

which finally leads to the general definition of the relative synchrotron frequency for a trajectory with the Hamiltonian H:

$$\frac{\omega(H)}{\omega_s} = \frac{\sqrt{2}\pi}{\displaystyle\int_{\phi_l}^{\phi_u} \frac{1}{\sqrt{H/\omega_s^2 - W(\phi)}}\, d\phi} .$$

The maximum phase deviations of the trajectory on both sides of the synchronous phase are described by ϕ_l and ϕ_u.

The distribution of the synchrotron frequency period in a stationary bucket results from inserting Eq. (2.26) into Eq. (2.41) and can be written as

$$T(\Delta\phi_u) = \frac{2}{\omega_s} \int_0^{\Delta\phi_l} \frac{1}{\sqrt{\sin^2(\Delta\phi_m/2) - \sin^2(\Delta\phi/2)}}\, d(\Delta\phi) , \tag{2.42}$$

where the Hamiltonian of the trajectory has been replaced by the maximum phase excursion $\Delta\phi_u$ of the trajectory concerned. As the trajectory is symmetric around the bucket center, this is also true for the maximum phase excursions, namely $\Delta\phi_l = -\Delta\phi_u$. By the use of the substitution

$$\zeta(\Delta\phi) = \arcsin\left[\frac{\sin(\Delta\phi/2)}{\sin(\Delta\phi_u/2)}\right] ,$$

the integral in Eq. (2.42) reduces to the conventional form of the complete elliptic integral of the first kind $K(x)$. Finally, one obtains

$$\frac{\omega(\Delta\phi_u)}{\omega_s} = \frac{\pi}{2K[\sin(\Delta\phi_u/2)]} \simeq 1 - \frac{\Delta\phi_u^2}{16} \tag{2.43}$$

for the synchrotron frequency as a function of the maximum phase deviation of the particle (Fig. 2.7).

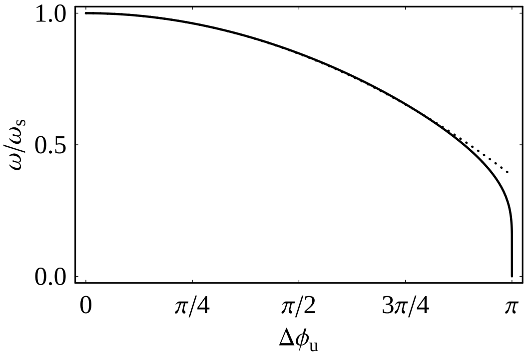

Fig. 2.7: Deviation of the synchrotron frequency versus maximum phase deviation of the trajectory in a stationary bucket. The exact curve is plotted as a solid line, while the approximation from Eq. (2.43) is dotted.

Clearly, $K[\sin(\Delta\phi_u/2)]$ becomes very large for $\Delta\phi_u = \pi$ meaning that the synchrotron oscillation becomes infinitely slow. The physical reason is that the particle motion theoretically comes to rest at the unstable fixed point.

In the case of an accelerating bucket generated by a single RF system, the calculation of a reasonable approximation is more lengthy (see App. D). The application of the Hamiltonian averaging technique [32] finally leads to [33, 34]

$$\frac{\omega(\Delta\phi_u)}{\omega_s} = 1 - \frac{1 + 2/3\sin^2\phi_0}{16(1 - \sin^2\phi_0)}\, \Delta\phi_u^2 . \tag{2.44}$$

2.3 Isolated and barrier buckets

Whereas most circular accelerators are operated with single or double harmonic sinusoidal RF systems, the derivation of the longitudinal Hamiltonian is not limited to sinusoidal amplitudes. Several applications demand other types of field configurations [16, 35, 36, 37], e.g. to generate very long buckets wherein particles can be held coasting beam-like, or to get a single, isolated RF bucket without neighbors.

Isolated and barrier buckets can be generated by a pulsed oscillating amplitude function $g(\phi)$ with only a single or a few localized RF periods per turn [38]. Depending on the polarity of the amplitude, either an isolated bucket or a barrier consisting of two open bucket boundaries is generated. Suppression of buckets [39] can be useful to avoid disturbing a stored beam by the influence of useless buckets, and barriers [40, 41] serve to create long buckets in between them. Fig. 2.8 schematically shows a sketch of amplitude, potential and longitudinal phase space for both cases.

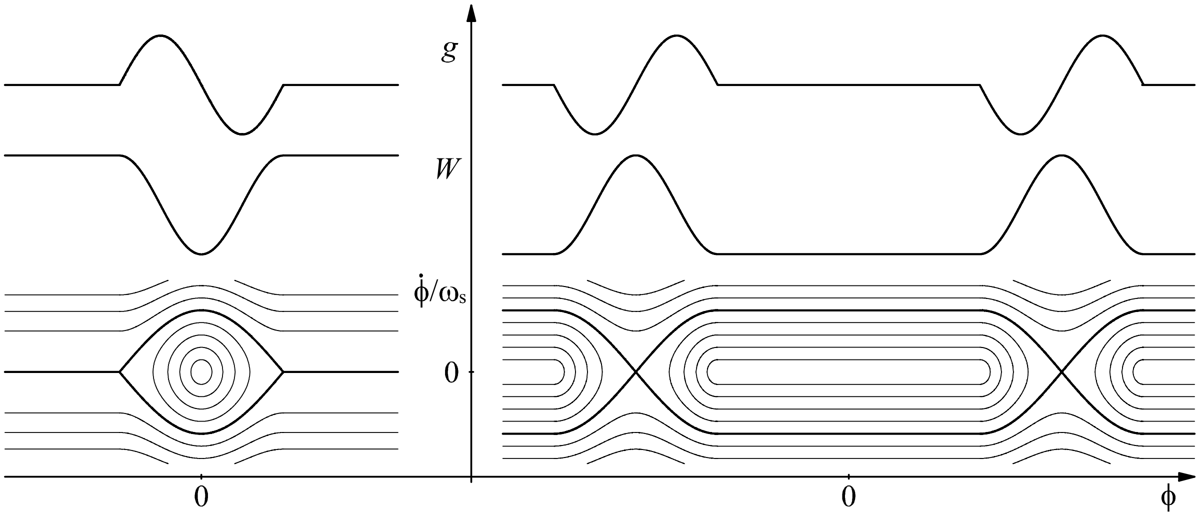

Fig. 2.8: RF amplitude g, potential W and the ϕ-$\dot{\phi}/\omega_s$-phase space of an isolated bucket (left) and a barrier bucket (right). Both cases are shown for the stationary case above transition energy.

In general, the RF amplitude of the single pulses does not need to be sinusoidal [42]. Triangular or square wave pulses can also be used, but they are more difficult to generate because of large amplitude components at higher harmonics of the revolution frequency. However, for a given peak voltage (see Tab. 2.1) a square wave bucket has the maximum energy acceptance and bucket area.

Wave form	Bucket height, $\dot{\phi}/\omega_s$ [rad/s]	Bucket area [rad^2/s]
Sinusoidal	2	16
Square wave	$\sqrt{2\pi} \simeq 2.51$	$4(2\pi)^{3/2}/3 \simeq 21.0$
Triangular	$\sqrt{\pi} \simeq 1.77$	$4\pi^{3/2}/\sqrt{2} \simeq 15.7$

Tab. 2.1: Comparison of normalized bucket height and area for different RF wave forms. For a given peak voltage, the square wave amplitude function generates the largest possible buckets.

2.3.1 Accelerated barrier buckets

In general, the total RF amplitude consists of an arbitrary number of single sinusoidal pulses centered around the phases $\phi_{b,n}$. Each of these pulses is defined by

$$g_n(\phi) = \begin{cases} \sin[h_b(\phi_{b,n} - \phi)] \ , & \phi_{b,n} - \dfrac{\pi}{h_b} \le \phi \le \phi_{b,n} + \dfrac{\pi}{h_b} \\ 0 \ , & \text{elsewhere} \end{cases} \ ; \tag{2.45}$$

the barrier frequency is defined by the harmonic number $h_b = 2\pi f_\mathrm{b}/\omega_0$, which is not necessarily an integer value as for a conventional RF system. The whole ensemble of pulses is periodic with the particle revolution. It is assumed for the subsequent derivations that $\phi_{b,n+1} > \phi_{b,n} + 2\pi/h_{b,n}$, namely that the sinusoidal pulses do not overlap each other.

The total RF amplitude is given by the sum $g(\phi) = \sum_n g_n(\phi)$ of these pulses and, according to Eq. (2.25), the potential function for an arbitrary number of isolated or barrier buckets can be written as

$$W(\phi) = -\frac{1}{\cos\phi_0} \begin{cases} g_0\phi + \dfrac{1}{h_b}\displaystyle\sum_n \left\{\cos\left[h(\phi - \phi_{b,n})\right] + 1\right\} \ , & \phi_{b,n} - \dfrac{\pi}{h_b} \le \phi \le \phi_{b,n} + \dfrac{\pi}{h_b} \\ g_0\phi \ , & \text{elsewhere} \end{cases} \ , \tag{2.46}$$

where g_0 is the normalized energy gain or loss per turn due to acceleration or synchrotron radiation. As for the conventional bucket, the stable phase angles and bucket boundaries can be found from the analysis of the potential $W(\phi)$.

The separatrix function is again obtained by equating $H(\phi, \dot{\phi}) = W(\phi_m)$:

$$\dot{\phi}(\phi) = \sqrt{\frac{2\omega_s^2}{\cos\phi_0}} \begin{cases} \sqrt{g_0(\phi_m - \phi) + \dfrac{1}{h_b}\displaystyle\sum_n \{\cos[h_b(\phi_1 - \phi_{b,n})] - \cos[h_b(\phi - \phi_{b,n})]\}} \ , \\ \qquad\qquad \phi_{b,n} - \dfrac{\pi}{h_b} \le \phi \le \phi_{b,n} + \dfrac{\pi}{h_b} \\ \sqrt{g_0(\phi_m - \phi) + \dfrac{1}{h_b}\displaystyle\sum_n \{\cos[h_b(\phi_1 - \phi_{b,n})] + n\}} \ , \\ \qquad\qquad \text{elsewhere} \end{cases} \ , \tag{2.47}$$

where the relative energy loss or gain can be written as $g_0 = \sin\phi_0$. It should be mentioned that the synchronous phase ϕ_0 represents only a parameter being defined via g_0. Two examples for accelerated barrier buckets are shown in Figs. 2.9 and 2.10. In fact, three different possibilities for the behaviour of a particle in such a long bucket can be distinguished:

Firstly, the particle is reflected at both of the potential barriers. The outer trajectories of the bucket in Fig. 2.9 behave like this. Secondly, the particle is reflected at one barrier but never reaches the second one. This can be the case when the energy loss or gain per turn is large enough so that the particle reaches the reference energy without any additional kicks from the RF system (inner trajectories of the phase space illustration in Fig. 2.9) . Thirdly, the energy deviation per turn can be so large that a particle in the inner region of a bunch never leaves the range of the first barrier. In such a case, it behaves exactly as in a conventional RF bucket. Furthermore, one can see from Figs. 2.9 and 2.10 that the symmetry of long barrier buckets is very sensitive to any kind of energy losses or gains, because a small g_0 causes significant distortion of the bucket. It is worth noting that a distortion of the barrier bucket potential due a resistive impedance can also initiate an asymmetry of a long bunch [43].

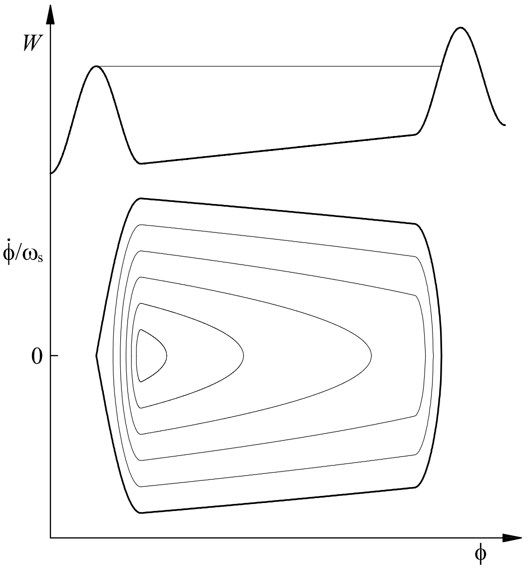

Fig. 2.9: Potential function and longitudinal phase space for a barrier bucket between two sinusoidal RF pulses. The synchronous phase parameter g_0 is 0.03.

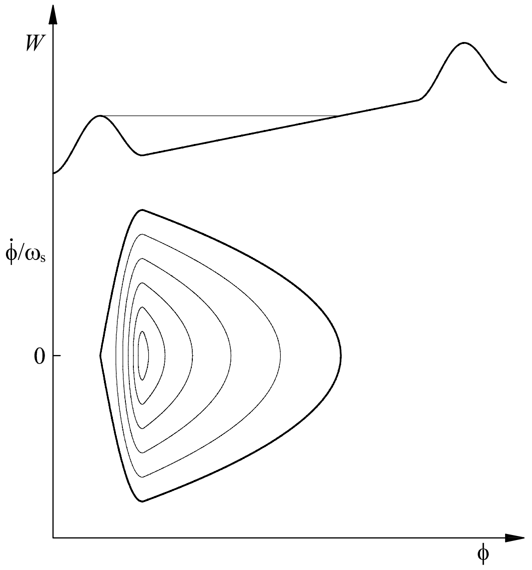

Fig. 2.10: Same plot as in Fig. 2.9 but for $g_0 = 0.12$. The bucket is very asymmetric and no particle can reach the second barrier.

The asymmetry of an accelerated barrier bucket can be compensated by means of special devices generating a pulsed field of constant amplitude g_0 during the passage of the long bunch.

2.3.2 Synchrotron frequency distribution

The synchrotron frequency distribution in an accelerated barrier bucket can be obtained again by differentiation of the action-angle variable J as shown in Sec. 2.2.6. It is calculated versus the distance of the a certain trajectory from the bucket center. For simplicity, the parameter ξ as defined in Fig. 2.11 has been chosen to characterize the trajectory. It describes the normalized phase difference between the position of the stable fixed point (synchronous particle) and the phase at which the trajectory crosses the reference energy.

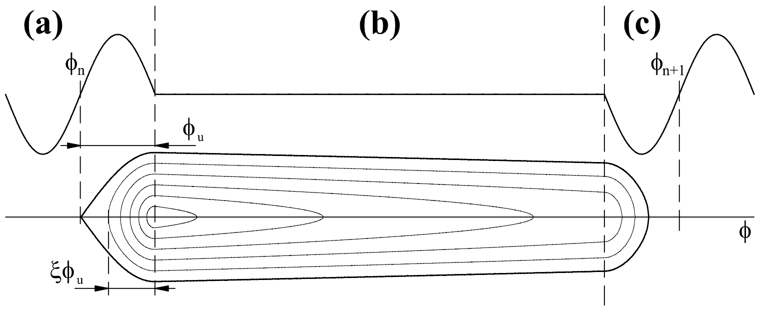

Fig. 2.11: Definition of the trajectory parameter ξ. Note that ϕ_u is slightly smaller then half of the barrier voltage pulse length $2\pi/h$.

The full synchrotron frequency distribution for barrier buckets with different synchronous phase angles ϕ_0 is illustrated in Fig. 2.12. At large synchronous phases, the synchrotron frequency distribution is very similar to the one in an ordinary RF bucket (see Fig. 2.7). However, in the stationary case $\phi_0 = 0$ it is completely different: particles with a small energy deviation oscillate very slowly. This is also the case for particles which are reflected in region

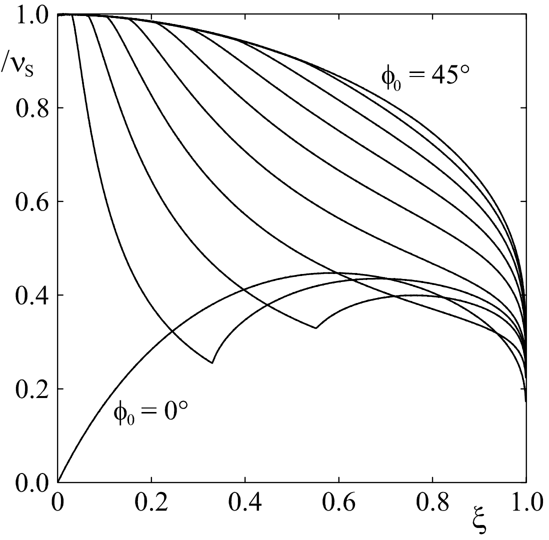

Fig. 2.12: Normalized synchrotron frequency versus trajectory parameter ξ. A value of $\xi = 0$ defines a particle at the stable fixed point, and $\xi = 1$ is the trajectory of the separatrix. The synchronous phase angle is decreased by 5^0 from one trace to the next.

(b) of Fig. 2.11. Especially when they approach the reference energy, the motion nearly comes to rest. For particles being reflected at the second barrier, the synchrotron frequency increases again. Clearly, the reflection under the influence of the RF focusing is faster than the reflection in the absence of RF focusing mentioned before.

2.4 Longitudinal particle tracking

Numerical tracking of particles is a complementary tool for the analysis of the longitudinal phase plane. Whereas the Hamilton technique delivers the whole ensemble of phase space trajectories, the same trajectories can be calculated iteratively by following a particle turn by turn.

The main advantage of numerical particle tracking is its full flexibility with respect to the variation of any external parameters like energy or RF amplitudes during the tracking. Therefore, a complete acceleration cycle or even complex manipulation of the RF voltage $U(\theta)$ or amplitude and phase modulations can be directly calculated.

Furthermore, effects caused by self-fields like space charge can be easily included in the simulation, provided that they can be described by an additional energy loss or gain per turn.

2.4.1 Mapping equations

To track a single particle for several revolutions in an accelerator, a one dimensional leap-frog algorithm is commonly used. As one simulation step per revolution is normally sufficient, it is assumed that all RF stations are concentrated at a single position in the machine. Starting from a given energy deviation of the test particle, its deviation of the revolution frequency with respect to the synchronous particle is calculated. This leads to the time or the phase θ at which the test particles arrives at the RF system. The particle gets an energy kick simply defined by the RF voltage at the time of the bunch passage. According to the energy kick, the energy deviation from the synchronous particle changes and the algorithm is restarted again by calculating the new revolution frequency of the subsequent turn (Fig. 2.13).

This algorithm can be expressed in the form of two tracking equations which are a discrete

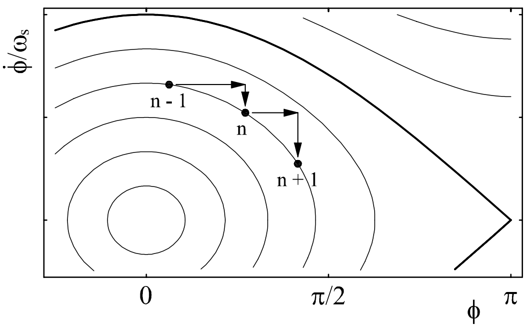

Fig. 2.13: Schematic illustration of the longitudinal tracking scheme. The new phase coordinate after one revolution is calculated and used to determine the jump in energy.

formulation of the two fundamental Hamilton equations (2.16) and (2.17):

$$\theta_{n+1} = \theta_n + 2\pi\,\eta/\beta^2(E_n/E_0 - 1) \tag{2.48}$$

$$E_{n+1} = E_n + q[U(\theta_{n+1}) + U_{\mathrm{sf}}(\theta_{n+1}) + \ldots]\,. \tag{2.49}$$

The combination of a phase variable θ to describe the particles position with respect to the RF system and the energy E or the energy deviation ΔE of the particle is the most common set of variables chosen for longitudinal particle tracking [44, 45, 46]. All RF systems which contribute to $U(\theta)$ are conventionally described by their frequency or harmonic number, their amplitude and their phase.

The special choice of phase space variables makes it very convenient for the simulation of RF systems at integer harmonics of the revolution frequency, because the phase angle is by definition periodic with the revolution frequency. However, particle tracking with non-integer harmonic RF systems, e.g. as longitudinal blow-up system, becomes more difficult: the phase of the RF must be recalculated for each revolution.

In most cases where particle parameters do not vary significantly during one revolution time, it is sufficient to update the Eqs. (2.48) and (2.49) once per revolution. However, in special cases like particle tracking under strong space charge forces or under the influence of a non-negligible energy loss per turn due to synchrotron radiation, the equations need to be updated several times per revolution.

As the mapping equations are directly based on the definition of the phase slip factor Eq. (2.12), their validity is not preserved in the vicinity of the transition energy. Higher order terms in Eq. (2.48) proportional to $(E_n/E_0 - 1)^2$ and higher orders have to be taken into account [47, 48, 45] if calculations around the transition energy or even of transition crossing have to be performed.

2.4.2 Initial beam distributions

The tracking of only few macro-particles is not sufficient to get the full information of the beam behaviour in a circular particle accelerator. Therefore, appropriate initial beam or bunch distributions have to be tracked to calculate parameters like phase and energy projections or emittance.

One can distinguish between two main classifications of distribution functions: those which have independent one-dimensional distributions along both axes and those which only have a radial distribution function and are symmetric in azimuth. The first group can be used to initiate a coasting beam as its initial phase distribution is uniform, while the latter is important to generate realistic bunches in the longitudinal phase space. The distributions and the projections of the two-dimensional distributions are summarized in Tab. 2.2 for the most common bunch types with a conventional RF field.

	One-dimensional	Two-Dimensional	Projection
Uniform	$\frac{1}{2\Delta\phi_m}$	$\frac{1}{\pi\Delta\phi_m\Delta E_m}$	Elliptic
Elliptic	$\frac{2}{\pi}\sqrt{1-\frac{\Delta\phi^2}{\Delta\phi_m^2}}$	$\frac{3}{2\pi}\sqrt{1-\frac{\Delta\phi^2}{\Delta\phi_m^2}-\frac{\Delta E^2}{\Delta E_m^2}}$	Parabolic
Parabolic	$\frac{3}{4}\left(1-\frac{\Delta\phi^2}{\Delta\phi_m^2}\right)$	$\frac{2}{\pi}\left(1-\frac{\Delta\phi^2}{\Delta\phi_m^2}-\frac{\Delta E^2}{\Delta E_m^2}\right)$	$\frac{8}{3\pi}\left(1-\frac{\Delta\phi^2}{\Delta\phi_m^2}\right)^{3/2}$
Gaussian	$\frac{1}{\sqrt{\pi}}e^{-\Delta\phi^2/\Delta\phi_m^2}$	$\frac{1}{\pi}e^{-\Delta\phi^2/\Delta\phi_m^2-\Delta E^2/\Delta E_m^2}$	Gaussian

Tab. 2.2: Common one- and two-dimensional particle distributions and their projection functions in normalized form. The function given for the one-dimensional distributions is only valid between $-\Delta\phi_m$ and $\Delta\phi_m$. The two dimensional distributions are defined in the range of $\Delta\phi^2/\Delta\phi_m^2 - \Delta E^2/\Delta E_m^2 \leq 1$ and vanish elsewhere. Only the Gaussian distribution is defined from minus to plus infinity.

Numerically, an arbitrary two-dimensional distribution $f(x, y)$ of random points can be calculated by generating equally distributed triplets of random numbers (x, y, z). If $f(x, y) > z$ the pair (x, y) is kept, otherwise it is rejected. Finally, the remaining points are distributed as defined by $f(x, y)$ [49].

2.5 Concept of emittance preservation

The area in the longitudinal phase space which is enclosed by the trajectory of a particle is called longitudinal single particle emittance. The emittance of a whole particle distribution is given by the phase space area occupied by the full set of particles. In a perfect accelerator without random energy dissipation like e.g. synchrotron radiation and without coupling between longitudinal and transverse planes, emittance is a parameter preserved throughout the acceleration cycle because of Liouville's theorem, which will be proven after an introduction to the different definitions of the longitudinal emittance.

2.5.1 Emittance definition

The emittance may be defined in many different ways whereof the most common one is the root mean square (RMS) emittance defined according to the convention from [50, 51]. For continuous distributions it can be written as

$$\varepsilon_{\mathrm{RMS}} = 4\sqrt{\overline{\Delta\phi^2}\cdot\overline{\Delta\dot{\phi}^2} - \overline{\Delta\phi\,\Delta\dot{\phi}}^2} \qquad \text{or} \qquad \varepsilon_{\mathrm{RMS}} = \frac{4}{N}\sqrt{\sum_{i=1}^{N}\Delta\phi_i^2\cdot\sum_{i=1}^{N}\Delta\dot{\phi}_i^2 - \left(\sum_{i=1}^{N}\Delta\phi_i\Delta\dot{\phi}_i\right)^2} \tag{2.50}$$

for an ensemble of N particles at positions $(\Delta\phi_i, \Delta\dot{\phi}_i)$ around the bunch center. The advantage of the RMS emittance definition is that it can be calculated for any arbitrary particle distribution. However, as there is no straightforward relationship to the phase space area occupied by the bunch, its physical interpretation may be ambiguous.

The elliptic emittance ε_l, which can be calculated by fitting an encircling ellipse around a certain fraction of the particle ensemble, is of equal importance. It gives directly the occupied phase space area, but may sometimes include plenty of empty phase space when the bunch distribution is totally non-elliptic. The elliptic emittance is very powerful with respect to the analysis of RF manipulations (see Chapter 3) because, as stated in the preceding sections, trajectories in the center of a harmonic bucket are also elliptic. Thus, even if plenty of empty phase space is included in the emittance area, this phase space will be consequently filled during the subsequent filamentation caused by the non-linearities of the bucket.

The scaling laws between both emittance definitions for the most common bunch distributions are summarized in Tab. 2.3.

	Uniform	Elliptic	Parabolic	Gaussian	
$\varepsilon_{\mathrm{RMS}} =$	$\frac{1}{\pi} \simeq 0.318$	$\frac{4}{5\pi} \simeq 0.255$	$\frac{2}{3\pi} \simeq 0.212$		ε_l (100 % inside)
				$\simeq 0.213$	ε_l (95 % inside)

Tab. 2.3: Scaling factors between RMS and elliptic emittance for the most common bunch distributions.

2.5.2 Liouville's theorem

Generally speaking, the motion of phase space density distribution behaves like an incompressible fluid [52].

Considering the evolution of a non-dissipative system containing a large number of mass points described by canonically conjugated pairs of space and momentum coordinates p_i and q_i, the equations of motion can be written in the form of the Hamilton equations, namely

$$\dot{q}_i = \frac{\partial H}{\partial p_i} \qquad \text{and} \qquad \dot{p}_i = -\frac{\partial H}{\partial q_i}\,, \tag{2.51}$$

where the dot denotes a time derivative. The Hamiltonian generally depends on the space and momentum coordinates as well as directly on time $H = H(p_i, q_i, t)$. Furthermore, a so-called velocity vector $\vec{v}_i = \{\dot{q}_i, \dot{p}_i\}$, which describes the particle velocity in the p-q-phase space can be defined. For a large number of particles, this velocity vector can be written in a continuous form $\vec{v}(p,q) = \{\dot{q}(q,p), \dot{p}(q,p)\}$ depending on the continuous position (p,q) in the phase space.

The change of the phase space volume occupied by the particle ensemble is expressed by the integrated flux through the surface $d\vec{f}$ of the volume according to

$$\frac{dV(t)}{dt} = \int \vec{v}\, d\vec{f}\,. \tag{2.52}$$

Following Gauss's law the surface integral can be converted to a volume integral

$$\int \vec{v}\, d\vec{f} = \int (\nabla \cdot \vec{v})\, dv = \int \left(\frac{\partial}{\partial q}\dot{q} + \frac{\partial}{\partial p}\dot{p}\right) dv = \int \left(\frac{\partial^2 H}{\partial q \partial p} - \frac{\partial^2 H}{\partial q \partial p}\right) dv = 0\,, \tag{2.53}$$

where $\nabla = \{\partial/\partial q, \partial/\partial q\}$ is the space momentum derivative operator. Applying the continuous form of the Hamilton equations (2.51) to the volume integral in Eq. (2.53) finally proves that the time derivative $dV(t)/dt = 0$ vanishes and that the phase space volume occupied by the particle ensemble remains constant. In particles accelerators, Liouville's theorem applies to the six-dimensional phase space spanned by three coordinates and their canonically conjugated momenta. Assuming small coupling between longitudinal and transverse motion, one may also apply the theorem to the two-dimensional longitudinal phase space.

Though the physical space volume is constant, the numerical values may, however, change with energy depending on the scaling of their reference frame. It is thus more convenient to express phase space area in units like [time · energy] = eVs where it remains invariant [21].

It is worth noting two major limitations of the rigorous validity of Liouville's theorem to particle bunches. On the one hand, it is restricted to continuous phase space distributions. Albeit each particle bunch typically contains some $N \simeq 10^9 \ldots 10^{13}$, it should be kept in mind that the number is finite. This granularity is used for the stochastic beam cooling [53, 54], which essentially moves empty phase between the particles from inner to outer regions of the bunch by exploiting deviations from a uniform continuous beam distribution. On the other hand, Liouville's theorem is only valid for non-dissipative systems. Energy exchange between two beams of different particle species can introduce such a dissipation mechanism, which is applied in electron cooling [55, 56], where the individual particles of a high energy proton or ion beam dissipate fractions of their individual transverse and momentum deviations to a cold electron beam.

2.5.3 Filamentation and emittance dilution

Emittance preservation on the basis of Liouville's theorem has been proven in the preceding paragraph. However, the boundary of the occupied phase space area can become arbitrary complex. In fact, filamentation can become so complex that it practically becomes impossible to distinguish between small theoretically unoccupied regions and occupied phase space areas. Literally, an infinite number of tiny regions of empty phase space is mixed with the bunch, and the macroscopic emittance grows while its microscopic counterpart remains unchanged.

An example of such an emittance dilution caused by a longitudinal mismatch between bunch and bucket is illustrated in Fig. 2.14. The development of RMS as well as elliptic encircling emittance (100 % of the particles inside) is given in Fig. 2.15. Clearly, the relative emittance growth in terms of RMS values is much smaller than what can be expected from the emittance growth calculated by encircling emittances. In fact, the particle density in the large outer

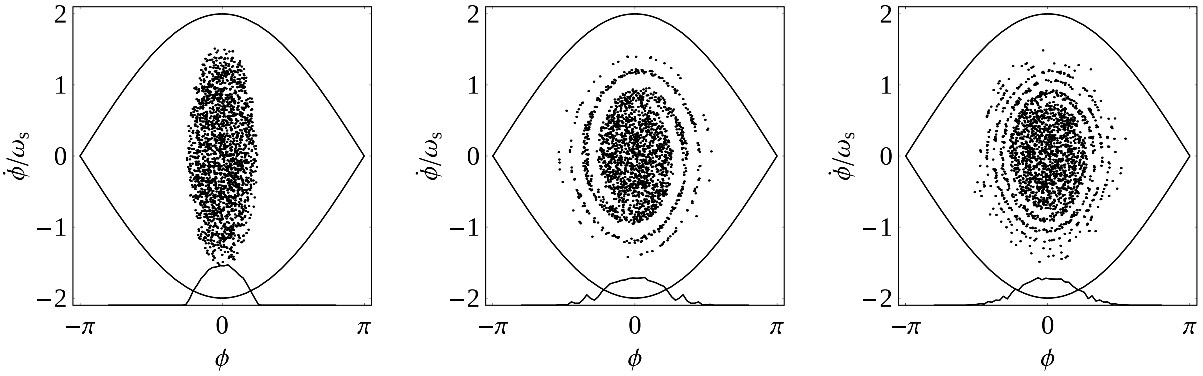

Fig. 2.14: Normalized longitudinal phase space plots of an unmatched bunch in a stationary RF bucket. The initial elliptic particle distribution is shown in the left picture. The distribution is strongly filamented after particle tracking for 10 (center) and 20 periods of the synchrotron frequency $2\pi/\omega_s$. Only every 10th particle of the distribution is plotted.

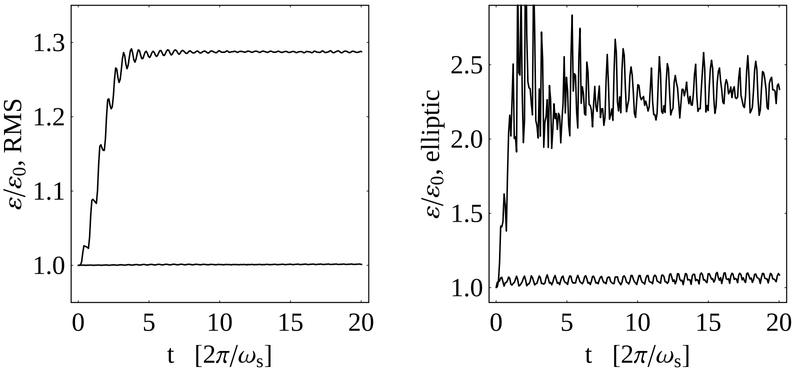

Fig. 2.15: Development of RMS (left) and elliptic (right) emittance of the bunch shown in Fig. 2.14. For reference, the emittances are also shown for a matched distribution. The small residual ripples on the elliptic emittance are caused by an initial mismatch of the elliptic bunch to the non-linear RF bucket. Note that the vertical scale of both plots is different.

regions of the diluted bunch is low, which has a significant effect on the elliptic emittance, as it contains all particles, but has a rather small effect on the RMS value.

Theoretically, macroscopic phase space dilution is reversible, e.g. transition crossing reverses the sign of motion in the longitudinal space charge, but practically this is of no use. Moreover, non-linear contributions to the particle motion generated by the self-fields of the beam cancel the reversibility.

2.6 Matched beam distribution

In the preceding sections only the interaction of a single particle with an external RF voltage or beam distributions adapted to a conventional RF field have been considered. For the calculation of all longitudinal beam parameters like mean and average current or bunching factor, it is mandatory to fill the RF bucket with a realistic beam distribution being matched to any kind of field configuration.

The distribution has to be chosen such that it is stationary in time, meaning that the synchrotron oscillations of the individual particles have no influence on the form of the distribution. In principle, all distributions $f(\phi,\dot{\phi})$ in the longitudinal phase space which can be expressed as a function of the Hamiltonian Eq. (2.24) are possible.

In proton and heavy ion accelerators it can be observed that the line density $\lambda(\phi)$ of a stationary bunch kept by a single RF system is mostly parabolic:

$$\lambda(\phi) = \frac{3N}{4\phi_m}\left(1 - \frac{\phi^2}{\phi_m^2}\right) . \tag{2.54}$$

As the line density is defined by the phase projection of the longitudinal distribution, it is simply given by [57]

$$f(\phi,\dot{\phi}) = \frac{3N}{2\pi}\sqrt{1 - \frac{\phi^2}{\phi_m^2} - \frac{\dot{\phi}^2}{\dot{\phi}_m^2}} . \tag{2.55}$$

Both line density and longitudinal distribution are normalized to the number of particles N in the bunch. The bunch is symmetric and ranges from $-\phi_m$ to ϕ_m and from $-\dot{\phi}_m$ to $\dot{\phi}_m$. It will be shown in the following section that a local elliptic $\dot{\phi}$ distribution can be matched to a more general RF amplitude $g(\phi)$. These distributions are stationary, even in the presence of space charge or an inductive wall impedance (see Sec. 2.7).

2.6.1 Local elliptic distribution

To account for the space charge or for an inductive wall like impedance, an additional self field term has to be added to the general Hamiltonian given in Eq. (2.24). As the additional voltage, which is generated by the longitudinal self-field of the beam, is proportional to the derivative $\partial\lambda(\phi)/\partial\phi$ of the line density, its contribution to the Hamiltonian is linear. According to the additional self-field term

$$W_{\mathrm{sf}} = c_{\mathrm{sf}}[\lambda(0) - \lambda(\phi)] \tag{2.56}$$

the potential function from Eq. (2.25) is replaced by

$$W(\phi) = W_{\mathrm{RF}} + W_{\mathrm{sf}} = \frac{1}{\cos\phi_0}\left[\int g(\phi)\,d\phi - g(\phi_0)\phi\right] + c_{\mathrm{sf}}[\lambda(0) - \lambda(\phi)]\,, \tag{2.57}$$

where c_{sf} is a constant scaling factor of the self-field contribution (see Sec. 2.7).

The $\dot{\phi}$ projection of distribution $f(\phi,\dot{\phi})$ must reproduce the line density given by the bunch boundary trajectory in the longitudinal phase space. Therefore, a distribution composed of slices in ϕ being elliptic with respect to $\dot{\phi}$ is assumed [58]. The energy width of each slice is defined according to the value of the bunch boundary trajectory, and the general ansatz for the longitudinal particle distribution becomes

$$f(\phi,\dot{\phi}) \propto \sqrt{2[H_0 - \omega_s^2 W(\phi)] - \dot{\phi}^2}\,, \tag{2.58}$$

where H_0 is the Hamiltonian of the boundary trajectory. The projection of this distribution becomes

$$\begin{aligned} \lambda(\phi) &= 2\lambda_0\omega_s^2[W(\phi_m) - W(\phi)] \\ &= 2\lambda_0\omega_s^2[W_{\mathrm{RF}}(\phi_m) - W_{\mathrm{RF}}(\phi) + c_{\mathrm{sf}}\lambda(\phi)]\,, \end{aligned} \tag{2.59}$$

where $\lambda(\phi)$ is generally still present on both sides of the equation.

Solving Eq. (2.59) for λ and subsequent normalization cancels the self-field contribution to the line density which can be reduced to

$$\lambda(\phi) = \frac{N}{u_m}[W_{\mathrm{RF}}(\phi_m) - W_{\mathrm{RF}}(\phi)] \quad \text{with} \quad u_m = \int_{\phi_m}^{\phi_n} W_{\mathrm{RF}}(\phi_m) - W_{\mathrm{RF}}(\phi)\,d\phi\,. \tag{2.60}$$

The absence of the self-field terms in the line density indicates that a bunch of the given distribution generates an additional RF amplitude $U_{\mathrm{sf}}(\phi)$ of exactly the same ϕ dependence as the external RF voltage. The remaining effect is an additional longitudinal focusing or defocusing [59]. A schematic illustration of a stationary distribution in a double harmonic RF system is shown in Fig. 2.16. In the region of the bunch, the calculated bucket including space charge (Fig. 2.16, solid lines) is slightly smaller than that without any self fields (dashed lines). However, the form of the trajectories remains the same. As expected for a linear RF amplitude $g(\phi) \propto \phi$, the line density Eq. (2.60) as well as the longitudinal distribution function Eq. (2.58) reduce to Eqs. (2.54) and (2.55).

2.6.2 Single harmonic matching conditions

For a single harmonic RF system in an accelerator at fixed energy and negligible energy loss per turn due to effects like synchrotron radiation, the matching conditions can be calculated

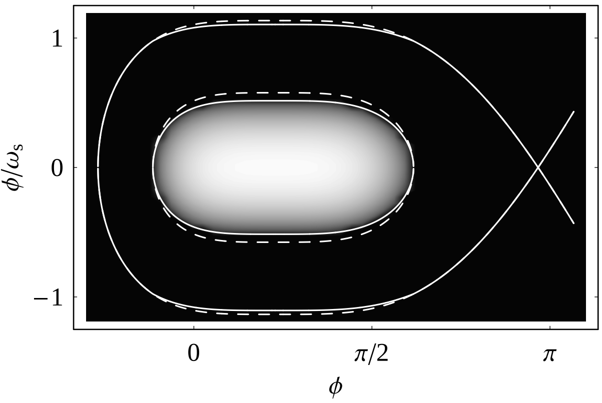

Fig. 2.16: Stationary longitudinal distribution of a bunch in an accelerating double harmonic RF system. Each vertical slice of the bunch represents an elliptic distribution. The dashed lines represent separatrix and bunch boundary trajectory neglecting linear space charge. It is taken into account for the calculation of the continuous lines.

analytically. According to the RF potential function $W_{\mathrm{RF}}(\phi) = 1 - \cos\phi$ the matched line density from Eq. (2.60) is written as

$$\lambda(\phi) = \frac{N}{u_m}(\cos\phi - \cos\phi_m) \quad \text{with} \quad u_m = 2(\sin\phi_m - \phi_m \cos\phi_m) \tag{2.61}$$

where it was assumed that the bunch is symmetric around $\phi = 0$ and extends to $\pm\phi_m$. It is worth noting that replacement of the sin and cos functions in Eq. (2.61) by their third and second order Taylor series approximation again results in the line density Eq. (2.54).

By inserting the line density into Eq. (2.57), one obtains the Hamiltonian

$$\begin{aligned} H(\phi,\dot{\phi}) &= \frac{1}{2}\dot{\phi}^2 + \omega_s^2\left(1 + c_{\mathrm{sf}}\frac{N}{2[\sin\phi_m - \phi_m\cos\phi_m]}\right)(1-\cos\phi) \\ &\simeq \frac{1}{2}\dot{\phi}^2 + \omega_s^2\left(1 + c_{\mathrm{sf}}\frac{3N}{2\phi_m^3}\right)\frac{1}{2}\phi^2 \end{aligned} \tag{2.62}$$

for the stationary bucket, including the effects of space charge and inductive wall impedance. In fact, the particles follow elliptic trajectories

$$\frac{\dot{\phi}^2}{\omega_s^2[1 + 3c_{\mathrm{sf}}N/(2\phi_m^3)]\phi_m^2} + \frac{\phi^2}{\phi_m^2} = 1$$

whose axes ratio is defined by $\dot{\phi}/\phi = \omega_s[1 + 3c_{\mathrm{sf}}N/(2\phi_m^3)]^{1/2}$.

By expressing the bunch length in terms of the emittance $\varepsilon_l = \pi\Delta\phi\Delta E$ one obtains

$$\phi_m^2 = \frac{1}{\sqrt{1 + 3c_{\mathrm{sf}}N/(2\phi_m^3)}}\frac{h^2\omega_0^2|\eta|}{E\beta^2}\frac{\varepsilon_l}{\pi\omega_s}\,, \tag{2.63}$$

where ϕ_m still appears on both sides of the equation. However, Eq. (2.63) is of the cubic type and can be solved analytically. As the solution is rather lengthy, it shall not be given here.

Neglecting the self field term $c_{\mathrm{sf}} = 0$, bunch length and energy spread simply become

$$\phi_m^4 = \frac{2\pi|\eta|h^3\omega_0^2}{E\beta^2\, e\pi^2 U_0}\varepsilon_l^2 \quad \text{and} \quad (\Delta E_m)^4 = \frac{hU_0\, E\beta^2 e\omega_0^2}{2\pi^3|\eta|}\varepsilon_l^2\,. \tag{2.64}$$

The bunch length in units of RF phase shrinks only inversely proportional to the fourth root of the RF voltage. Bunch length control by variation of the RF voltage is thus not very efficient.

2.7 Space charge and inductive wall impedance

Only the dynamics of single particles have been covered so far, and no interaction of the particles has been considered. However, all particles of the beam have the same charge, resulting in a repulsive force between the particles. In the ultra-relativistic case, space charge does not harm the particle bunches as the electric field around each particle is Lorentz boosted to a disk so that the influence on other particles is strongly suppressed. In low and medium energy accelerators, space charge is an important issue. As will be shown, the influence of the beam pipe walls can also influence the beam behaviour similarly to space charge effects, but its influence does not vanish at high energies.

2.7.1 Longitudinal space charge voltage

For the derivation of the longitudinal self-field caused by the space charge, a particle beam with a radius a is assumed to circulate in a beam pipe of the radius b. The line density of the particle beam is defined as $\lambda(z) = \omega_0/(\beta c)\lambda(\phi)$. The definitions of variables and the choice of the coordinate system are sketched in Fig. 2.17.

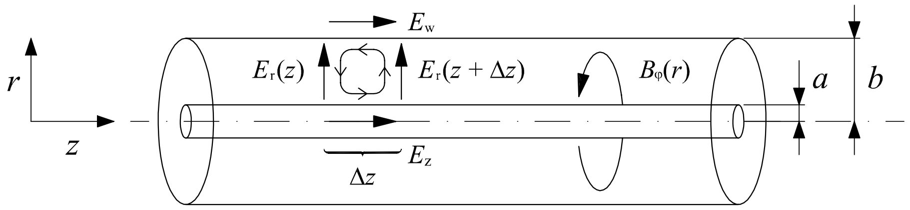

Fig. 2.17: Definition of variables and integration path for the derivation of space charge field E_z as well as the influence of finite conductivity of the beam pipe wall represented by $E_w \neq 0$.

The radial electric field of the beam can be written as

$$E_r(r,z) = \frac{e\lambda(z)}{2\pi\epsilon_0}\frac{r}{a^2} \quad \text{at} \quad r \leq a \qquad \text{and} \qquad E_r(r,z) = \frac{e\lambda(z)}{2\pi\epsilon_0}\frac{1}{r} \quad \text{at} \quad r > a \tag{2.65}$$

and the azimuthal magnetic induction as

$$B_\varphi(r,z) = \frac{\mu_0 e\lambda(z)\beta c}{2\pi}\frac{r}{a^2} \quad \text{at} \quad r \leq a \qquad \text{and} \qquad B_\varphi(r,z) = \frac{\mu_0 e\lambda(z)\beta c}{2\pi}\frac{1}{r} \quad \text{at} \quad r > a\,. \tag{2.66}$$

As long as the variation of $\lambda(z)$ is small compared to the transverse dimensions of the beam pipe, the other field components can be neglected. For low and medium energy accelerators this is certainly the case, as typical bunch lengths are of the order of several meters, while the beam pipe radius is only a few centimeters.

Using the fields from Eqs. (2.65) and (2.66), application of the curl-E Maxwell equation

$$\oint \vec{E}\, d\vec{l} = -\frac{\partial}{\partial t}\int \vec{B}\, d\vec{\varrho} \tag{2.67}$$

along the integration path illustrated in Fig. 2.17 reduces Eq. (2.67) to

$$(E_z - E_w)\Delta z + \frac{e}{4\pi\epsilon_0}\left(1 + 2\ln\frac{b}{a}\right)[\lambda(z+\Delta z) - \lambda(z)] = -\frac{\mu_0 e\beta c}{4\pi}\frac{\partial\lambda(z)}{\partial t}\left(1 + 2\ln\frac{b}{a}\right)\Delta z\,,$$

where the difference quotient $[\lambda(z+\Delta z)-\lambda(z)]/\Delta z$ can be replaced by $\partial\lambda(z)/\partial z$ and $\partial\lambda(z)/\partial t = -\beta c\partial\lambda(z)/\partial z$. Resolving for the space longitudinal electric acting on the beam due to space charge (see Fig. 2.17), one obtains

$$E_z = -\frac{e}{4\pi\epsilon_0} g_0 \left(1-\beta^2\right) \frac{\partial\lambda(z)}{\partial z} + E_w \qquad \text{with} \qquad g_0 = 1 + 2\ln\frac{b}{a}\,. \tag{2.68}$$

It is worth noting that g_0 is a geometry factor [60] given for a circular beam pipe, but that it can be modified by form factors so that the space charge field derivation remains approximately valid also for ellipsoidal or rectangular beam pipes [61]. The voltage contribution per turn is calculated by integration over one revolution according to

$$U_s = -e\beta c R \frac{\partial\lambda(z)}{\partial z} \frac{g_0 Z_0}{2\beta\gamma^2} + 2\pi R E_w\,, \tag{2.69}$$

where $Z_0 = \sqrt{\mu_0/\epsilon_0}$ is the free space impedance. As the integration has to be done in a reference frame which is rotating with the beam resulting in a constant $\lambda(z)$, it simplifies to a multiplication with the circumference of the accelerator. For perfectly conducting beam pipes, the field E_w along the wall vanishes.

Below the transition energy, space charge acts against an external RF voltage and thus has a defocusing effect. Above transition, the space charge impedance generates additional focusing. The influence is however small because of the energy scaling proportional to $1/(\beta\gamma^2)$.

2.7.2 Wall coupling impedance

To calculate the contribution of the beam pipe wall in terms of a frequency dependent impedance, Eq. (2.69) must be analyzed for a single Fourier component of the beam current. In general, the beam current can be written as

$$I(z,t) = I_0 + \sum_n I_n e^{i(n\,z/R-\omega t)} \tag{2.70}$$

a Fourier sum where I_0 is the average DC current. Inserting a single component I_ω into the space charge induced voltage from Eq. (2.69) it reduces to

$$U_\omega = Z I_\omega = I_n e^{i(n\,z/R-\omega t)} \left[-i\frac{g_0 Z_0}{2\beta\gamma^2} + Z_w\right]\,, \tag{2.71}$$

where the line density was replaced by the beam current according to $I_n = \beta c e \lambda_n$. The mode number n is defined with respect to the bunch frequency $h\omega_0$. In the case of a circular accelerator symmetrically filled with h identical bunches [44], the normalized impedance can be written as

$$\frac{Z}{nh} = -i\frac{g_0 Z_0}{2\beta\gamma^2} + \frac{Z_w}{nh}\,. \tag{2.72}$$

Clearly, the space charge impedance acts capacitively on the beam, and the longitudinal space charge effect can be partly compensated or even completely canceled by introducing a special, inductive wall impedance. Dedicated devices may consist of special coil configurations [62] or ferrite loaded structures around the beam pipe [63].

Finally, the total voltage contribution induced by space charge and wall coupling impedance can be written as

$$U_s = -eh^2\frac{\beta c}{R}\left(Z_w - \frac{g_0 Z_0}{2\beta\gamma^2}\right)\frac{\partial\lambda(\phi)}{d\phi} \tag{2.73}$$

and the contribution of the self-field as introduced in Sec. 2.6.1 is consequently defined by

$$c_{\text{sf}} = \frac{1}{U_0 \cos \phi_0} e h^2 \frac{\beta c}{R} \left(Z_w - \frac{g_0 Z_0}{2\beta\gamma^2} \right) . \tag{2.74}$$

Eq. (2.73) is also employed to include space charge and wall coupling effects into numerical tracking calculation as it delivers the voltage U_{sf} (see Sec. 2.4.1) for the projection $\lambda(\phi)$ of an arbitrary bunch shape [64].

2.8 Synchrotron radiation

Accelerated charged particles emit radiation in the form of electromagnetic waves. In circular accelerators, each bending magnet causes transverse acceleration and thus initiates the emission of so-called synchrotron radiation. As will be briefly shown, synchrotron radiation is an important issue in electron accelerators, but is strongly suppressed in hadron machines because of their larger particle mass. Even though the effect of synchrotron radiation below the TeV energy region is negligible in proton accelerators, it has already been observed [65].

The emitted energy per revolution can be calculated by integrating the instantaneous power radiated by transverse acceleration over the path of the particle through the bending magnets [66]:

$$\Delta E_{\text{rad}} = \frac{e^2}{3\epsilon_0 (m_0 c^2)^4} \frac{E^4}{R_{\text{mag}}} , \tag{2.75}$$

where R_{mag} is the average bending radius as used in Sec. 2.1.2. Clearly, the energy loss depends on the fourth power of the rest mass of the particle species, and a proton emits only $8.8 \cdot 10^{-14}$ times the energy of an electron at the same energy.

The total average radiated power

$$P_{\text{rad}} = 88.5\,\text{kW} \cdot \frac{(E/\text{GeV})^4}{R_{\text{mag}}/\text{m}} \cdot I_b/\text{A} \text{ for electrons and } P_{\text{rad}} = 7.79\,\text{kW} \cdot \frac{(E/\text{TeV})^4}{R_{\text{mag}}/\text{m}} \cdot I_b/\text{A} \text{ for protons} \tag{2.76}$$

in units of $[P] = \text{kW}$ can be obtained by summing over the total charge of the beam and taking into account that the average beam current is defined as $I_b = Ne\omega_0/(2\pi)$. Note that the energy unit in both equations between quantities is different.

In the LHC at an energy of 7 TeV, the average energy loss per turn is about 6.71 keV. Depending on the focusing RF voltage acting on the beam, the synchrotron radiation loss may be neglected. This is certainly the case for the nominal RF system, which will deliver some 16 MV to the beam.

Chapter 3

Longitudinal Beam Gymnastics

In the preceding chapter, the interaction between a particle beam and an RF systems with constant parameters has been analyzed. However, parameters need to be changed during the acceleration cycle, and it is mandatory to modify the RF settings in the presence of the beam. The most obvious example is the RF capture, where the RF amplitude is slowly increased to form a bunch structure after beam injection from a linear accelerator. Furthermore, it may be necessary to prepare a special longitudinal beam configuration with respect to the number of bunches, the bunch current or the bunch length for an experiment or a downstream accelerator. Changing the longitudinal beam parameters can also be required to maintain beam stability during an acceleration cycle. These so-called longitudinal beam gymnastics are addressed in the following sections.

An introduction to the concept of adiabaticity for beam manipulations is given, followed by the fundamentals of the different types of longitudinal beam manipulations relevant for the different options of the beam preparation in the LHC and its injectors. Finally, the longitudinally matched beam transfer between two circular accelerators is discussed.

3.1 Adiabaticity

The reference time scale for motion in the longitudinal phase space is the period of the synchrotron motion $2\pi/\omega_s$. As long as an external variation of the RF parameters is slow compared to this period, the particles can follow the slowly changing trajectories without perturbation. If the parameter variation is too fast, a mismatch between bunch and bucket occurs which results in filamentation and macroscopic emittance blow-up.

Therefore two different types of RF manipulations can be distinguished: adiabatic and non-adiabatic RF gymnastics. The first group is based on slow variations of the RF parameters. In the limit of perfect adiabaticity, meaning infinite duration, these manipulations virtually generate no dilution in the phase space. Additionally, adiabatic beam manipulations are generally reversible.

On the contrary, their non-adiabatic counterparts are based on a well defined mismatch between bunch and bucket to excite an oscillation or a fast motion of the bunch. Precise timing is mandatory for non-adiabatic RF manipulations.

A dimensionless parameter to specify whether an RF manipulation is adiabatic or not is called adiabaticity coefficient α [67]. In general, it is defined as the relative variation of the characteristic oscillation frequency within a single oscillation period[1]:

$$\alpha = 2\pi \frac{1}{\omega^2} \frac{d\omega}{dt} \,. \tag{3.1}$$

It should be mentioned that there is no strict limit between adiabatic and non-adiabatic motion with is respect to the adiabaticity coefficient. However, if α stays well below unity, the bunch motion is assumed to be mostly adiabatic. In fact, adiabaticity is a trade-off between the time duration available for a certain RF manipulation and the dilution of the particle distribution. Additionally, dilution caused by intensity dependent effects may also influence the optimum duration of beam manipulations.

3.2 Adiabatic RF gymnastics

Ideally, adiabatic RF gymnastics preserve the equilibrium bunch distribution at all times during the procedure, and the longitudinal emittance remains constant. It should be noted that adiabaticity in longitudinal beam dynamics is conventionally not defined exactly the same way as in thermodynamics, where adiabaticity means the preservation of the intrinsic energy. Consequently, adiabaticity in accelerator physics should be referred to as reversibility.

3.2.1 Bunching and debunching

The longitudinal structure of a particle beam coming from a linear accelerator used as pre-accelerator is different from the required RF structure in a synchrotron. Generally the injected beam is held at constant energy without any RF voltage to let the longitudinal beam distribution debunch.

The resulting coasting beam is then bunched by a slowly increasing RF amplitude at an integer harmonic of the revolution frequency. This amplitude variation can be optimized with respect to adiabaticity: the synchrotron frequency ω_s (see Eq. 2.19) is proportional to the square root of the RF amplitude so that amplitude variation has to be slower in the region of small amplitudes to preserve the longitudinal emittance. Optimized RF amplitude ramps with a constant adiabaticity parameter can be obtained by inserting $\omega_s(U)$ into the definition Eq. (2.19), which leads to the adiabaticity parameter

$$\alpha = \frac{2\pi}{\omega_0} \sqrt{\frac{2\pi E \beta^2}{h|\eta|e}} \cdot \frac{1}{2U(t)^{3/2}} \frac{d}{dt} U(t) \tag{3.2}$$

with respect to an arbitrary RF voltage function $U(t)$. By solving this differential equation for $U(t)$ the iso-adiabatic voltage curves can be written as

$$U(t) = \frac{U_1}{\left(1 - \frac{t}{t_{\text{bunch}}} \frac{\sqrt{U_2} - \sqrt{U_1}}{\sqrt{U_2}}\right)^2} \,, \tag{3.3}$$

where U_1 and U_2 are the RF voltages before and after the bunching procedure. The bunching time is given by

$$t_{\text{bunch}} = \frac{2\pi}{\omega_0} \sqrt{\frac{2\pi E \beta^2}{h|\eta|e}} \frac{\sqrt{U_2} - \sqrt{U_1}}{\sqrt{U_1 U_2}} \frac{1}{\alpha} \,. \tag{3.4}$$

---

[1] The adiabaticity parameter is sometimes given in a convention exclusive of 2π, see [68].

Clearly, the choice of the bunching time is a compromise according to its inverse proportionality to the adiabaticity parameter [69]. The non-zero initial voltage arises no practical problem as the smallest RF voltage technically achievable is limited anyway and blow-up caused by a finite voltage during injection is small [70].

The emittance blow-up during RF capture can be calculated by particle tracking. The typical development of the RMS emittance as well as the RF amplitude ramp is sketched in Fig. 3.1. After the bunching procedure, the particle tracking was continued for ten periods of the revolution frequency to allow further filamentation to a quasi equilibrium distribution. It is worth noting that especially the bunching procedure to capture the injected beam is influenced by longitudinal space charge forces [71], as it is performed at low particle energy.

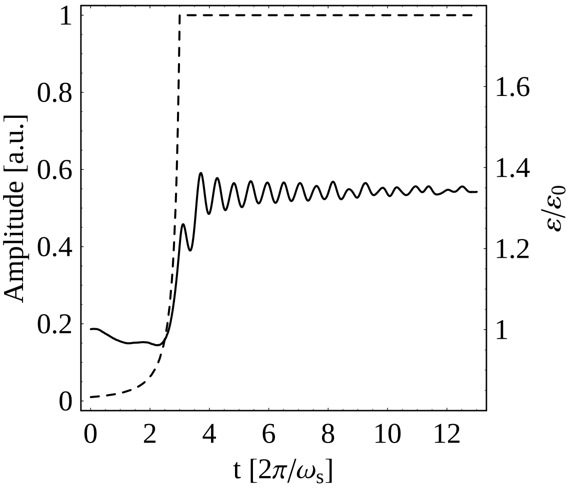

Fig. 3.1: RMS emittance development during bunching with an iso-adiabatic RF amplitude ramp with $\alpha = 3$ (continuous, right scale). The dashed curve represents the normalized RF amplitude (left scale). The voltage ratio between initial and final amplitude is 0.01. The tracking calculation was continued for ten periods of the synchrotron frequency to include the macroscopic emittance growth due to filamentation.

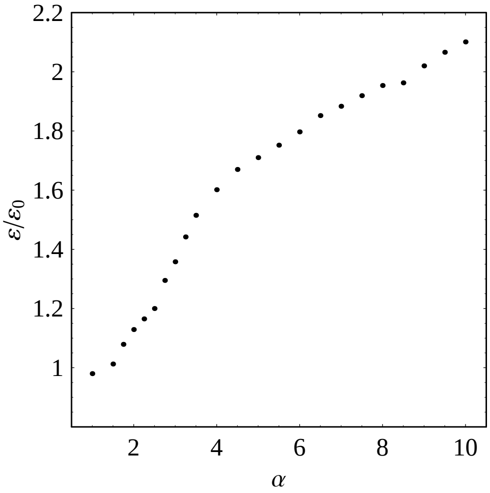

Fig. 3.2: Macroscopic emittance blow-up versus adiabaticity coefficient. For the same conditions as the example in Fig. 3.1. For an adiabaticity parameter below unity, the capture can be theoretically performed with negligible dilution in the longitudinal phase space.

Of equal importance for the dilution of the bunches in the longitudinal phase space is the capture frequency. For the simulations above it is an integer harmonic of the revolution frequency. However, the revolution frequency is not known exactly, since the output energy of a linear accelerator as pre-accelerator may jitter from pulse to pulse.

Furthermore, the RF amplitude is often not raised to its maximum value at fixed beam energy. The acceleration is started as soon as the beam is sufficiently bunched, and a further increase of the RF amplitude compensates the shrinkage of the bucket area due to the increasing synchronous phase angle (see Sec. 2.2.5). In such a way, the transition between injection at constant energy and acceleration can be performed smoothly.

3.2.2 Bunch merging and splitting

In order to increase the intensity per bunch, two or even more bunches can be joined together by the use of a double harmonic RF system. This manipulation is called bunch merging [72, 73], which belongs to the group of adiabatic RF manipulations. The reverse process, bunch splitting

[74], increases the number of bunches in the accelerator. During bunch merging, the potential well between two neighboring RF buckets is removed by slowly switching to a lower harmonic RF system. The splitting manipulation is more delicate because an initial bunch has to be divided in two equal parts, requiring an RF potential of well defined symmetry.

The RF potential generated by a double RF system with the two harmonics $h_1 = 2h_0$ and $h_2 = h_0$ and the amplitudes U_1 and U_2 can be written as

$$W(\phi) = \frac{1}{h_0}[U_1(\cos h_0\phi - 1) + \frac{U_2}{2}(\cos 2h_0 - 1)]\,. \tag{3.5}$$

The merging or splitting process is then controlled by the variation of the two voltages U_1 and U_2. A straightforward choice for the voltages are linearly time dependent functions:

$$U_1(\xi) = U_{1,0}\xi \qquad \text{and} \qquad U_2(\xi) = U_{2,0}(1 - \xi)\,, \tag{3.6}$$

where the parameter ξ describes the normalized fraction of the procedure. For such a simple case, the evolution of amplitudes, separatrix function and bucket center is illustrated in Fig. 3.3. One bunch has to be slightly accelerated while the other one is decelerated at the same rate so that they meet in the center. For linear amplitude ramps the motion of the bucket centroid starts slowly but ends abruptly after two thirds of the process. This sudden variation may cause emittance dilution. Potential improvements of this scheme are discussed in Sec. 5.2.5.

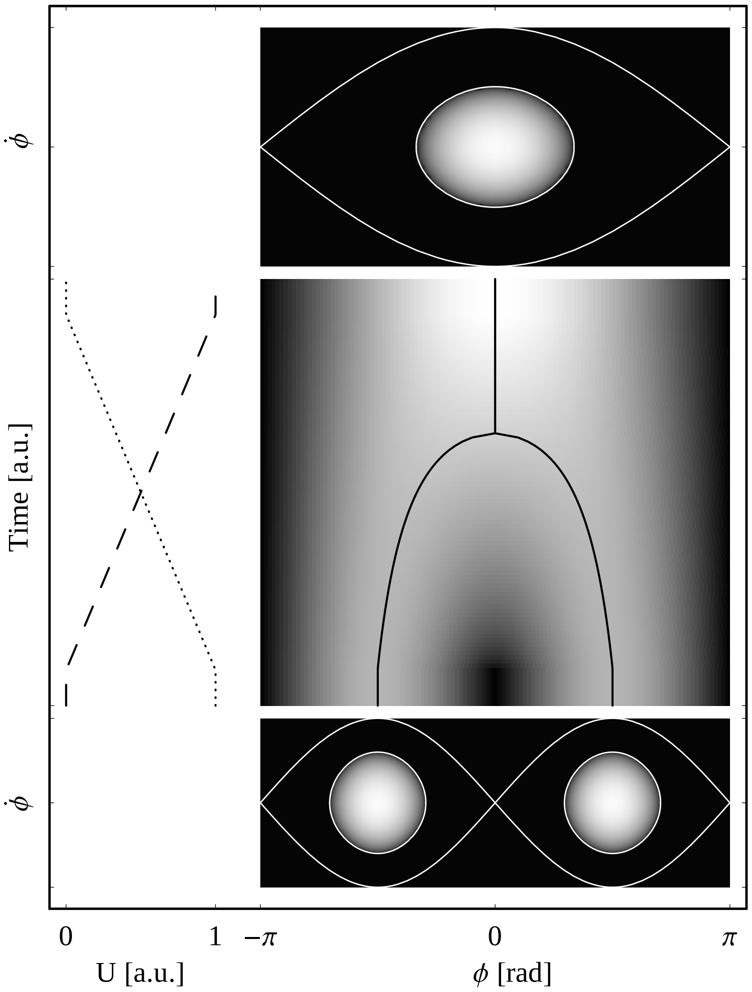

Fig. 3.3: Evolution of RF amplitudes (left, dashed and dotted), separatrix function and bucket center position (continuous) with time during bunch pair merging (time goes from bottom to top) or bunch pair splitting (time goes from top to bottom). The gray level is proportional to the height of the separatrix function $\dot\phi(\phi)$.

As the particle intensity is doubled during bunch merging, the longitudinal emittance of the final bunch cannot be smaller than the sum of both initial bunches. The final bunch length and energy spread are simply defined by placing a bunch with the given emittance into a matched bucket as calculated in Eq. (2.64). For a constant ratio between bunch length and energy spread before and after a bunch merging or bunch splitting, the higher harmonic RF amplitude $U_{2,0}$ has to be half of the RF amplitude at the half of the frequency $U_{1,0} = U_{2,0}/2$. Both bunch length and energy spread grow by a factor of $\sqrt{2}$ in the perfect case [72].

Bunch merging and splitting turn out to be experimentally clean procedures, and the macroscopic emittance dilution can be kept in the range of some 10-20 % [75]. Bunch pair merging as well as splitting and also splitting of a single bunch into three equal parts has been proven to work reliably in synchrotrons [76]. More sophisticated merging or splitting procedures are theoretically possible [77], at the expense of a large number of RF systems acting simultaneously on the beam.

So far it was assumed that only the amplitudes of the RF systems are varied while their phase angle remain constant with respect to each other. This implies a symmetry between the two bunches being merged. By an additional variation of the phase, the clean merging of two bunches with different longitudinal emittances and different bunch population can be achieved [78]. Even the extreme case, where a populated bunch is asymmetrically merged with a bunch of zero emittance, is very useful: it redistributes the longitudinal particle density so that the bunch is turned inside out [79, 80], resulting in a hollow bunch distribution. The appropriate phase and amplitude ramps can be calculated from the derivation of the ratio of both sub-buckets during the bunch merging.

3.2.3 Batch compression

Bunch merging or splitting affects the number of bunches, but their distribution around the ring remains unchanged. However, it is also possible to modify the length of a whole bunch train, called batch, by means of RF manipulation [81, 82].

A bunched beam held by an RF system working at the harmonic h_1 can be transferred to the buckets of a second RF system operating on harmonic h_2 provided that the two harmonics are not too different, e.g. $h_2 = h_1 + 1$. These bunches can be handed over adiabatically by slowly decreasing the amplitude of the lower harmonic while simultaneously increasing the amplitude of the higher harmonic. As the batch length is given by the RF wavelength multiplied by the number of bunches in the batch, the whole batch is thus compressed by a factor of h_2/h_1. Repetitive application of this harmonic hand-over allows batch compression from any harmonic number to another harmonic number as long as the required frequencies are covered by the RF system. Additionally, a limitation of the RF amplitude may lead to insufficient bucket area at the end of the compression manipulation. According to Eq. (2.38), the bucket area shrinks at constant RF amplitude proportionally to $1/h^{3/2}$, while the bunch emittance stays constant or increases during the process.

Furthermore, the presence of two RF harmonics at the same time leads to amplitude modulation, which effectively modulates the RF focusing and the bucket area along the bunch train. According to

$$\begin{aligned} U_1 \sin(h_1 \omega_0 t) + U_2 \sin(h_2 \omega_0 t) = {} & (U_1 - U_2) \sin(h_1 \omega_0 t) \\ & + U_2 \left[2 \sin\left(\frac{h_1 + h_2}{2} \omega_0 t \right) \cos\left(\frac{h_1 - h_2}{2} \omega_0 t \right) \right] , \end{aligned} \tag{3.7}$$

the beat frequency occurs at half the revolution frequency $(h_2 - h_1)/2\omega_0 = \omega_0/2$ if the two harmonics differ by unity. The modulation is strongest when both RF amplitudes are equal.

An example of the evolution of the buckets during batch compression is given in Fig. 3.4. Starting from four bunches held by an RF system at the fourth harmonic, the bunch train is gradually transferred to $h = 6$ and this compressed by a factor of 1.5. For simplicity, all voltage variations are assumed to be linear. As expected, the four buckets are always identical when only one RF system is present, while quadrupole-like oscillations of the bucket shape can be observed during the hand-over process. These oscillations, caused by the amplitude modulation mentioned above, are much stronger for the two buckets at the end of the batch.

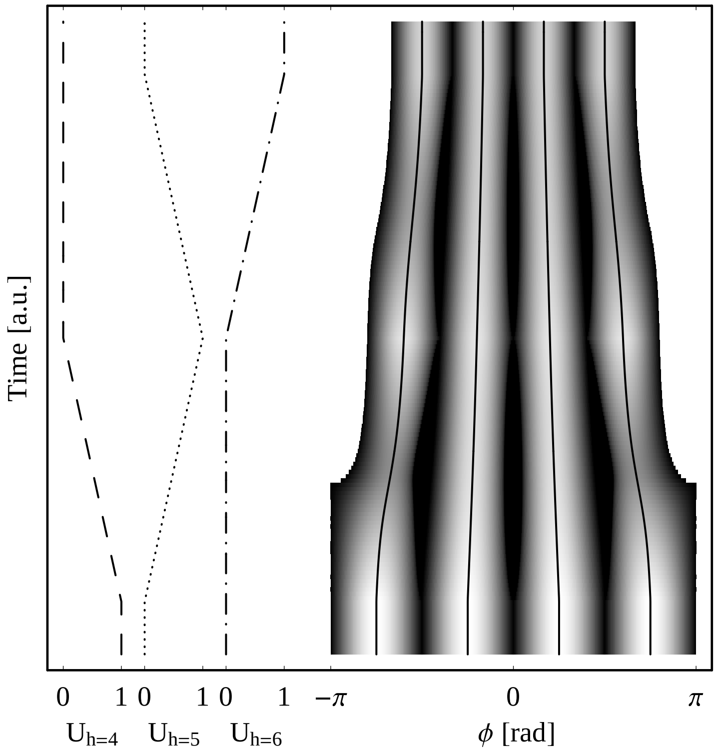

Fig. 3.4: Evolution of RF amplitudes (left, dashed, dotted, dashed-dotted) for three different RF harmonics from $h = 4$ to $h = 6$, separatrix function and bucket center positions (continuous) with time during batch compression. The direction of the time axis is from bottom to top. The gray level is proportional to the height of the separatrix function $\dot{\phi}(\phi)$.

It should be mentioned that even though the trajectories in the longitudinal phase space calculated with the Hamilton technique are symmetric around the reference energy axis and the center of the batch compression, this does not apply to the real bunch motion. As the outer bunches have to be accelerated or decelerated with respect to the center bunches, their centers of gravity ascend or descend during each batch compression harmonic hand-over. However, the motion is symmetric around the center point $(\Delta\phi = 0, \Delta E = 0)$ of the batch compression. A detailed optimization with respect to this effect is given in Sec. 5.2.4.

The same behaviour can be clearly observed in the evolution of the bucket areas during the process (Fig. 3.5). In the middle of the hand-over process, the bucket areas become minimal. The buckets at the ends (dashed) suffer more from this area reduction than the center buckets (continuous).

When the bunch trains get longer, the bucket area modulation gets worse, and the bucket area at the end of the batch shrinks enormously. Complete buckets are in the region of low RF focusing, which is not the case for short batches where the effective RF voltage is small only for a fraction of the end buckets. This effect can be suppressed by additional amplitude modulation to increase the RF focusing at the end bunches (see Sec. 5.2.4).

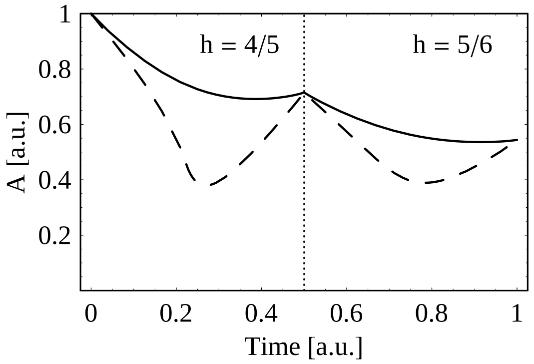

Fig. 3.5: Bucket area versus time for the same batch compression parameters as in Fig. 3.4. The two center buckets (continuous) have a significantly larger bucket area than the two bunches at the ends of the batch (dashed line).

Furthermore, the minimum bucket areas can be increased by a factor of $\sqrt{2}$ by changing the voltage program of each harmonic hand-over. If the higher harmonic RF amplitude is increased to its maximum value before the amplitude at the lower harmonic is decreased, both amplitudes are at their maximum value when the amplitude modulation is strongest [81].

3.3 Non-adiabatic RF gymnastics

A different class of longitudinal beam manipulations is represented by non-adiabatic RF gymnastics, where the RF parameters change much faster that the period of the synchrotron frequency, i.e. $\alpha \gg 1$.

Two examples for non-adiabatic manipulations that are important for the long bunch scheme for LHC are described in the subsequent sections: bunch rotation and bunch lengthening by fast stretching at the unstable fixed point. By use of these schemes, bunch length and energy spread can be controlled. Two methods for the production of high intensity bunches are briefly presented at the end of this section.

3.3.1 Bunch rotation

According to the analysis in Sec. 2.6.2, Eq. (2.64), bunch length and energy spread of a matched bunch can be controlled by varying the RF amplitude U_0. This method is however not very efficient because both parameter only scale with its fourth root. On the one hand, the available RF voltage may not be sufficient for an adiabatic bunch compression to a desired length. On the other hand, it may be impossible to lengthen a bunch by lowering the RF voltage, as the bucket area becomes too small or the beam induced voltage hampers the precise amplitude control in the low voltage regime. Bunch shortening or lengthening is mostly needed to prepare the bunches for extraction to a downstream accelerator [83, 84] or a target [85]. In such cases a dedicated excitation of a coherent quadrupole mode by sudden change of the RF amplitude called bunch rotation, combined with a fast ejection of the bunch at the right instant, allows to generate bunch parameters which would be conventionally inaccessible within the limits of the RF system [86].

Neglecting effects originating from the self field of the beam, the compression factor is derived from the simple synchrotron Hamiltonian [87]. The combination of both Eqs. (2.64) defines the RF voltage for a matched bunch of given length to energy spread ratio:

$$\frac{U}{h} = \frac{2\pi|\eta|}{E\beta^2 e} \cdot \left(\frac{\Delta E_m}{\Delta\phi_m}\right)^2 . \tag{3.8}$$

Assuming that the RF system is switched to an amplitude U_f, a particle starting at $(\Delta\phi = \Delta\phi_i, \Delta E = 0)$ moves to $(\Delta\phi = 0, \Delta E = \Delta E_f)$ within one quarter period of the synchrotron frequency. A particle starting at maximum energy deviation of the initial bunch is simultaneously converted into a particle with largest energy deviation $\Delta\phi_f$. Application of Eq. (3.8) according to

$$\frac{U_i}{h_i} \propto \left(\frac{\Delta E_i}{\Delta\phi_i}\right)^2, \quad \frac{U_f}{h_f} \propto \left(\frac{\Delta E_f}{\Delta\phi_i}\right)^2 \quad \text{gives} \quad \chi = \frac{\Delta\phi_f}{\Delta\phi_i} = \frac{\Delta E_i}{\Delta E_f} = \sqrt{\frac{U_i h_f}{U_f h_i}} \tag{3.9}$$

for the compression ratio between initial and final bunch length. Clearly, for an unchanged harmonic number $h_i = h_f$ the bunch length now depends on the square root of the RF voltage, and a bunch rotation is thus much more efficient than an adiabatic bunch compression. A recapture of the rotating bunch requires a voltage U_r as calculated from Eq. (2.64). The relation between the three RF amplitudes concerned can be written as $U_f^2 = U_i U_r$.

Due to the non-linearity of the synchrotron frequency as discussed in Sec. 2.2.6, this theoretical compression factor is only achieved in the center of the bucket. The distortion of the bunch caused the synchrotron frequency distribution is illustrated in Fig. 3.6. The bunch core is rotated linearly by $\pi/2$, whereas the outer regions of the distribution suffer from a reduced synchrotron frequency resulting in tails. This can be observed in the line density projection plot (Fig. 3.6, right).

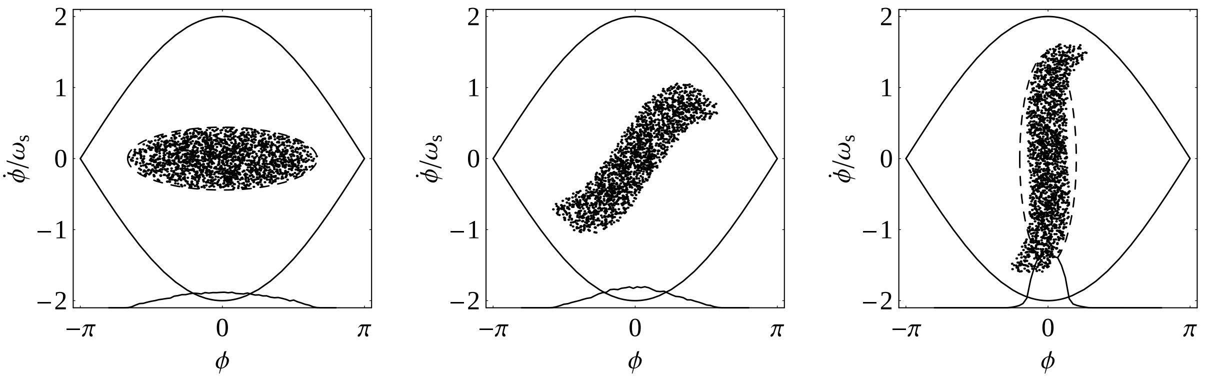

Fig. 3.6: Longitudinal phase space during bunch rotation of a bunch covering about two thirds of the bucket, with a compression factor of $\chi \simeq 3.4$. If the rotation was perfectly linear, the final bunch (right) would match the emittance ellipse (dashed). The RMS emittance is diluted by some 10 %. Only every 10th particle of the tracked distribution is plotted.

The non-linearity of the synchrotron frequency can be suppressed by adding a higher harmonic RF amplitude in order to obtain a triangular-like waveform in the range of the bucket (see App. C). The RF voltage demanded for bunch compression is reduced by another factor of almost two if the RF focusing is increased during bunch rotation such that each particle is affected by a locally constant amplitude [88]. This is achieved by the use of a double harmonic RF system which linearizes the RF amplitude during the first part of the bunch rotation when the bunch still covers a large fraction of the bunch. Thereafter, the higher harmonic amplitude is reduced to zero and finally increased with the opposite phase, to improve the RF focusing around the bunch, which then covers only a small fraction of the bucket length.

It is worth noting that the performance of the bunch rotation may be restricted by the longitudinal space charge effect as it counteracts the external RF focusing [89, 90, 91].

3.3.2 Bunch stretching at the unstable fixed point

In principle, the easiest way to stretch bunches in a circular particle accelerator is to switch off all RF systems and let the bunches decay due to dispersion. The initial bunch is sheared, and for a distribution with an elliptic boundary trajectory the bunch length $\Delta\phi_m(t)$ increases according to

$$\Delta\phi_m(t) = \Delta\phi_m(0)\sqrt{1+\frac{t^2}{t_d^2}} \qquad \text{with} \qquad t_d = \frac{E}{2|\eta|h\omega_0\beta^2}\cdot\frac{\Delta\phi_m(0)}{\Delta E_m} = \frac{\tau(0)}{2|\eta|\Delta p/p}\,, \tag{3.10}$$

where t_d is the so-called debunching time and $\tau(t)$ the bunch length in time units [92]. Its inverse proportionality to the energy spread leads to slow lengthening of bunches with a small energy spread.

For a faster bunch stretching, the bunch can be moved to the unstable fixed point by an RF phase jump of π. Switching back the RF phase brings the bunch centroid back to the stable fixed point again, but now it is mismatched to the RF amplitude and starts to rotate in the longitudinal phase space [93] as described above.

An example of bunch stretching at the unstable fixed point is shown in Fig. 3.7. The RMS emittance stays nearly constant for about an eighth rotation and starts to grow exponentially afterwards.

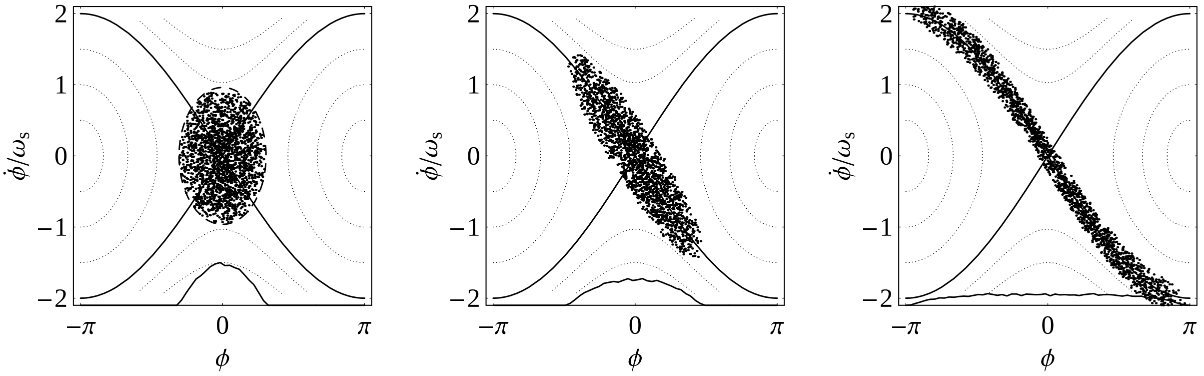

Fig. 3.7: Development of a bunch with an elliptic boundary trajectory matched to the bucket (left) at the unstable fixed point. After one eighth of the period of the synchrotron frequency the bunch is stretched with virtually no dilution (center). Finally, after a quarter of the period $2\pi/\omega_s$ it is already distorted (right).

Neglecting the non-linearity of the RF bucket, the equation of motion of a particle around the stable fixed point is simply a harmonic oscillation as the potential function $W(\Delta\phi)$ is proportional to the $\Delta\phi^2$ (see Sec. 2.2.3). At the unstable fixed point the sign of the RF amplitude as well as the sign of the potential changes by π and $W(\Delta\phi) \propto -(\Delta\phi)^2$. The equation of motion for a particle starting on the boundary trajectory becomes

$$\frac{d}{dt}\Delta\phi_m(t) - \omega_s^2\Delta\phi_m(t) = 0$$

with the solution

$$\Delta\phi_m(t) = \Delta\phi_m(0)e^{\omega_s t} \qquad \text{and} \qquad \Delta E_m(t) = \Delta E_m(0)e^{-\omega_s t} \tag{3.11}$$

for the exponential growth of the bunch length. The longitudinal emittance, which is proportional to $\Delta E_m \Delta\phi_m$ for a bunch with an elliptic boundary, needs to stay conserved during the stretching. As a result the energy spread of the bunch is simultaneously compressed.

Such a bunch stretching is a common technique for the generation of a mismatch between bunch and bucket to initiate a rotation for bunch compression. Only the RF phase must be manipulated, which is a major advantage of this technique.

3.3.3 Bunch coalescing

Bunch rotation cannot only be applied to a single bunch, but also to a complete batch of bunches. This procedure, called bunch coalescing[2], is used for the production of high intensity bunches in storage rings [95, 96, 97]. The three steps of bunch coalescing for a batch of three bunches are illustrated in Fig. 3.8. The two bunches shaded in gray show that the gaps at both ends of the batch are mandatory.

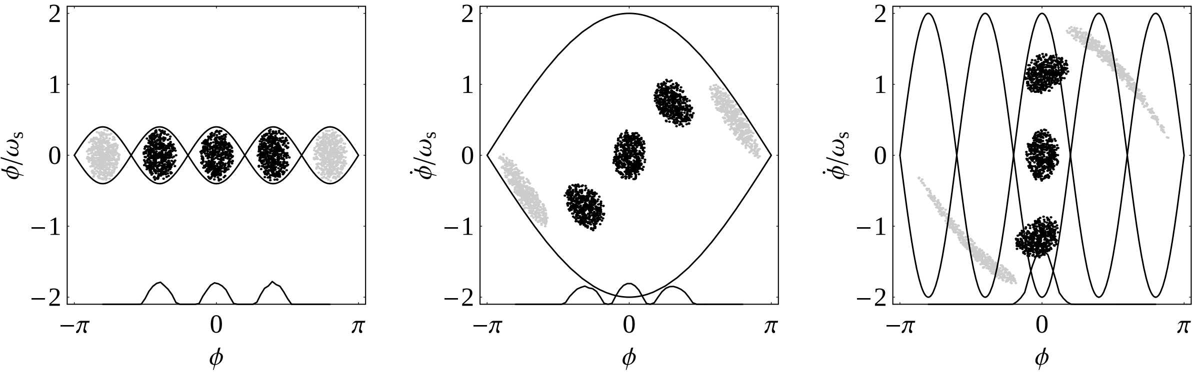

Fig. 3.8: Bunch coalescing of three bunches to a single high intensity bunch. The initially matched batch (left) is rotated in a lower harmonic bucket, whose bunch length covers more than the batch length. When the bunches are stacked vertically, the whole batch is short enough to be recaptured in one of the initial buckets, but at much higher voltage (right). After several periods of the synchrotron frequency, the subsequent filamentation enforces a matched bunch. Two additional bunches (shaded) have been tracked to show that the bucket during rotation needs to be significantly longer than the batch. As these bunches are not mapped to a bucket, they must not be populated to prevent them from unintentionally being distributed over several buckets.

Starting from a batch of n matched bunches (Fig 3.8, left) held by an RF system at the harmonic h_1, the RF amplitude at h_1 is rapidly switched off while a second RF at significantly lower harmonic h_2 is switched on (center). The lower harmonic h_2 is chosen so that the bucket length covers more than the whole length of the initial batch, namely $h_2 \lesssim 2/3 h_1/n$. Similar to the bunch rotation the whole ensemble of bunches starts to rotate in the longitudinal phase space and the bunch configuration is literally modified from a horizontal bunch train to a stack of bunches placed vertically in the longitudinal phase space. The approximate RF voltage for the batch rotation can be determined according to Eqs. (2.64) assuming that the center bunch remains matched. The voltage therefore given by $U_{\text{rot}} \simeq h_1/h_2 U_i$. It can be optimized more accurately by numerical tracking calculations so that the bunches are closely piled up on top of each other and the longitudinal emittance blow-up is minimized.

---

[2] In the literature a different procedure to combine electron bunches by bunch interchange between two circular accelerators is also known as bunch coalescing [94].

Finally, after a quarter period of the synchrotron frequency π/ω_s the whole vertical bunch stack is recaptured into a single bucket of the original harmonic number h_1 (Fig. 2.64, right), but at much larger voltage. The final bucket needs to provide a bucket height as large as the RF bucket during rotation and becomes $U_f \simeq h_1/h_2 U_{\mathrm{rot}} = (h_1/h_2)^2 U_i$. Even if the bunches are perfectly stacked on top of each other, the final RF amplitude $U_f \simeq n^2 U_i$ must be significantly larger than the initial amplitude.

The subsequent filamentation removes the structure of the initial bunches, and a single matched and dense bunch with n times the initial bunch intensity remains. It is worth noting that the main disadvantages of bunch coalescing are its inherent longitudinal emittance blow-up and the large dynamic range required for the amplitude of the RF system.

3.3.4 Slip stacking

A significant increase of the bunch intensity can also be achieved by a similar vertical stacking method called slip stacking [98]. It is based on the fact that two particles with different energy slip in phase with respect to each other. The phase difference per turn is calculated according to Eq. (2.14). This is also true for complete bunches with an energy offset, but as mentioned in Sec. 3.3.2, without RF focusing the bunches themselves also decay under the influence of the energy dependent revolution frequency of the individual particle. However, as the energy separation of both bunches is large enough, RF focusing can be provided for each bunch individually, because the trajectories of stationary buckets with an energy deviation much larger than the bucket height approach straight lines. The bucket for the first bunch has thus negligible influence on particles of the second bunch that are sufficiently far away from the center energy of the bucket and vice versa.

For slip stacking, two bunches or even batches of bunches are either injected off-energy [99, 100] or separated in energy by accelerating the first while decelerating the second batch [101, 102]. The energy separation of both batches during the relative drift should be as large as possible, but it is limited by the energy acceptance of the accelerator (Fig. 3.9, top).

The energy separation is defined by a dimensionless parameter in terms of frequency separation normalized to the synchrotron frequency $\alpha = \Delta f / f_s$. According to the height of the stationary bucket as given in Eq. (2.37) it can be easily shown that $\alpha = 4$ for an energy separation of two bucket heights so that the separatrices just touch. The choice of α depends on the available energy acceptance as well as on the length of the time interval during which the batches are drifting. The parameter α usually ranges from five to ten [101].

When both bunches or batches have the same phase position so that they are on top of each other, a separation in the range of $\alpha \gtrsim 3$ is however too large for a recapture of pairs of bunches into common buckets. Consequently, the energy separation is reduced by decelerating and accelerating both beam fractions closer to the reference energy (Fig. 3.9, bottom left). The emittance dilution caused by the insufficient energy separation is not severe since the rapprochement can be fast with respect to the synchrotron frequency. Finally, the two bunches or batches have the same phase position and a small energy deviation with respect to the reference energy. The off-energy RF systems acting on one half of the particles each with slightly different frequencies can then be switched off and the full beam is handed over to a third RF system generating buckets large enough to enclose pairs of original bunches at reference energy. After recapture, the bunch intensity is doubled (Fig. 3.9, bottom left). The final RF amplitude must be at least four times larger than each of the initial voltages, because the double bucket height is needed to capture the two bunches. As in the case of bunch coalescing, the two bunches are merged and diluted into a bunch being matched to a bucket of the final RF

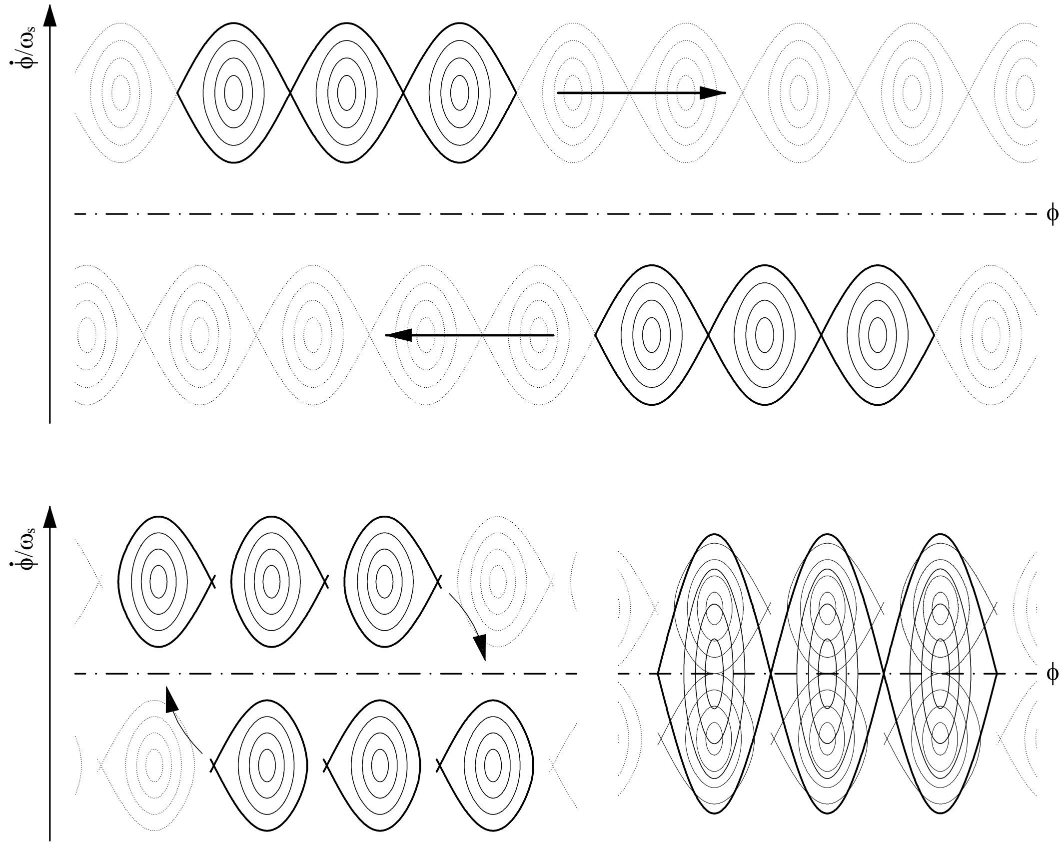

Fig. 3.9: Schematic sketch of the longitudinal phase space during slip stacking of two three bunch batches. Initially, the batches are positioned at an energy offset causing a phase slip with respect to each other (top). To prevent the dispersive decay of the bunches, each batch is held by its own RF system creating off-energy buckets. The separation parameter is $\alpha \simeq 7$. To approach both batches for recapture with a single RF system, the two batches are accelerated and decelerated closely to the reference energy (bottom left). When both batches have the same phase and their energy difference has been minimized, the bunches are recaptured in pairs so that the bunch intensity is doubled.

amplitude whose center energy coincides with the reference energy of the accelerator.

Slip-stacking has the same disadvantage as bunch coalescing: a non-negligible blow-up of the longitudinal emittance cannot be avoided as the last step of the manipulation is not adiabatic. The RF voltage has to be lowered towards the recapture and therefore its control is not trivial at high beam currents [103] because of the beam induced voltage (beam loading).

3.4 Barrier bucket RF gymnastics

Barrier buckets enable many RF manipulations which are not accessible with conventional RF gymnastics. These manipulations are mostly based on the possibility of arbitrary phase variations of the RF barriers. Various schemes for acceleration [104], bunch compression [105, 106], longitudinal beam stacking [36, 107, 108], bunch core separation [109, 110] and beam cooling [111] have been suggested or already put into operation.

3.4.1 Adiabatic moving barrier compression

In contrast to a conventional bucket created by one or more sinusoidal RF amplitudes, barrier buckets offer a further degree of freedom which enables an additional class of adiabatic longitudinal beam manipulations: the RF phase between the two ends of the buckets, the potential barriers, is not fixed anymore. By moving the phase of the barrier at one side of a barrier bucket, the bucket in between can be stretched or compressed. According to Liouville's theorem, the occupied longitudinal phase space stays constant and the energy spread increases or decreases simultaneously with decreasing or increasing bunch length.

When the phase variation of the barrier pulse is fast compared to the particle motion, the moving barrier can cause a dilution of the macroscopic emittance. The condition for adiabaticity according to Eq. (3.1) cannot be applied directly to barrier buckets because of their large synchrotron frequency spread (see Sec. 2.3.2) which grows almost proportionally to the energy spread.

The fundamental blow-up mechanism of an RF barrier moving in phase with respect to the revolution frequency is illustrated in Fig. 3.10. A particle being reflected at the barrier has an increased energy deviation induced by the movement of the barrier. The RF barrier can be treated as two open halves of a conventional stationary bucket. If the particle is reflected within the linear region, the increase in energy deviation can be written as

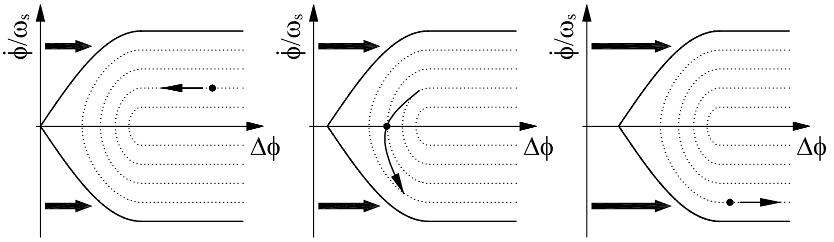

Fig. 3.10: Sketch of one particle being reflected at a moving barrier. The phase movement of the barrier gives the an additional energy kick to the particle such that it energy deviation ΔE increases during the reflection.

$$\dot{\phi}_f = \dot{\phi}_i + \frac{1}{2}\hat{\dot{\phi}}\left.\frac{d\phi}{dt}\right|_{\text{barrier}}\frac{\pi}{\omega_s}\,, \tag{3.12}$$

where $\hat{\dot{\phi}}$ is the bucket height of the stationary bucket and ω_s its synchrotron frequency as calculated in Sec. 2.2. The phase velocity of the RF barrier is described by $d\phi/dt|_{\text{barrier}}$. The particle on a trajectory on the bunch boundary has an initial energy deviation of $\dot{\phi}_i$, which changes to $\dot{\phi}_f$ after the reflection.

In the case of perfect adiabaticity, the energy spread of the bunch boundary also grows as the barrier bucket is slowly compressed during the barrier movement, and the bunch emittance remains constant. For a long barrier bucket where the phase space area inside the RF barriers is negligible compared to the area of the homogeneous section, the bunch emittance is approximately twice the product of bunch length and energy deviation at the boundary trajectory of the bunch.

Equating the bunch emittance before and after half a period of the synchrotron frequency during barrier movement, the growth of energy deviation becomes

$$\dot{\phi}_f|_{\text{adiab.}} = \frac{\phi_l}{\phi_l - \pi/\omega_s \cdot d\phi/dt|_{\text{barrier}}}\,\dot{\phi}_i\,, \tag{3.13}$$

where ϕ_l is the initial phase length of the long bunch. A dimensionless parameter for the adiabaticity is obtained by comparing the ideal increase in energy spread $\dot{\phi}_f|_{\text{adiab.}}$ with the energy spread according to Eq. (3.12):

$$\beta = \left(\dot{\phi}_i + \frac{1}{2}\hat{\dot{\phi}}\,\frac{d\phi}{dt}\bigg|_{\text{barrier}} \frac{\pi}{\omega_s} \right) \left(\phi_l - \frac{\pi}{\omega_s} \cdot \frac{d\phi}{dt}\bigg|_{\text{barrier}} \right) / \phi_l \dot{\phi}_i \,. \tag{3.14}$$

The adiabaticity parameter should be chosen as close to unity as possible. It is worth noting that the phase velocity of the moving barrier can be increased during the bunch compression because, as on can see from Eq. (3.14), the adiabaticity parameter β shrinks with increasing $\dot{\phi}_i$.

Adiabatic bunch compression by moving barriers takes a rather long time compared to the timescale of conventional RF gymnastics: therefore, compression schemes with improved performance have already been proposed [106].

3.4.2 Non-adiabatic barrier RF stacking

An important example for non-adiabatic manipulations with barrier buckets is the so-called barrier RF stacking [112, 113, 114]. For this manipulation, a moving RF barrier is used to convert an injected coasting beam which occupies a rectangular shape in the longitudinal phase space to a right triangular distribution. Reflecting the pointed edge of the triangle with a second RF barrier again delivers a rectangular distribution in the longitudinal phase space. However, the final distribution is shorter than the initial one, allowing to accumulate more batches from an injector synchrotron than by simple longitudinal stringing of the batches.

It is not mandatory for the generation of a barrier bucket to generate symmetric RF pulses. The only constraint is that the average RF amplitude integrated over one turn vanishes. Consequently, a barrier bucket can be set-up between a negative and a positive RF pulse. Such a reduced configuration is shown in Fig. 3.11. The potential, which is shown as a continuous line in the upper plot, has the shape of a bath tube. As there are no adjacent buckets, it is also called isolated barrier bucket.

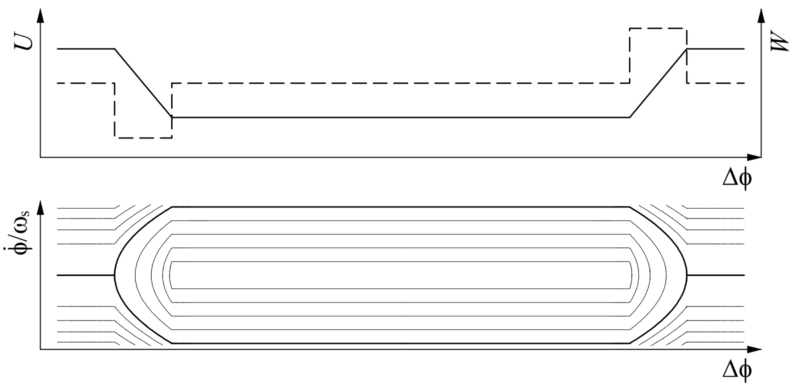

Fig. 3.11: RF amplitude (dashed), potential (both top) and longitudinal phase space of a barrier bucket (bottom) generated by two separated asymmetric pulses with opposite sign. Clearly, the potential has a bathtub-like form so that there are no neighboring buckets.

The shaping of the batch outline in the longitudinal phase space for the beam stacking procedure is mainly performed by a single moving barrier pulse. The main steps of the stacking manipulation are illustrated in Fig. 3.12, where the outlines of a rectangular bunch have been tracked. The example shown in the figure is based on beam parameters similar to those of the beam in the Main Injector at Fermilab [115, 116], which is operated below transition energy. Firstly, a coasting beam with a rectangular outline is injected with a negative energy offset directly next to a positive RF pulse (Fig. 3.12, top left). The phase length of the injected batch is given by the length the upstream accelerator reduced by the length of a short kicker gap. While the longitudinal dispersion causes the batch to move towards the RF pulse, the pulse

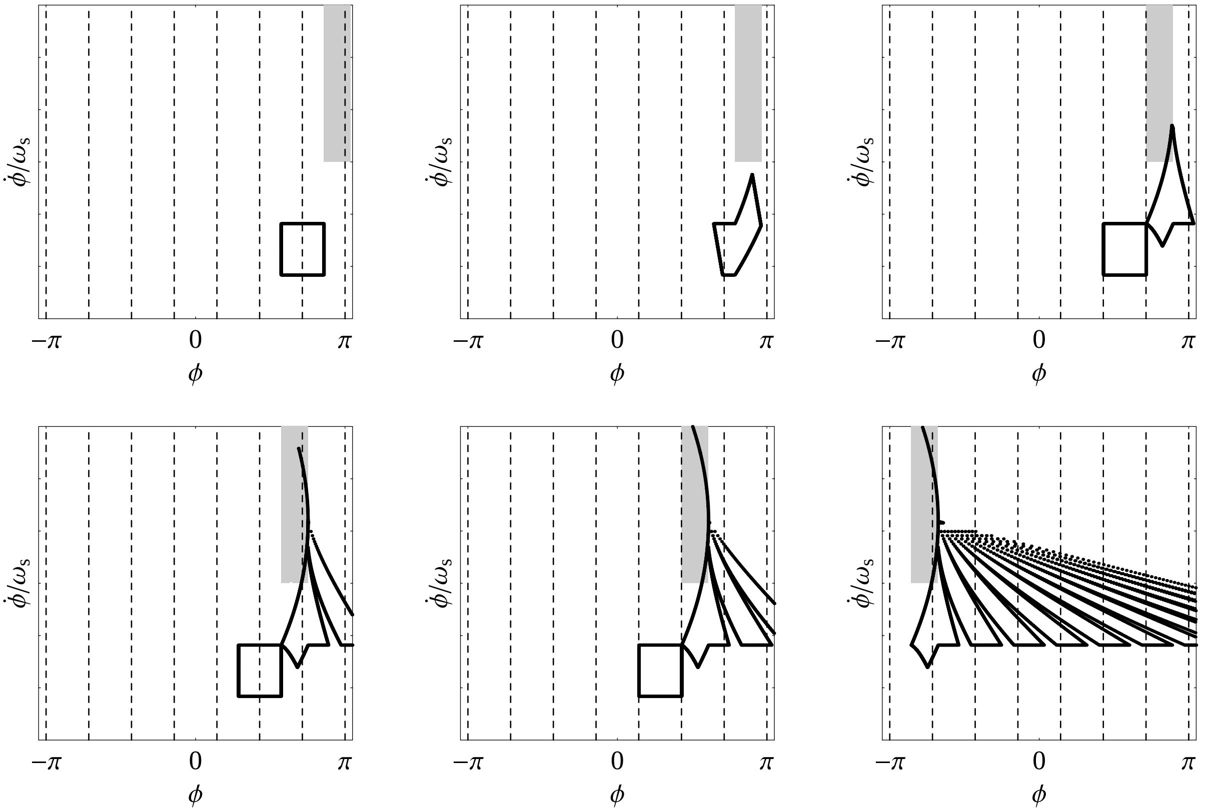

Fig. 3.12: Development of injected beam batches under the influence of a moving RF barrier. The upper left plot shows the initial configuration of the first batch being injected next to the barrier (shaded area). The batch is accelerated by the moving barrier (top center) until the position next to the barrier is empty again and ready for the subsequent injection. Repetition of this procedure builds up an intensive stack (bottom row).

itself is simultaneously shifted to the batch. Particles in the region of non-zero RF voltage are accelerated, while the rest of batch decays asymmetrically under the influence of the dispersion and non-zero momentum compaction factor (top center). For square wave barriers the energy gain per turn is constant and simply defined by $\Delta E = eU_0$, where U_0 is the voltage of the pulse. If the phase velocity of the moving barrier is the opposite value of the drift velocity of an upper energy particle in the batch, one comes up with a situation shown in Fig. 3.12, top right: the last particle touches the barrier pulse at the initial center position of the batch. The initial shape of the batch is obviously already distorted to an almost triangular distribution. It is worth noting that the phase velocity of the RF pulse is non-adiabatic, and part of the batch has already passed across.

So far, no assumption on the initial energy offset of the injected batch, which is limited by the energy acceptance, has been made. For a fast and continuous stacking process, the subsequent batch has to be injected as soon as the longitudinal phase space for the next moving barrier is not occupied anymore by parts of the preceding batch. This means that the time a particle with maximum energy $\Delta E_{\max}$ needs to drift along half of the batch length.

According to Eq. (2.14), the relation defining the length of the drift time τ with respect to the maximum energy can be written as

$$\frac{\phi_b}{2} = \frac{\eta\omega_0}{E\beta^2}\Delta E_{\text{max}}\tau \,. \tag{3.15}$$

Assuming that the batch has a symmetric energy distribution around its average energy ΔE_b, defined as an offset from the center energy E_0 of the receiving accelerator, the required injection energy becomes $E_0 - \Delta E_b = E_0 - \Delta E_{\text{max}} - \Delta E_{\text{spread}}$. The drift time τ corresponds to the total cycle time of the injector, which is needed to prepare a new batch. Under these conditions, the second batch is finally injected as shown in Fig. 3.12, top right. Note that the phase offset between two subsequent injections is half of the batch length in phase units. The diagrams of bottom row of Fig. 3.12 sketch the development after three (left), four (center) and twelve (right) injections. As each batch is injected next to the RF barrier, the procedure is repetitive.

However, without counter measure the stacked beam, whose net distribution has an outline similar to a right triangle, decays due to the longitudinal dispersion as can be seen in Fig. 3.12, bottom right. Placing additional RF barriers to reflect the low energy part of the stacked beam results in an almost rectangular stack (Fig. 3.13) that is symmetric around the center energy of the accelerator.

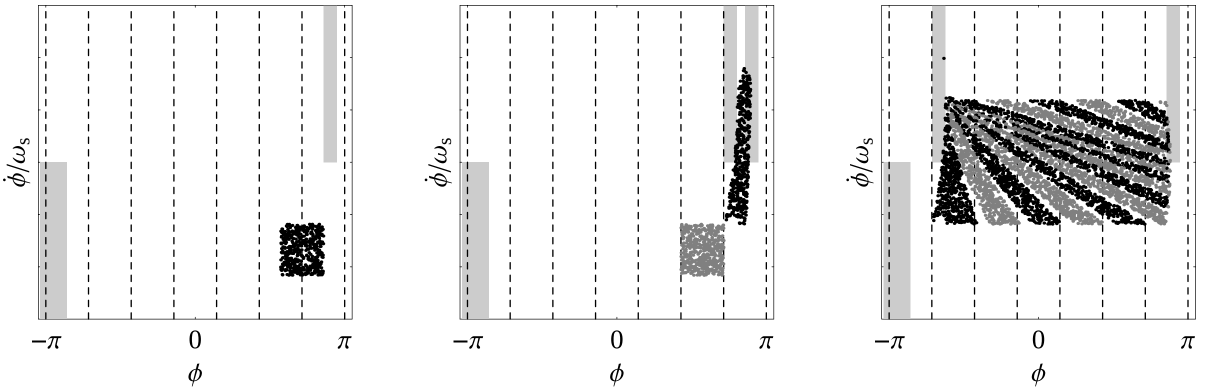

Fig. 3.13: Illustration of a complete stacking procedure for uniform density batches. Batches injected with an energy offset are accelerated and reflected by a moving barrier (left, center). After several injections a dense rectangular stack is build up which is centered around the reference energy of the accelerator (right). Shaded areas in the upper half of the plots represent a positive RF pulse and areas below their negative counterparts.

As the batches are placed half a batch length apart from each other, the intensity is theoretically doubled compared to simply stringing the batches longitudinally in a barrier bucket. The drawbacks of this type of manipulation are that a small fraction of the particles gets lost to high energies and that there is an inherent dilution of the emittance which lowers the effective longitudinal density.

Even though barrier RF stacking is a special RF gymnastics which can only be applied in two circular accelerators with particular parameters referring cycle time, transverse energy acceptance and beam energy spread, it shows that the barrier bucket technique offers a wide range of sophisticated longitudinal bunch manipulations.

3.5 Beam transfer between circular accelerators

Albeit the beam transfer between two accelerators is not directly a longitudinal beam manipulation, it can have severe consequences on the motion of the bunch or batch in the longitudinal phase space after the injection. Therefore this section discusses the longitudinal matching between two circular accelerators.

Extraction of an ensemble of bunches and injection into a downstream accelerator are transient processes where the different circumferences and phase slip factors between injecting and receiving machines must be taken into account. Depending on the bunch pattern in the sending accelerator, the RF frequency of the receiving machine has to be a rational multiple of the RF frequency of the upstream synchrotron in such a way that each bunch will be placed at a bucket center. The dispersive effect of the transfer line itself can be neglected, because the relative energy spread of the beams under consideration is small, typically in the range of $10^{-4} \ldots 10^{-3}$ (e.g. [117]). Therefore it can be assumed that the bunches arrive in the receiving accelerator with the same length as during ejection. Application of Eq. (3.8) to both machines and assuming constant bunch parameters simplifies to

$$\frac{U_1}{U_2} = \left(\frac{R_1}{R_2}\right)^2 \left|\frac{\eta_1}{\eta_2}\right| \frac{h_2}{h_1} \tag{3.16}$$

for matching of small bunches during the transfer. Additionally, RF phase and energy errors during injection contribute to blowing-up the macroscopic beam emittance, because they induce a coherent dipole oscillation of the bunch centroid which smears out after several synchrotron oscillation periods [118]. If this dipole oscillation is not actively damped, the resulting macroscopic emittance growth can be calculated from Eqs. (2.64) according to

$$\frac{\varepsilon_l(\Delta\phi_{\mathrm{err}})}{\varepsilon_0} = \frac{(\phi_m + \Delta\phi_{\mathrm{err}})^2}{\phi_m^2} \qquad \text{and} \qquad \frac{\varepsilon_l(\Delta E_{\mathrm{err}})}{\varepsilon_0} = \frac{(\Delta E_m + \Delta E_{\mathrm{err}})^2}{\Delta E_m^2}\,, \tag{3.17}$$

where $\Delta\phi_{\mathrm{err}}$ and ΔE_{err} are phase and energy deviation between bunch centroid and bucket center.

Similar conditions can be given for an RF amplitude mismatch where an undamped bunch rotation is excited leading to dilution of the longitudinal emittance. In the case of a voltage being either too small or too large in the receiving accelerator (see Eq. 3.8), the relative emittance growth can be written as

$$\frac{\varepsilon_l(\Delta U)}{\varepsilon_0} = \frac{U_0}{U_0 - \Delta U_{\mathrm{err}}}\,,\ \Delta U_{\mathrm{err}} < 0 \qquad \text{and} \qquad \frac{\varepsilon_l(\Delta U)}{\varepsilon_0} = \frac{U_0 + \Delta U_{\mathrm{err}}}{U_0}\,,\ \Delta U_{\mathrm{err}} > 0\,, \tag{3.18}$$

assuming that the bunch remains in the linear region of the bucket.

Though strongly transient, the matched transfer between two circular accelerators can be regarded as a reversible process. The beam bunches may be re-injected into the sending machine under the same conditions as vice versa.

Chapter 4

Luminosity Optimization with Long Bunches

A large variety of options to maximize the luminosity of the LHC by decreasing or increasing the bunch length is under discussion [119, 120]. This chapter covers the analysis of three different longitudinal bunch configurations.

Firstly, bunches having a length similar to nominal bunches are referred to as short bunches throughout this report, namely well below one meter. In this case it is worth noting that the bunch length is in the order of the length of the interaction region during a collision of two short bunches. Secondly, long bunches which have at least a few times the length of the nominal bunch so that their length is in the range of several meters. The third group of possible bunch configurations is referred to as superbunches where the total number of particles in each ring is merged to one coasting beam-like bunch per ring, with a bunch length of some 300 m.

Consistent derivations of luminosity and beam-beam tune shift for Gaussian as well as longitudinal rectangular bunches of arbitrary bunch length are presented at the beginning of this chapter. Thereafter, the considerations for perfectly rectangular bunches are extended to non-perfect flat bunches held by RF systems with multiple harmonics, and their benefit for the luminosity is analyzed. In the second part, after a short introduction to the relevant nominal and ultimate LHC parameters, various upgrade schemes according to the three categories mentioned above are studied. The chapter concludes with a summarizing table for the various longitudinal upgrade options of the LHC.

4.1 Luminosity

The luminosity $\mathcal{L}$ is the main figure of merit for colliders serving for particle physics. In fact, the luminosity represents the crossing rate dN/dt per unit of cross section during the collision of projectile particles on target particles. Thus, the event rate can be written as

$$\frac{dN}{dt} = \varsigma \cdot \mathcal{L} \,, \tag{4.1}$$

where ς represents the cross section of the interaction concerned. The luminosity is mostly given in units of $[\mathcal{L}] = \mathrm{cm}^{-2}\mathrm{s}^{-1}$. The definition contains no assumption on the type or velocity of the colliding particles, and the target may also be a particle beam which is brought to collision with the counter projectile particles as in the case of the LHC. For an efficient operation of large accelerator facilities like the LHC, optimization of the luminosity is the primary goal.

Therefore, general expressions for the luminosity for the collision of Gaussian as well as rectangular bunches starting from basic principles will be derived in the following sections.

4.1.1 Luminosity of ultra-relativistic bunch crossings

Considering the collision of two volumes containing the particle densities n_1 and n_2, the derivative of the event rate in any arbitrary frame of the reference can be expressed by [121]:

$$\frac{d^2N}{dt\,dV} = \varsigma n_1 n_2 \sqrt{(\vec{v}_1 - \vec{v}_2)^2 - \frac{(\vec{v}_1 \times \vec{v}_2)^2}{c^2}}\,, \tag{4.2}$$

where $\vec{v}_1$ and $\vec{v}_2$ are the velocities of the two volumes and ς is the cross section of the interaction concerned. The first term $\vec{v}_1 - \vec{v}_2$ is predominant for two volumes colliding at small angles, as in the case of most colliding beam facilities. It is worth noting that the interaction rate is invariant under Lorentz transformations.

For two ultra-relativistic beams with $|\vec{v}_1|$, $|\vec{v}_2| \simeq c$ and $\vec{v}_1$, $\vec{v}_2$ enclosing the angle φ, the two terms in Eq. (4.2) can be expressed as $(\vec{v}_1 - \vec{v}_2)^2 \simeq 4c^2\sin^2(\varphi/2)$ and $(\vec{v}_1 \times \vec{v}_2)^2/c^2 \simeq 4c^2\sin^2(\varphi/2)\cos^2(\varphi/2)$. In this case the interaction rate per volume reduces to

$$\frac{d^2N}{dt\,dV} = \varsigma n_1 n_2 2c \sin^2\frac{\varphi}{2}\,. \tag{4.3}$$

For two colliding bunches or beams, the crossing angle is chosen such that the velocity vectors v_1 and v_2 are in parallel but are in opposite directions for zero crossing angle (see Fig. 4.1). The interaction rate is finally written as

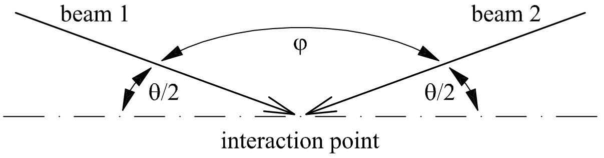

Fig. 4.1: Sketch of the choice of the angles between of two crossing beams. The total crossing angle is θ.

$$\frac{N^2}{dt\,dV} = \varsigma n_1 n_2 2c\cos^2(\theta/2)\,. \tag{4.4}$$

According to Eq. (4.1) the general luminosity of a single bunch crossing becomes

$$\mathcal{L} = 2cf_0\cos^2(\theta/2)\int n_1 n_2\,dV dt\,, \tag{4.5}$$

where f_0 is the revolution frequency. In case of more than one bunch crossing per revolution, the luminosity has to be multiplied by the number of bunch crossings. The particle densities are generally time and space dependent. For the subsequent luminosity derivations two coordinate systems (x_1, y_1, z_1) and (x_2, y_2, z_2) are chosen both of which are in opposite direction and tilted in x-z-plane by an angle of $\theta/2$ with respect to the arbitrary laboratory frame [122]:

$$\begin{array}{rcl} x_1 &=& x\cos(\theta/2) - z\sin(\theta/2) \\ y_1 &=& y \\ z_1 &=& x\sin(\theta/2) + z\cos(\theta/2) \end{array} \quad \text{and} \quad \begin{array}{rcl} x_2 &=& -x\cos(\theta/2) - z\sin(\theta/2) \\ y_2 &=& y \\ z_2 &=& x\sin(\theta/2) - z\cos(\theta/2) \end{array}\,. \tag{4.6}$$

It should be mentioned that calculations taking the coordinate system of one beam as reference frame [123] reproduce the same final results.

4.1.2 Collisions of Gaussian bunches

The particle density distribution of a bunch with a Gaussian distribution in the longitudinal as well as in both transverse directions is given by

$$n(x,y,z,t) = \frac{N}{(2\pi)^{3/2}\sigma_x\sigma_y\sigma_z} \exp\left[-\frac{1}{2}\left(\frac{x^2}{\sigma_x^2} + \frac{y^2}{\sigma_y^2} + \frac{(z-ct)^2}{\sigma_z^2}\right)\right] . \tag{4.7}$$

The bunch dimensions are defined by σ_x, σ_y, σ_z and the total number of particles is N. According to Eq. (4.5) the luminosity of a single crossing between two such bunches can be written as

$$\begin{aligned}\mathcal{L} = 2cf_0\cos^2(\theta/2)\frac{N_1N_2}{(2\pi)^3}\frac{1}{\sigma_{z_1}\sigma_{z_2}}\int\frac{1}{\sigma_{x_1}\sigma_{y_1}}\frac{1}{\sigma_{x_2}\sigma_{y_2}}\\ \times\exp\left\{-\frac{1}{2}\left[\frac{x_1^2}{\sigma_{x_1}^2} + \frac{x_2^2}{\sigma_{x_2}^2} + \left(\frac{1}{\sigma_{y_1}^2} + \frac{1}{\sigma_{y_2}^2}\right)y^2 + \frac{(z_1-ct)^2}{\sigma_{z_1}^2} + \frac{(z_2-ct)^2}{\sigma_{z_2}^2}\right]\right\} dV\,dt\,,\end{aligned} \tag{4.8}$$

where the transverse beam dimensions σ_x and σ_y can vary along the bunch. Using the relations

$$\int_{-\infty}^{\infty} e^{-ax^2}\,dx = \sqrt{\frac{\pi}{a}} \qquad \text{and} \qquad \int_{-\infty}^{\infty} e^{-ax^2+bx}\,dx = \sqrt{\frac{\pi}{a}}\,e^{b^2/(4a)}$$

the integration over y and t in Eq. (4.8) can be performed in a straightforward way combined with Eqs. (4.6) it leads to

$$\begin{aligned}\mathcal{L} = 2f_0\cos^2(\theta/2)\frac{N_1N_2}{(2\pi)^2}\frac{1}{\sqrt{\sigma_{z_1}^2+\sigma_{z_2}^2}}\int\frac{1}{\sigma_{x_1}\sigma_{x_2}}\frac{1}{\sqrt{\sigma_{y_1}^2+\sigma_{y_2}^2}}\\ \times\exp\left(-\frac{1}{2}\left\{x^2\cos^2(\theta/2)\left(\frac{1}{\sigma_{x_1}^2}+\frac{1}{\sigma_{x_1}^2}\right) + z^2\left[\sin^2(\theta/2)\left(\frac{1}{\sigma_{x_1}^2}+\frac{1}{\sigma_{x_1}^2}\right) + \frac{4\cos^2(\theta/2)}{\sigma_{z_1}^2+\sigma_{z_2}^2}\right]\right.\right.\\ \left.\left. +2xz\sin(\theta/2)\cos(\theta/2)\left(\frac{1}{\sigma_{x_2}^2}-\frac{1}{\sigma_{x_1}^2}\right)\right\}\right)\,dx\,dz\,,\end{aligned} \tag{4.9}$$

which is identical to the intermediate result given in [124, 122]. Assuming that the bunch parameters $\sigma = \sigma(z)$ are functions depending only on the longitudinal distance z from the interaction point in the laboratory frame, the x-integration is evaluated according to

$$\begin{aligned}\mathcal{L} = 2f_0\cos(\theta/2)\frac{N_1N_2}{(2\pi)^{3/2}}\frac{1}{\sqrt{\sigma_{z_1}^2+\sigma_{z_2}^2}}\int\frac{1}{\sigma_{x_1}\sigma_{x_2}}\frac{1}{\sqrt{\sigma_{y_1}^2+\sigma_{y_2}^2}}\bigg/\sqrt{\frac{1}{\sigma_{x_1}^2}+\frac{1}{\sigma_{x_2}^2}}\\ \exp\left\{-2z^2\left[\frac{\sin^2(\theta/2)}{\sigma_{x_1}^2\sigma_{x_2}^2}\bigg/\left(\frac{1}{\sigma_{x_1}^2}+\frac{1}{\sigma_{x_2}^2}\right)+\frac{\cos^2(\theta/2)}{\sigma_{z_1}^2+\sigma_{z_2}^2}\right]\right\}\,dz\,.\end{aligned} \tag{4.10}$$

If the transverse beam dimensions are nearly constant along the interaction region as in the case of a constant β-function along a short bunch, the remaining two integrations are carried out analytically, and Eq. (4.9) reduces to

$$\mathcal{L} = f_0N_1N_2\frac{\cos(\theta/2)}{2\pi}\frac{1}{\sqrt{\sigma_{y_1}^2+\sigma_{y_2}^2}}\frac{1}{\sqrt{\left(\sigma_{x_1}^2+\sigma_{x_2}^2\right)\cos^2(\theta/2)+\left(\sigma_{z_1}^2+\sigma_{z_2}^2\right)\sin^2(\theta/2)}}\,. \tag{4.11}$$

For two identical bunches with $N_1 = N_2$, $\sigma_{x_1} = \sigma_{x_2} = \sigma_x$, $\sigma_{y_1} = \sigma_{y_2} = \sigma_y$ and $\sigma_{z_1} = \sigma_{z_2} = \sigma_z$ this result further simplifies to

$$\mathcal{L} = f_0 N^2 \frac{1}{4\pi} \frac{1}{\sigma_y \sqrt{\sigma_x^2 + \sigma_z^2 \tan^2(\theta/2)}} \tag{4.12}$$

For small crossing angle θ as well as round bunches $\sigma_x = \sigma_y = \sigma^*$ the luminosity can be finally written as

$$\mathcal{L} = \frac{f_0 N^2}{4\pi\sigma^{*2}} \Bigg/ \sqrt{1 + \left(\frac{\sigma_z \theta}{2\sigma^*}\right)^2}\,, \tag{4.13}$$

where σ^* is the RMS beam radius at the interaction point. For the nominal LHC beam, the simplifying assumptions that were made above are well fulfilled, and consequently the result of Eq. (4.13) multiplied by the number of bunch crossings per turn agrees with the luminosity given in [15].

Besides the fact that the luminosity increases linearly with the number of bunches, it is also proportional to the square of the bunch intensity. Furthermore, the reduction of the transverse beam size is an effective possibility to improve the luminosity. The luminosity reduction by the finite crossing angle can hardly be avoided as each beam is bent from its own beampipe towards the interaction point. Additionally, it can be shown that large crossing angles are even favorable for a large luminosity (see Sec. 4.2.5).

4.1.3 Collisions of rectangular bunches

The luminosity calculation of a single crossing between two longitudinally rectangular bunches is similar to the derivation given above. However, the distribution function for each bunch is now given by

$$n(x,y,z,t) = \frac{N}{l_b} \frac{1}{2\pi\sigma_x\sigma_y} \exp\left[-\frac{1}{2}\left(\frac{x^2}{\sigma_x^2} + \frac{y^2}{\sigma_y^2}\right)\right] \zeta(z - ct)\,, \tag{4.14}$$

with the longitudinal distribution function being defined by a combination of two unit step functions

$$\zeta(z) = \left\{ \begin{array}{ll} 1 & -l_b/2 \leq z \leq l_b/2 \\ 0 & \text{elsewhere} \end{array} \right. . \tag{4.15}$$

The luminosity integral becomes

$$\begin{aligned} \mathcal{L} = 2cf_0 \cos^2(\theta/2) \frac{1}{(2\pi)^2} \frac{N_1 N_2}{l_{b_1} l_{b_2}} \int \frac{1}{\sigma_{x_1}\sigma_{y_1}} \frac{1}{\sigma_{x_2}\sigma_{y_2}} & \\ \times \exp\left\{-\frac{1}{2}\left[\frac{x_1^2}{\sigma_{x_1}^2} + \frac{x_2^2}{\sigma_{x_2}^2} + \left(\frac{1}{\sigma_{y_1}^2} + \frac{1}{\sigma_{y_2}^2}\right) y^2\right]\right\} \zeta(z_1 - ct)\zeta(z_2 - ct)\, dV\, dt\,. & \end{aligned} \tag{4.16}$$

It should be noted that any contribution outside $-l_{b_1} \leq z_1 - ct \leq l_{b_1}/2$ and $-l_{b_2} \leq z_1 - ct \leq l_{b_2}/2$ to the overlap integral vanishes. Again, the integration over y can be easily performed, and Eq. (4.16) reduces to

$$\begin{aligned} \mathcal{L} = 2f_0 \cos^2(\theta/2) \frac{1}{(2\pi)^{3/2}} \frac{N_1 N_2}{l_{b_1} l_{b_2}} \int \frac{1}{\sigma_{x_1}\sigma_{x_2}} \frac{1}{\sqrt{\sigma_{y_1}^2 + \sigma_{y_2}^2}} & \\ \times \exp\left[-\frac{1}{2}\left(\frac{x_1^2}{\sigma_{x_1}^2} + \frac{x_2^2}{\sigma_{x_2}^2}\right)\right] \zeta(z_1 - ct)\zeta(z_2 - ct)\, dx\, dz\, dt\,. & \end{aligned} \tag{4.17}$$

If both superbunches are of equal length, the time integration can be calculated analytically according to

$$\int \zeta(z_1 - ct)\zeta(z_2 - ct)\,dt = \begin{cases} \dfrac{l_b}{c}\left(1 - \dfrac{|z_1 - z_2|}{l_b}\right), & |z_1 - z_2| \leq l_b \\ 0\,, & \text{elsewhere} \end{cases} \tag{4.18}$$

so that the luminosity becomes

$$\mathcal{L} = 2f_0 \cos^2(\theta/2) \frac{1}{(2\pi)^{3/2}} \frac{N_1 N_2}{l_b c} \int \frac{1}{\sigma_{x_1}\sigma_{x_2}} \frac{1}{\sqrt{\sigma_{y_1}^2 + \sigma_{y_2}^2}} \times \exp\left[-\frac{1}{2}\left(\frac{x_1^2}{\sigma_{x_1}^2} + \frac{x_2^2}{\sigma_{x_2}^2}\right)\right]\left(1 - \frac{2|z|\cos(\theta/2)}{l_b}\right) dx\,dz \tag{4.19}$$

for $2|z|\cos(\theta/2) \leq l_b$. The integrand vanishes elsewhere.

In the case of round beams the x-integration can also be calculated analytically. However, the variation of the beam size along the interaction region has to be taken into account. According to $\sigma_{x_1} = \sigma_{x_2} = \sigma_{y_1} = \sigma_{y_2} = \sigma(z)$ the luminosity can be written as

$$\mathcal{L} = \frac{f_0 N^2}{2\pi\, l_b} \cos(\theta/2) \int_{-l_{\text{det}}/2}^{l_{\text{det}}/2} \frac{1}{\sigma(z)^2} \exp\left(-\frac{z^2 \sin^2(\theta/2)}{\sigma(z)^2}\right)\left(1 - \frac{2|z|\cos(\theta/2)}{l_b}\right) dz\,, \tag{4.20}$$

where l_{det} defines the length of the detector. Again, the integrand is zero outside $2|z|\cos(\theta/2) \leq l_b$ so that the integration has to be performed only from $-l_b/(2\cos\theta)$ to $l_b/(2\cos\theta)$ if $l_{\text{det}} > l_b/\cos\theta$. In the case of rectangular bunches which are much longer than the interaction length, $2|z|\cos(\theta/2)/l_b$ is small everywhere where the rest of the integrand in Eq. (4.20) gives a significant contribution so that long rectangular bunches deliver the same luminosity as a coasting beam:

$$\mathcal{L} = \frac{f_0 N^2}{2\pi\, l_b} \cos(\theta/2) \int_{-l_{\text{det}}/2}^{l_{\text{det}}/2} \frac{1}{\sigma(z)^2} \exp\left(-\frac{z^2 \sin^2(\theta/2)}{\sigma(z)^2}\right) dz\,. \tag{4.21}$$

In a focusing magnet system where the beam sizes at the interaction point are minimized to an RMS radius σ^*, the beam size grows proportionally to the square root of the so-called beta function. The beta function itself behaves like $\beta(z) = \beta^*(1 + z^2/\beta^{*2})$ with the interaction point at $z = 0$, and the RMS beam radius becomes

$$\sigma(z) = \sigma^* \sqrt{1 + \frac{z^2}{\beta^{*2}}}\,. \tag{4.22}$$

By inserting Eq. (4.22) into Eq. (4.20) and transforming to the new integration variable $u = z/\beta^*$, the luminosity for one rectangular bunch crossing at small crossing angle can be written as

$$\mathcal{L} = \frac{f_0 N^2}{2\pi\, l_b} \left[\frac{\beta^*}{\sigma^{*2}} \int_{-l_{\text{det}}/(2\beta^*)}^{l_{\text{det}}/(2\beta^*)} \frac{1}{1+u^2} \exp\left(-\frac{\beta^{*2}\theta^2}{4\sigma^{*2}} \frac{u^2}{1+u^2}\right) du - \frac{4\beta^{*2}}{l_b \sigma^{*2}} \int_0^{l_{\text{det}}/(2\beta^*)} \frac{u}{1+u^2} \exp\left(-\frac{\beta^{*2}\theta^2}{4\sigma^{*2}} \frac{u^2}{1+u^2}\right) du\right], \tag{4.23}$$

where the first term is consistent with the result for the crossing of a two coasting beams calculated in [123]. The integral can be evaluated numerically or approximated for the case of large crossing angles $\beta^*\theta \gtrsim 10\sigma^*$. The series expansion of the exponential terms in Eq. (4.23) shows that

$$\frac{1}{1+u^2}\exp\left[-\left(\frac{\beta^*\theta}{2\sigma^*}\right)^2\frac{u^2}{1+u^2}\right] \simeq \exp\left[-\left(\frac{\beta^*\theta}{2\sigma^*}\right)^2 u^2\right] .$$

and the luminosity expression for large crossing angles is approximated to

$$\mathcal{L} = \frac{f_0 N^2}{2\pi\, l_b}\left\{\frac{\beta^*}{\sigma^{*2}}\int_{-l_{\text{det}}/(2\beta^*)}^{l_{\text{det}}/(2\beta^*)}\exp\left(-\frac{\beta^{*2}\theta^2}{4\sigma^{*2}}u^2\right)du - \frac{8}{l_b\theta^2}\left[1-\exp\left(-\frac{\theta^2 l_{\text{det}}^2}{16\sigma^{*2}}\right)\right]\right\} , \tag{4.24}$$

where l_{det} has to be exchanged by l_b for $l_{\text{det}} > l_b$. This gives

$$\mathcal{L} = \frac{f_0 N^2}{\pi l_b \theta}\left[\frac{\sqrt{\pi}}{\sigma^*}\text{Erf}\left(\frac{\theta l_b}{4\sigma^*}\right) - \frac{4}{l_b\theta}\left\{1-\exp\left[-\left(\frac{\theta l_b}{4\sigma^*}\right)^2\right]\right\}\right] . \tag{4.25}$$

For short bunches colliding at small crossing angles so that $\theta l_b/\sigma^* \lesssim 1$, the luminosity can be approximated by the Taylor series of both terms in Eq. (4.25). Considering leading and next to leading order contributions in $\theta l_b/(4\sigma^*)$, the luminosity formula can be approximated by

$$\mathcal{L} = \frac{f_0 N^2}{4\pi\sigma^{*2}}\left[1-\frac{2}{3}\left(\frac{\theta l_b}{4\sigma^*}\right)^2\right] . \tag{4.26}$$

In contrary, the first leading order contribution of the second term in Eq. (4.25) can be estimated for bunches with an intermediate length so that the replacement of the integration limits in Eq. (4.24) to infinity is justified on the one hand. On the other hand, such bunches still have a finite bunch length so that the second term of the luminosity expression causes a non-negligible contribution. Following these assumptions, Eq. (4.25) is reduced to

$$\mathcal{L} = \frac{f_0 l_b \lambda^2}{\pi\theta}\left(\frac{\sqrt{\pi}}{\sigma^*} - \frac{4}{l_b\theta}\right) , \tag{4.27}$$

The second term vanishes completely for $\theta \gg 4\sigma^*/(\sqrt{\pi} l_b)$, which shows that the crossing angle, below which the non-linear influence of the bunch length has to be taken into account, scales proportionally to the beam size σ^* at the interaction point and inversely proportional to the bunch length.

For bunches which are much longer than the interaction region, the luminosity can be finally simplified to [125]

$$\mathcal{L} = \frac{f_0 l_b \lambda^2}{\sqrt{\pi}}\frac{1}{\sigma^*\theta} , \tag{4.28}$$

where $\lambda = N/l_b$ denotes the longitudinal particle density. The same result can be obtained for coasting beams. Again, the luminosity is proportional to the square of the longitudinal particle density. Longer bunches can also increase the luminosity, but it should be kept in mind that the total charge also increases proportionally to this parameter. Furthermore, the reduction of the crossing angle seems to result in larger luminosity. However, as will be shown in the following derivation of the incoherent beam-beam tune shift, this is not true, because beams crossing at small angles are influenced by the electromagnetic field of the counter-rotating beam along a much longer path than two beams crossing at a larger angle.

Comparing the luminosity in Eq. (4.13) for a Gaussian bunch crossing with the analogous expression for rectangular bunch crossings Eq. (4.28), it becomes obvious that the luminosity of a rectangular bunch crossing with bunches of identical peak intensity and the same bunch population reaches $\sqrt{2}$ times more luminosity than the crossing of long Gaussian bunches.

4.2 Incoherent beam-beam tune shift

Albeit the crossing angle should be kept as small as possible for maximum luminosity with a fixed number of particles, it must be considered that both beams are close and influence each other within a long region in such a case. Additionally, individual particles are affected differently according to their transverse position within the beam. The global effect is thus incoherent and difficult to compensate. It can therefore be regarded as a fundamental limitation of the beam current in hadron colliders.

The incoherent beam-beam tune shift can be calculated by deriving the electromagnetic force of a beam with respect to a test particle in the second beam. The integral effect of these forces is a shift of the betatron frequencies of the individual particles, which may result in a significant tune spread.

In the following, the electric and magnetic field of one beam in the reference frame of the test particle is analyzed. Moreover, the integral effect of these forces is expressed as a betatron tune shift, taking into the longitudinal beam distribution account that may be either rectangular or Gaussian. A short derivation on how to convert additional focusing or defocusing forces to a betatron tune shift is given in App. E. It should be noted that most considerations are valid for round beams only, which represents the most relevant case for the LHC.

4.2.1 Lorentz force of long bunches

The electromagnetic forces of a particle bunch can be easily calculated for the case that the transverse bunch dimensions are much smaller than the longitudinal intensity variation. Even for nominal LHC bunches this is certainly the case, as the RMS bunch length is almost five thousand times larger than the beam radius at the interaction point. It is thus convenient to start from a particle density given by

$$\rho(x,y,z) = \frac{\lambda(z)\,e}{2\pi\sigma_x\sigma_y}\exp\left[-\frac{1}{2}\left(\frac{x^2}{\sigma_x^2}+\frac{y^2}{\sigma_y^2}\right)\right] \quad \text{resp.} \quad \rho(r,z) = \frac{\lambda(z)\,e}{2\pi\sigma^2}\exp\left(-\frac{r^2}{2\sigma^2}\right) , \tag{4.29}$$

where $\lambda(z)$ is the longitudinal density in units of particles per length. For constant or small varying $\lambda(z)$, the only non-vanishing field components are the radial electric field E_r and the azimuthal magnetic induction B_ϕ. The first one can be derived from Gauss's law using

$$2\pi r E_r = \frac{1}{\epsilon_0}\int_0^r 2\pi r'\rho(r')\,dr' \quad \Rightarrow \quad E_r = \frac{\lambda\,e}{2\pi\epsilon_0 r}\left[1-e^{-r^2/(2\sigma^2)}\right] , \tag{4.30}$$

and the latter is calculated by the application of Ampère's law according to

$$2\pi r B_\phi = \mu_0\int_0^r 2\pi\beta c r'\rho(r')\,dr' \quad \Rightarrow \quad B_\phi = \frac{\mu_0\beta c\,\lambda\,e}{2\pi r}\left[1-e^{-r^2/(2\sigma^2)}\right] = \frac{\beta}{c}E_r\,. \tag{4.31}$$

The Lorentz force $\vec{F}_L = e(\vec{E}+\vec{v}\times\vec{B})$ consists only of its radial component which, by combination of Eqs. (4.30) and (4.31), can be written as

$$|\vec{F}_L| = F_r(r) = \frac{\lambda\,e^2}{2\pi\epsilon_0 r}(1+\beta^2)\left[1-e^{-r^2/(2\sigma^2)}\right] . \tag{4.32}$$

From Eq. (4.32) it becomes clear that the beam-beam force acts like a defocusing element. In Cartesian coordinates, the force transforms to [126]

$$\begin{aligned} F_x^*(x^*, y^*) &= F_r(r)\frac{x^*}{r} = 2m_0(1+\beta^2)c^2\lambda\, r_p \left[1 - e^{-r^2/(2\sigma^2)}\right]\frac{x^*}{r^2} \,, \\ F_y^*(x^*, y^*) &= F_r(r)\frac{y^*}{r} = 2m_0(1+\beta^2)c^2\lambda\, r_p \left[1 - e^{-r^2/(2\sigma^2)}\right]\frac{y^*}{r^2} \,, \end{aligned} \tag{4.33}$$

where r_p denotes the classical particle radius being $r_p = 1/(4\pi\epsilon_0 c^2)e^2/m_p$ for protons. The asterisks indicate that the forces are given in a reference frame aligned with the beam. So far, the fields and forces have been calculated in the reference frame of the beam. A test particle traveling with the second, opposite beam moves in a reference frame denoted without asterisks which is tilted in the x-z plane by the crossing angle θ (see Eq. 4.6):

$$\begin{array}{rcl} x^* &=& x\cos\theta - z\sin\theta \\ y^* &=& y \\ z^* &=& x\sin\theta + z\cos\theta \end{array} \quad \text{and} \quad \begin{array}{rcl} x &=& x^*\cos\theta + z^*\sin\theta \\ y &=& y^* \\ z &=& -x^*\sin\theta + z^*\cos\theta \end{array} \,. \tag{4.34}$$

It is worth noting that the calculation of beam-beam effects in a coordinate system rotated with respect to both beams, as it was used for the derivations of the luminosity, would be rather inconvenient because of the problem of symmetry.

According to $\vec{F} = e[\vec{E} + (0,0,-c) \times \vec{B}]$ the Lorentz force in the reference frame of the test particle aligned with the opposite beam, the force transforms to

$$\begin{aligned} F_x &= e(E_x + cB_y) = e(E_x^*\cos\theta + cB_y^*) = \frac{1+\cos\theta}{2}F_x^* \,, \\ F_y &= e(E_y - cB_x) = e(E_y^* + cB_x^*\cos\theta) = \frac{1+\cos\theta}{2}F_y^* \,, \end{aligned}$$

where the opposite beam directions have been taken into account by the sign of the velocity. Finally, the force of the beam on the test particle traveling in the opposite direction can be expressed as

$$\begin{aligned} F_x(x,y,z) = 2m_0\beta^2c^2\lambda\, r_p(1+\cos\theta)&\frac{x\cos\theta - z\sin\theta}{(x\cos\theta - z\sin\theta)^2 + y^2} \\ &\times \left\{1 - \exp\left[-\frac{(x\cos\theta - z\sin\theta)^2 + y^2}{2\sigma(z)^2}\right]\right\} \end{aligned} \tag{4.35}$$

and

$$\begin{aligned} F_y(x,y,z) = 2m_0\beta^2c^2\lambda\, r_p(1+\cos\theta)&\frac{y}{(x\cos\theta - z\sin\theta)^2 + y^2} \\ &\times \left\{1 - \exp\left[-\frac{(x\cos\theta - z\sin\theta)^2 + y^2}{2\sigma(z)^2}\right]\right\} \,. \end{aligned} \tag{4.36}$$

For a bunch which also has a Gaussian distribution in the longitudinal direction and whose RMS bunch length is much larger than its transverse dimensions, the force has to be complemented by an exponential factor $\exp[(z+z^*)^2/(2\sigma_z^2)]$. This factor depends on the sum of the position z of the test particle and the center position z^* of the counter-rotating bunch. The Lorentz force can therefore be written in terms of Eqs. (4.35) and (4.36) as

$$F_{x,y}^{\text{Gaussian}}(x,y,z) = F_{x,y}(x,y,z)\exp\left[-\frac{(z + z\cos\theta + x\sin\theta)^2}{2\sigma_z^2}\right] \,. \tag{4.37}$$

For a rectangular bunch the longitudinal density factor is given by $\zeta(z)$ as defined in Sec. 4.1.3, and the beam-beam force can be written as

$$F_{x,y}^{\text{rectangular}}(x,y,z) = F_{x,y}(x,y,z)\,\zeta(z + z\cos\theta + x\sin\theta)\,. \tag{4.38}$$

4.2.2 Incoherent beam-beam tune shift

As shown in App. E an additional focusing or defocusing force caused by a another beam can be regarded as an extra optical element which changes the machine lattice such that the betatron frequency is perturbed. This so-called tune shift can be derived according to

$$\Delta Q_{x,y} = \frac{1}{4\pi}\int \Delta k_{x,y}(z)\beta_{x,y}(z)\,dz\,, \tag{4.39}$$

where $\Delta k_{x,y}(z)$ is the perturbing quadrupole strength along the z-axis and $\beta(z)$ is the beta function. The perturbing quadrupole strength in terms of an electromagnetic force becomes

$$\Delta k_x = \frac{e}{p}\frac{dB_y^{\text{quad}}}{dx} = -\frac{1}{m_0\gamma\beta^2c^2}\frac{dF_x}{dx} \quad \text{and} \quad \Delta k_y = -\frac{1}{m_0\gamma\beta^2c^2}\frac{dF_y}{dy}\,,$$

with $B_{x,y}^{\text{quad}}$ being the magnetic induction of the equivalent quadrupole.

The incoherent beam-beam tune shift is now derived by inserting the expression of the beam-beam force from Eq. (4.37) into Eq. (4.39). The most important parameter is, however, the tune spread of the full bunch and not the tune shift of the individual particle. The spread is simply given by the tune shift of the test particle which suffers most from the influence of the opposing beam, namely a particle at $x = y = 0$. Therefore, the derivatives of the electromagnetic force have to be evaluated at this position only, and the maximum tune shifts can be written as

$$\Delta Q_x = -\frac{1}{4\pi}\int_{-l/2}^{l/2}\frac{1}{m_0\gamma\beta^2c^2}\left.\frac{dF_x}{dx}\right|_{x=y=0}\beta_x(z)\,dz\,, \tag{4.40}$$

$$\Delta Q_y = -\frac{1}{4\pi}\int_{-l/2}^{l/2}\frac{1}{m_0\gamma\beta^2c^2}\left.\frac{dF_y}{dy}\right|_{x=y=0}\beta_y(z)\,dz\,, \tag{4.41}$$

where l denotes the length along which both beams interact without a shielding between them.

4.2.3 Beam-beam tune spread of Gaussian bunches

According to Eqs. (4.40) and (4.41) the beam-beam tune spread is calculated by evaluating the derivative of the electromagnetic force Eq. (4.37). Furthermore it is assumed as in Sec. 4.1.3 that the beta function grows quadratically around its minimum value β^* at the interaction point and that the RMS beam radius $\sigma(z)$ behaves according to Eq. (4.22). After some algebraic manipulations, the horizontal and vertical betatron tune spread due to the beam-beam interaction become [126]

$$\begin{aligned}\Delta Q_x = {} & \frac{N r_p \beta^*}{(2\pi)^{3/2}\sigma_z\gamma}(1+\cos\theta)\int_{-l/2}^{l/2}\left(1+\frac{z^2}{\beta^{*2}}\right)\exp\left[-\frac{z^2(1+\cos\theta)^2}{2\sigma_z^2}\right] \\ & \times\left\{\left[\frac{\cos\theta}{z^2\sin^2\theta}-\frac{1+\cos\theta}{\sigma_z^2}\right]\left[1-\exp\left(-\frac{z^2\sin^2\theta}{2\sigma(z)^2}\right)\right]-\frac{\cos\theta}{\sigma(z)^2}\exp\left(-\frac{z^2\sin^2\theta}{2\sigma(z)^2}\right)\right\}dz\,,\end{aligned} \tag{4.42}$$

$$\Delta Q_y = \frac{N r_p \beta^*}{(2\pi)^{3/2}\sigma_z \gamma}(1+\cos\theta)\int_{-l/2}^{l/2}\left(1+\frac{z^2}{\beta^{*2}}\right)\exp\left[-\frac{z^2(1+\cos\theta)^2}{2\sigma_z^2}\right] \times \frac{1}{z^2\sin^2\theta}\left[1-\exp\left(-\frac{z^2\sin^2\theta}{2\sigma(z)^2}\right)\right] dz\,, \quad (4.43)$$

where the line density λ has been replaced by $N/(\sqrt{2\pi}\sigma_z)$. Considering a double ring collider with two diametrically opposed interaction points where the first bunch crossing is in the horizontal plane and the second in the vertical plane, so-called alternating beam crossings, the total beam-beam tune spread is obtained as the sum of ΔQ_x and ΔQ_y, namely [126]

$$\Delta Q_{\text{tot}} = -\frac{N r_p \beta^*}{(2\pi)^{3/2}\sigma_z \gamma}(1+\cos\theta)\int_{-l/2}^{l/2}\left(1+\frac{z^2}{\beta^{*2}}\right)\exp\left[-\frac{z^2(1+\cos\theta)^2}{2\sigma_z^2}\right] \times\left\{\left[\frac{1-\cos\theta}{z^2\sin^2\theta}+\frac{1+\cos\theta}{\sigma_z^2}\right]\left[1-\exp\left(-\frac{z^2\sin^2\theta}{2\sigma(z)^2}\right)\right]+\frac{\cos\theta}{\sigma(z)^2}\exp\left(-\frac{z^2\sin^2\theta}{2\sigma(z)^2}\right)\right\} dz\,. \quad (4.44)$$

This general result is simplified following some assumptions on the crossing angle and the bunch parameters. In the region of small crossing angles Eq. (4.44) reduces to

$$\Delta Q_{\text{tot}} = -\frac{N r_p \beta^*}{\sqrt{2}\pi^{3/2}\sigma_z \gamma}\int_{-l/2}^{l/2}\left(1+\frac{z^2}{\beta^{*2}}\right)\exp\left(-\frac{2z^2}{\sigma_z^2}\right) \times\left\{\frac{2}{\sigma_z^2}\left[1-\exp\left(-\frac{z^2\theta^2}{2\sigma_z^2}\right)\right]+\frac{1}{\sigma(s)^2}\exp\left(-\frac{z^2\theta^2}{2\sigma_z^2}\right)\right\} dz\,. \quad (4.45)$$

For bunches which are much longer than the beam radius at the interaction point but still short enough against the beta function $\sigma \ll \sigma_z \ll \beta^*$ so that the RMS beam radius are assumed to be constant $\sigma(s) = \sigma^*$ along the interaction region, the z-integration can be solved analytically:

$$\Delta Q_{\text{tot}} = -\frac{N r_p \beta^*}{2\pi\gamma\sigma_z^2}\left\{\left(\frac{\sigma_z^2}{\sigma^{*2}}-2\sqrt{\pi}\right)\Bigg/\sqrt{1+\frac{\sigma_z^2\theta^2}{4\sigma^{*2}}} +1+\frac{\sigma_z^2\theta^2}{4\sigma^{*2}}-\left(\frac{\sigma_z}{2\sigma^{*2}}+1\right)\sigma_z^2\Bigg/\left[2\beta^*\left(1+\frac{\sigma_z^2\theta^2}{4\sigma^{*2}}\right)^{3/2}\right]\right\}.$$

Under the assumptions mentioned above, only the first term is predominant so that the total tune spread finally simplifies to

$$\Delta Q_{\text{tot}} = -\frac{N r_p \beta^*}{2\pi\gamma\sigma^{*2}}\Bigg/\sqrt{1+\left(\frac{\sigma_z\theta}{2\sigma^*}\right)^2}\,. \quad (4.46)$$

4.2.4 Beam-beam tune spread of rectangular bunches

The calculation of the beam-beam tune shift for rectangular bunches is analogous to the derivation shown above, and the horizontal tune can be written as

$$\begin{aligned}\Delta Q_x = {} & \frac{\lambda r_p \beta^*}{2\pi\gamma}(1+\cos\theta)\left[\cos\theta\int_{-l/2}^{l/2}\left(1+\frac{z^2}{\beta^{*2}}\right)\zeta(z+z\cos\theta)\right.\\ & \left.\times\left\{\frac{1}{z^2\sin^2\theta}\left[1-\exp\left(-\frac{z^2\sin^2\theta}{2\sigma(z)^2}\right)\right]-\frac{1}{\sigma(z)^2}\exp\left(-\frac{z^2\sin^2\theta}{2\sigma(z)^2}\right)\right\}dz\right.\\ & \left.-\begin{cases}\dfrac{4(\cos\theta+1)}{l_b}\left[1+\dfrac{l_b^2}{4\beta^{*2}(\cos\theta+1)^2}\right]\left[1-\exp\left(-\dfrac{l_b^2\sin^2\theta}{8(\cos\theta+1)^2\sigma(z)^2}\right)\right], & \\ \hfill l_b/(\cos\theta+1)<l & \\ 0\,,\quad \text{elsewhere} & \end{cases}\right] . \end{aligned} \tag{4.47}$$

The first term is in fact consistent with the tune spread of a coasting beam except that the integration is only performed along half of the bunch projection. The second term in Eq. (4.47) only contributes if the ends of the bunch are within the integration range. However, as this term only occurs due to an edge effect at the bunch ends, it is generally much smaller than the integral expression. The vertical tune spread can be expressed accordingly as

$$\Delta Q_y = -\frac{\lambda r_p \beta^*}{2\pi\gamma}(1+\cos\theta)\int_{-l/2}^{l/2}\left(1+\frac{z^2}{\beta^{*2}}\right)\zeta(z+z\cos\theta)\frac{1}{z^2\sin^2\theta}\left[1-\exp\left(-\frac{z^2\sin^2\theta}{2\sigma(z)^2}\right)\right]dz\,, \tag{4.48}$$

which is again identical to the tune spread of a coasting beam if $l_b/(1+\cos\theta) > l$. The total tune spread for two alternating crossings is again given by the sum of horizontal and vertical tune spreads and, neglecting the edge term from Eq. (4.47), becomes

$$\begin{aligned}\Delta Q_{\text{tot}} = {} & \frac{\lambda r_p \beta^*}{2\pi\gamma}(1+\cos\theta)\int_{-l/2}^{l/2}\left(1+\frac{z^2}{\beta^{*2}}\right)\zeta(z+z\cos\theta)\\ & \times\left\{(\cos\theta-1)\frac{1}{z^2\sin^2\theta}\left[1-\exp\left(-\frac{z^2\sin^2\theta}{2\sigma(z)^2}\right)\right]-\frac{\cos\theta}{\sigma(z)^2}\exp\left(-\frac{z^2\sin^2\theta}{2\sigma(z)^2}\right)\right\}dz\,. \end{aligned} \tag{4.49}$$

For small crossing angles θ and long bunches the general solution Eq. (4.49) can be simplified significantly to

$$\Delta Q_{\text{tot}} = -\frac{\lambda r_p}{\pi\gamma}\frac{\beta^{*2}}{\sigma^{*2}}\int_{-l/(2\beta^*)}^{l/(2\beta^*)}\frac{1}{1+u^2}\exp\left(-\frac{\beta^{*2}\theta^2}{2\sigma^{*2}}\frac{u^2}{1+u^2}\right)du\,. \tag{4.50}$$

In analogy to the approximation discussed in Sec. (4.1.3) the integral can be approached for large crossing angles and small beam radius at the interaction point $\beta^*\theta/\sigma^* \gg 1$, and finally becomes [125]

$$\Delta Q_{\text{tot}} = -\sqrt{\frac{2}{\pi}}\frac{\lambda r_p \beta^*}{\gamma\sigma^*\theta}\,. \tag{4.51}$$

It is worth noting that this is the same result as for Gaussian bunches in the limit of $\sigma_z\theta/(2\sigma^*) \gg 1$ and an equivalent longitudinal density $\lambda = N/(\sqrt{2\pi}\sigma_z)$ (see Eq. 4.46).

4.2.5 Maximum luminosity of long bunch crossings

Regarding the total incoherent beam-beam betatron tune shift for two alternating interaction points as an absolute limit for the maximum beam intensity and thus for the maximum luminosity, this luminosity is calculated in terms of total tune shift following the analysis presented above. At least for the approximated luminosity and tune shift formulae analytical expressions can be given.

In the case of Gaussian bunches, the combination of Eqs. (4.13) and (4.46) leads to a luminosity of

$$\mathcal{L} = \frac{\pi f_0 \gamma^2 \sigma^{*2}}{r_p^2 \beta^{*2}} \sqrt{1 + \left(\frac{\sigma_z \theta}{2\sigma^*}\right)^2}\, \Delta Q_{\text{tot}}^2 \tag{4.52}$$

for a bunch total bunch intensity of

$$N = -\frac{2\pi\gamma\sigma^{*2}}{r_p \beta^*} \sqrt{1 + \left(\frac{\sigma_z \theta}{2\sigma^*}\right)^2}\, \Delta Q_{\text{tot}} \,. \tag{4.53}$$

This result can be further simplified for large crossing angles or bunch lengths so that the second term under the square root is dominant according to

$$\mathcal{L} = \frac{\pi}{2} \frac{f_0 \gamma^2 \sigma^* \sigma_z}{r_p^2 \beta^{*2}}\, \theta\, \Delta Q_{\text{tot}}^2 \qquad \left(\text{for} \quad N = -\frac{\pi\gamma\sigma^*\sigma_z\theta}{r_p\beta^*}\Delta Q_{\text{tot}}\right) . \tag{4.54}$$

The formulae for rectangular bunch crossings are obtained by combining Eqs. (4.28) and (4.51) which can be written as

$$\mathcal{L} = \frac{\sqrt{\pi}}{2} \frac{f_0 \gamma^2 \sigma^* l_b}{r_p^2 \beta^{*2}}\, \theta\, \Delta Q_{\text{tot}}^2 \qquad \left(\text{for} \quad \lambda = -\sqrt{\frac{\pi}{2}} \frac{\gamma\sigma^*\theta}{r_p\beta^*}\Delta Q_{\text{tot}}\right) . \tag{4.55}$$

It is now easy to show that the luminosity of a rectangular bunch crossing is by a factor of $\sqrt{2}$ larger than that of a Gaussian bunch crossing with identical intensity so that $l_b = \sqrt{2\pi}\sigma_z$, which means that the peak intensity $\lambda_{\text{peak}} = N/(\sqrt{2\pi}\sigma_z)$ of the Gaussian bunch corresponds the line density λ of the rectangular long bunch. Fig. 4.2 illustrates the line density of a Gaussian and the equivalent rectangular bunch. Both bunches have the same peak intensity and contain the same total number of particles. Therefore, their total tune spread is identical and, according to Eqs. (4.54) and (4.55), the crossing of the rectangular bunches delivers more luminosity.

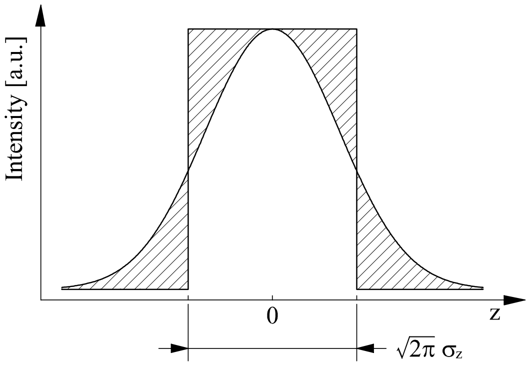

Fig. 4.2: Comparison of the line density of Gaussian and rectangular bunches both having the same peak and total intensity as well as the same total maximum beam-beam tune shift. However the crossing of rectangular bunches results in $\sqrt{2}$ times more luminosity. The hatched areas are of equal size.

From Eqs. (4.54) and (4.55) it becomes clear that the luminosity increases linearly with the bunch length while keeping the maximum line density constant. However, one should keep in mind that there is no additional luminosity gain by further increasing the bunch length with respect to the total intensity: increasing the bunch length requires a proportional rise of the total beam intensity to re-establish the initial peak line density and beam-beam tune shift. If the total beam intensity is to be kept constant, the number of bunches must be decreased proportionally to the increase in bunch length, and the luminosity gain is finally eaten up as the luminosity is also directly proportional to the number of bunch crossings per turn. However, longer bunches have a slightly more favorable beam-beam behaviour. Thus, the maximum total beam intensity can be increased for longer bunches without violating the maximum incoherent beam-beam tune shift.

The second parameter to increase the luminosity while keeping the beam-beam tune shift constant is the crossing angle θ. This behaviour is not obvious from the luminosity formulae only (see Eqs. 4.13 and 4.28), which suggest that a crossing angle as small as possible reaches maximum luminosity. This is only true as long as the total number of particles is kept constant and the beam-beam limit is neglected. Small crossing angles lead to long regions of electromagnetic interaction between both beams and thus to a large beam-beam tune shift. If the incoherent beam-beam tune shift is regarded as upper limit for the beam current the luminosity can be optimized by increasing the crossing angle which allows an improved total beam intensity. However, other limiting effects for the beam current, like total synchrotron radiation losses or beam stability, might limit the beam current.

For the calculation of an absolute luminosity, two restrictions have to be taken into account: both the total beam current and the beam-beam tune spread must not exceed a certain limit. As the total tune spread is proportional to the instantaneous longitudinal peak density of the beam, the latter automatically defines the peak density.

In the case of long rectangular bunches crossings under large angles, these limits as well as the luminosity dependence on the total beam length $n_b l_b$ of n_b bunches with a total length of l_b each, can be presented as shown in Fig. 4.3. Clearly, the absolute maximum luminosity is obtained when current and beam-beam limit are reached simultaneously (marked by a black dot in Fig. 4.3).

Analytical expressions for the maximum luminosity can be derived from Eqs. (4.55) and the absolute maximum luminosity becomes

$$\mathcal{L}_{\max} = \frac{1}{\sqrt{2}} \frac{f_0 \gamma}{r_p \beta^*} N_{\max} \Delta Q_{\mathrm{tot}} \,. \tag{4.56}$$

The total beam length to achieve this luminosity can be written as

$$n_b l_b = -\sqrt{\frac{2}{\pi}} \frac{r_p \beta^*}{\gamma \sigma^* \theta} \frac{N_{\max}}{\Delta Q_{\mathrm{tot}}} \,. \tag{4.57}$$

It is remarkable that this luminosity does not depend on the crossing angle nor on the beam size at the interaction point, as long as the crossing angle θ is sufficiently large so that Eq. (4.55) remains valid. According to the set of crossing parameters used for Fig. 4.3, the maximum luminosity for LHC operated at twice its nominal total beam intensity and at maximum total tune spread of $\Delta Q_{\mathrm{tot}} = -0.01$ the optimum luminosity is $\mathcal{L}_{\max} = 10^{35}\ \mathrm{cm}^{-2}\mathrm{s}^{-1}$ (see Sec. 4.3.5).

The maximum tune shift that can be attained in hadron colliders without significant reduction of the beam lifetime is not defined as a strict limitation. Albeit the linear theory of beam optics predicts a maximum beam-beam tune shift for an arbitrary betatron tune, this limit could not be achieved in any existing accelerator [128]. Therefore, the maximum tolerable beam-beam tune spread in the LHC is estimated on the basis of the experience with past and

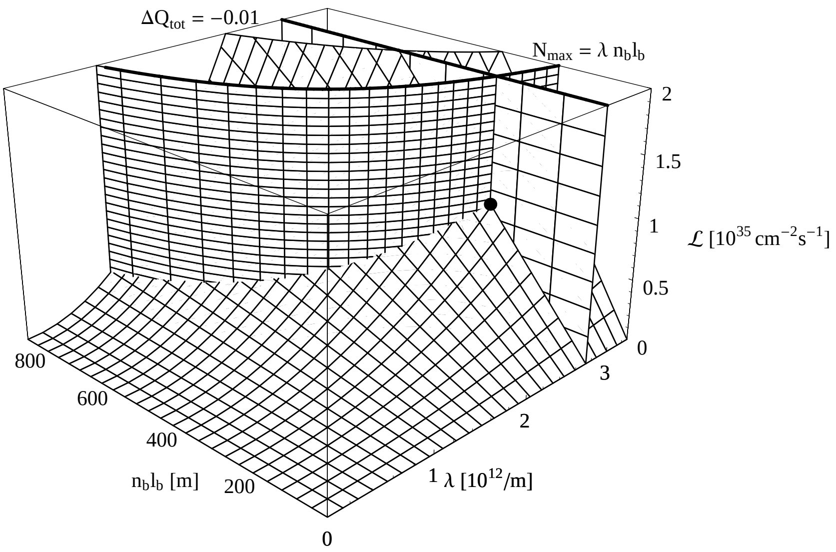

Fig. 4.3: Beam luminosity versus total bunch length $n_b l_b$ and longitudinal particle density λ. The vertical walls show the total limit of circulating beam $N_{\max} = \lambda n_b l_b$ and the maximum beam-beam tune spread limit. The crossing parameters are chosen according to the superbunch option proposed in [127]: $\theta = 1\,\text{mrad}$, $\beta^* = 0.25\,\text{m}$, $\sigma^* = 11.2\,\mu\text{m}$.

Machine	Year	Particles	$2\pi R$	E_0	$\lvert\Delta Q\rvert$	Ref.
ISR (CERN)	1971-1983	p-p	0.94 km	26 GeV	$\simeq 0.0004$	[129, 130]
Sp$\bar{\text{p}}$S (CERN)	1981-1990	p-$\bar{\text{p}}$	6.9 km	315 GeV	0.020	[131, 132]
Tevatron (FNAL)	1987-	p-$\bar{\text{p}}$	6.3 km	980 GeV	0.010	[133, 134]
LHC (CERN)	2007-	p-p	26.7 km	7 TeV	0.01	[135, 119, 136]

Tab. 4.1: Maximum beam-beam tune shift achieved with past and present hadron colliders.

present hadron collider facilities. A brief overview is compiled in Tab. 4.1. From this experience $\Delta Q = -0.01$ is assumed as a reasonable maximum beam-beam tune shift[1], and all maximum beam intensities calculated below are scaled to this value. Both large hadron colliders, the Sp$\bar{\text{p}}$S and the Tevatron, have been operated for luminosity production with zero crossing angle only. However, successful beam tests in the Sp$\bar{\text{p}}$S with collisions at angles up to 600 μrad ensure that there are no fundamental limitations imposed by the non-vanishing crossing angle [138].

4.3 Luminosity upgrade schemes for the LHC

The equations derived above give a complete set of relations to handle luminosity and incoherent beam-beam tune shift for Gaussian or rectangular bunches. Based on these formulae, the luminosity for different short and long bunch options as well as for the operation with a single superbunch per LHC ring are calculated and compared to the nominal LHC beam.

---

[1] Some authors assume 0.015 as the maximum tolerable beam-beam tune spread, see e.g. [137].

4.3.1 Nominal and ultimate LHC bunch crossings

The nominal LHC beam consists of twice 2808 bunches accelerated and held by a 400.8 MHz superconducting RF system. The particle distribution of the bunches is assumed to be Gaussian in all three dimensions. The relevant bunch and accelerator parameters for luminosity and beam-beam tune shift for a nominal LHC bunch crossing are summarized in Tab. 4.2 for nominal and ultimate beam intensity [139, 140, 15]. The LHC will initially operate with four interaction points in total. Two of them, the so-called high luminosity interaction points, will deliver the nominal luminosity of $1.00 \cdot 10^{34}\,\mathrm{cm}^{-2}\mathrm{s}^{-1}$, while the two other beam intersections have significantly lower luminosity. However, for the calculation of the maximum beam-beam tune spread the contributions of three interaction points have to be taken into account, which leads to a total vertical spread of 0.01. The parameters given in the column named ultimate of Tab. 4.2 are supposed to be reached without a major hardware upgrade of the nominal LHC, just by increasing the intensity per bunch until a total beam-beam tune spread of 0.01 for two high luminosity intersection points is reached. The nominal and ultimate schemes consider two alternate high luminosity beam crossings in combination with two additional low luminosity crossings. It is worth noting that an ultimate scheme with two alternating beam crossings could allow $1.85 \cdot 10^{11}$ particles per bunch and a luminosity of $2.56 \cdot 10^{34}\,\mathrm{cm}^{-2}\mathrm{s}^{-1}$ for the maximum tune shift $\Delta Q_{\mathrm{tot}} = \Delta Q_x + \Delta Q_y = -0.01$. The incoherent total tune spread of 0.01 will also be taken as limiting reference parameter for the discussion of LHC upgrade scheme in this report.

		nominal	ultimate
Number of bunches, n_b		2808	
Intensity per bunch		$1.15 \cdot 10^{11}$	$1.70 \cdot 10^{11}$
Average beam current, I_0	[A]	0.58	0.86
RMS bunch length, σ_z	[cm]	7.55	
RMS beam size at interaction points, σ^*	[μm]	16.7	
Beta function at interaction points, β^*	[m]	0.55	
Full crossing angle, θ	[μrad]	285	
Piwinski parameter, $\theta\sigma_z/(2\sigma^*)$ [141, 142]		1.29	
Horizontal beam-beam tune spread, ΔQ_x		-0.00287	-0.00422
Vertical beam-beam tune spread, ΔQ_y		-0.00339	-0.00502
Luminosity per bunch crossing, $\mathcal{L}$	[cm^{-2}s^{-1}]	$3.55 \cdot 10^{30}$	$7.72 \cdot 10^{30}$
Total luminosity, $\mathcal{L}_{\mathrm{tot}}$	[cm^{-2}s^{-1}]	$1.00 \cdot 10^{34}$	$2.18 \cdot 10^{34}$

Tab. 4.2: Relevant beam and accelerator parameters for nominal and ultimate bunch crossings in the LHC. The ultimate bunch intensity is calculated so that the total vertical incoherent beam-beam tune spread does not exceed 0.01 for two interaction points.

4.3.2 Bunch length dependence of luminosity and beam-beam tune shift

The crossing of long bunches, meaning that the bunches are long compared to the interaction length, has been analyzed in Sec. 4.2.5. Especially the behavior of the beam-beam tune shifts changes significantly if the bunch length is comparable to the interaction length.

For short round bunches, the tune shifts in both horizontal and vertical planes are of the same order of magnitude $\Delta Q_x \simeq Q_y$. In a collider equipped with multiple interaction regions the total tune shift is obtained by just summing up the individual shifts, and there is no restriction to the different crossing planes. The longitudinal regions which contribute to luminosity and beam-beam tune shift are identified by analyzing the derivative of $\Delta Q_{x,y}$ versus position z around the interaction point as presented for a nominal LHC bunch crossing in Fig. 4.4. In fact, this corresponds to the integrand of Eqs. (4.10) and (4.42, 4.43).

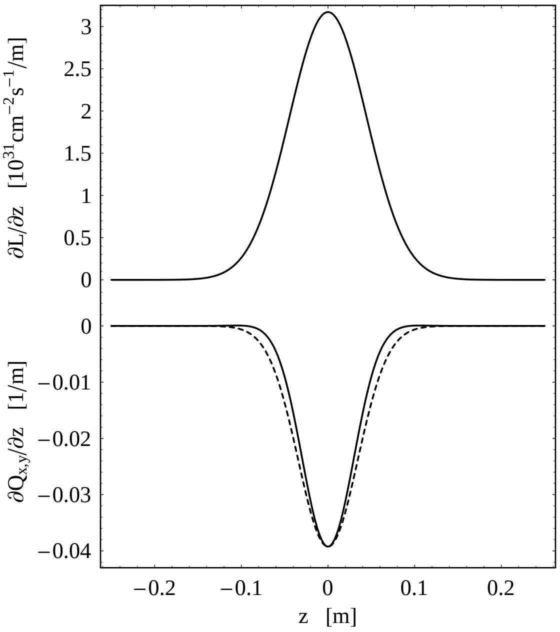

Fig. 4.4: Derivative of the luminosity and horizontal (continuous)/vertical (dashed) beam-beam tune shift versus longitudinal position of a short Gaussian bunch. The crossing parameters are $\theta = 285\,\mu$rad, $\beta^* = 0.55\,$m, $\sigma^* = 16.7\,\mu$m. The bunch intensity is $N = 1.15\cdot10^{11}$ particles and the bunch length is $\sigma_z = 7.55\,$cm. The integral tune shifts are $\Delta Q_x = -0.0029$ and $\Delta Q_y = -0.0034$.

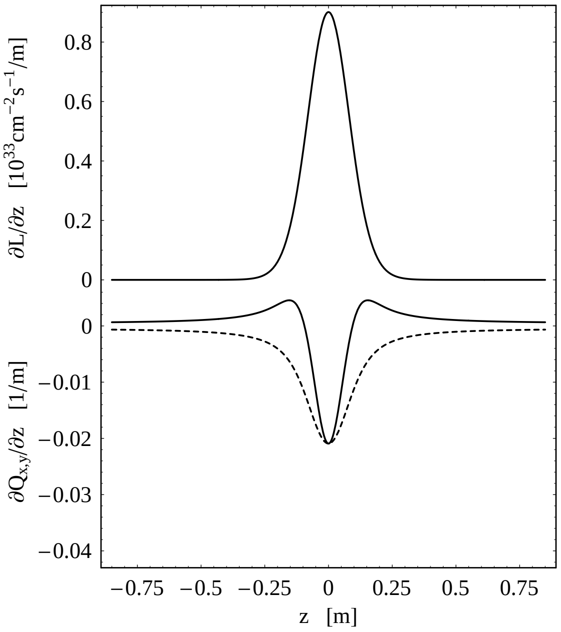

Fig. 4.5: Same illustration as Fig. 4.4 but for a long Gaussian bunch which is 100 times longer with $\sigma_z = 7.55\,$m. To obtain the same total tune shift $\Delta Q_x + \Delta Q_y$ for two alternate interaction points, the bunch intensity was set to $6.13\cdot10^{12}$ particles. The integral tune shifts are $\Delta Q_x = 0.0042$ and $\Delta Q_y = -0.0104$. The total tune shift Q_{tot} is almost equal to -0.0061 in both cases.

Due to the crossing symmetry of bunches which are much longer than the interaction length, the tune shift now has a partly positive sign in the horizontal plane and a negative sign in the vertical plane. Because of this, the collider must be equipped with at least two or any other even number of symmetric intersection points with alternating horizontal-vertical crossing angle for any long bunch scheme [136]. The effect is illustrated in Fig. 4.5. It should be mentioned that the tune shifts are given for an infinite length of interaction region so that both beams are not shielded against each other. In a real accelerator the beams are shielded from each other after a certain distance from the intersection point. Whereas the total tune shift for two alternating intersections remains almost constant, ΔQ_x decreases while ΔQ_y increases.

Furthermore, the dependence of the luminosity on the bunch length differs for Gaussian and rectangular bunches. As has been shown in Sec. 4.2.5, the formulae for long Gaussian and rectangular bunches, which are much longer than the interaction region, suggest that the luminosity of two alternate bunch crossings of rectangular bunches is $\sqrt{2}$ larger at constant total beam-beam tune shift than Gaussian bunch crossings. In fact, the approximations for Gaussian bunches applied to reduce luminosity and beam-beam tune shifts to Eqs. (4.13) and (4.46) remain valid for all cases considered in the LHC: for none of the upgrade schemes the crossing angle grows above several mrad, and the transverse beam parameters in the μm-range stay well below the bunch length being in the order of centimeters, even when the LHC is operated with short bunches [119]. Additionally, the short bunch options include a reduced beta function and thus a smaller transverse beam size σ^* at the interaction point.

In the case of rectangular bunches with crossing parameters and bunch lengths comparable to the nominal LHC beam, the approximations made to calculate the maximum luminosity in Sec. 4.2.5 cannot be applied anymore as they do not include the finite bunch length of the rectangular beam, and the more correct formulas Eqs. (4.20) or (4.24) and (4.47, 4.48) have to be evaluated. Especially this region of bunch length is of interest, as it is relatively easy to generate rectangular bunches held by a multi-harmonic RF system containing multiples of the nominal RF frequency $n \cdot 400.8\,\mathrm{MHz}$.

Starting from the ultimate LHC scheme (see Tab. 4.2) with slightly increased bunch intensity and alternating beam crossings, the luminosity provided by longer Gaussian bunch crossings and crossings with equivalent rectangular bunches is illustrated in Fig. 4.6. For both bunch profiles, the luminosity increases almost proportionally to the bunch length as expected from the relations derived in Sec. 4.2.5. It is worth noting that the total beam intensity in the accelerator has to be increased approximately proportional to the luminosity to reach the beam-beam limit.

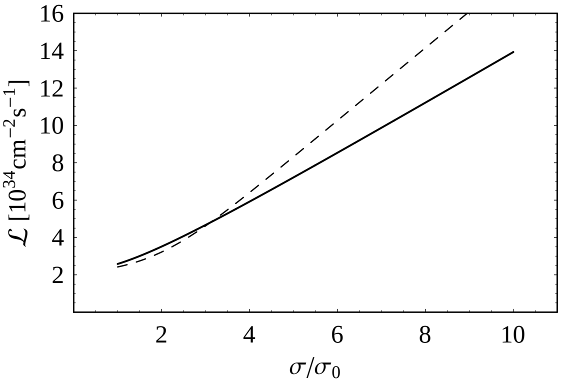

Fig. 4.6: Luminosity versus bunch length for Gaussian (continuous) and rectangular bunches for a maximum constant total beam-beam tune shift of $\Delta Q_{\mathrm{tot}} = -0.01$ according to Eqs. (4.20, 4.44) and Eqs. (4.10, 4.49). The interaction and bunch parameters correspond to the ultimate LHC parameters as presented in Tab. 4.2; only the bunch intensity at $\sigma/\sigma_0 = 1$ has been increased to $1.85 \cdot 10^{11}$ to reach the maximum tune shift for alternating crossings. The crossing angle is $\theta = 285\,\mu\mathrm{rad}$ and the bunch length is normalized to 7.55 cm.

However, the interaction between rectangular bunches, whose bunch lengths are equivalent to the nominal Gaussian bunch length, does not even yield the luminosity of the interaction between Gaussian bunches. Even for bunches being ten times longer than nominal, the luminosity gain of 1.3 is still significantly below the long bunch limit. The relative luminosity gain attained by rectangular bunch crossings instead of Gaussian crossings is shown in Fig. 4.7 for different crossing angles from $285\,\mu$rad to 5 mrad. Firstly, one can see from Fig. 4.7 that rectangular bunches in the LHC are of special interest either for long bunches which have at least 10 times the length of the nominal beam. Secondly, in the region of very large crossing angles above 5 mrad, which would be compatible with certain upgrade schemes of the LHC interaction regions [143], where the luminosity can be potentially improved by short rectangular bunch crossings.

For superbunches of at least some 10 m bunch length, the luminosity degradation due to their finite longitudinal dimensions vanishes and the theoretical luminosity gain of $\sqrt{2}$ is obtained for a crossing angle of $285\,\mu$rad.

4.3.3 Optimization of flat bunches held by multi-harmonic RF systems

In the derivations above it has been assumed that the longitudinal line density of the long bunch has a perfect rectangular form. In a real accelerator such a line density cannot be obtained easily, and a real bunch will always have some ripple along its flat region and tails of finite length. Of special interest are long and flat bunches held by a limited number of harmonic

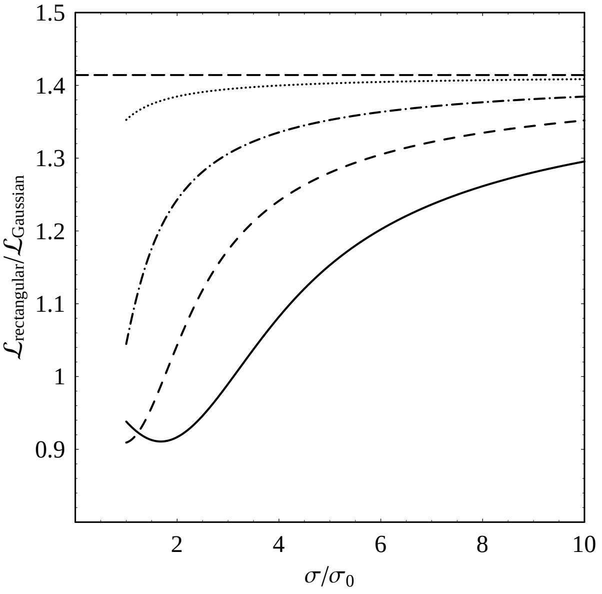

Fig. 4.7: Luminosity ratio of rectangular and Gaussian bunch crossing at constant total beam-beam tune shift ΔQ_{tot} for two alternating interaction points for different crossing angles. As in Fig. 4.6, σ_0 corresponds to the nominal bunch length. The curves show the ratio for $\theta = 285\,\mu$rad (continuous), $500\,\mu$rad (dashed), 1 mrad (dot-dashed) and 5 mrad (dotted).

RF systems operating on a multiples of the fundamental bunch frequency. The subsequent calculations will show that the imperfections due to a limited number of RF systems do not cause significant luminosity degradation compared to a rectangular line density profile.

With a crossing angle large enough for the local bunch intensity variation to be low compared to the interaction region length, the luminosity degradation due to a non-ideal longitudinal line density can be estimated analytically. The normalized line density profile of both bunches is described by a function $\zeta(z)$. To separate the luminosity effect of the bunch profile alone, the peak value of this function should be normalized as well as the integral which is proportional the total bunch intensity. Furthermore, $\zeta(z)$ has to be symmetric around the bunch center at $z = 0$. In this case the luminosity form factor $\chi_{\mathcal{L}}$ with respect to Eq. (4.5) can be defined by

$$\frac{\mathcal{L}}{\mathcal{L}_0} = \chi_{\mathcal{L}} = \int_{-\infty}^{\infty} \zeta(z)^2 \, dz \,. \tag{4.58}$$

The square of the integrand comes from the fact that a local longitudinal density $\zeta(z)$ from one beam collides with the same longitudinal density from the second one (see Fig. 4.8). It becomes clear why Eq. (4.58) is only an approximation for slow varying line density. If $\zeta(z)$ varies significantly along the interaction region, the full overlap integral has to be evaluated according to Eq. (4.5). For conventional bunches, $\chi_{\mathcal{L}} = 1/\sqrt{2}$ for Gaussian, 0.8 for parabolic

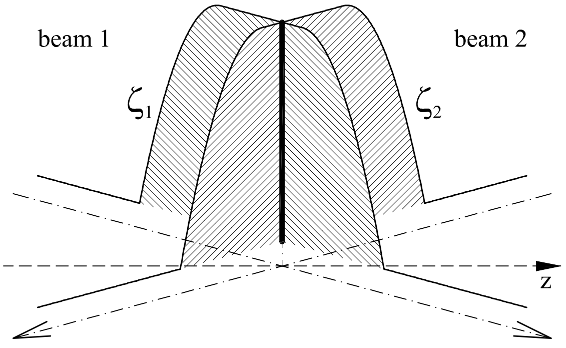

Fig. 4.8: Illustration of the local line density of a bunch crossing. Both bunches have the save line density function $\zeta_1(z) = \zeta_2(-z) = \zeta(z)$. For large crossing angles the local line density does not vary significantly along the length of the interaction region (thick line) and the form factor can be approximated according to Eq. (4.58).

and, as the maximum limit, $\chi_{\mathcal{L}} = 1$ for an ideal rectangular bunch. The result is consistent with the luminosity derivations above (see Sec. 4.1.2 and 4.1.3).

For an RF installation of n different groups of RF systems, $3n$ degrees of freedom are theoretically available: harmonic number, phase and amplitude. As the harmonic numbers have to be integer multiples of each other, they remain fixed during the luminosity optimization. The phase of the fundamental RF frequency, with the lowest harmonic number, can be arbitrarily set to zero, as it defines the absolute position of the bunches with respect to the laboratory frame. Furthermore, considering that the bucket should be symmetric around its center, the phase of all higher harmonic RF systems can only be either 0 or π. It is thus justified to reduce all phases to zero and to include higher harmonic phases as signs of their amplitudes. Finally, a set of n degrees of freedom remains, being the RF amplitudes which have to be optimized numerically such that $\chi_{\mathcal{L}}$ in Eq. (4.58) becomes largest.

To be sure to find the absolute maximum of $\chi_{\mathcal{L}}$, the optimization is performed in two steps. For a first approximation, the number of independent parameters is reduced to a global barrier harmonic number h_b according to Fig. 4.9 (see Sec. 2.3.1) of the barrier bucket and to a global voltage scaling. The relative amplitude scaling for the individual RF systems are taken from the Fourier coefficients of a single sinusoidal pulse, with a time length defined by the harmonic number h_b:

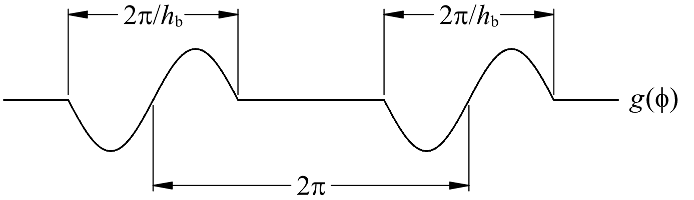

Fig. 4.9: Definition of the barrier harmonic h_b.

$$\left.\begin{array}{ll}\sin(h_b\phi), & -\frac{\pi}{h_b}\le\phi\le\frac{\pi}{h_b}\\ 0, & \text{elsewhere}\end{array}\right\} = \frac{\cos(h_b\pi)}{h_b} + \sum_{h\neq h_b}\frac{2h\cos(h_b\pi)\sin(h_b/h\,\pi)}{\pi(h^2-h_b^2)}. \tag{4.59}$$

Examples of such an optimization for two to five different harmonic numbers are shown in Figs. 4.10 to 4.13. In the case of the double harmonic RF system, the amplitudes of both harmonics are plotted directly. There is no absolute maximum of the form factor $\chi_{\mathcal{L}}$ for two harmonics, as the situation improves for larger RF voltages (see Fig. 4.13).

Once the region of interest is found, each of the amplitudes is varied individually until the absolute maximum is found. The numerical results of such an optimization are given in Tab. 4.3. All parameters like the luminosity form factor or the peak current are calculated under the assumption of a stationary distribution being parabolic in energy for all slices in z, which is matched to the multi-harmonic RF bucket. This assumption is consistent with the model by Hofmann and Pedersen introduced in Sec. 2.6. As can be seen from Tab. 4.3, the optimum bunch form is typically reached for a peak current that is significantly lower than the peak current of an LHC nominal bunch. Therefore the average bunch current can be increased to re-establish the original peak current and thus the original beam-beam tune shift.

The equivalent rectangular bunch length stated in Tab. 4.3 refers to an ideal rectangular bunch with the same peak and average beam intensity as the bunch kept in the multi-harmonic RF configuration. Fig. 4.14 illustrates an example for an optimized flat bunch kept by three RF harmonics and its rectangular equivalent.

The absolute values for the RF voltages in Tab. 4.3 are calculated for the special case of long and flat bunches consisting of 16 almost nominal bunches each in order to fit the longitudinal

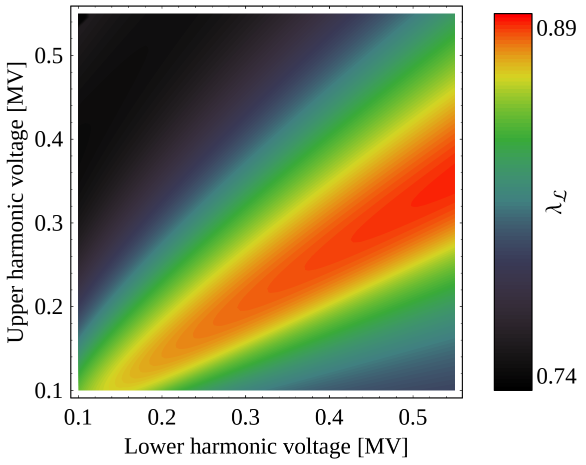

Fig. 4.10: Form factor $\chi_{\mathcal{L}}$ (color scale from blue to red) versus both voltages of a double harmonic RF system. Maximum form factor is reached for a voltage ratio of about 0.66.

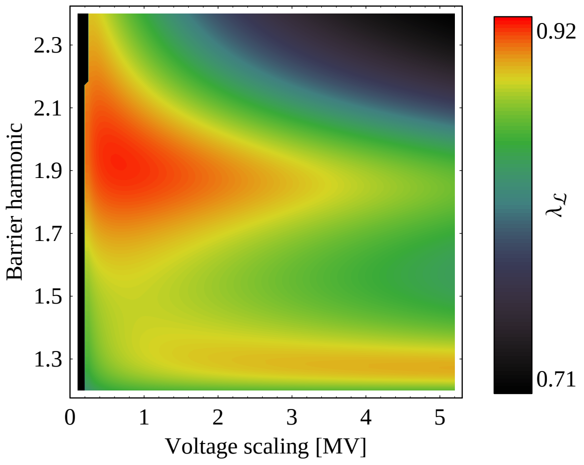

Fig. 4.11: Luminosity form factor versus barrier harmonic and general voltage scaling for three different RF harmonics.

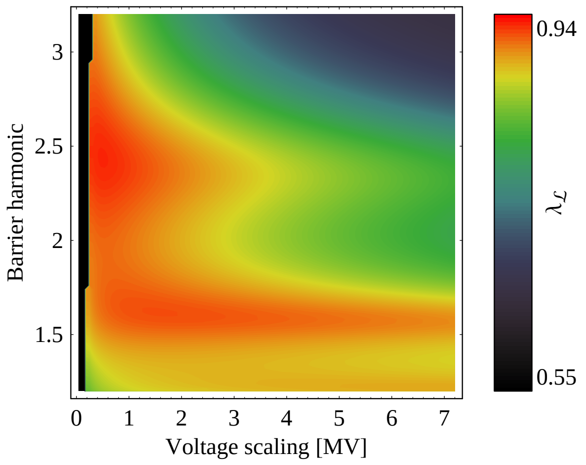

Fig. 4.12: Luminosity form factor versus barrier harmonic and general voltage scaling for four different RF harmonics.

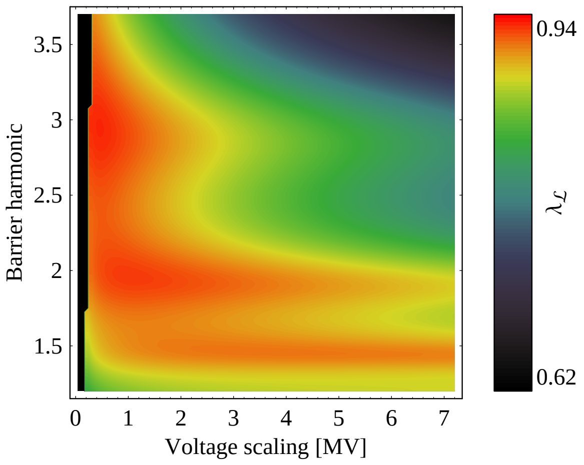

Fig. 4.13: Luminosity form factor versus barrier harmonic and general voltage scaling for five different RF harmonics.

emittance (see Sec. 4.3.6). However, the luminosity degradation factor $\chi_{\mathcal{L}}$ and the relative bunch length normalized to the bucket depend on the number of available RF systems only. These are the two important ingredients to scale the final luminosity.

4.3.4 Short bunch schemes

Throughout this report, short bunch upgrade options are referred to as schemes for which the bunch length remains in the order of magnitude as the nominal LHC bunches[2]. This would be advantageous because one could make use of the standard 400.8 MHz so that the bunch frequency stays the same. Theoretically, there are two different approaches for a luminosity improvement.

---

[2] The short bunch schemes in this report are different from what is presented as short bunch options in [119] as bunches shorter than nominal using an RF system at 1.2 GHz are considered in that reference.

			Long and flat bunch			
		nominal bunch	(16 bunches, $16 \cdot 1.5\,\text{eVs}$)			
Number of RF harmonics		1	2	3	4	5
Longitudinal emittance, ε	[eVs]	2.5	24.0	24.0	24.0	24.0
Fundamental harmonic, h_0		35640	3564	3564	3564	3564
RF voltages	[MV]	16.00	0.54	0.58	0.31	0.26
			-0.34	-0.60	-0.39	-0.38
				0.24	0.27	0.34
					-0.09	-0.19
						0.06
Total RF voltage	[MV]	16.00	0.88	1.42	1.05	1.23
Normalized peak current		1	0.92	0.80	0.68	0.63
Bucket filling factor		0.33	0.46	0.39	0.48	0.47
Luminosity form factor, $\chi_{\mathcal{L}}$		0.71	0.89	0.93	0.95	0.96
Equivalent rectangular length,	[m]	0.19	3.64	4.19	4.90	5.26
(normalized to bucket length)		0.25	0.49	0.56	0.65	0.70

Tab. 4.3: Effective luminosity form factor $\chi_{\mathcal{L}}$ for flat bunches held by different numbers of RF harmonics. The nominal LHC bunch is compared to a long and flat bunch consisting of 16 almost nominal LHC bunches with a longitudinal emittance of 1.5 eVs each. The long bunch is held in a multiple harmonic RF system with $3564 \cdot f_0 = 40.08\,\text{MHz}$. The double harmonic RF system is given for reference.

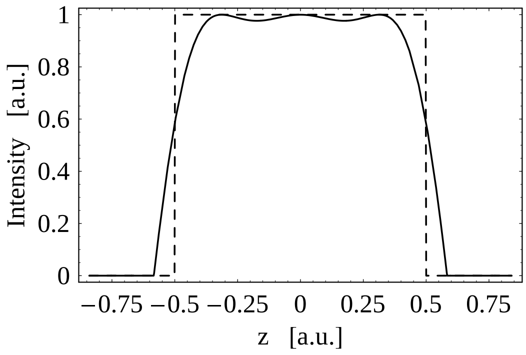

Fig. 4.14: Normalized line density of a bunch held by three multiple RF harmonics h, $2h$ and $3h$ (continuous line) compared to an ideal rectangular bunch having the same peak and total particle intensity.

On the one hand, the bunch length could be increased by a reduction of the RF amplitude and an increase of the longitudinal beam intensity so that the original peak current is reconstituted. The expected luminosity starting from an ultimate bunch has already been presented in Fig. 4.7 (continuous line). However, as the bunch length only increases proportionally to the fourth root of the amplitude (see Sec. 2.6.2) and the bucket area shrinks according to the square root, insufficient bucket area immediately limits this way to increase luminosity in the LHC. This idea will therefore not be considered further.

On the other hand, the bunch length can be increased while simultaneously improving the bunch profile to a more rectangular-like bunch by using multi-harmonic RF systems at multiples of 400.8 MHz. It is clear from the bunch length dependence of the luminosity gain that for small crossing angles below several mrad the luminosity gain is mostly due to the longer bunches and thus due to an increased total beam intensity. If the crossing angle could be raised while simultaneously increasing the total beam intensity for constant beam-beam tune shift, the luminosity profits from an additional form factor of about 1.3 (see Fig. 4.7).

An overview on the parameters of the LHC operated with short rectangular bunches at a very large crossing angle of $\theta = 5\,\mathrm{mrad}$ and for the nominal number of bunches is given in Tab. 4.4. Due to the luminosity loss caused by the large crossing angle, the performance of a scheme with initial bunches of even four times the nominal intensity can hardly surpass the luminosity of the nominal LHC beam. Reaching the beam-beam limit at $\Delta Q_{\mathrm{tot}} = -0.01$ with such a beam requires a bunch intensity of about 50 times the intensity of nominal bunches, respectively an average circulating current of nearly 30 A, which is obviously not compatible with respect to the present LHC design.

		four times nominal intensity	beam-beam ultimate intensity
Number of bunches, n_b		2808	
RF systems	[MHz]	400.8/801.6/1202.4	
Intensity per bunch, N_b		$4.6 \cdot 10^{11}$	$57.3 \cdot 10^{11}$
Average beam current, I_0	[A]	2.33	29.0
Total bunch length, l_b	[m]	0.42	
RMS beam size at interact. points, σ^*	[μm]	11.2	
Beta function at IP, β^*	[m]	0.25	
Full crossing angle, θ	[mrad]	5.0	
Horiz. beam-beam tune spread, ΔQ_x		-0.000012	-0.00014
Vertical beam-beam tune spread, ΔQ_y		-0.000793	-0.0099
Total beam-beam tune spread, ΔQ_{tot}		-0.0008	-0.01
Luminosity per bunch crossing, $\mathcal{L}$	[cm^{-2}s^{-1}]	$5.65 \cdot 10^{30}$	$8.79 \cdot 10^{32}$
Total luminosity (rectangular), $\mathcal{L}_{\mathrm{tot}}$	[cm^{-2}s^{-1}]	$1.58 \cdot 10^{34}$	$2.47 \cdot 10^{36}$
Degradation due to multi-harmonic approximation		0.93	
Total luminosity, $\mathcal{L}_{\mathrm{tot}}$	[cm^{-2}s^{-1}]	$1.48 \cdot 10^{34}$	$2.29 \cdot 10^{36}$

Tab. 4.4: Beam and crossing parameters for an operation of the LHC with short rectangular bunches at very large crossing angles around 5 mrad.

In conclusion, the collision of short bunches under large crossing angles of several mrad pushes the beam-beam limit by more than an order of magnitude. However, the luminosity degradation induced by the crossing angle has to be compensated by an enormous increase in total beam intensity. This problem applies to rectangular or rectangular-like bunches as well as to Gaussian beam packages. Therefore, short rectangular bunch schemes will not be analyzed further.

4.3.5 Superbunch schemes

Superbunches in the LHC have already been proposed in [16, 144, 119]. A superbunch hadron collider is operated with one or few bunches confined in a small fraction of the circumference which contains the total beam intensity. In fact, the particles within the homogeneous section of the bunch can be approximated as a coasting beam. To prevent the bunch structure from dispersive decay, RF pulses have to be applied at both ends of the bunch in order to generate potential barriers in the longitudinal phase space. In Sec. 2.3 the dynamics of the longitudinal phase space is discussed in detail. The bunch length and longitudinal density can be controlled by the time interval between the two RF pulses limiting the bunch, resulting in a high flexibility with respect to the longitudinal beam parameters.

In superbunch hadron colliders the available longitudinal phase space is used more efficiently than in conventional hadron colliders operated with bunched beam, where only small regions, namely the populated buckets are filled with a large longitudinal particle density. However, it is worth noting that the luminosity gain from the bunch form alone compared to a bunch with longitudinal Gaussian distribution is never above $\sqrt{2}$.

Relevant parameters of the superbunch option presented in [127] and of a superbunch scheme at the beam-beam limit are summarized in Tab. 4.5. A luminosity of $9 \cdot 10^{34}\,\mathrm{cm}^{-2}\mathrm{s}^{-1}$, which is almost one order of magnitude above the nominal luminosity of the LHC, can be reached by doubling the total beam intensity.

		superbunch see [127]	beam-beam, ultimate density
Number of bunches, n_b		1	
Intensity per bunch, N_b		$6.44 \cdot 10^{14}$	λl_b
Average beam current, I_0	[A]	1.16	$0.0049 \cdot l_b$
Longitudinal density, λ	[1/m]	$2.47 \cdot 10^{12}$	$2.73 \cdot 10^{12}$
Total bunch length, l_b	[m]	260	l_b
RMS beam size at interact. points, σ^*	[μm]	11.2	
Beta function at IP, β^*	[m]	0.25	
Full crossing angle, θ	[mrad]	1.0	
Total beam-beam tune spread, ΔQ_{tot}		-0.0091	-0.01
Luminosity per bunch crossing, $\mathcal{L}$ (equivalent to total luminosity)	[$\mathrm{cm}^{-2}\mathrm{s}^{-1}$]	$9.05 \cdot 10^{34}$	$4.25 \cdot 10^{32} \cdot l_b$

Tab. 4.5: Relevant parameters for an operation of the LHC with one long superbunch per beam (see Eqs. 4.55). The second column shows that the luminosity can be improved by increasing total beam current and bunch length while keeping constant longitudinal density. Neglecting small beam gaps for the RF barriers and for the RF system to compensate synchrotron radiation, the coasting beam luminosity limit at $\Delta Q_{\mathrm{tot}} = -0.01$ is $\mathcal{L}_{\mathrm{max}} = 1.13 \cdot 10^{37}$. However, the average beam current to get this luminosity would be about 130 A.

The main disadvantages of long superbunches are that they require sophisticated and costly high power wide-band RF systems for the confinement of the bunches and for the compensation of synchrotron radiation losses. Additionally, no realistic scheme to generate such long bunches in the LHC has been proposed so far. Apart from that, the experiments would have to be modified extensively, since a superbunch crossing delivers a much higher event rate and does not allow for an easy tagging of the collision times. However, the numbers stated in Tab. 4.5 serve as reference parameters for comparison with different long bunch schemes.

4.3.6 Long bunch schemes

The so-called long bunch schemes are a compromise between the two options, optimized short bunches and superbunches, discussed above. According to Fig. 4.15, there is no fundamental necessity that all bunches have to be kept in a single superbunch. Theoretically, equal lumi-

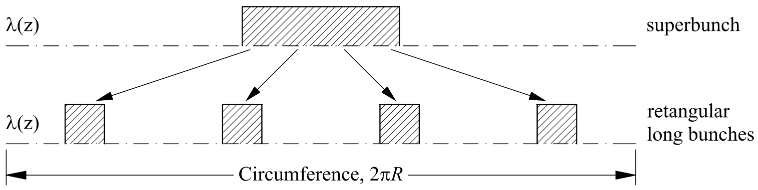

Fig. 4.15: Comparison of a single superbunch to several rectangular long and flat bunches. Cutting superbunches into rectangular pieces and redistributing them along the circumference of a circular accelerator leaves the total luminosity and beam-beam tune spread unaffected.

nosity is achieved by cutting the single superbunch into several rectangular slices which could be distributed homogeneously around the ring. The physics detectors profit from such a scheme as the enormous total event rate of the superbunch crossings is also subdivided into smaller units with a certain time for event data handling between the bunch crossings. Practically, the RF gymnastics does not start from one superbunch, as illustrated, being subdivided into shorter buckets, but from a bunched beam with properties close to the nominal LHC beam. An RF procedure to combine a batch of a bunched beam to the long and flat bunches is analyzed in detail in Chapter 5. This RF gymnastics is capable of compressing and merging 2^n nearly nominal LHC bunches with the nominal inter-bunch time of 25 ns to one dense long and flat bunch kept by an RF system operating at multiples of 40.08 MHz.

Tab. 4.6 gives a comprehensive overview of different long and flat bunch options limited either by the average beam current or by the maximum beam-beam tune shift. The four columns on the left hand side present schemes where 16 nearly nominal LHC bunches are compressed and merged to long and flat bunches, while the right columns analyze the combination of 32 bunches. The main difference between these two options is the effective beam length which is twice as long for the 16-bunch schemes as for 32 bunches, because twice the number of final bunches is generated. This means that the beam-beam limit is reached at half the luminosity and half the average beam current as for 32-bunch options compared the confinement of 16 bunches. From this analysis it becomes obvious why other schemes, e.g. the compression and merging of 8 or 64 nominal bunches, are not attractive in the LHC:

Confining 8 initial bunches would push the beam-beam limit to an average current being twice 3.21 A, which can neither be obtained nor handled in the LHC under realistic conditions.

Starting from 64 bunches would, in contrast, reduce the maximum luminosity to about half the value given in the last column of Tab. 4.6. Furthermore it requires enormous RF voltages at 40.08 MHz and harmonics, because doubling the emittance compared to the 32-bunch options demands four times more RF voltage.

By comparing the luminosity figures for the different schemes to the ultimate LHC luminosity $\mathcal{L}_{\text{tot}} = 2.2{\cdot}10^{34}$ (see Tab. 4.2) it becomes clear that crossing of long bunches under small crossing angles is not an attractive option for the LHC. Because of the contribution of the square root factor in the total beam-beam tune shift expression for Gaussian bunches (see Eq. 4.46), the beam-beam limit is reached at a lower average beam current for rectangular bunches than for Gaussian bunches. Colliding long and flat rectangular bunches at nominal beam crossing parameters (Tab. 4.2, left two columns) is only interesting if the total beam intensity is limited by other effects and if as much luminosity as possible has to be produced with the available beam current. However, as the beam-beam tune spread limits the intensity to 1.2 times the nominal one, the luminosity attained never exceeds the regular LHC ultimate scheme.

This situation is improved significantly by an increase of the crossing angle to 1 mrad which has already been proposed for the superbunch option. In the case of long bunches consisting of 16 initial bunches (two center columns of Tab. 4.2) the beam-beam limit is pushed so far that a maximum average beam current of more than 3 A could be reached if there were no other current limitations in the LHC. Operating the LHC with a reduced total tune spread of $\Delta Q_{\text{tot}} = -0.003$ still delivers a luminosity of $\mathcal{L}_{\text{tot}}$ slightly above the luminosity of the ultimate scheme.

A remarkable luminosity improvement is achieved by confining batches of 32 nearly nominal LHC bunches each to a long and flat one. For twice the nominal beam current, 55 % of the luminosity of superbunch crossing, for which a similar beam intensity is assumed, and about twice the luminosity of the LHC ultimate scheme are within reach. Again, this is well below the

Long bunch consists of		16 near nominal LHC bunches				32 LHC bunches	
		nominal crossing		superbunch crossing		superbunch crossing	
		nominal	beam-beam ultimate	twice nominal	beam-beam ultimate	twice nominal	beam-beam ultimate
Number of bunches, n_b		156		156		78	
Intensity per bunch, N_b		$1.84 \cdot 10^{12}$	$2.17 \cdot 10^{12}$	$3.68 \cdot 10^{12}$	$1.14 \cdot 10^{13}$	$7.36 \cdot 10^{12}$	$1.14 \cdot 10^{13}$
Average beam current, I_0	[A]	0.52	0.61	1.03	3.21	1.03	1.60
Longitudinal density, λ	[1/m]	$4.39 \cdot 10^{11}$	$5.18 \cdot 10^{11}$	$8.79 \cdot 10^{11}$	$2.72 \cdot 10^{12}$	$1.75 \cdot 10^{12}$	$2.72 \cdot 10^{12}$
Total bunch length, l_b	[m]	4.19		4.19		4.19	
Total beam length, $n_b l_b$	[m]	327		327		653	
RMS beam size at interact. points, σ^*	[μm]	16.7		11.2		11.2	
Beta function at IP, β^*	[m]	0.55		0.25		0.25	
Full crossing angle, θ	[mrad]	0.285		1.0		1.0	
Horiz. beam-beam tune spread, ΔQ_x		0.00068	0.00081	0.00043	0.00135	0.00087	0.00135
Vertical beam-beam tune spread, ΔQ_y		-0.00916	-0.01081	-0.00781	-0.01136	-0.00732	-0.01136
Total beam-beam tune spread, ΔQ_{tot}		-0.00848	-0.01	-0.00323	-0.01	-0.00645	-0.01
Luminosity per bunch crossing, $\mathcal{L}$	[cm^{-2}s^{-1}]	$1.05 \cdot 10^{32}$	$1.47 \cdot 10^{32}$	$1.82 \cdot 10^{32}$	$1.75 \cdot 10^{33}$	$7.30 \cdot 10^{32}$	$1.75 \cdot 10^{33}$
Total luminosity, $\mathcal{L}_{\text{tot}}$	[cm^{-2}s^{-1}]	$1.64 \cdot 10^{34}$	$2.29 \cdot 10^{34}$	$2.85 \cdot 10^{34}$	$2.73 \cdot 10^{35}$	$5.69 \cdot 10^{34}$	$1.37 \cdot 10^{35}$
Degradation due to multi-harmonic approximation		0.93		0.93		0.93	
Total luminosity, $\mathcal{L}_{\text{tot}}$	[cm^{-2}s^{-1}]	$1.53 \cdot 10^{34}$	$2.13 \cdot 10^{34}$	$2.64 \cdot 10^{34}$	$2.54 \cdot 10^{35}$	$4.92 \cdot 10^{34}$	$1.27 \cdot 10^{35}$

Tab. 4.6: Relevant parameters for an operation of the LHC with long and flat bunches held by multi-harmonic RF systems. The first two columns show luminosity and beam-beam tune spread for collisions with nominal crossing parameters at nominal intensity and ultimate intensity for $\Delta Q_{\text{tot}} = -0.01$. It is assumed that 16 bunches are combined to one long and flat bunch. The center two columns present two similar schemes at superbunch collision parameters. The beam-beam limit is pushed to a total average beam current of 3.2 A, which is not compatible with the present LHC design but shows its theoretical potential, assuming that all other beam current limitations can be cured. The last two columns illustrate options where 32 initial LHC bunches have to be confined to one long bunch. For an average beam current comparable to the superbunch option (Tab. 4.5), already 55 % of the luminosity of the superbunch LHC is within reach. When increasing the beam current to the beam-beam limit, the luminosity increases even above the classical superbunch option. It is worth noting that the number of bunches is calculated assuming the same fraction of gaps as for the nominal LHC beam, i.e. $n_b = 2808/3564 \cdot 198 = 156$, respectively $2808/3564 \cdot 99 = 78$.

beam-beam limit. Pushing the average beam current to 1.6 A, at which the beam-beam limit is reached for such long bunches, the maximum luminosity increases up to $\mathcal{L}_{\text{tot}} = 1.27 \cdot 10^{35}\,\text{cm}^{-2}\text{s}^{-1}$. This increase even above the luminosity of the superbunch scheme is due to the improved effective beam length so that the beam-beam limit is violated at a larger average beam current.

It should be mentioned that the analysis above assumes an RF system with three different RF harmonics. However, according to the relative rectangular bunch to bucket length ratio given in Tab. 4.3 in combination with Eqs. (4.56) and (4.57) it is easy to rescale the luminosity values for a different number of RF harmonics.

4.4 Summary

A summary of the three different options discussed above, short rectangular bunches, long rectangular bunches and very long superbunches as well as its estimated impact on the upgrade of the LHC and its physics detectors is given in Tab. 4.7.

	short and flat bunch	long and flat bunch	superbunch
Total bunch length, l_b	$40\ldots 50\,\text{cm}$	$4\ldots 5\,\text{m}$	$200\ldots 400\,\text{m}$
Total beam intensity for $\mathcal{L}_{\text{tot}} = 10^{35}\,\text{cm}^{-2}\text{s}^{-1}$	enormous	high	high
Additional RF systems	reasonable: 800/1200 MHz	reasonable: 40/80/120 MHz	extensive: Barrier bucket RF at $\simeq 10\,\text{MHz}$
Consequences for physics experiments	limited	significant modifications	extensive modifications
Consequences the accelerator hardware	limited	significant/difficult modifications	extensive/impossible modifications
RF gymnastics to generate long bunches	easy	sophisticated	presently no realistic scheme
Synchrotron radiation compensation	unnecessary	unnecessary	necessary and difficult
Details	see Tab. 4.4	see Tab. 4.5	see Tab. 4.6

Tab. 4.7: Comparison of the different flat bunch luminosity upgrade options in the LHC sorted by ascending bunch length.

The short rectangular bunch option seems to be attractive because of its simplicity. Most of the beam parameters like bunch spacing or bunch pattern, which have an impact on other accelerator subsystems like beam diagnostics and timing, remain unchanged with respect to the nominal LHC beam. However, as shown in Sec. 4.3.4, the crossing angle and the total beam intensity has to be increased enormously to profit from these advantages.

The superbunch option offers the best flexibility concerning the total length of the beam and luminosity. The modifications necessary at the physics experiments to prepare them for a huge event rate during a superbunch crossing has not been explored yet, but these surely require a very challenging redesign of large parts of detectors and read-out electronics. Furthermore, so far no consistent, realistic RF gymnastics scheme has been found that could generate superbunches of a few hundred meters bunch length in the LHC.

The most favorable option is represented by the class of long and flat bunch schemes where a batch of 16 or 32 almost nominal LHC bunches is compressed and merged to a single dense bunch held by RF systems operated at multiple harmonics of 40.08 MHz. Although significant modifications of the accelerator and the physics detectors will be necessary to operate the LHC in such a long bunch mode, the scheme is a quite realistic means to aim at twice the luminosity of the ultimate scheme.

Chapter 5

Generation of Long Bunches in the LHC

Whereas the benefits of different kinds of long and flat bunches have been discussed with respect to the strong incoherent beam-beam limit, this chapter is devoted to the creation of these bunches by means of longitudinal RF manipulations as introduced in Chapter 3.

The generation of the beam for the nominal LHC scheme and especially its bunch pattern defines the initial conditions for the long bunch creation. It is therefore described in the first part of this chapter. Secondly, schemes to combine several, nearly nominal LHC bunches to long and flat bunches are examined. It is shown that the straightforward approach to confine the long bunches between barrier buckets has inherent disadvantages.

An RF manipulation scheme based on well-proven RF gymnastics, namely batch compression and bunch pair merging, is proposed and worked out in detail in the last part of this chapter. The discussion of high intensity effects will be addressed in a separate chapter.

5.1 Generation of the nominal and ultimate LHC beam

The parameters of the proton beam and its final parameters during injection into the LHC at an energy of 450 GeV strongly depend on the parameters of the upstream accelerators in the injector chain. Before entering the LHC, the protons have to pass through a linear accelerator and three synchrotrons of different size and properties. Albeit extensive upgrades have been carried out [145, 146, 147, 148], these accelerators have intrinsic limitations like direct space charge in the low energy regime, which cannot be circumvented. Basic parameters like injection and ejection energy or the circumference require unreasonable effort or are even impossible to be implemented at existing accelerators. Furthermore, the beam structure delivered by an accelerator depends on the parameters of the various subsystems with which it is equipped, e.g. the frequency of the RF system that defines the possible bunch spacings which can be accelerated.

A brief overview on the different accelerators in the LHC injector chain is given in the subsequent sections. Their fundamental limitations will also be introduced to sketch their basic capabilities of delivering modified beam parameters so that the bunches at the SPS ejection could be used as an starting point for the generation of long and flat bunches in the LHC.

5.1.1 Proton injectors for the LHC

Before injection into one of the two LHC rings, the particles coming from a linear accelerator (Linac2) are accelerated in three circular accelerators, namely the Proton Synchrotron Booster (PSB), the Proton Synchrotron (PS) and the Super Proton Synchrotron (SPS). The proton injector chain is sketched in Fig. 5.1. A non-exhaustive list of the relevant parameters of the circular accelerators relevant for proton injection into the LHC is compiled in Tab. 5.1.

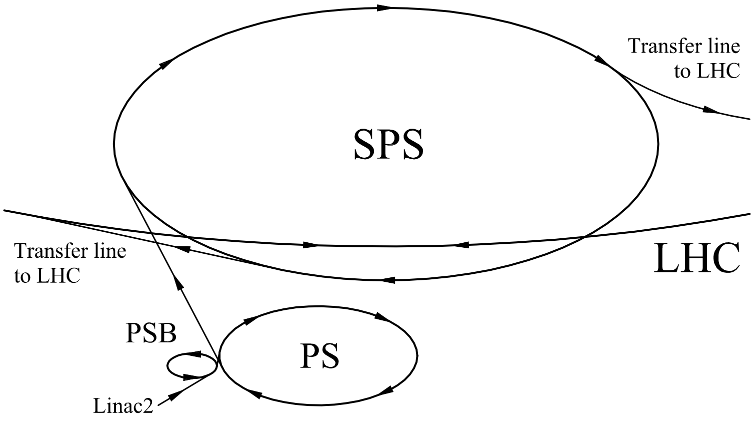

Fig. 5.1: Sketch of the proton injector chain of the LHC: the protons are pre-accelerated in Linac2 up to a kinetic energy of 50 MeV. The PSB boosts their kinetic energy to 1.4 GeV for injection into the PS. After extensive RF manipulations and acceleration to a total energy of 26 GeV, they are transferred to the SPS which finally accelerates the beam to the LHC injection energy of 450 GeV. Note that PSB and PS are sketched four times too large compared to SPS and LHC. The PSB is made up of four rings which are not shown in the sketch. Note that the LHC consists of two storage rings for the counter-rotating proton beams.

Linear Accelerator (Linac2)

The linear accelerator Linac2 mainly consists of three cavity sections with Alvarez structures working at 202.5 MHz. It accelerates the beam from a kinetic energy of 750 keV to 50 MeV [149]. Linac2 is fed by radio frequency quadrupole (RFQ), a special cavity type which can perform bunching, acceleration and transverse focusing of low energy beams simultaneously. The maximum output current has been optimized to 190 mA to fulfill the intensity requirements of the LHC beam and to deliver at least 180 mA to the PSB.

Proton Synchrotron Booster (PSB)

The PSB is a synchrotron which actually consists of four identical rings stacked on top of each other [150, 151]. It was originally installed to overcome the space charge limitation imposed by direct injection from the linac to the PS. Since then its ejection energy has been upgraded twice from to 800 MeV via 1 GeV to finally 1.4 GeV, in order to push the space charge limitation during transfer from the PSB to the PS. The second upgrade to 1.4 GeV was implemented especially for the production of the ultimate beam for the LHC which would have an excessive space charge induced betatron tune shift ΔQ at 1 GeV. With its four rings, the PSB accelerates four times the intensity per ring in one cycle. In the case of the nominal and ultimate LHC beams, the PSB provides one bunch per ring using RF operating on the first harmonic of the revolution frequency [152, 153, 154]. To optimize the ratio of peak to average intensity,

Machine:		PSB (four rings)	PS	SPS
Circumference, $2\pi R$	[m]	157.1	628.3	6911.5
(normalized to PS)		1/4	1	11
Injection energy, E_{inj}	[GeV]	$0.05 + E_0$	$1.4 + E_0$	26.0
Ejection energy, E_{ej}	[GeV]	$1.4 + E_0$	26.0	450
Filling scheme		1 bunch	2 PSB batches	2/3/4 PS bats.
Number of bunches, n_b		1	$4 + 2 \longrightarrow 72$	144/216/288
Bunch spacing, t_b	[ns]		$327 \longrightarrow 25$	25
RF harmonics, h		1+2	$7 \rightarrow 21 \rightarrow 84$	4620
Fund. RF frequencies, f_{RF}	[MHz]	0.6–1.7	3.1/9.3–10/40	200.4
Long. emittance at inj.	[eVs]			0.35
Long. emittance at ej.	[eVs]	1	0.35	0.70
Nominal scheme:				
Beam int. at inj., N_{tot}		$1.87 \cdot 10^{12}$ /rg.	$9.66 \cdot 10^{12}$	$1.66/2.48/3.31 \cdot 10^{13}$
		$I_L = 180\,\mathrm{mA}$		
Beam int. at ejection, N_{tot}		$1.63 \cdot 10^{12}$ /rg.	$8.28 \cdot 10^{12}$	$1.66/2.48/3.31 \cdot 10^{13}$
Ultimate scheme:				
Beam int. at inj., N_{tot}		$2.76 \cdot 10^{12}$ /rg.	$1.43 \cdot 10^{12}$	$2.45/3.67/4.90 \cdot 10^{13}$
		$I_L = 180\,\mathrm{mA}$		
Beam int. at ejection, N_{tot}		$2.41 \cdot 10^{12}$ /rg.	$1.22 \cdot 10^{13}$	$2.45/3.67/4.90 \cdot 10^{13}$

Tab. 5.1: Relevant parameters of the circular accelerators in the LHC injector chain.

a second harmonic RF system is used to flatten the bunches and thus to decrease the peak intensity [155, 156]. For the LHC beam each PSB bunch has an intensity of some $1.6 \cdot 10^{12}$ protons, slightly more than twelve times the intensity of an LHC bunch because of losses during transfer and capture in the PS. The transfer between the four rings of the PSB and the PS is sketched in Fig. 5.2. During the first transfer, bunches from all four booster rings are stringed up in the PS. One PSB machine cycle later (corresponding to 1.2 s), half of the rings are used to deliver two more bunches. Finally, six of seven PS buckets are populated. The empty bucket is needed for the transfer from the PS to the SPS to preserve a gap for the beam ejection.

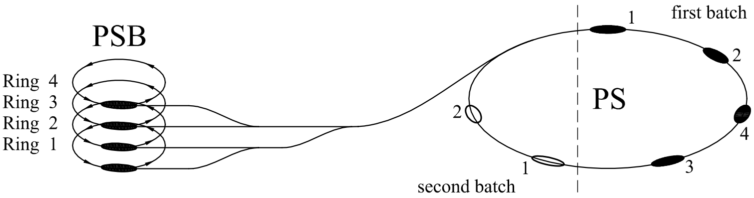

Fig. 5.2: Double batch transfer scheme from PSB to PS. For the injection into the PS all four booster rings are used, each delivering one bunch. The second injection is performed with two booster bunches only.

Proton Synchrotron (PS)

The PS is a combined function alternating gradient synchrotron which accelerates the proton beam to a total energy of up to 26 GeV [157, 158, 159]. However, acceleration is not the only function of the PS in the LHC injector chain [160]. It also has to prepare the bunch structure for the LHC: bunches with an intensity of slightly more than $1.15 \cdot 10^{11}$ protons with a bunch spacing of 25 ns. Successive longitudinal splitting procedures are performed to meet these requirements.

The longitudinal emittance at ejection from the PS must be around 0.35 eVs, much below the final nominal emittance of 2.5 eVs in the LHC, to fit the bunches into the rather small buckets of the 200 MHz RF system in the SPS.

As the six bunches coming from the PSB are injected at $h = 7$, the bunch spacing at final energy would be some 300 ns, and the longitudinal emittance would be much too large to capture these bunches in the SPS. Therefore each bunch is split into twelve equal fractions, which reduces the longitudinal emittance per bunch to a value that is acceptable for the SPS. The bunch spacing is also divided by twelve to the nominal LHC parameter of 25 ns. The splitting factor can be decomposed to $12 = 3 \cdot 2 \cdot 2$, so that one triple-splitting and two bunch pair splittings are performed (see Sec. 3.2.2). To keep the RF frequencies during acceleration within the capabilities of the main RF system in the PS (2.8 to 10 MHz) [161, 162], the triple splitting is initiated during the injection flat-bottom at 1.4 GeV [163]. Thereafter the beam is accelerated on $h = 21$ and subsequently the bunches are split twice to $h = 42$ and finally to $h = 84$. The RF gymnastics for the preparation of the LHC beam in the PS is illustrated in Fig. 5.3. Finally one ends with a batch of 72 bunches and, as the empty bucket splits exactly like the bunches, a gap of 12 non-populated buckets. This gap is sufficiently long to allow the extraction kicker magnet to be switched on without perturbing the beam.

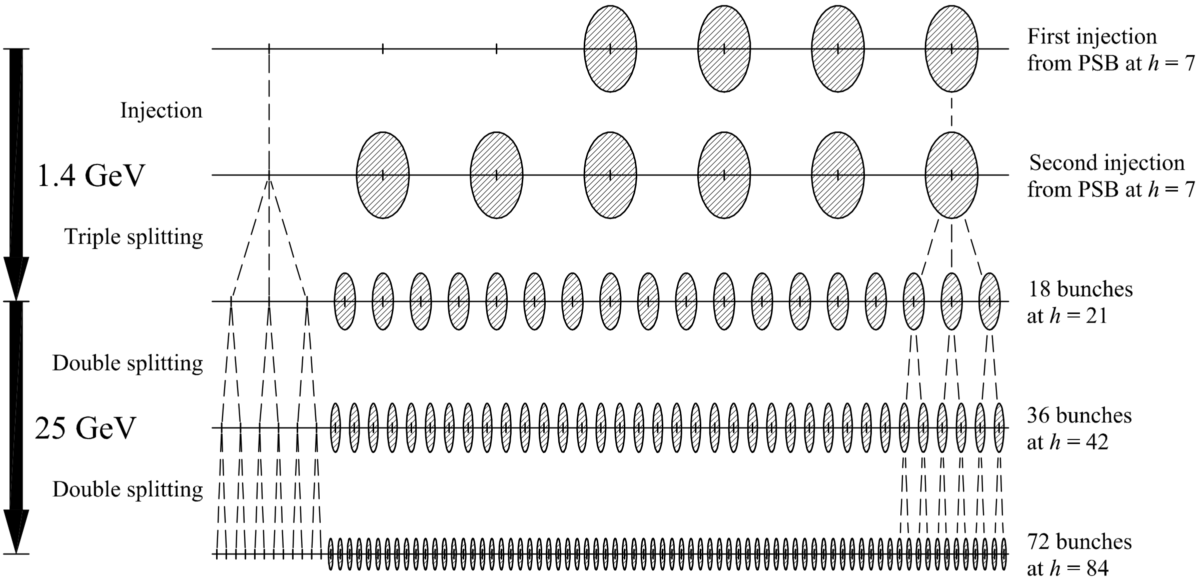

Fig. 5.3: Acceleration and bunch splitting scheme of the nominal LHC beam in the PS. Starting from $4 + 2$ bunches from the PSB each of them is split twelve times in total so that on ends up with a batch of 72 bunches at $h = 84$ with 25 ns. The empty bucket is also multiplied, and the gap is therefore 12 bunch positions long.

However, the bunches after the last double bunch splitting are held with some 100 kV at 40 MHz, where their bunch length of 12 ns is still too long to fit into the SPS 200 MHz buckets. Since the voltage required in the PS to shorten them adiabatically would be unreasonably large, a non-adiabatic rotation (see Sec. 3.3.1) of the bunches in the longitudinal phase space is used for bunch compression before extraction [164, 165]. By rapidly switching the RF amplitude at 40 MHz ($h = 84$) to 300 kV and additionally applying some 600 kV at 80 MHz ($h = 168$), the bunch length is reduced to 4 ns [166] after some 600 turns in the PS, well below the bucket length of 5 ns in the SPS. Fast extraction delivers the batch of 72 bunches to matched 200 MHz buckets in the SPS.

Super Proton Synchrotron (SPS)

The batches coming from the PS are accumulated and accelerated in the SPS up to the injection energy of the LHC at 450 GeV. As mentioned in App. A, the SPS is a separated function alternating gradient synchrotron [167] equipped with a special traveling wave RF system for acceleration. Its circumference of 6.9 km is exactly eleven times as long as the circumference of the PS. However, eleven PS batches consisting of 72 bunches cannot be accelerated in the SPS because the total beam intensity is presently limited to some $5 \cdot 10^{13}$ by the maximum power that can be transferred to the proton beam during its passage through the RF cavities.

Two, three or four PS batches are therefore accumulated at flat-bottom in the SPS, corresponding to an intensity of 1.7, 2.5 or $3.3 \cdot 10^{13}$ protons (see Tab. 5.1). No special RF gymnastics during the injection procedure is necessary, as the beam is prepared by the PS to fit in matched 200 MHz buckets. It is worth noting that the whole intensity is confined within 2/11, 3/11 or 4/11 of the circumference, and that the RF power must be delivered to the beam within this fraction of the revolution period during each turn.

After an injection flat-bottom of some 3.6/7.2/10.8 s, the beam is accelerated to 450 GeV within some 8.3 s and ejected to the LHC. During acceleration the bunch emittance is intentionally blown-up to twice its initial value to avoid longitudinal instabilities. This blow-up in effective longitudinal emittance is achieved by either introducing noise to the RF amplitude at 200 MHz or by an additional RF amplitude at 800 MHz, the fourth harmonic of the fundamental RF system [168]. The bunches with nominal intensity have a longitudinal emittance below 0.6 eVs at extraction from the SPS [169].

Large Hadron Collider (LHC)

Each of the LHC rings will be filled by 12 injections at 450 GeV. The two rings will be equipped with a superconducting RF system consisting of eight cavities per ring that are capable to deliver up to 16 MV to the beam [170]. As the 400.8 MHz buckets in the LHC cannot be exactly matched to the bunch length to energy spread ratio of the injected bunches, a longitudinal emittance blow-up of some 25 % to 0.8 eVs hast to be accepted. On the one hand, the maximum voltage of the 200.4 MHz RF system is not enough to match the beam to the LHC buckets, and on the other hand, the RF voltage in the LHC cannot be lowered because of insufficient bucket area. A detailed analysis of the injection procedure can be found in [118].

After injection, the two beams are accelerated to the collision energy of 7 TeV. As longitudinal instabilities are expected during acceleration for low-emittance bunches, the longitudinal emittance is again intentionally blown up to $1 \ldots 1.5$ eVs. Due to the long ramping time of 20 min that is limited by the ramp rate of the superconducting magnets, acceleration takes place at a moderate rate of 485 keV/turn.

The expected final bunch parameters at 7 TeV, which are the basis for the RF gymnastics for long and flat bunches, are presented in Fig. 5.4 and Tab. 5.2. The longitudinal emittance of the bunches will be deliberately blown up to 2.5 eVs during acceleration to prevent from unwanted emittance dilution due to intra-beam scattering at collision energy. However, 1 eVs at the end of the acceleration cycle should be within reach.

It should be mentioned that synchrotron radiation can be neglected for the calculation of the nominal bunch parameters. Although it is important for the heat load on the superconducting magnets, the average energy loss as calculated in Sec. 2.8 is with 6.71 keV per turn negligible compared to the external RF voltage of 16 MV. The resulting synchronous phase angle becomes $\phi_0 = (180 - 0.024)^0$.

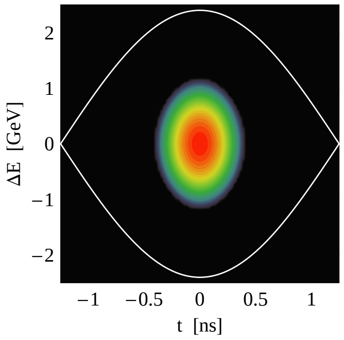

Fig. 5.4: LHC bunch at 7 TeV energy with $\varepsilon_l = 1.5$ eVs.

	Small emittance	Nominal
Bucket area, A	7.62 eVs	
Bucket length	0.748 m (2.5 ns)	
Bucket height	2.4 GeV	
Long. emittance, ε_l	1.0 eVs	2.5 eVs
Bunch length	0.20 m (0.66 ns)	0.32 m (1.08 ns)
Energy spread	0.97 GeV	1.51 GeV
(relative)	$(0.13 \cdot 10^{-3})$	$(0.22 \cdot 10^{-3})$
Peak current (par.)	42.3 A	26.5 A

Tab. 5.2: Relevant parameters of a nominal LHC bucket and bunch with a longitudinal emittance of 1.0 or 2.5 eVs.

Nominal bunch pattern in the LHC

For the filling of one LHC ring, twelve SPS cycles containing three or four PS batches each will be required. At a bunch spacing of 25 ns the LHC has 3564 possible bunch positions, but not all of these bunch positions can be populated by a bunch, as there are several restriction imposed by the injector chain as presented above and by the LHC itself [171, 172]:

Firstly, the transfer of multiple batches from PS to SPS demands for a gap of at least 8 bunch positions as the SPS injection kicker magnet needs to be switched on between subsequent batches. It should be mentioned that the gap between two batches in the SPS is shorter than the extraction kicker gap in PS. Secondly, a gap of 38 or 39 empty bunch positions, depending on the number of PS batches delivered from the PS, must be provided for the injection kicker magnet in the LHC. The largest gap in the LHC bunch pattern assigns the time for the so-called beam dump kicker. As this kicker magnet must be activated at the collision energy of 7 TeV, its rise time is significantly longer than those of the kicker magnets considered above. At least 119 bunch positions (3 μs) must be kept free from particles to allow save abort of beam at full energy to the dump.

Various bunch patterns for the different operation modes, i.e. different bunch spacing or ions instead of proton beams, have been analyzed. As an example for a standard bunch pattern, the nominal filling scheme for high luminosity operation with 25 ns bunch spacing is described below. The filling procedure is sketched in Fig. 5.5. Following the bunch pattern notation

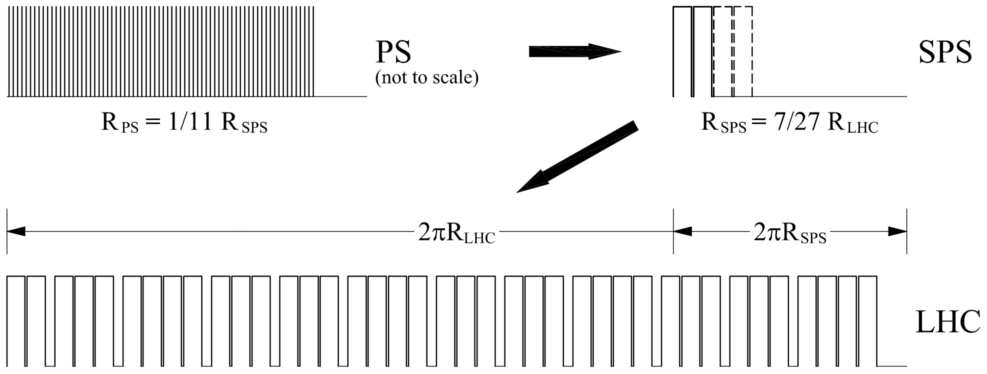

Fig. 5.5: Nominal filling scheme from PS to LHC for luminosity production with 25 ns bunch spacing. The bunch patterns in SPS and LHC are drawn to scale whereas the PS bunch pattern is magnified.

in [173, 174] where b denotes a populated bucket and e an empty bunch position, the filling scheme in the PS can be simply written as

$$\mathrm{fs_{PS}} \oplus 4 \otimes e = (72 \otimes b \oplus 8 \otimes e) \oplus 4 \otimes e\,,$$

so that $\mathrm{fs_{PS}}$ denotes the PS bunch pattern that reappears in SPS and LHC (see Fig. 5.5, top left). The operators marked by a circle can be regarded as non-commutative additions and multiplications. The pattern in the SPS can be composed of a string of PS patterns and of padding with empty buckets to end up with 924 possible bunch positions.

The full bunch pattern in the LHC can be described by the a sequence of digits defining the number of PS batches per SPS cycle, namely

$$\{234\}\ \{334\}\ \{334\}\ \{334\}\,.$$

Resolving this pattern according to the notation introduced above, the full nominal filling scheme for the LHC becomes

$$\begin{aligned} \mathrm{fs_{LHC}} = \{ & 2 \otimes \mathrm{fs_{PS}} \oplus 30 \otimes e \oplus 3 \otimes \mathrm{fs_{PS}} \oplus 30 \otimes e \oplus 4 \otimes \mathrm{fs_{PS}} \oplus 31 \otimes e\} \\ & \oplus 3 \otimes \{2 \otimes [\mathrm{fs_{PS}} \oplus 30 \otimes e] \oplus 4 \otimes \mathrm{fs_{PS}} \oplus 31 \otimes e\} \oplus 80 \otimes e\,, \end{aligned}$$

where the curly brackets are set corresponding to the bunch pattern above. The complete filling scheme can thus be written as

$$\begin{aligned} \mathrm{fs_{LHC}} = \{ & 2 \otimes (72 \otimes b \oplus 8 \otimes e) \oplus 30 \otimes e \\ & \oplus 3 \otimes (72 \otimes b \oplus 8 \otimes e) \oplus 30 \otimes e \oplus 4 \otimes (72 \otimes b \oplus 8 \otimes e) \oplus 31 \otimes e\} \\ & \oplus 3 \otimes \{2 \otimes [3 \otimes (72 \otimes b \oplus 8 \otimes e) \oplus 30 \otimes e] \oplus 4 \otimes (72 \otimes b \oplus 8 \otimes e) \oplus 31 \otimes e\} \oplus 80 \otimes e\,. \end{aligned} \tag{5.1}$$

By setting b and e to unity it can easily been shown that the total number of bunch positions is 3564. Furthermore, setting $b = 1$, $e = 0$ shows that the number of bunches per LHC ring is 2808.

The bunch pattern can by modified as long as the bunch train structure $\mathrm{fs_{PS}}$ remains unchanged. However, the generation of long bunches in the LHC as described below already requires modifications of the bunch pattern in the PS.

5.1.2 Limitations of the LHC injector chain

Several limitations of the existing accelerator complex may restrict the performance of an upgraded LHC, as the injector chain will already have a hard time providing the protons required for the ultimate scheme.

At low energy, the total beam intensity is limited by the tune shift induced by the transverse self-field of the beam. The space charge force acts incoherently on the individual particles depending on their position inside the beam. A short derivation of the space charge tune shift is given in App. F. Similar to beam-beam tune spread in high energy colliders, the so-called space charge limit is extremely difficult to compensate and, in analogy to the beam-beam limit, it is regarded as the fundamental current limitation for circular hadron accelerators in the low energy regime.

Furthermore, extremely high beam intensities may result in a significant radioactive irradiation of the accelerators if beam losses are not well under control. As most of the uncontrolled beam losses take place at low energies where lost particles deposit their energy almost completely within the accelerator components, this is of special concern for the injector chain of the LHC.

Various options for increasing the beam intensity as well as reducing the uncontrolled beam losses in the LHC injector chain are under discussion [175] to remove its limitations at low beam energy. Although the maximum bunch intensity within the beam quality requirements for the LHC is presently limited to $1.5 \cdot 10^{11}$ protons per bunch (about 20 % above the bunch intensity needed for the nominal LHC scheme) in the PS, especially the installation of a new high energy injector linear accelerator, the so-called Superconducting Proton Linac (SPL), would increase the available bunch intensity to some $4 \cdot 10^{11}$ protons [175]. This improvement comes from the fact that such a linear accelerator would allow injection into the PS at an energy of 2.2 GeV where the direct space charge limitation is suppressed by a factor of $\beta\gamma^2|_{2.2\,\mathrm{GeV}}/\beta\gamma^2|_{1.4\,\mathrm{GeV}} \simeq 1.9$ compared to the present transfer energy between PSB and PS.

For the further analysis in this report it is assumed that the injector chain does not impose a strict intensity limitation for the LHC, and that it is capable of delivering a beam similar to the nominal LHC beam but with intensities up to three to four times its bunch population at ejection from the SPS.

5.2 Generation of long and flat bunches

Starting from an almost standard LHC beam configuration with 25 ns bunch spacing, different schemes to confine batches of nominal bunches to long and flat bunches or even single superbunches per beam have been discussed in Chapter 4.

5.2.1 Direct approach

A straightforward approach to form long and flat bunches at flat-top energy in the LHC would be the merging of each PS batch with its length of 72 bunches at a time distance of 25 ns each into one long bunch held by barrier buckets [176]. According to the total number of PS batches in the LHC, 39 long and flat bunches would finally remain. It should be mentioned that synchrotron radiation is assumed to be properly compensated at 7 TeV by a dedicated RF installation during the manipulations described below.

Fig. 5.6 illustrates the longitudinal phase space during the subsequent steps of the scheme. Before the generation of long and flat bunches, the beam is injected and accelerated according to the scheme for the nominal LHC beam. At the injection flat-top, barrier buckets are positioned in the $9 \cdot 25\,\mathrm{ns} = 225\,\mathrm{ns}$ long gaps between two adjacent PS batches in a first step. In a second step the amplitude of the harmonic RF system holding the beam is decreased adiabatically so that the bunch trains are debunched to the barrier bucket placed around the batch. This debunching procedure can be performed either directly starting from the 400.8 MHz RF system, or the bunches could be handed over to an RF system at 40.08 MHz. An RF system at 40.08 MHz would be compatible with the nominal bunch spacing of 25 ns and could serve as a mediator between the 400.8 MHz RF buckets and the RF barriers pulses whose pulse length corresponds to a frequency of some 10 MHz.

After debunching, coasting beam-like flat bunches with a length of approximately 1.8 μs are confined by the barrier pulses (Fig. 5.6, center). It is worth mentioning that debunching with 400.8 MHz would lead to a much reduced longitudinal density because only every tenth bucket at an RF frequency is occupied in the nominal scheme so that less than 10 % of the batch length

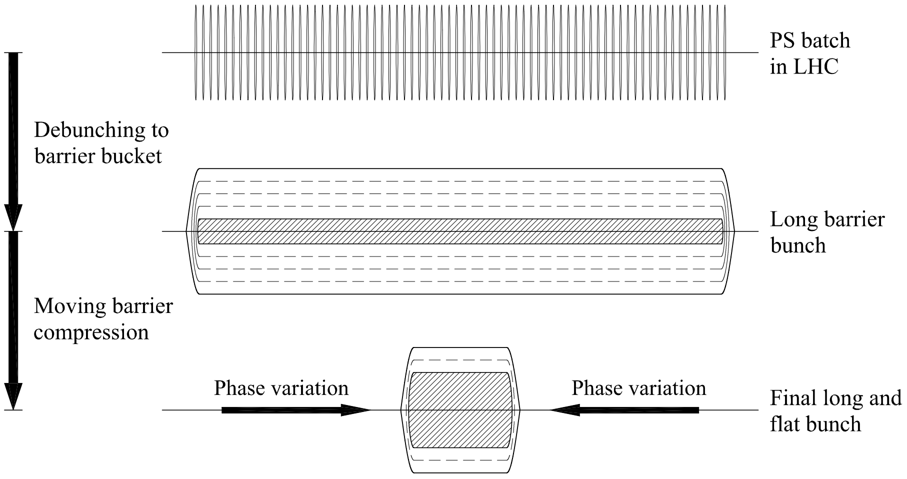

Fig. 5.6: Overview of the simple scheme which combines a batch of 72 initial bunches to a single long and flat bunch. The batch is debunched to a barrier bucket and the long bunch is finally compressed by moving barriers.

is populated with particles. The collision of such long and low density bunches cannot deliver reasonable luminosity.

To preserve the longitudinal particle density, debunching should rather be done with 40.08 MHz. Bunch compression is performed in a third step. As has been introduced in Sec. 3.4.1, the length of a barrier bucket can be manipulated by adiabatically moving the barriers in phase with respect to each other. This phase motion compresses the bunch in between, while the longitudinal particle density and momentum spread increase simultaneously. The barrier bucket compression is applied in the LHC until the original momentum spread of the initial bunches is re-established, which also corresponds to the restoration of the original longitudinal density.

Although the scheme described above seems to promise a simple creation of long and flat bunches, it has several inherent drawbacks which nearly exclude its application to a high intensity beam in the LHC [176]:

Firstly, the adiabatic bunch compression by moving RF barriers would take a time in the order of several ten minutes to keep the longitudinal emittance dilution within reasonable limits. Following the adiabaticity criterion introduced in Sec. 3.4.1 the compression would diminish the integral of the luminosity over time by lengthening the filling and beam preparation time so that the luminosity gain due to the long and flat bunches would be reduced significantly.

Secondly, assuming barrier pulses at frequencies around 7.5 . . . 10 MHz, which represents the upper technical limit of inductively loaded broad band RF cavities, the final bunches would have a considerable fraction of their particles within the tails, and the luminosity gain obtained by crossing such bunches is below the theoretical limit of $\sqrt{2}$ (see Chapter 4).

Thirdly, the beam is accelerated to the collision energy of 7 TeV by the superconducting RF system at 400.8 MHz and this RF system will be also present and influence the beam during the generation of the long and flat bunches. However, especially the very long coasting beam-like bunches are prone to perturbing RF voltages after debunching into the barrier buckets. Even though the superconducting RF system will be equipped with an efficient vector feedback to suppress transient beam loading [177], it will not be capable to reduce the RF voltage reliably enough as required for the generation of long and flat bunches.

Fourthly, the effect of the average energy loss of the particles at collision energy caused by synchrotron radiation must be compensated. This requires an RF system generating a constant voltage of some 6.7 kV along the full PS batch length of 1.8 μs. As the RF systems have to be free from of DC components, the long positive pulse must be followed by a short negative pulse of large amplitude which is generated within the gap of two PS batches. Such a compensation, which is necessary in addition to the barrier bucket system to confine the long bunches, presents a challenging and expensive task.

Finally, the momentum spread after debunching to the barrier bucket is small compared to the spread of the nominal LHC bunches. The thresholds for the microwave instability (see Chapter 6) are therefore much below the estimated longitudinal impedance in the LHC. As a result, the beam is unstable during the creation of the long and flat bunches.

These major disadvantages of the straightforward scheme of long bunch generation in the LHC demand new approaches to perform the necessary RF manipulations. A more promising scheme is therefore presented below.

5.2.2 Overview of the long bunch generation scheme

The RF gymnastics to generate long and flat bunches, about one order of magnitude longer than the nominal LHC bunches, mainly consists of three ingredients. Two of them, batch compression and bunch pair merging, have been briefly introduced in Chapter 3. The third ingredient, the final formation of the long and flat bunch, is very similar to a bunch pair merging with three or more harmonics which is just stopped in the middle of the process.

Batch compression serves to increase the harmonic number in a circular accelerator from h_1 to h_2. The difference of the two harmonics is chosen small enough so that the bunches can follow the buckets during the harmonic hand-over (see Sec. 3.2.3). The bunch spacing decreases and it is therefore used to push the batches of bunches together more closely. In the nominal LHC scheme, only every tenth bucket is a possible bunch position. Starting the batch compression at the nominal RF harmonic of $h = 35640$ would be inconvenient, because the number of empty buckets between two bunches remains the same. Therefore, the generation of long and flat bunches starts from an RF system at ten times lower RF harmonic $h = 3564$ (40.08 MHz), where every bucket serves as a bunch position. Stepwise increase of the harmonic number up to $h = 7128$ (80.16 MHz) causes the bunch spacing to shrink by a factor of two to 12.5 ns, whereas the number of bunches stays constant throughout the procedure.

To re-establish the original bunch spacing and to reduce the number of bunches, the complementary procedure, bunch pair merging, is applied where the RF amplitude at $h = 7128$ is adiabatically decreased while simultaneously increasing the amplitude at $h = 3564$. The bunch spacing increases again to 25 ns but the number of bunches is halved with respect to the initial state.

Repetitive application of this sequence of batch compression and bunch pair merging allows to progressively confine dense bunches as illustrated in Fig. 5.7. It is obvious that the number of initial bunches must be a power of two so that the confinement is restricted to $4, 8, 16, 32, 64 \ldots 2^n$ bunch batches. A reasonable choice of this batch length is explained in what follows.

Choice of batch length

Two main arguments determine the number of initial bunches to be combined to one long and flat bunch in the LHC:

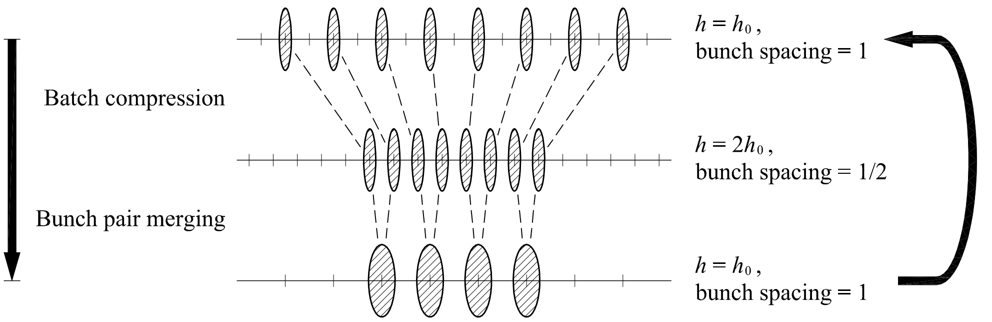

Fig. 5.7: Subsequent application of batch compression and bunch pair merging gradually reduces the number of bunches and increases the intensity per bunch.

Firstly, assuming a constant emittance per bunch, the required RF voltage for the creation and the storage of the long and flat bunches is proportional to the square of the number of combined bunches. The absolute voltages necessary to store the final bunches after the combination of batches of 16 bunches can be found in Tab. 4.3. A reasonable RF voltage providing sufficient bucket area during the creation of these bunches is somewhat larger, namely about 1.5 MV.

Secondly, the number of remaining bunches, multiplied by their bunch length, can be considered as an effective beam length. Following the derivations in Sec. 4.2.5, this effective beam length $n_b l_b$ should be chosen so that the maximum beam-beam tune shift is reached with the maximum available average beam current (see Fig. 4.3).

The relevant beam parameters for different numbers of bunches confined to one long bunch are given in Tab. 5.3.

Number of initial bunches per long and flat bunch		1	4	8	16	32	64
Total number of bunches, n_b		2808	624	312	156	78	39
Effective beam length, $n_b l_b$ (rectangular equivalent, 3 harmonics)	[m]	531	2613	1306	653	327	163
Average current for $\Delta Q = -0.01$, I_0 (alternate beam crossings)	[A]	0.94	12.8	6.4	3.2	1.6	0.8
RF voltage for the generation of long bunches, U_{RF}	[MV]		0.1	0.4	1.5	6	24

Tab. 5.3: Parameters for the choice of the number of initial bunches to generate a long and flat bunch. The longitudinal emittance per initial bunch is taken to be 1 eVs at the LHC injection flat-bottom. The total number of long and flat bunches per beam is based on the empty to occupied bucket factor 2808/3564 of the nominal LHC beam.

As already pointed out in Sec. 4.3.6, a very high luminosity could be achieved with options confining less than 16 initial bunches, but at the expense of excessively high and unpractical total beam currents.

On the other hand, compressing more than 32 LHC bunches requires a considerable RF voltage to generate the long bunches, and the beam-beam limit restricts the beam intensity in the range of the intensity of the ultimate LHC scheme (see Tab. 4.2). However, it will be very difficult for the experiments to cope with the event rate associated with this very small number of superbunches in the LHC.

Therefore, the only remaining two options of combining either 16 or 32 almost nominal LHC bunches to one long bunch are considered realistic and worth being discussed in more detail.

Total batch length in the LHC

Direct batch compression of batches of 16 or 32 bunches close to each other without any gap in between is excluded for two reasons: firstly, because the harmonic number 3564 is neither divisible by 16 nor 32, and secondly because, during batch compression, the effective RF amplitude is modulated along the batch so that at least the edge buckets cannot be populated with particles.

As the harmonic number $h = 3564$ decomposes to $2^2 \cdot 3^4 \cdot 11$, the favorable batch lengths leaving at least one empty bucket at each end are $n_\mathrm{batch} = 2 \cdot 3^2 = 18$ for 16 respectively $n_\mathrm{batch} = 2^2 \cdot 3^2 = 36$ for 32 bunches. The fundamental harmonic of the batch confinement RF gymnastics is thus 198 or 99 which corresponds to the number of available bunch positions for the final long and flat bunches. Furthermore, the step width in harmonic number of the hand-overs during batch compression is also defined by this step of $\Delta h = 198$ or $\Delta h = 99$.

The complete schedule for the harmonic number changes during batch compression as well as the increase of the number of buckets per batch is illustrated in Figs. 5.8 and 5.9. The bunch patterns are given for the first batch compression. For subsequent compressions the number of bunches is less while the number of empty bucket positions is larger.

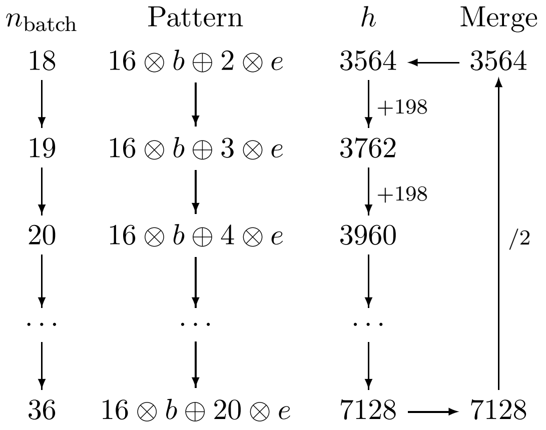

Fig. 5.8: Schedule of harmonic numbers and bunch patterns during long bunch combination of 16 initial bunches.

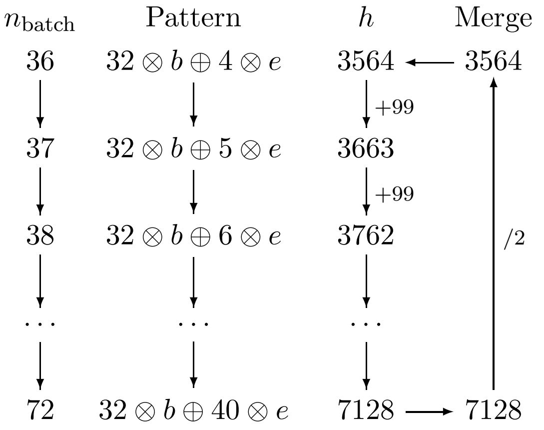

Fig. 5.9: Same harmonic schedule as in Fig. 5.8 but for a batch of 32 initial bunches. The bunch pattern notation is introduced at the end of Sec. 5.1.1.

It can be seen from the harmonic schedule that the RF systems for the batch compression have to cover the frequency range from 40.08 ($h = 3564$) to 80.16 MHz ($h = 7128$), no matter whether 16 or 32 bunches are combined. However, no more than two RF harmonics are acting on the beam simultaneously so that the complete RF gymnastics can be covered by two tunable groups of RF systems. It should be mentioned that the final formation of the long and flat bunches may require additional fixed frequency RF systems if more than two harmonics are applied to flatten the bunch shape.

The new LHC cycle

At the collision energy of 7 TeV, each beam with nominal intensity contains some 362 MJ ($2808 \cdot 1.15 \cdot 10^{11}$ protons), which makes the machine extremely sensitive to any kind of beam losses. At injection energy, the acceptable losses are 15 times larger. As complicated RF gymnastics can cause small beam losses, it is clearly preferable to perform most of the beam gymnastics at the injection flat-bottom of the LHC.

Neglecting the effects of bucket area reduction during batch compression, a change of the harmonic number at constant RF voltage causes the bucket area to shrink according to $1/h^{3/2}$ so that the smallest bucket area occurs at the end of the batch compressions. The bucket area for relevant harmonic numbers together with the bunch emittances are shown in Fig. 5.10. It becomes clear that in the 16 bunch scheme as well as in the 32 bunch scheme the initial batch can be combined to two remaining buckets held at $h = 3564$ at injection energy.

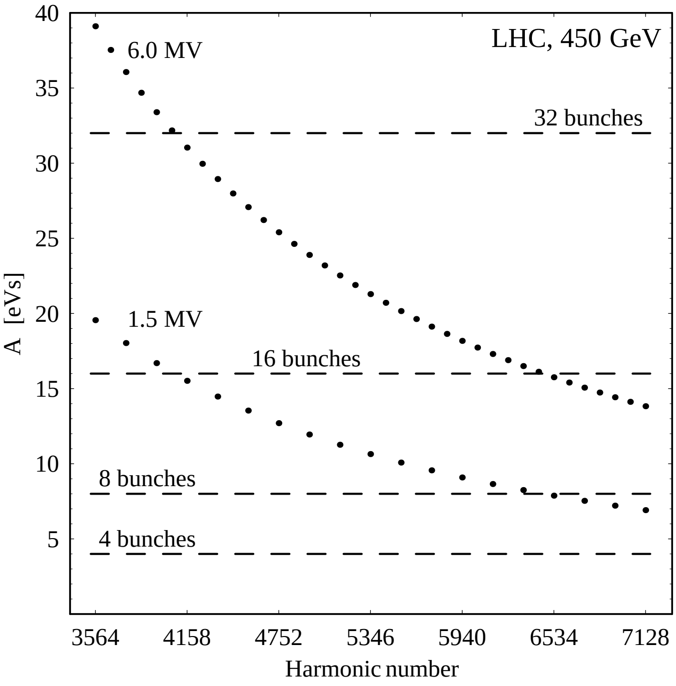

Fig. 5.10: Bucket area versus harmonic number for relevant RF frequencies between 40.08 and 80.16 MHz at constant voltage of 1.5 and 6 MV at the injection flat-bottom in the LHC. The dashed lines show the total emittance of 2^n initial bunches.

While the bunch emittance stays virtually constant during acceleration, the bucket area grows proportionally to $\sqrt{E/|\eta|} \simeq \gamma_{\mathrm{tr}}\sqrt{E} \propto \sqrt{E}$ so that it is 3.9 times larger at collision energy. Therefore the last batch compression and the final formation of the long and flat bunches must be carried out at the LHC flat-top.

Batches of two bunches according to the bunch pattern of $2\otimes b\oplus 16\otimes e$ (16 initial bunches) or $2\otimes b\oplus 34\otimes e$ (32 initial bunches) are accelerated with the 40.08 MHz RF system. The moderate average energy gain of 485 keV/turn results in a synchronous phase of $\phi_0 = (180 - 18.8)^0$ respectively $(180 - 4.6)^0$, and the bucket area reduction as sketched in Fig. 2.5 due to the synchronous phase is not critical during acceleration.

It is important to point out that an additional benefit of shifting as much of the RF manipulations to the injection flat-top is offered by the scaling of the synchrotron frequency proportional to $\sqrt{|\eta|/E} \simeq 1/(\gamma_{\mathrm{tr}}\sqrt{E}) \propto 1/\sqrt{E}$. To keep the same adiabaticity during the process, the manipulation can be executed four times faster at 450 GeV.

5.2.3 Beam transfer from SPS to LHC

As the batch confinement RF gymnastics is based on RF systems at harmonic numbers between 3564 and 7128, the beam from the SPS is injected into large 40.08 MHz buckets at the LHC flat-bottom. Furthermore, the estimation of the beam loading voltage induced to the superconducting 400.8 MHz cavities (see Sec. 6.5) shows that they even have to be removed for operation with long bunches. Parallel operation of both the standard superconducting RF system and a 40.08 MHz RF installation is impossible with reasonable power capabilities.

The condition for a longitudinally matched bunch to bucket transfer between two circular accelerators has been derived in Sec. 3.5 so that the voltage ratio optimum between SPS and LHC is given by

$$\frac{V_{\mathrm{SPS}}}{V_{\mathrm{LHC}}} = \left(\frac{R_{\mathrm{SPS}}}{R_{\mathrm{LHC}}}\right)^2 \left|\frac{\eta_{\mathrm{SPS}}}{\eta_{\mathrm{LHC}}}\right| \frac{h_{\mathrm{LHC}}}{h_{\mathrm{SPS}}} = 0.38 \cdot \frac{h_{\mathrm{LHC}}}{h_{\mathrm{SPS}}} \,. \tag{5.2}$$

For matched injection into 40.08 MHz buckets the voltage ratio becomes 0.29. However, as an additional constraint, the bucket area must be sufficient in both accelerators.

The bucket area of the 200 MHz SPS buckets at extraction flat-top is plotted in Fig. 5.11 versus the available RF voltage. Assuming a bunch emittance of 0.6 to 0.7 eVs at 450 GeV, the bucket area should be at least three times as large as the bunch emittance to keep the bunch within the linear region of the bucket. Therefore, the minimum RF voltage limitation in the SPS for extraction into a 40.08 MHz RF system in the LHC is about 3 MV. The upper voltage limit is simply given by the available RF power, which limits the maximum RF voltage to some 8 MV.

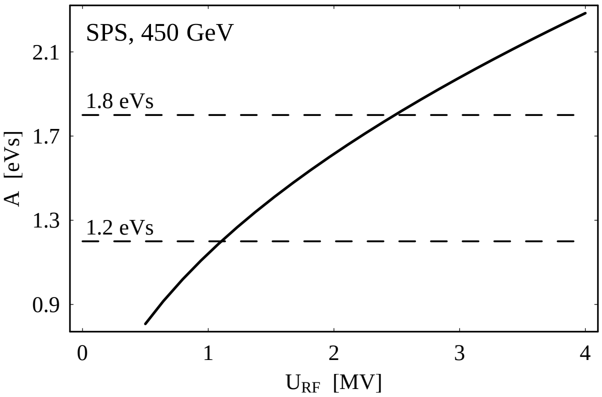

Fig. 5.11: Bucket area of the 200 MHz RF system in the SPS versus its RF amplitude.

Beam transfer by bunch rotation

Depending on whether 16 or 32 initial bunches should be combined to one long and flat bunch, the available RF voltage at 40.08 MHz in the LHC will be either $2 \cdot 1.5$ MV or $2 \cdot 6$ MV.

In the case of 3 MV, the corresponding RF voltage in the SPS according to Eq. (5.2) is only 0.87 MV so that the bucket area would be insufficient. Therefore, a virtual reduction of the RF voltage by bunch rotation is foreseen, to obtain a ratio of bunch length to energy spread of about 0.87 MV at extraction. The bunches are rotated in the longitudinal phase space in the SPS, and the extraction to the LHC takes place when the bunch length is largest, respectively after a rotation by a quarter of a turn.

Following the analysis in Sec. 3.3.1, the maximum bunch lengthening factor reachable by an instantaneous voltage step down from 8 to 3 MV is 1.63. After rotation in the longitudinal phase plane, when the bunch is longest, it has similar parameters as a bunch kept in a stationary bucket with 1.1 MV, except that such a bunch would be significantly stretched out in the non-linear regions of the bucket as its emittance is close to the bucket area (see Fig. 5.11).

Tracking calculations of the beam transfer scheme by bunch rotation show that a small but non-negligible emittance blow-up occurs. Starting from a matched bunch of 0.65 eVs longitudinal emittance in the SPS, the RF amplitude is raised adiabatically from 3 MV to 8 MV and then suddenly switched back to 3 MV. After one quarter of a period at the synchrotron frequency, the bunch is transferred to the LHC and tracked for further 0.2 s to observe residual mismatch. The longitudinal emittance blow-up caused by such a transfer between SPS and LHC with optimized parameters is illustrated in Fig. 5.12. As expected, the longitudinal emittance remains constant during the adiabatic voltage increase within the first 200 ms. The bunch rotation itself is by far too fast to be visible on the timescale of Fig. 5.12; the bunch is extracted some 2.5 ms after the instantaneous voltage reduction. After injection into the LHC, an oscillation of the effective longitudinal emittance with the synchrotron frequency can be observed. It is caused by the residual longitudinal mismatch of the injected bunch. After filamentation, the final bunch has an emittance of some 0.8 eVs and the transfer blow-up is about 23 %. It should be pointed out that the residual longitudinal mismatch comes from a non-ideal bunch rotation: a significant fraction of particles suffers from the reduced synchrotron frequency at large oscillation amplitudes. Therefore, the optimum rotation time must be $1.25 \cdot \pi/(2\omega_s)$ to obtain minimum transfer blow-up, slightly longer than a quarter period of the linear synchrotron frequency.

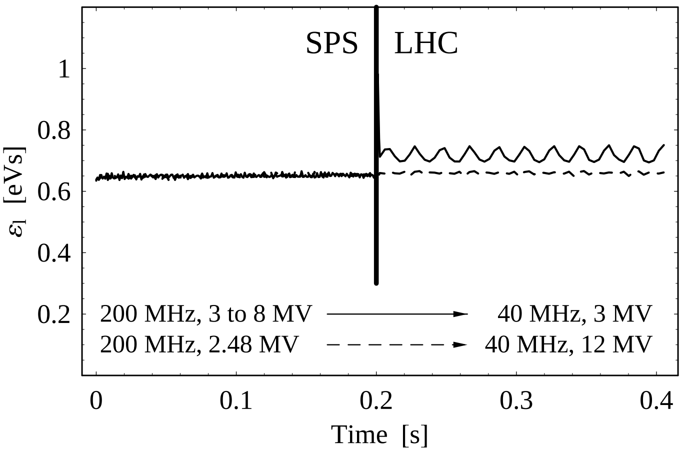

Fig. 5.12: Longitudinal emittance during a bunch transfer from SPS to LHC including bunch lengthening by bunch rotation in the SPS (continuous line). The dashed line represents the transfer to 12 MV at 40.08 MHz in the LHC. The longitudinal emittance is defined as the area of the encircling ellipse containing 99 % of the bunch particles normalized to 0.65 eVs at the beginning of the process.

Direct transfer

In the case of 32 initial bunches combined to one long and flat bunch, the available RF voltage has to be about $2 \cdot 6$ MV at 40.08 MHz and, according to Eq. (5.2), the corresponding RF voltage in the SPS is about 3.5 MV. It is expected that the matched transfer causes virtually no longitudinal emittance blow-up (see Fig. 5.12, dashed line).

However, the bucket area of a 40.08 MHz RF system in the LHC is much larger than the emittance of the injected bunches resulting in low synchrotron frequency spread and virtually no Landau damping. This might restrict the maximum RF amplitude during injection, and the bunch rotation scheme might be favorable even if more RF voltage would be available.

Albeit the ideal longitudinal emittance after beam transfer to the LHC is estimated to be below 0.8 eVs, an additional blow-up caused by a higher harmonic RF system to re-establish

Landau damping (see Sec. 6.3.6) must be taken into account. Therefore the subsequent analysis of the RF gymnastics assumes a longitudinal emittance of 1 eVs.

It is important to point out that the transfer of nominal bunches from the SPS (8 MV) to the 400.8 MHz RF system (8 MV) also causes a longitudinal emittance blow-up. Instead of stretching the bunches as suggested above, a bunch rotation might be an option to shorten the bunches and to suppress the mismatch [178].

5.2.4 Batch compression

After beam injection, the RF manipulation to generate the long and flat bunches commences. The harmonic number is raised in steps of 198, respectively 99, which corresponds to a step of unity with respect to the local harmonic number of the batch (see Figs. 5.8 and 5.9). The lower harmonic RF amplitude at h_1 is adiabatically decreased while the higher harmonic RF at $h_1 + 198$ or $h_1 + 99$ is increased simultaneously.

When both harmonics are of equal RF voltage, the beat frequency at $h_2 - h_1$ has the same amplitude as the two main carriers so that the effective RF focusing is large at the center of the batch but decreases to nearly zero at the very ends of the batch. This problem is most critical at the beginning of the first harmonic hand-over as only the last (16 initial bunches) or the last two (32 initial bunches) buckets are kept empty at both ends of the batch. An example of the separatrices and bucket areas for the worst case during the first harmonic hand-over of the combination of 32 bunches is shown in Fig. 5.13. In the case of 16 initial bunches, the situation is similar. The bucket area of the populated buckets varies from 8.1 to 17.9 eVs in this case, and the empty bucket at the end of batch has an area of 4.1 eVs.

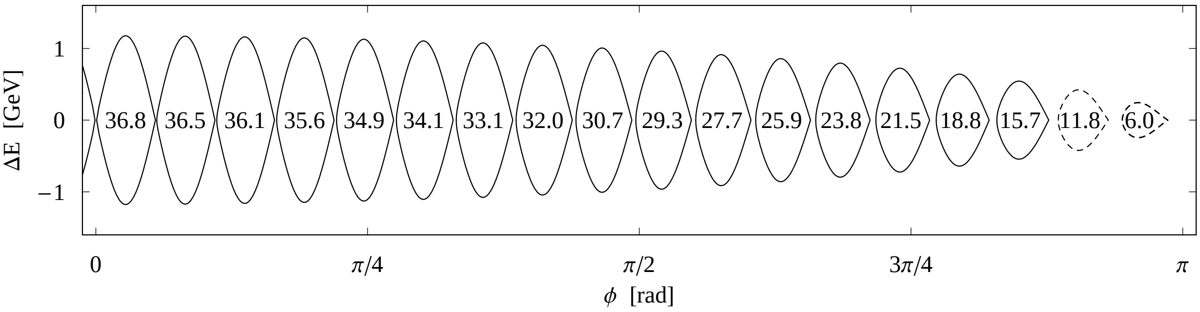

Fig. 5.13: Separatrices in the middle of the first harmonic hand-over from $h = 3564$ to $37/36 \cdot 3564 = 3663$ when both RF voltages are equal and at half of their maximum amplitude, namely 3 MV each. The separatrices of empty buckets are plotted with dashed lines. As the stationary trajectories are symmetric around $\phi = 0$ only one half is shown. The buckets areas (in the center of the separatrices) are given in units of eVs.

The analysis above seems to suggest that the gaps in between the batches are not mandatory. However, despite of their function to make the bunch pattern compatible with the LHC with its global harmonic of 3564, it is important to point out that the bucket area dynamically oscillates from the stationary value as shown in Fig. 5.10 to the minimum value (Fig. 5.13) within each single harmonic hand-over. In the adiabatic limit, the bunch inside the bucket must be able to follow this quadrupole excitation caused be the bucket motion without dilution in the longitudinal phase space. The development of the bucket areas of center (dashed line) and tail buckets is presented in Figs. 5.14 and 5.15. While the area of the center bucket shrinks smoothly, the outer buckets, especially the last one, are strongly modulated. This behaviour

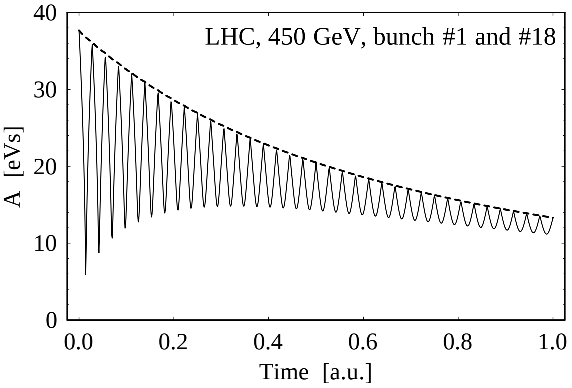

Fig. 5.14: Development of the bucket area during batch compression from $h = 3564$ to 7128 in steps of $\Delta h = 99$. While the center bunch mainly shrinks proportional $1/h^{3/2}$ (dashed line), the last bunch shows a strong modulation of the bucket area with each harmonic hand-over (continuous).

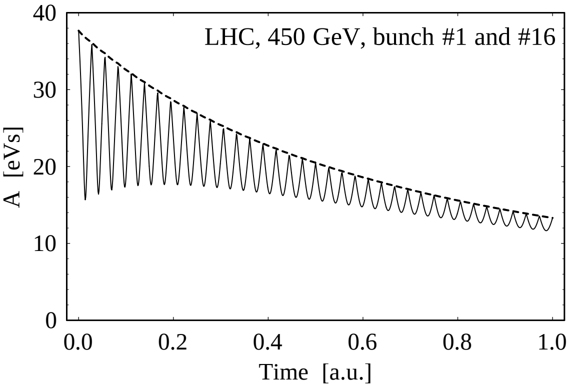

Fig. 5.15: Comparison of the bucket area development of center (dashed line) and last populated bucket (continuous). The bucket area is still strongly modulated, but the variation is already significantly reduced compared to the last, empty bucket (Fig. 5.14).

can cause emittance dilution if the bucket area is modulated so fast that the bunch is not able to follow the rapid changes of the bucket.

For the calculation of Figs. 5.14 and 5.15 the time for each harmonic hand-over was assumed to be constant. Since the degree of modulation is largest for the first sub-steps of the batch compression, they should be lengthened so that the time derivative of the effective RF focusing does not surpass a certain limitation during the batch compression manipulation.

Time optimization

From the analytical calculation of RF potential or separatrices during batch compression, one could get the impression that the RF manipulation is symmetric in the sense that both ends of the batch move to the center simultaneously. However, it should be kept in mind that, above transition, the bunch at the front of the batch must be slightly accelerated while the bunch at the back must be decelerated to initiate their relative phase motion with respect to the batch center.

Therefore a batch compression can also be regarded as sketched in Fig. 5.16. Each

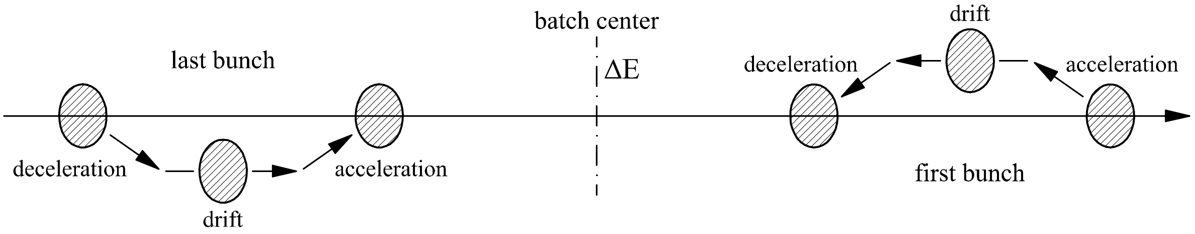

Fig. 5.16: During batch compression, each bunch of the batch has to be slightly accelerated or decelerated to move them towards the center. The offset energy of this acceleration or deceleration increases with the distance of the bunch from the center of the batch.

bunch is slightly displaced in energy where it drifts in phase to reach its new position after the batch compression. It becomes clear that the bunch motion of the front and the back half are reflections in a point around the batch compression center.

It is worth noting that this view of the batch compression manipulation is not taken into account in the calculations of buckets via the Hamiltonian theory. A simple harmonic hand-over between two harmonics, where the lower harmonic is decreased linearly while the higher harmonic is also increased linearly, the motion of the bucket center switches non-adiabatically from $d\phi_0/dt = 0$ to $d\phi_0/dt \neq 0$. This effect excites a dipole oscillation of the bunch, which causes emittance dilution and thus a blow-up of the effective longitudinal emittance. Especially the bunches at the tails of the batch suffer from this effect.

Therefore, a simple equilibration of the voltage ramps is presented in what follows. This equilibration ensures that the bunches are slowly accelerated and decelerated at the beginning and at the end of the batch compression.

For the optimization, the following parameters are assumed at the beginning and at the end of the batch compression:

	before		after
Harmonic, h	h_0	$\longrightarrow$	$2h_0$
Total batch length, l	l_0	$\longrightarrow$	$l_0/2$
Time, t	0	$\longrightarrow$	τ_{bc} .

For simplicity it is assumed that the harmonics number does not change stepwise, but that the effective harmonic number varies smoothly with time, namely

$$h(t) = h_0 \left(\frac{t}{\tau_{\mathrm{bc}}} + 1 \right) , \tag{5.3}$$

so that the length of the batch develops according to

$$l(t) = l_0 \Big/ \left(\frac{t}{\tau_{\mathrm{bc}}} + 1 \right) . \tag{5.4}$$

This function has a gradient at $t = 0$ and $t = \tau_{\mathrm{bc}}$ so that the buckets switch from stationary to moving instantaneously, which is strongly non-adiabatic. Especially at the beginning of the process a large energy offset of the tail bunches is required.

An optimized function of the time dependent bunch length $l(t)$ should be smooth and have vanishing derivatives at $t = 0$ and $t = \tau_{\mathrm{bc}}$. Trigonometric functions can fulfill these requirements, and a reasonable choice can be written as

$$l_{\mathrm{opt}}(t) = \left[\frac{3}{4} + \frac{1}{4} \cos \left(\pi \frac{t}{\tau_{\mathrm{bc}}} \right) \right] l_0 . \tag{5.5}$$

The improved batch length function is plotted in Fig. 5.17. One can observe that the batch length starts to shrink smoothly.

The time scaling function to achieve the improved batch length shrinkage can be found easily by demanding that $l_{\mathrm{opt}}(t) = l(t_1)$, where t_1 is the new time function which itself depends on the original time t. Finally, this function becomes

$$t_1(t) = \left[\frac{1}{3/4 + 1/4 \cdot \cos(\pi t/\tau_{\mathrm{bc}})} - 1 \right] \tau_{\mathrm{bc}} . \tag{5.6}$$

The time function can be used to convert the linear amplitude ramp functions of the batch compression to such amplitude where the end of the batch moves according to Eq. (5.5).

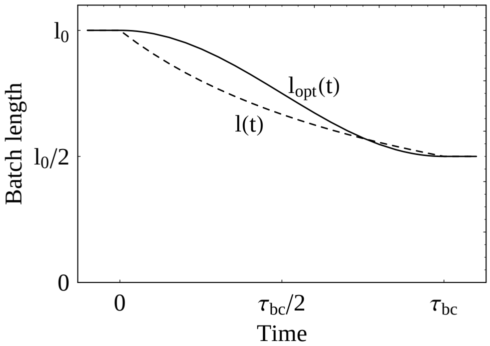

Fig. 5.17: Improved batch length function versus time (continuous line). As a reference, the batch length function of a non-equilibrated batch compression is also shown.

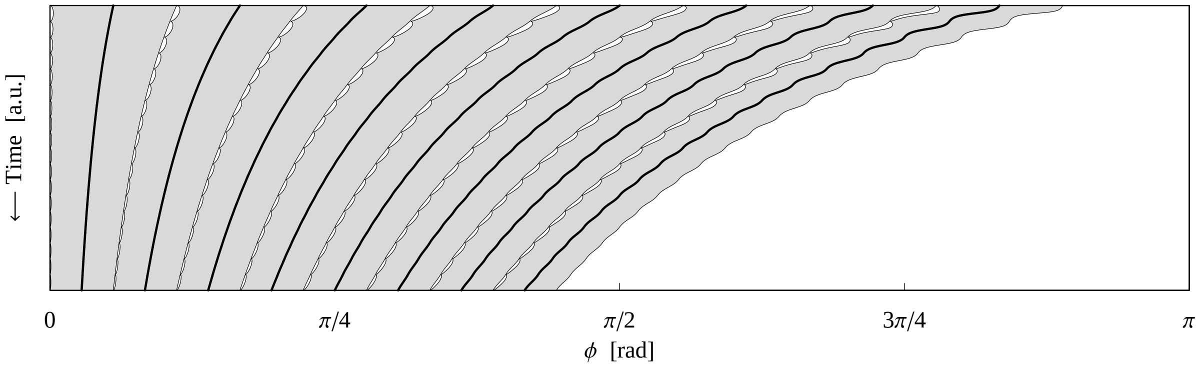

Fig. 5.18: Movement of the bucket centers during the first batch compression for a simple scheme. The thick lines mark the center positions of the buckets while the shaded areas enclosed by thin lines represent the total longitudinal extent of the buckets. Only one half of the batch is shown.

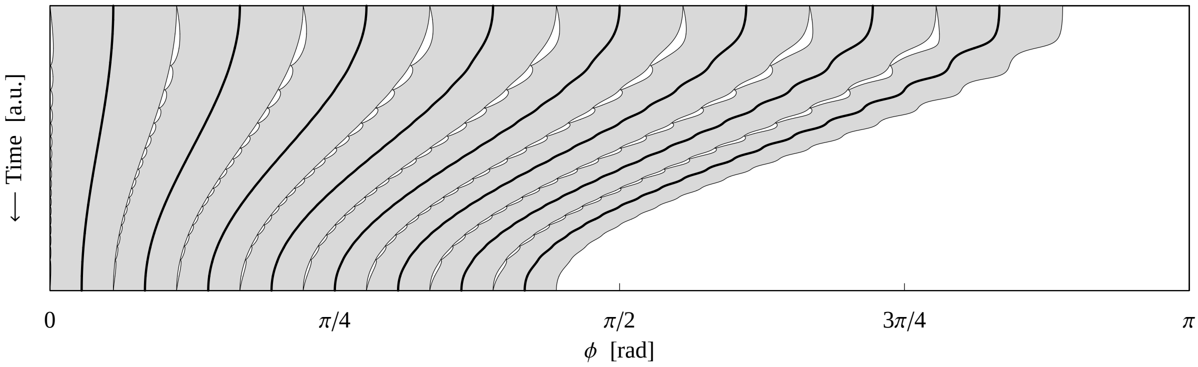

Fig. 5.19: Same representation of bucket centers and bucket lengths as in Fig. 5.18 but for an improved scheme with a batch length variation according to Eq. (5.5).

The resulting movement of the buckets in the case of non-equilibrated voltage ramps during batch compression of 16 bunches is sketched in Fig. 5.18, while the optimized case is presented in Fig. 5.19. Clearly, especially the edge bunches are accelerated respectively decelerated smoothly at the beginning and at the end of the batch compression.

The harmonic program and the RF amplitude ramps for an equilibrated batch compression of a batch of 16 bunches with 2 empty buckets in between are illustrated in Fig. 5.20. Essentially the first and the last harmonic hand-over from $h = 3564$ to $3564 + 198$ and from $h = 7128 - 198$ to 7128 have to be performed with non-linear amplitude ramps because the acceleration and

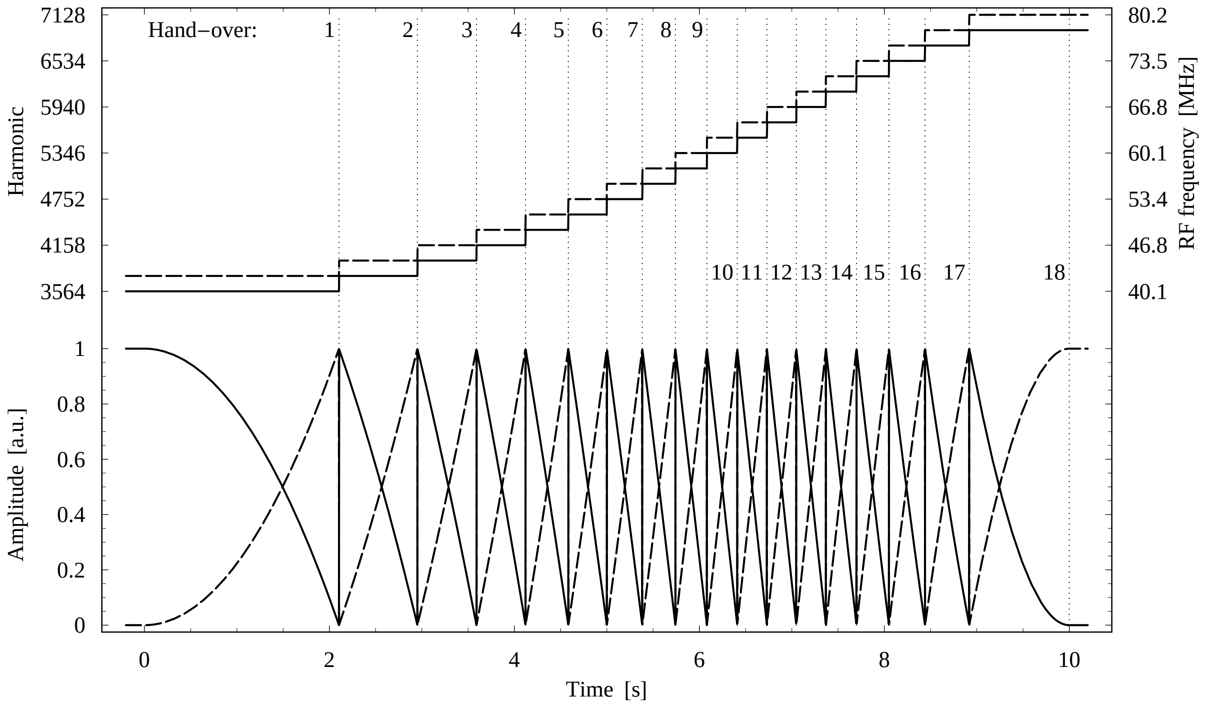

Fig. 5.20: Harmonic and voltage ramps for an optimized batch compression of the bunch pattern $16 \otimes b \oplus 2 \otimes e$ from $h = 3564$ to 7128 by 18 stepwise harmonic hand-overs. The lower harmonic and the related amplitude are plotted as continuous lines while the higher harmonic and amplitude are represented as a dashed line.

deceleration of the tail bunches needs to be initiated. The intermediate harmonic hand-overs still have almost linear variation of the RF amplitudes; they are just shifted together in time.

Tracking studies demonstrate the effect of the equilibration during batch compression on the longitudinal emittance: Figs. 5.21 and 5.22 show the development of the longitudinal RMS emittance during the first batch compression of a batch of 16 bunches with a gap of two empty buckets between adjacent batches. The initial bunches have a parabolic distribution with a total emittance of 1 eVs. Each of them consists of some 2000 macro particles. Collective effects are not taken into account. In the case of a constant time for each harmonic hand-over, the emittance of the tail bunch is diluted significantly due to the non-adiabatic modulation of the RF focusing. It is worth noting that the subsequent bunch mergings become asymmetric even if only the last bunch suffers from this excitation. This leads to additional emittance dilution. However, in the case of the equilibrated batch compression with amplitude ramps according to Fig. 5.20, virtually no longitudinal emittance dilution is visible although the batch compression has the same total duration as assumed in the non-optimized case.

Amplitude modulation

It is shown in Fig. 5.13 that the effective RF focusing is strongly modulated along the batch when the two RF system acting on the beam have the same amplitude. This modulation, from which especially the tail buckets may suffer, has a negative effect on the bunches at the ends of the batch because, as mentioned above, the fast variation in RF focusing can excite a quadrupole oscillations if the RF manipulation is not perfectly adiabatic. The possible benefit of an additional amplitude modulation to counteract the bucket area variation along the batch

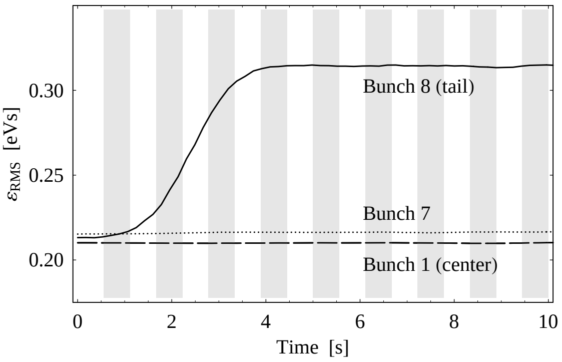

Fig. 5.21: Emittance development of center and tail bunches during batch compression of a 16 bunch batch in the LHC from $h = 3564$ to 7128. Each harmonic hand-over has the same duration. The tracking calculation was performed starting with 1 eVs bunches at an energy of 450 GeV (emittance conversion from total to RMS see Tab. 2.3).

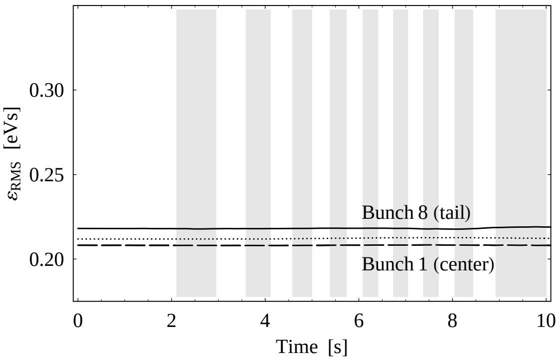

Fig. 5.22: Same representation as in Fig. 5.21 but for the equilibrated batch compression. There is virtually no longitudinal emittance dilution visible anymore although the manipulation takes the same time as in the bare case. The alternating white and gray striped regions indicate the harmonic hand-overs.

is therefore analyzed in this paragraph.

Assuming that the bunches are handed over from the harmonic h_1 to h_2, both RF amplitudes are modulated with the batch frequency given by $(h_2 - h_1)\omega_0$. In the frequency domain, an amplitude modulated signal consists of a main carrier at e.g. $h_1\omega_0$ with the batch frequency ω_0 and of two carriers which are just $(h_2 - h_1)\omega_0$ apart. RF cavities with a high quality factor do not have sufficient bandwidth to follow the fast amplitude modulation at the batch frequency with reasonable drive power, and additional RF systems would have to be installed to generate the modulation side bands. The technical implementation would thus be an approach in the frequency domain, too.

Adding the side band amplitudes U_{s1} and U_{s2} to the unmodulated combination of two RF carriers at h_1 and h_2 as stated in Eq. (3.7) results in a total RF amplitude which can be written as

$$\begin{aligned} U(t) = &-\underbrace{U_{\mathrm{s1}}\sin\left[(2h_1 - h_2)\omega_0 t\right]}_{\text{lower side band of } h_1} &&+ \underbrace{(U_1 - U_{\mathrm{s2}})\sin(h_1\omega_0 t)}_{\text{main carrier } h_1 \text{ and lower side band of } h_2} \\ &+\underbrace{(U_2 - U_{\mathrm{s1}})\sin(h_2\omega_0 t)}_{\text{main carrier } h_2 \text{ and upper side band of } h_1} &&- \underbrace{U_{\mathrm{s2}}\sin\left[(2h_2 - h_1)\omega_0 t\right]}_{\text{upper side band of } h_2}, \end{aligned} \qquad (5.7)$$

where the terms are given in the order of ascending frequency. The upper side band of the carrier at h_1 coincides with the carrier at h_2. The lower side band of the main carrier at the harmonic h_2 has the same frequency as the carrier at h_1. Finally, only two additional RF systems operating on the harmonics $2h_1 - h_2$ and $2h_2 - h_1$ are required to generate the amplitude modulation of both carriers at the batch frequency.

The modulation amplitude of the side bands $U_s = U_{\mathrm{s1}} = U_{\mathrm{s2}}$ is calculated numerically from the condition that the center and the last occupied bucket have identical areas. In analogy to the bucket area distribution along the batch as sketched in Fig. 5.13 for the first harmonic hand-over, Fig. 5.23 illustrates the same situation, but with additional side bands according to Eq. (5.7). The areas of center and tail bucket are equal by definition. However, center and tail buckets now have the smallest areas while the largest buckets are situated in the center of each half of the batch.

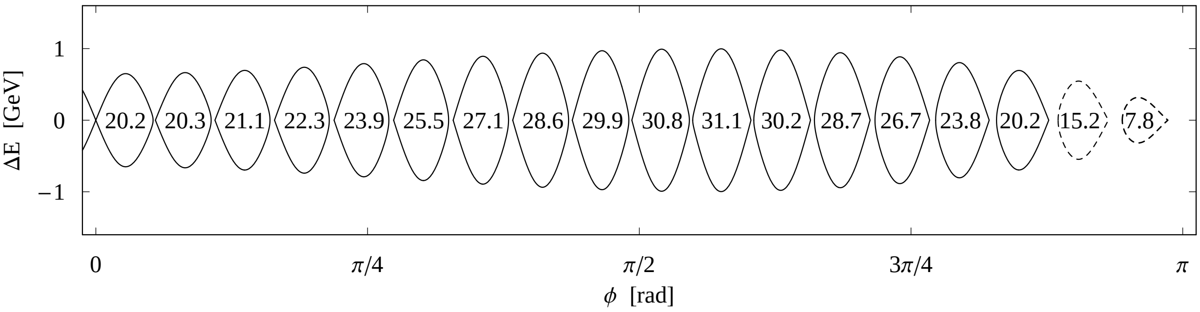

Fig. 5.23: Separatrices and bucket areas as in Fig. 5.13, but with amplitude modulation of both RF amplitudes so that the bucket area of the center and the tail bunches is identical. Again only one half of the 32 buckets of the batch is shown. The optimum voltage ratio is $U_{s1}/U_1 = U_{s2}/U_2 = 0.348$.

The maximum modulation amplitude is only needed at the instant when both RF amplitudes are equal during a harmonic hand-over. It must be zero in between, when the beam is held by one RF frequency only. The modulation side bands are therefore increased during each harmonic hand-over until both main RF amplitudes are equal. Then the modulation amplitude reaches its maximum to equilibrate the bucket areas as shown in Fig. 5.23. The side band amplitudes are decreased again towards the end of the harmonic hand-over so that they vanish when a higher harmonic main RF carrier holds the beam.

Analyzing the development of the longitudinal emittance with numerical tracking calculations shows that the additional amplitude modulation has a positive effect on the longitudinal dilution of the tail bunches (see Fig. 5.24). Even though the additional amplitude modulation causes a variation of the effective RF focusing of the center buckets during each harmonic hand-over, no significant dilution of the bunches in those buckets can be observed. However, when the batch has a total length of four bunches and the remaining bunches have large emittances, all bucket areas are equal with amplitude modulation but slightly smaller than the bucket areas without modulation. The tracking calculations show that this results in a bucket area limitation so that particles get lost during the last batch compression with four remaining buckets at 450 GeV.

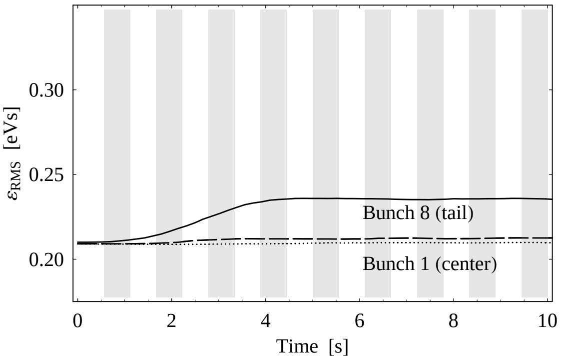

Fig. 5.24: Emittance development of center and tail bunches during batch compression as shown in Fig. 5.21 but with additional amplitude modulation during the harmonic hand-over. The center bunches are not affected significantly by the quadrupole oscillations of their buckets.

Keeping in mind that two additional RF systems with non-negligible voltage demands of some 40 % of the two main RF system would have to be installed, amplitude modulation might be an option when the batch compression is limited by insufficient area of the tail buckets. As this is not the case for analyzed batch compressions which are performed during the long and flat bunch combination scheme in the LHC (see Fig. 5.13), amplitude modulation is not necessary. The reduced blow-up of the tail bunches as illustrated in Fig. 5.24 is not significant as it is compensated by the time optimization scheme anyway.

Modified amplitude functions

For all schemes considered so far (see also Sec. 3.2.3) it was assumed that the higher harmonic amplitude would be increased while decreasing the lower harmonic amplitude simultaneously. In this case, both amplitudes are equal and have half of their maximum value at the middle of each harmonic hand-over.

An increase of the minimum bucket area during the harmonic hand-overs of $\sqrt{2}$ is achieved by the voltage ramps as sketched in Fig. 5.25 [81]. It should be mentioned that it is not mandatory that the amplitude ramps are linear. Time equilibration of the procedure for smooth acceleration and deceleration of the tail bunches can be reached as in the case of bare batch compression. Firstly, the RF amplitude at the larger harmonic h_2 is increased while the amplitude at h_1 stays constant. In the middle of the process, both voltages are equal and at their maximum values. Secondly, the amplitude at the lower harmonic is decreased to zero so that the bunches are held by the RF system at h_2 alone.

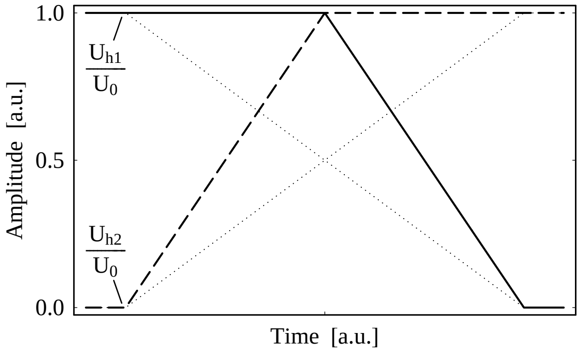

Fig. 5.25: Amplitude ramps (continuous and dashed) for harmonic hand-overs with increased bucket area during the process. The linear voltage functions (dotted) are shown for comparison only.

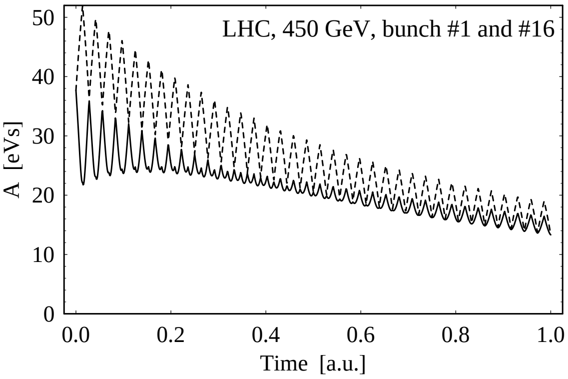

Fig. 5.26: Comparison of the bucket area development of center (dashed) and last populated bucket (continuous). Each of the 36 harmonic hand-overs is performed by voltage curves as shown in Fig. 5.25. Compared to Fig. 5.15 both buckets have a strongly modulated effective RF focusing.

Fig. 5.26 presents the modulation of center (dashed) and tail (continuous) bucket for a complete compression of 32 bunches with four empty buckets between the batches. In direct comparison to Fig. 5.15 one can clearly see that the bucket area modulation of the tail buckets is reduced by a factor of $\sqrt{2}$. However, the area of the center buckets is now also modulated significantly. Even if only at reduced strength, all other buckets are additionally modulated by the special amplitude ramps as shown in Fig. 5.25.

Batch compression with the amplitude ramping scheme discussed above has been in operation for the preparation of the primary proton beam in PS for antiproton production at CERN [73, 82]. As the bunch emittance becomes close to the bucket area limitation, one can profit from the increased effective RF focusing. For the batch combination scheme proposed for the LHC, the buckets are sufficiently large compared to the small bunch emittance at the beginning of the procedure so that the application of these modified amplitude functions during harmonic hand-over is not necessary. The bunches would even suffer from increased longitudinal emittance dilution.

Summary of batch compression options

Several possible options to improve the batch compression manipulation are analyzed in the preceding sections. Tab. 5.4 gives an overview of these options with the bare batch compression as reference. While the standard batch compression with harmonic hand-overs having linear RF amplitude ramps results in reasonable performance with respect to the dilution of the longitudinal emittance, the effect can be reduced significantly by time optimization. It is important to point out that this optimization requires no additional hardware installations.

	Bucket area	Long. Emittance	Add. Hardware
Bare scheme	reference	reference	none
Time optimization	unchanged	reduced blow-up of tail bunches	none
Amplitude modulation	first and last bucket equilibrated	reduced blow-up of tail bunches	two additional RF systems
Modified amplitude functions	bucket area increased	slight blow-up of center bunches	none

Tab. 5.4: Benefits of different optimization options of the long and flat bunch combination RF gymnastics.

Adding amplitude modulation during each sub-step of the harmonic increment also reduces the longitudinal dilution of the tail bunches. However, a supplementary RF system capable of generating some 40 % of the amplitude of the RF systems for the main carriers must be installed to generate the amplitude modulation side bands.

The choice of a special amplitude function during each harmonic hand-over has a negligible effect on the longitudinal emittance of the beam. As the bucket areas generated by a 40.08 MHz long and flat bunch combination RF system in the LHC are sufficiently large compared to the bunch emittance during the first steps of batch compression, there are no strong arguments to apply it for the proposed scheme to gain the factor of $\sqrt{2}$ in bucket area. However, it might be an option if the RF amplitude must be kept small for beam stability reasons during the first batch compression.

5.2.5 Bunch pair merging

After each compression, the batch is held by an RF system operated at 80.16 MHz ($h = 7128$). To reduce the number of bunches by a factor of two and to re-establish the initial RF frequency of 40.08 MHz ($h = 3564$), bunch pair merging is applied (see. Figs. 5.8 and 5.9). This type of RF manipulation has already been introduced as an example for an adiabatic procedure in Sec. 3.2.2. An improvement option to optimize the voltage ramps with respect to adiabaticity during the process analogous to the optimization of the batch compression is discussed in what follows.

Time optimization of bunch pair merging

An equivalent time optimization as presented for the batch compression in the preceding section can be performed for bunch pair merging because the initial bunches have to be accelerated and decelerated towards the common center of gravity. According to Eq. (3.5) and (3.6), the RF potential during bunch pair merging is given by

$$W(\phi) = \frac{1}{h_0}\left[\frac{t}{\tau_{\mathrm{bm}}}\sin h_0\phi + \frac{1}{2}\left(1-\frac{t}{\tau_{\mathrm{bm}}}\right)(\cos 2h_0\phi - 1)\right], \tag{5.8}$$

where τ_{bm} denotes the time duration of the bunch merging. The position of the bucket centers is derived from the minima of the potential, namely

$$\phi_0\left(\frac{t}{\tau_{\mathrm{bm}}}\right) = \begin{cases} \pm\dfrac{1}{h_0}\arccos\dfrac{t/\tau_{\mathrm{bm}}}{2(t/\tau_{\mathrm{bm}}-1)}, & t/\tau_{\mathrm{bm}} < 2/3 \\ 0, & \text{elsewhere} \end{cases} \tag{5.9}$$

The motion of the bucket centers is illustrated in Fig. 5.27 (thick lines). After two thirds of the process, the separated sub-buckets vanish completely, and a single bucket reaching from $-\pi$ to π remains (Fig. 5.27, thin lines). The positions of the sub-bucket centers vary quickly, resulting in a large energy offset of the particles inside. This energy offset may cause emittance dilution when the phase velocity $d\phi_0/dt$ abruptly decreases to zero at $t/\tau_{\mathrm{bm}} = 2/3$.

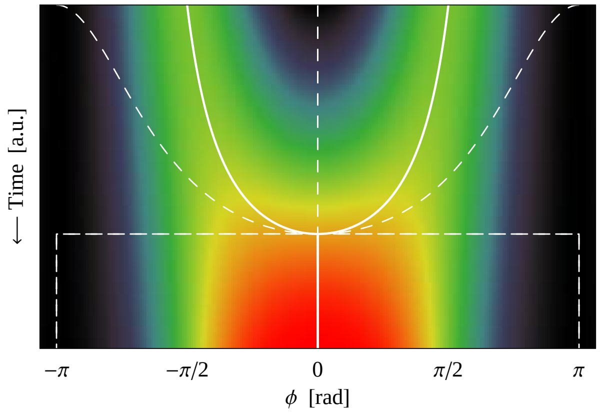

Fig. 5.27: Phase motion of the bucket centers (thick line) and the region of the sub-buckets (enclosed by the thin lines) during bunch pair merging with linear voltage ramps ($h_0 = 1$).

Demanding that the motion of the sub-buckets should follow a cosine function so that the bunches are smoothly accelerated and decelerated during the first two thirds of the merging process

$$\phi_{\mathrm{opt}}\left(\frac{t}{\tau_{\mathrm{tm}}}\right) = \pm\frac{\pi}{4h_0}\left[3-\cos\left(\frac{3\pi}{2}\frac{t}{\tau_{\mathrm{tm}}}\right)\right] \tag{5.10}$$

the time function to get the desired bucket motion is obtained as

$$t_1(t) = \frac{\tau_{\mathrm{bm}}}{1-\dfrac{1}{2}\Big/\cos\left\{\dfrac{\pi}{4}\left[3-\cos\left(\dfrac{3\pi}{2}\dfrac{t}{\tau_{\mathrm{bm}}}\right)\right]\right\}} \tag{5.11}$$

by equating Eqs. (5.10) and (5.9). The equilibrated bucket motion is shown in Fig. 5.28; in fact, the buckets are now smoothly accelerated and decelerated toward each other. The time dependent voltage ramps are derived inserting Eq. (5.11) into Eq. (3.6) and can be finally written as

$$U_1(t) = U_0\cdot\begin{cases} \dfrac{1}{1-\dfrac{1}{2}\Big/\cos\left\{\dfrac{\pi}{4}\left[3-\cos\left(\dfrac{3\pi}{2}\dfrac{t}{\tau_{\mathrm{bm}}}\right)\right]\right\}}, & t/\tau_{\mathrm{bm}} < 2/3 \\ t/\tau_{\mathrm{bm}}, & \text{elsewhere} \end{cases} \quad \text{and} \tag{5.12}$$

$$U_2(1) = 1 - U_1(t).$$

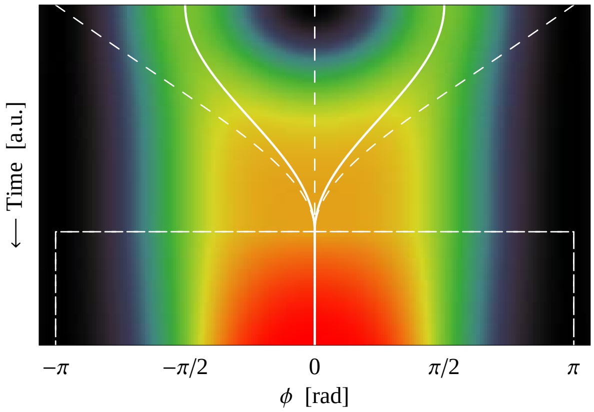

Fig. 5.28: Phase motion of the bucket centers (thick line) and the region of the sub-buckets (enclosed by the thin lines) during bunch pair merging as in Fig. 5.27 but with optimized voltage ramps ($h_0 = 1$).

Fig. 5.29 illustrates these amplitude ramps (continuous) together with the simple, linear amplitude functions (dashed). Comparing both functions shows a lack of adiabaticity in the middle of the process which is compensated by the time equilibration. After two thirds of the process, the sub-buckets vanish, and linear amplitude curves can be applied as the bucket center does not move anymore. The scheme has also been checked by numerical tracking calculations but no beneficial effect on the longitudinal emittance is observed. As long as the bunch merging is carried out sufficiently adiabatically, the final emittance of the merged bunch is almost the same for linear and time optimized amplitude ramps. In case of a fast bunch merging for which a longitudinal emittance blow-up is observed, the time optimized amplitude ramps sometimes even have an adverse effect on the longitudinal emittance. Therefore, the linear amplitude functions are kept for the long and flat bunch combination scheme for the LHC.

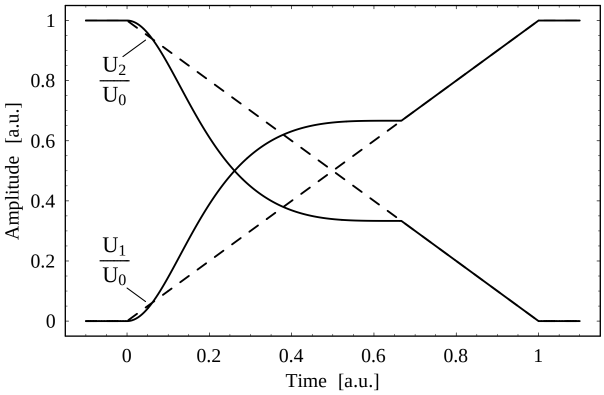

Fig. 5.29: Optimized amplitude ramps during bunch pair merging according to Eq. (5.12) for a smooth bucket motion (continuous, see Fig. 5.28) compared to linear amplitude functions (dashed, see Fig. 5.27).

5.2.6 Final formation of long and flat bunches

The final formation of the long and flat bunch is supposed to be a rather simple RF manipulation with which the last two remaining buckets held at the harmonic 7128 (80.16 MHz) are transferred to a single flattened bucket. In fact, this RF gymnastics is very similar to a bunch pair merging which is halted in the middle of the process, except that more RF systems contribute. For simplicity the optimum final amplitudes as given in Tab. 4.3 are set linearly. Neglecting synchrotron radiation, the final longitudinal phase space of a long and flat bunch held by two respectively three different RF harmonics is illustrated in Fig. 5.30 and 5.31. Even for three RF harmonics, the resulting bunches approximates the rectangular shape reasonably well. It is worth noting that the maximum longitudinal density starting from bunches with a fixed

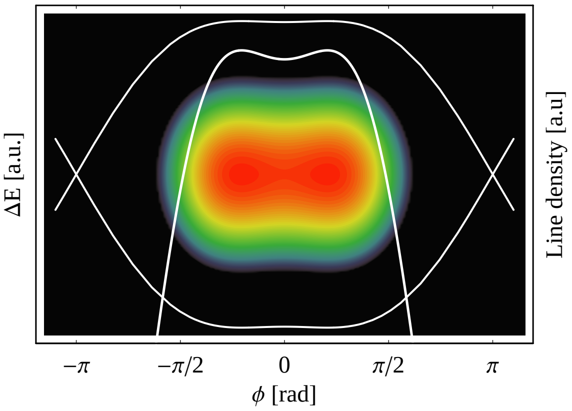

Fig. 5.30: Longitudinal phase space and line density of a final long and flat bunch held by a double harmonic RF system.

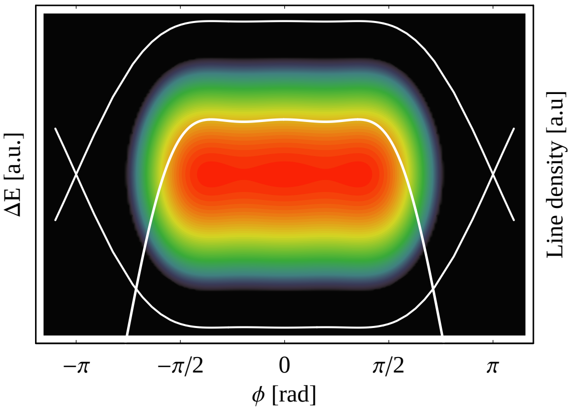

Fig. 5.31: Same representation as is Fig. 5.31 but for three multiple RF harmonics at 40.08, 80.16 and 120.24 MHz. The peak current is lowered for fixed intensity because of the longer bunches.

intensity decreases with increasing number of harmonics due to an increase of the bunch length (see Tab. 4.3).

5.2.7 The complete combination scheme

Arranging the RF manipulations successively results in a complete manipulation scheme to combine 16 or 32 bunches to one long and flat bunch. An overview of the bunch pattern during the procedure is given in Tab. 5.5, while the development of the buckets is illustrated in Figs. 5.32 and 5.33. From the bucket motion the time optimization of the batch compression manipulations becomes clearly visible as expected: the buckets are slowly accelerated and decelerated during each process to avoid the excitation of a dipole mode at the transition from stationary to moving bucket.

Manipulation	16 initial bunches	32 initial bunches	Energy
Initial bunch pattern	$16 \otimes b \oplus 2 \otimes e$	$32 \otimes b \oplus 4 \otimes e$	450 GeV
Batch compression	$16 \otimes b \oplus 20 \otimes e$	$32 \otimes b \oplus 40 \otimes e$	
Bunch merging	$8 \otimes b \oplus 10 \otimes e$	$16 \otimes b \oplus 20 \otimes e$	
Batch compression	$8 \otimes b \oplus 28 \otimes e$	$16 \otimes b \oplus 56 \otimes e$	
Bunch merging	$4 \otimes b \oplus 14 \otimes e$	$8 \otimes b \oplus 28 \otimes e$	
Batch compression	$4 \otimes b \oplus 32 \otimes e$	$8 \otimes b \oplus 64 \otimes e$	
Bunch merging	$2 \otimes b \oplus 16 \otimes e$	$4 \otimes b \oplus 32 \otimes e$	
Batch compression		$4 \otimes b \oplus 68 \otimes e$	
Bunch merging		$2 \otimes b \oplus 34 \otimes e$	
Acceleration	$2 \otimes b \oplus 16 \otimes e$	$2 \otimes b \oplus 34 \otimes e$	
Batch compression	$2 \otimes b \oplus 34 \otimes e$	$2 \otimes b \oplus 70 \otimes e$	7 TeV
Final formation	$1 \otimes b \oplus 35 \otimes e$	$1 \otimes b \oplus 71 \otimes e$	

Tab. 5.5: Bunch pattern during the LHC combination scheme for 16 and 32 initial bunches.

To check the performance of the RF manipulation, batches of bunches consisting of some 2000 particles each have been tracked in the longitudinal phase space through the complete procedure in the LHC. To save calculation time, the acceleration itself was replaced by a simple

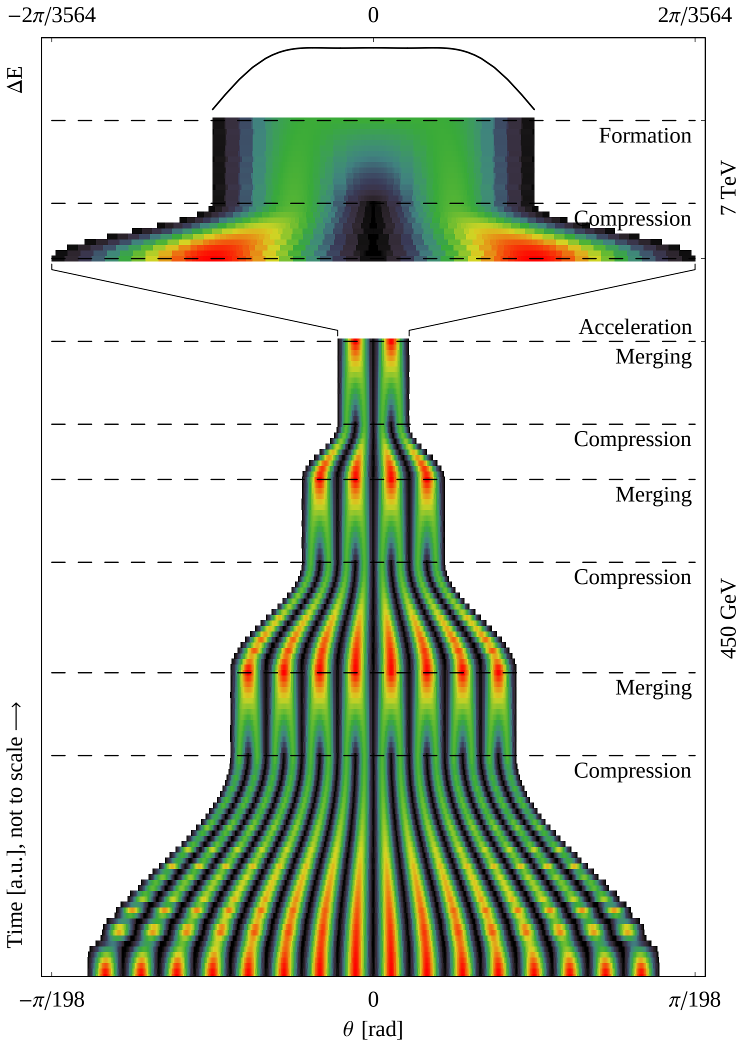

Fig. 5.32: Development of the buckets during the complete combination RF gymnastics of 16 bunches. The color scale is proportional to the height of the separatrix in energy. The final separatrix is shown on the top.

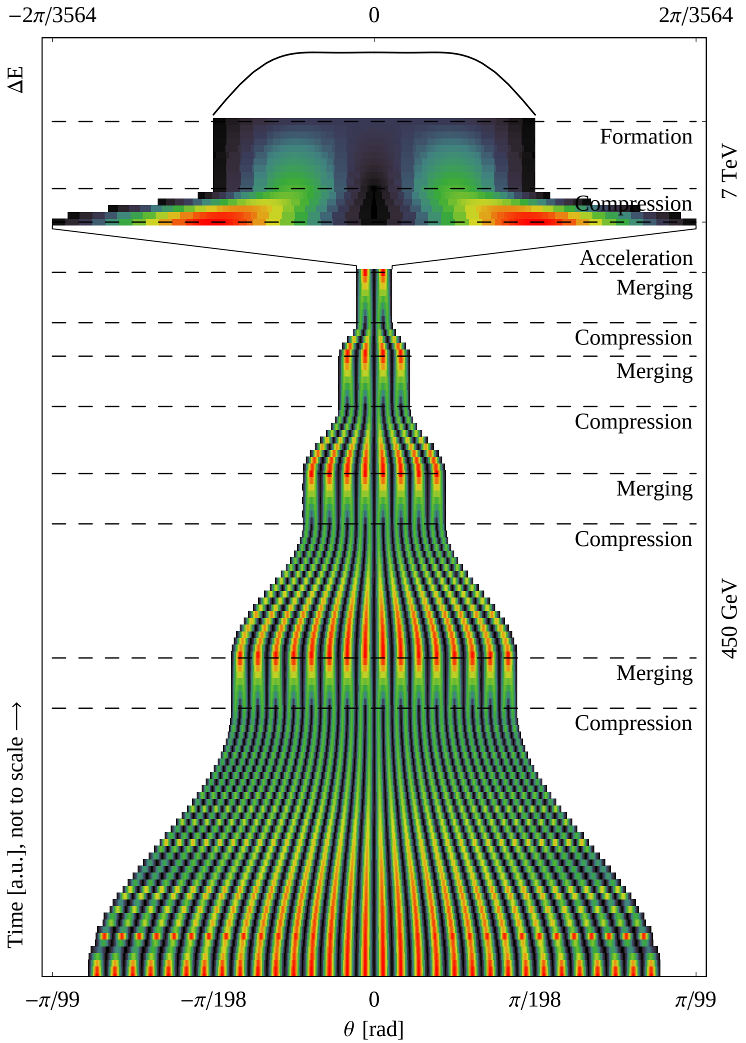

Fig. 5.33: Development of the buckets during the complete combination RF gymnastics of 32 bunches. The representation is equivalent to Fig. 5.32.

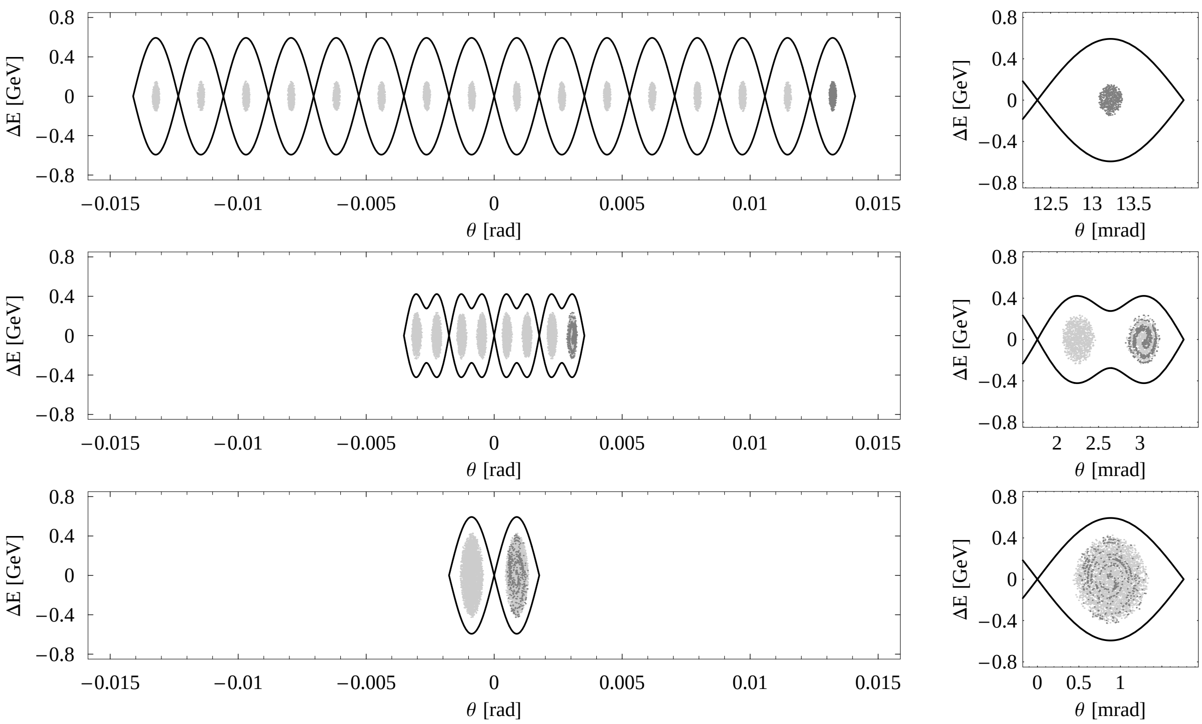

Fig. 5.34: Longitudinal phase space during the generation of a long and flat bunch at the beginning (top), in the middle (center) and at the end of the RF manipulation at the LHC flat-bottom. The last bunch of the batch (dark gray), which suffers most from the RF gymnastics, is magnified in the right plots.

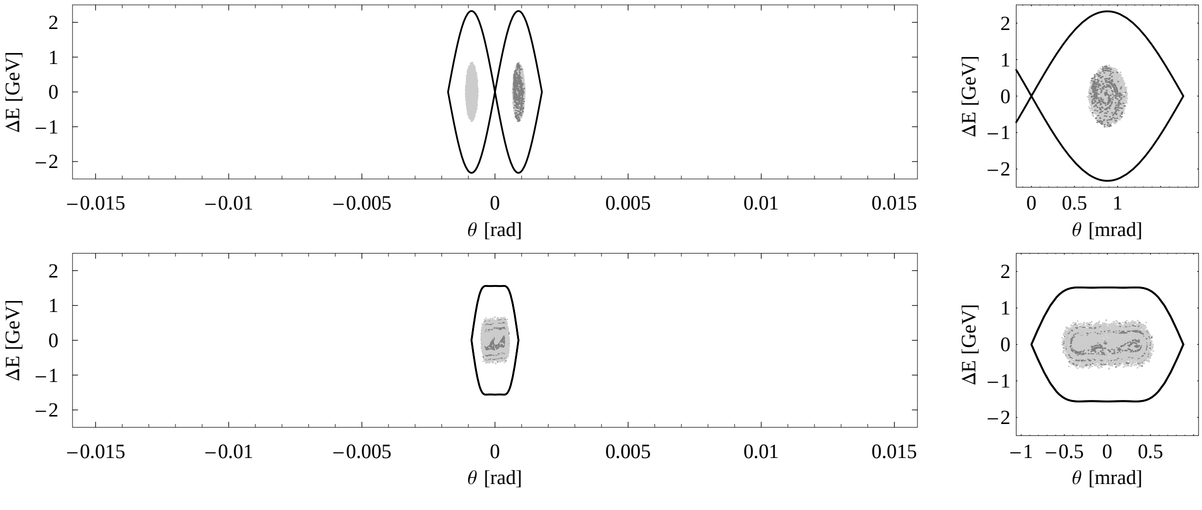

Fig. 5.35: Longitudinal phase space at beginning and end of the RF manipulation at flat-top. It is worth noting that the vertical scale is changed with respect to Fig. 5.34.

energy scaling of all particles. For the same reason, only particles within half of the batch have been taken into account as the second half of the batch is symmetric. The complete time optimized harmonic and RF amplitude program used for tracking is shown in Fig. 5.36. The acceleration in the LHC (represented by the dark gray line) will last some 20 minutes, which is more than an order of magnitude longer than the time needed for the generation of long and flat bunches. Virtually no longitudinal emittance blow-up is expected during acceleration from

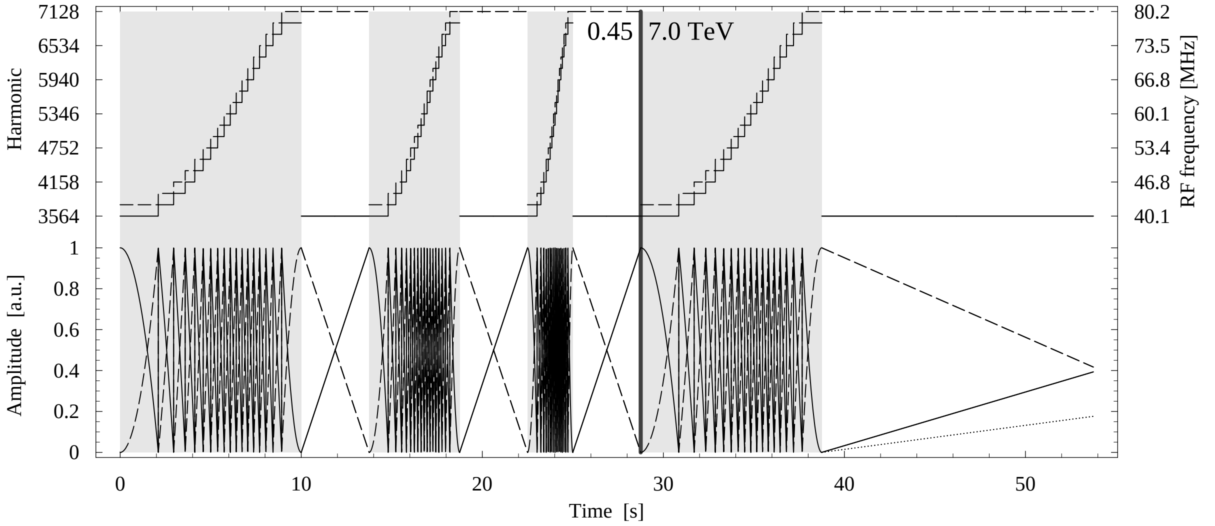

Fig. 5.36: Harmonic and voltage program for the complete long and flat bunch generation scheme. The thick gray line corresponds to acceleration with the 40.08 MHz RF system for about 20 minutes. For a detailed plot of the first batch compression see Fig. 5.20.

injection to collision energy.

To simplify the handling of the multi-bunch systems and sophisticated non-linear RF amplitude and harmonic functions, a dedicated tracking code has been developed. Firstly, this code is extremely flexible with respect to multi-bunch systems, e.g. it allows to logically merge or split bunches. All analysis functions like emittance derivation or bunch position calculation can be applied to the logical bunches individually. Secondly, as the code is implemented as a series of functional packages in Mathematica [179], most of the parameters can be handled as functions, and the full flexibility of Mathematica itself can be employed to construct them. Especially calculations including isolated or barrier buckets in combination with harmonic RF systems can be performed flexibly. Further examples of different RF manipulations which are evaluated with this code are presented in Chapter 3.

5.3 Adiabaticity and longitudinal emittance

Although adiabaticity is not a crucial parameter during the proposed long and flat bunch scheme, as the additional time needed is below 10 % of the acceleration time in the LHC, it is worth analyzing the expected emittance blow-up versus total duration of the RF manipulation.

The development of the longitudinal emittance during the combination of a batch of 32 initial 1 eVs bunches for different durations is shown in Figs. 5.37 to 5.40. Gray shaded areas are periods where batch compression is applied. The regions in between refer either to a bunch pair merging or the final formation of the long and flat bunch. As only half of the batch is tracked in the longitudinal phase space, the total emittance sums up to some 16 eVs. The upper curves in Figs. 5.37 to 5.40 show the encircling elliptic emittance of 99 % of the particles per bunch summed up over the 16 bunches. It has been re-scaled so that the initial emittance is again 16 eVs. The lower curves in the diagrams represent the sum of the RMS emittance being calculated for each bunch independently (see. Sec. 2.5.1).

The total duration has to be equal or larger than 77.5 s for the emittance blow-up to be

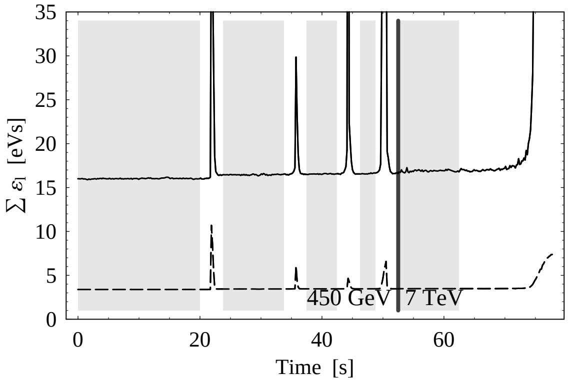

Fig. 5.37: Development of the elliptic (continuous) emittance containing 99 % of the particles and the RMS emittance (dashed) during the combination of batches of 32 bunches. The shaded areas indicate the regions of batch compression.

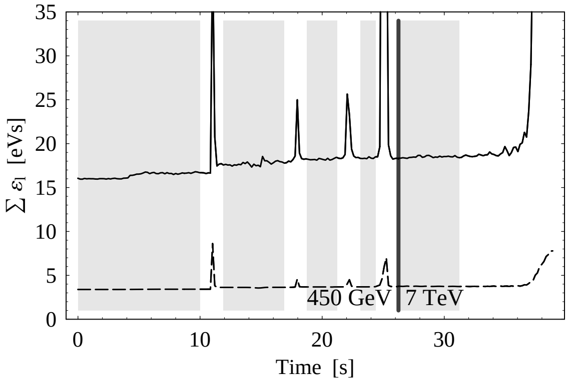

Fig. 5.38: Same representation as Fig. 5.37 but twice faster. An increased blow-up of the effective emittance becomes visible.

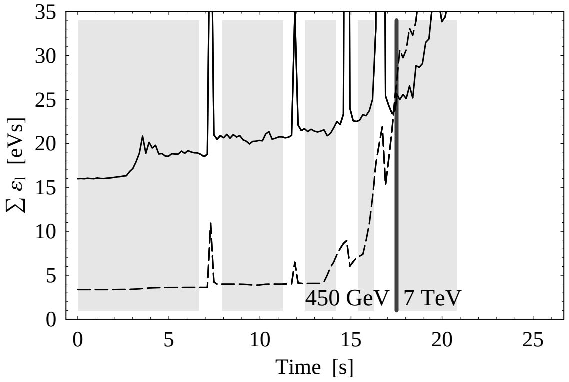

Fig. 5.39: Same representation as Fig. 5.37 but three times faster. The increased emittance growth is significantly stronger than in the figures above. During the last batch compression, particles get lost from their buckets.

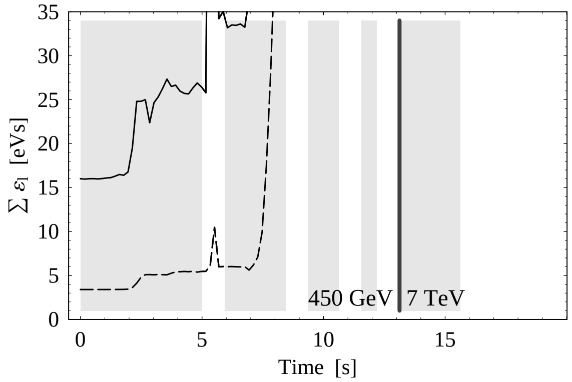

Fig. 5.40: Same representation as Fig. 5.37 but four times faster. Already during the second batch compression, particles get lost from their buckets which virtually leads to an exponential growth of the elliptic emittance because the particle distribution becomes non-elliptic.

negligible and the process quasi-adiabatic. It is worth mentioning that the apparent emittance growth at the end of the final long bunch formation comes from artifacts of the calculation method. As only half of the batch is taken into account for the tracking, the batch is virtually merged with empty bunches. This leads to an artificial blow-up of the RMS emittance by a factor of two whereas the effect on the elliptic emittance is even more severe because the final bunches have a non-elliptic longitudinal distribution.

In Fig. 5.38, where the sequence is executed in less than 39 s, first signs of emittance dilution during the RF manipulations become visible. The situation gets clearly worse when the total duration is reduced to 25.8 s (Fig. 5.39). During the last batch compression at 7 TeV particles start to escape and are lost. In the last case (Fig. 5.40) the result becomes even useless. Particles lost from the buckets cause an enormous emittance dilution, where the bunches are virtually distributed all along the circumference of the LHC and finally lost.

Therefore a total time duration of 77.5 s seems adequate. The first 52.4 s of this duration are spent on the flat-bottom at 450 GeV, while the remaining time is spent on the last batch compression and bunch merging at 7 TeV. This additional time needed to prepare the beam has a negligible effect on the integrated luminosity.

5.4 Summary

After the detailed analysis of the RF manipulations necessary for the combination of 16 or 32 nearly nominal bunches to a long and flat bunch, the expected performance with respect to the longitudinal emittance is summarized for the 16 bunch scheme in Tab. 5.6.

	RF parameters	Emit., ε_l	$\varepsilon_l/\varepsilon_0$
SPS ejection, 450 GeV	8 MV at 200 MHz (SPS)	0.8 eVs	
Bunch rotation and LHC injection	3 MV at 40 MHz (LHC)	1.0 eVs	25 %
Blow-up by 400.8 MHz RF system	3 MV at 40 MHz	1.1 eVs	10 %
Batch compression to two bunches	2×1.5 MV at 40 . . . 80 MHz	12.3 eVs	40 %
Acceleration to flat-top, 7 TeV	3 MV at 40 MHz	12.9 eVs	5 %
Final formation of the long bunch	2×1.5 MV at 40 . . . 80 MHz	28.5 eVs	10 %
Collision mode with long bunches	0.8/0.8/0.4 MV at 40/80/120 MHz	28.5 eVs	

Tab. 5.6: Emittance development during the long and flat bunch generation scheme for the LHC ($16 \otimes b \oplus 2 \otimes e$). The last column $\varepsilon_l/\varepsilon_0$ presents the relative blow-up of the effective longitudinal emittance estimated for the manipulation concerned. The necessity of an additional 400.8 MHz RF system causing about 10 % emittance blow-up is due to preservation of Landau damping which is analyzed in Chapter 6.

In case of combining 32 bunches, the emittance growth is expected to be slightly larger as an additional batch compression and bunch pair merging is inserted to the RF gymnastics: the final emittance can be estimated to be around $2 \cdot 28.5\,\text{eVs} \simeq 57\,\text{eVs}$. The RF amplitudes in Tab. 5.6 must be multiplied by a factor of four. The bunch rotation in the SPS to lengthen the bunches before extraction is not required for the combination of 32 bunches, as the RF voltage is sufficient to allow a matched bunch to bucket transfer. The batch combination scheme analyzed in this chapter has several advantages compared to a superbunch scheme with barrier buckets:

Although the RF manipulations are sophisticated, RF amplitudes at no more than two harmonics have to act on the beam simultaneously. The whole scheme can be performed with two or preferably three tunable RF systems in the frequency range of 40.08 to 80.16 MHz delivering about 1.5 MV (16 initial bunches) or 6 MV (32 initial bunches). As the LHC will be filled once or twice per day, a large tuning speed is not required, and it is thus reasonable to propose the use of vacuum cavities with high quality factor tuned by a mechanically moving gap for the large frequency variation. The PS is equipped with RF cavities at 40 MHz [180, 181] and 80 MHz [182] which make use of a special pneumatic gap switch operated in the ultra high vacuum of the beam pipe physically closing the accelerating gap. These cavities are operated very reliably and could serve as a starting point for the design of the cavities needed in the LHC. The large tuning range combined with a mechanical tuning element excludes the construction of superconducting RF cavities.

Furthermore, the two basic ingredients for the batch combination RF manipulation, batch compression and bunch pair merging are well-proven to work with a reasonable performance. Finally, the proposed scheme is fast in the sense that it can be performed adiabatically within less than a few minutes. A decrease of the integrated luminosity due to the long-winded RF gymnastics is thus not expected.

The scheme has been optimized neglecting collective beam effects like instabilities before, during or after the batch combination scheme. This important issue is addressed in the subsequent chapter.

Chapter 6

Collective Effects and Beam Loading

In Chapter 4 the optimum luminosity conditions are calculated under the assumption that no other collective effects than beam-beam interactions limit the longitudinal performance of the LHC. Also the optimization of the RF manipulations to create the long and flat bunches is presented with main focus on single particle dynamics. Therefore, the following chapter addresses two major longitudinal effects provoked by high intensity bunches: collective beam instabilities and beam loading.

During storage and collision of the final long and flat bunches, the region of homogeneous line density is considered as a coasting beam, and consequently the Keil-Schnell criterion is derived from first principles and applied to the expected long bunch parameters in the first part of this chapter. Secondly, criteria for bunched beams are introduced to estimate the beam stability during the injection plateau and during acceleration of the dense bunches by the 40.08 MHz RF system. Counter-measures, like the increase of the synchrotron frequency spread, are basic ingredients to improve longitudinal stability being discussed thereafter. Finally, the influence of steady-state and transient beam loading is analyzed to ensure that the new RF system could be controlled similarly as the superconducting 400.8 MHz cavities.

6.1 Vlasov equation and Keil-Schnell criterion

A simple estimate for the longitudinal stability of a particle beam of given intensity and a well defined momentum distribution is the so-called Keil-Schnell criterion. It has been originally developed from the stability of intense coasting proton beams in the Intersecting Storage Rings (ISR) at CERN [183, 184, 185]. However, if the growth rate of the longitudinal instability is large compared to the synchrotron frequency, the synchrotron motion of particles in a bunched beam can be considered as frozen on the time scale of the instability. The criterion derived in the following section may be applied to a bunched beam as a first guess in such cases.

6.1.1 Vlasov equation and dispersion relation

The longitudinal phase space density in its most general form can be expressed by the distribution function $g = g(\theta, \Delta E/\omega)$. The two independent variables are chosen as a canonically conjugated pair (see Sec. 2.2.2). According to Liouville's theorem each infinitesimal longitudinal density fraction described by g can move in the phase space, but the total time derivative of the distribution function stays constant:

$$\frac{d}{dt} g\left(\theta, \frac{\Delta E}{\omega}\right) = 0\,.$$

Expanding the total derivatives leads to the general equation of motion

$$\frac{\partial g(\theta, \Delta E/\omega)}{\partial \theta} \dot{\theta} + \frac{\partial g(\theta, \Delta E/\omega)}{\partial(\Delta E/\omega)} \dot{\left(\frac{\Delta E}{\omega}\right)} + \frac{\partial g(\theta, \Delta E/\omega)}{\partial t} = 0\,, \tag{6.1}$$

which is also called Vlasov equation. The dotted variables represent total time derivatives. As the revolution frequencies of the individual particles ω in a high energy beam are close to the average revolution frequency of the beam so that $\omega \simeq \omega_0$, the Vlasov equation reduces to [186]

$$\frac{\partial f(\theta, E)}{\partial \theta} \dot{\theta} + \frac{\partial f(\theta, E)}{\partial E} \dot{E} + \frac{\partial f(\theta, E)}{\partial t} = 0\,, \tag{6.2}$$

where $f = f(\theta, E)$ is the adapted longitudinal distribution function.

To drive the longitudinal instability, a perturbation voltage U_1 at an arbitrary frequency ω_1 is introduced according to $U(t) = U_1 \exp(-i\omega_1 t)$ and an individual particle gains or looses a certain amount of energy per turn given by (see Eqs. 2.2 and 2.6)

$$\Delta \dot{E} = \frac{e\omega U_1}{2\pi} e^{i(n\theta - \omega_1 t)} \simeq \frac{e\omega_0 U_1}{2\pi} e^{i(n\theta - \omega_1 t)}\,, \tag{6.3}$$

wherein n denotes the mode number of the excitation with respect to the revolution frequency. In the case of small perturbations it, can be assumed that the perturbation of the longitudinal density shows the same form as the excitation itself so that

$$f(\theta, E) = f_0(E) + f_1(E) e^{i(n\theta - \omega_1 t)} \tag{6.4}$$

is chosen as an ansatz representing the energy distribution of the unperturbed coasting beam $f_0(E)$ with a corresponding perturbation caused by $U(t)$.

Inserting the derivatives of Eq. (6.4) into the Vlasov equation under the assumption that the perturbation amplitude f_1 is much smaller than f_0, the unperturbed distribution can be written as

$$i(n\omega - \omega_1) f_1(E) e^{i(n\theta - \omega_1 t)} + \frac{df_0(E)}{dE} \frac{e\omega_0 U_1}{2\pi} e^{i(n\theta - \omega_1 t)} = 0\,. \tag{6.5}$$

Separation of the perturbation and energy integration of Eq. (6.5) gives

$$\underbrace{\int f_1(E)\, dE}_{I_1/(e\omega_0)}\; e^{i(n\theta - \omega_1 t)} = -\frac{ie\omega_0 U_1}{2\pi} e^{i(n\theta - \omega_1 t)} \int \frac{df_0(E)/dE}{\omega_1 - n\omega}\, dE\,, \tag{6.6}$$

where the left side is identified by the perturbing beam current. It is worth noting that the normalization of $f(\theta, E)$ is chosen according to

$$\int_0^{2\pi} \int_{-\infty}^{\infty} f(\theta, E)\, dE = N\,.$$

The integral on the right side of Eq. (6.6) can be written in a more convenient form by considering that

$$f_0(E) = \frac{d\omega}{dE} f_0^*(\omega) = -\frac{\eta}{\beta^2} \frac{\omega_0}{E} f_0^*(\omega)\,,$$

and the Vlasov equation becomes

$$I_1 e^{i(n\theta-\omega_1 t)} = \frac{ie^2\omega_0^3\eta}{2\pi E\beta^2} U_1 e^{i(n\theta-\omega_1 t)} \int \frac{df_0^*(\omega)/d\omega}{\omega_1 - n\omega}\, d\omega \,. \tag{6.7}$$

The term on the right side contains in fact the spectral component of the beam transfer function of a coasting beam at ω_1. Introducing a complex longitudinal coupling impedance between beam current $U_1 = -Z_\| I_1$ to feedback the beam current perturbation as an excitation, the dispersion relation of the coasting beam reduces to [61, 187]

$$1 = -\frac{ie^2\omega_0^3\eta Z_\|}{2\pi E\beta^2} \int \frac{df_0^*(\omega)/d\omega}{\omega_1 - n\omega}\, d\omega \,. \tag{6.8}$$

This dispersion relation is used as a starting point to derive a criterion for longitudinal beam stability.

6.1.2 Stability diagrams

For the calculation of stability diagrams and algebraic conditions for longitudinal beam stability the transformation of the dispersion relation to normalized variables is convenient. The width of one half of the half maximum frequency spread is defined by $S = -\eta\omega_0\Delta p/p$, where $\Delta p/p$ is referred to as half momentum spread at half maximum height[1]. Furthermore, the normalized frequency deviation of beam harmonic and excitation frequency from the average harmonic of the revolution frequency are defined by

$$\left.\begin{array}{rr} & n\omega - n\omega_0 = xnS \\ \text{and} & \omega_1 - n\omega_0 = x_1 nS \end{array}\right\} \ \omega_1 - n\omega = (x_1 - x)nS \,.$$

The distribution in revolution frequencies $f_0^*(\omega)$ is converted according to

$$F_0(x) = \frac{2\pi S}{N} f_0^*(x) \,,$$

which is then normalized properly. For energy distributions $F_0(x)$ being symmetric around $x = 0$, the normalization conditions can be written as [189]

$$\int_{-\infty}^{\infty} F_0(x)\, dx = 1 \qquad \text{and} \qquad F_0(x = \pm 1) = \frac{1}{2} F_0(x = 0) \,. \tag{6.9}$$

Finally, the normalized dispersion relation Eq. (6.8) in the new variables x, x_1 becomes

$$1 = \frac{ieI_0 Z_\|}{2\pi E\beta^2\eta(\Delta p/p)^2 n} \int \frac{dF_0(x)/dx}{x - x_1}\, dx \,, \tag{6.10}$$

where I_0 denotes the average beam current. As the longitudinal impedance $Z_\|$ is complex in general, Eq. (6.10) can be also represented in terms of a normalized impedance:

$$1 = (U' - iV') \int \frac{dF_0(x)/dx}{x - x_1}\, dx \qquad \text{and}$$

$$U' - iV' = -\frac{eI_0}{2\pi E\beta^2\eta(\Delta p/p)^2} \left(\text{Im}\{Z_\|/n\} - i\text{Re}\{Z_\|/n\}\right) \,. \tag{6.11}$$

---

[1] Some authors define $\Delta p/p$ as full momentum spread at half height [188] which is e.g. more convenient for the analysis of stacked beams.

This relation couples the normalized impedance $U' - iV'$ to the normalized complex frequency shift x_1 induced by the perturbation. The regions of impedances where the beam is stable or unstable can be explored by expressing the perturbing part of the beam distribution $f(\theta, E)$ in terms of this induced frequency shift x_1. As this contribution is proportional to $\exp[i(n\theta - \omega_1 t)]$, its frequency can be written as $n\dot{\theta} = n\omega - \omega_1 = nx_1 S$ so that

$$\exp[i(n\theta - \omega_1 t)] = \exp\left(i\mathrm{Re}\{x_1\} n\eta\omega_0 \frac{\Delta p}{p} t\right) \cdot \exp\left(-\mathrm{Im}\{x_1\} n\eta\omega_0 \frac{\Delta p}{p} t\right) .$$

In fact, the real part of the complex frequency shift x_1 leads to a frequency displacement, while the imaginary part of x_1 defines whether the excitation is damped ($\mathrm{Im}\{x_1\} < 0$ for $\gamma > \gamma_{\mathrm{tr}}$) or exponentially excited ($\mathrm{Im}\{x_1\} > 0$ for $\gamma > \gamma_{\mathrm{tr}}$). The trajectory in the complex impedance plane, for which the imaginary part of x_1 is zero, defines the limitation of longitudinal stability. Frequency shift and growth rate are given by

$$\Delta\omega_1 = -\eta\omega_0 \frac{\Delta p}{p} \mathrm{Re}\{x_1\} \quad \text{and} \quad \frac{1}{\tau} = -\eta\omega_0 \frac{\Delta p}{p} \mathrm{Im}\{x_1\} . \tag{6.12}$$

The full stability diagram of a given distribution is generated by evaluating the parameters $U'(x_1)$ and $V'(x_1)$ from Eq. (6.11) for different complex normalized frequency shifts x_1; preferably the parameter x_1 is chosen so that either its real or imaginary part is held constant. An example for such a stability diagram of a quartic distribution

$$F(x) = \frac{15a}{16}(1 - a^2x^2)^2 \quad \text{for} \quad |x| < \frac{1}{a} \quad \text{and} \quad a = \sqrt{1 - 1/\sqrt{2}}$$

is given in Fig. 6.1. The gray shaded area is the region of normalized impedances $U' - iV'$, which are tolerable for a stable beam. To simplify the calculation of stability diagrams, the

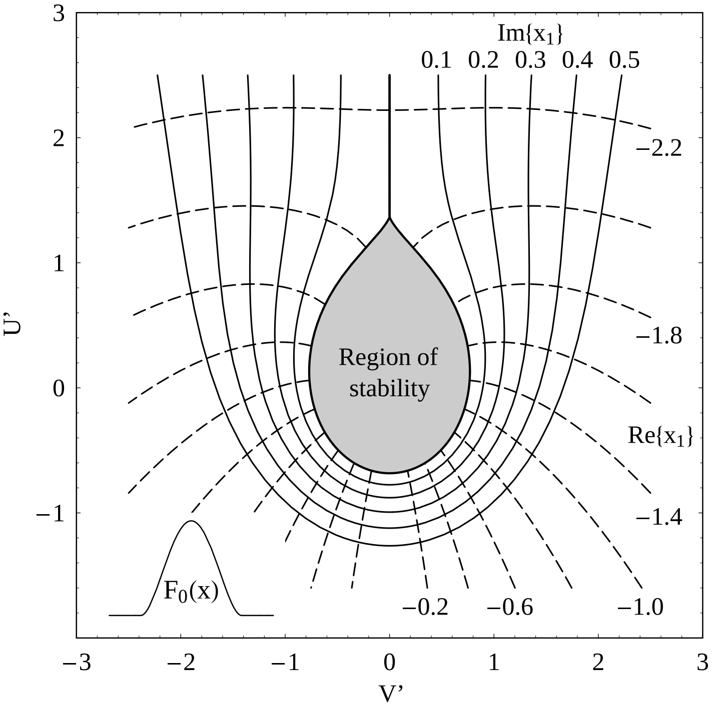

Fig. 6.1: Stability diagram of a coasting beam with a quartic energy distribution, $F_0(x) \propto (1 - a^2x^2)^2$. The gray shaded area represents the region of stability as $\mathrm{Im}\{x_1\}$ is negative ($\gamma > \gamma_{\mathrm{tr}}$) and an excitation of the beam is thus damped. The imaginary part of x_1 is kept constant along the continuous lines, while the real part remains unchanged along the dashed lines.

dispersion integral from Eq. (6.11) can be integrated partially for distribution functions $F_0(x)$ which vanish at $x = \pm\infty$ so that

$$U' - iV' = 1 \Big/ \int \frac{dF_0(x)/dx}{x - x_1}\, dx = 1 \Big/ \int \frac{F_0(x)}{(x - x_1)^2}\, dx \ . \tag{6.13}$$

As the integral from Eq. (6.11) contains a singularity within its integration limits are furthermore split into real and imaginary part according to

$$\int \frac{dF_0(x)/dx}{x - x_1}\, dx = \mathrm{PV} \int \frac{dF_0(x)/dx}{x - x_1}\, dx + \mathrm{sign}\left(\mathrm{Im}\{x_1\}\right)\, i\pi\, \frac{\partial F_0(x)}{\partial x}\bigg|_{x=x_1} \tag{6.14}$$

so that a numerical computation of the stability diagrams can be performed straightforward. The principal value is defined according to

$$\mathrm{PV} \int_{-\infty}^{\infty} \frac{dF_0(x)/dx}{x - x_1}\, dx = \lim_{\epsilon \to 0} \left[\int_{-\infty}^{x_1 - \epsilon} \frac{dF_0(x)/dx}{x - x_1}\, dx + \int_{x_1+\epsilon}^{\infty} \frac{dF_0(x)/dx}{x - x_1}\, dx \right] .$$

6.1.3 Keil-Schnell criterion

Although the explicit form of the region of beam stability is different for each distribution function $F_0(x)$, it is essentially centered around the origin of the stability diagram for reasonable distributions. The stability limitation being defined by $\mathrm{Im}\{x_1\} = 0$, as shown for a quartic distribution in Fig. 6.1, is illustrated for different functions $F_0(x)$ in Fig. 6.2 [189, 190, 191]. A common, stable region which is shared by most of the momentum distribution functions is represented by a simple circle (gray shaded area), whose radius can be described by $F \cdot 2/\pi$, where F is a from factor of the order of unity and the circle in Fig. 6.2 has a radius of $2/\pi$. It is important to point out that the tails of the momentum distribution $F_0(x)$ have a significant

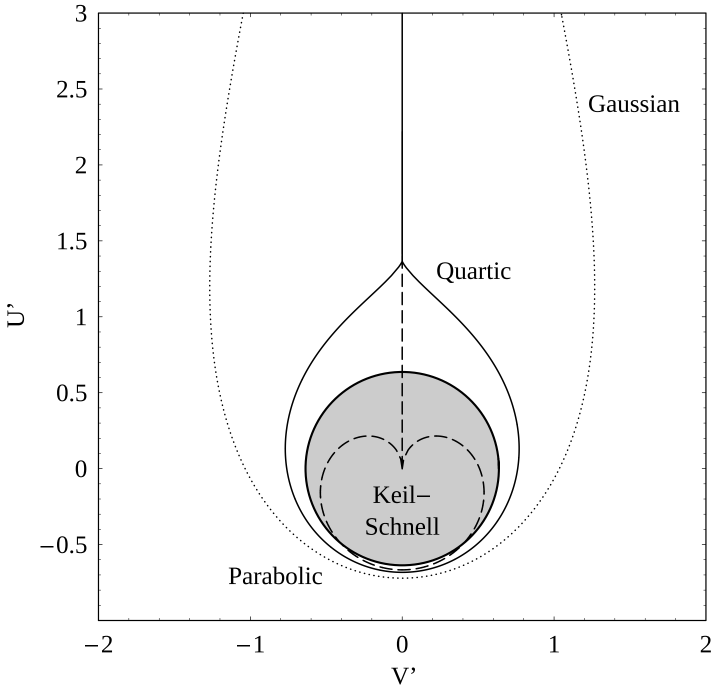

Fig. 6.2: Stability limitation for different momentum distributions in the complex impedance plane. The stable region of a Gaussian beam (dotted) is significantly larger than that of a beam with quartic distribution (continuous). The parabolic distribution shows the smallest area of stability. The gray shaded circle illustrates the stability assumption for the Keil-Schnell criterion.

influence on the longitudinal beam stability. The stability region shrinks for distributions without tails like parabolic or elliptic compared to Gaussian or quartic beams.

By replacing the inverse of the dispersion integral in Eq. (6.11) by the circular approximation leads to a stability limitation for the absolute tolerable impedance, namely [192]

$$\left|\frac{Z_{\|}}{n}\right| \leq F\frac{4E\beta^2|\eta|(\Delta p/p)^2}{eI_0}\,. \tag{6.15}$$

Originally published to estimate the beam stability in the ISR [188], this criterion has been proven to be very useful and is therefore known as Keil-Schnell criterion. In fact, the stability limitation depends inversely on the total beam current, and it is proportional to the square of the momentum spread. Beams with a sharp momentum spread are therefore prone to longitudinal instabilities.

Although the Keil-Schnell criterion has been derived for coasting beams only, its range of validity can be extended by considering the stability criterion as a local condition applied to a local fraction of the beam. If the growth rate of the instability (see Eq. 6.12) is much faster than the synchrotron motion, the external RF forces can be neglected and, as a first estimation, it may even be applied to bunched beams [193, 194, 195]. Consequently, the average beam current I_0 as well as the momentum spread $\Delta p/p$ have to be exchanged by their local values. This effect of a very fast growing bunch excitation is referred to as microwave instability as its presence is accompanied by a bunch signal in the microwave range above several hundred MHz, well above the bunch frequency [196]. It is worth noting that the term microwave instability is also used for several other instabilities having a high frequency bunch signal as its characteristic signature.

6.1.4 Stability of the LHC beam during long and flat bunch collision

By definition, the long and flat bunches or superbunches in collision mode have a region of nearly homogeneous line density with a length of at least some 10 ns. This coasting beam section can be treated as such if the inverse instability growth rate is faster than the drift time of the particles between the two bunch ends and if the coasting beam section is excited at frequencies well above 100 MHz.

The effective threshold impedance according to the Keil-Schnell criterion for coasting beams from Eq. (6.15) is illustrated in Fig. 6.3 for the long and flat bunches and compared to the maximum longitudinal density of nominal and low emittance nominal bunches. The total longitudinal impedance in an accelerator is evaluated by summing up all contributing elements installed in the vacuum chamber, each of which is analyzed by means electromagnetic field calculations for its specific geometry. A complete table of impedance estimations for the contributing elements is given in [197] and the total longitudinal impedance is estimated to $|Z_{\|}/n| = 0.076\,\Omega$.

Compared to the instability thresholds in Fig. 6.3, even the case of a superbunch with a longitudinal density at the beam-beam limit corresponding to a local current of some 131 A is stable with respect to the Keil-Schnell criterion. The limit is found to be around $|Z_{\|}/n| = 0.165\,\Omega$. It is worth noting that the local density of the nominal bunches as well as those of the low emittance nominal bunch has more than one order of magnitude of safety margin.

6.2 Landau damping

The so-called Landau damping is an effect of apparent natural damping which occurs when an ensemble of oscillators with slightly different resonant frequencies is excited by a coherent

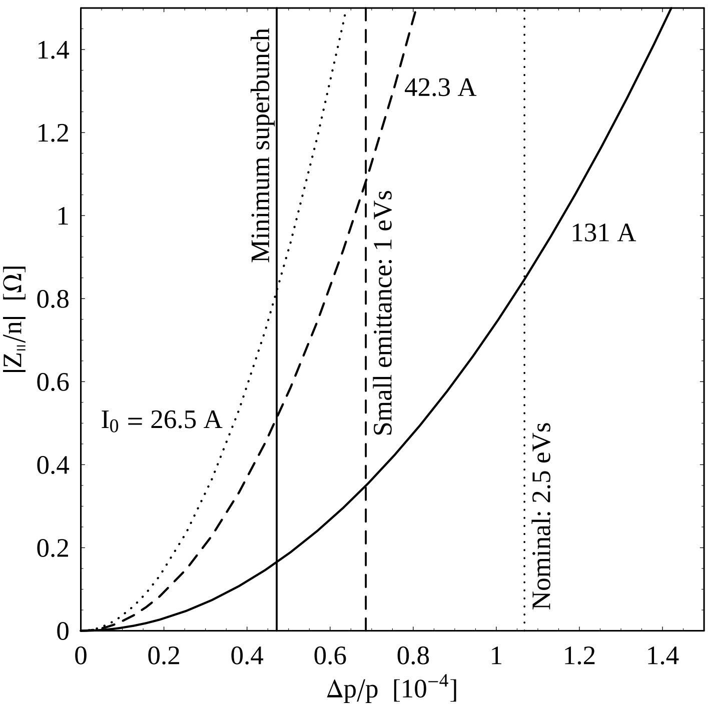

Fig. 6.3: The graphs represent the Keil-Schnell limit of the tolerable, effective longitudinal broad band impedance to preserve the stability of the coasting beam section of a long and flat bunch or a superbunch at collision energy. It is given for a local beam current of 26.5 (dotted), 42.3 (dashed) and 131 A (continuous) which corresponds to the local density of the nominal, the low emittance nominal (see Tab. 5.2 and the minimum emittance long or superbunch (see Tabs. 4.5 and 4.6). The momentum spread as half width half maximum of the corresponding parabolic distribution is indicated by the vertical lines.

signal [198]. In fact, a particle bunch treated in the longitudinal phase space plane is such a system: the individual particles oscillate around the center of gravity of the bunch while their individual oscillation frequencies vary with their maximum phase deviation from the center. This distribution of frequencies is calculated in Sec. 2.2.6 and in App. D. As becomes clear from Fig. 6.4, the beam behaviour of the individual particles depends on the RF configuration, even though the bunch projections might be identical. Therefore, only a small fraction of the particles in a bunch with a large synchrotron frequency spread (Fig. 6.4) are excited by an harmonic excitation, whereas a bunch with a small synchrotron frequency spread may be excited easily as a whole.

Landau damping of the longitudinal dipole motion can be investigated by calculating the average bunch motion from the subset of individual particles within the bunch [199]. The synchrotron oscillation of a single particle driven by a harmonic excitation is described by

$$\ddot{\phi} + \omega_s^2 \phi = e^{-i\omega t}\,, \tag{6.16}$$

where ϕ denotes the phase deviation from the bucket center and ω is the frequency of the driving term. The driving amplitude is arbitrarily normalized to unity. The single particle solution of Eq. (6.16) proportional to the driving term can be written as

$$\phi(t) = \frac{\hat{\phi}}{\omega_s^2 - \omega^2} e^{-i\omega t}\,.$$

The distribution of resonance frequencies of N particles in the bunch is represented by the function $G(\omega) = 1/N\, dN/d\omega_s$ and is normalized so that the integral over all frequencies gives unity. It is worth mentioning that this frequency distribution is also symmetric with respect to negative frequencies: $G(\omega_s) = G(-\omega_s)$. In fact, $G(\omega_s)\, d\omega_s$ is the fraction of individual oscillators having a resonance frequency between ω_s and $\omega_s + d\omega_s$.

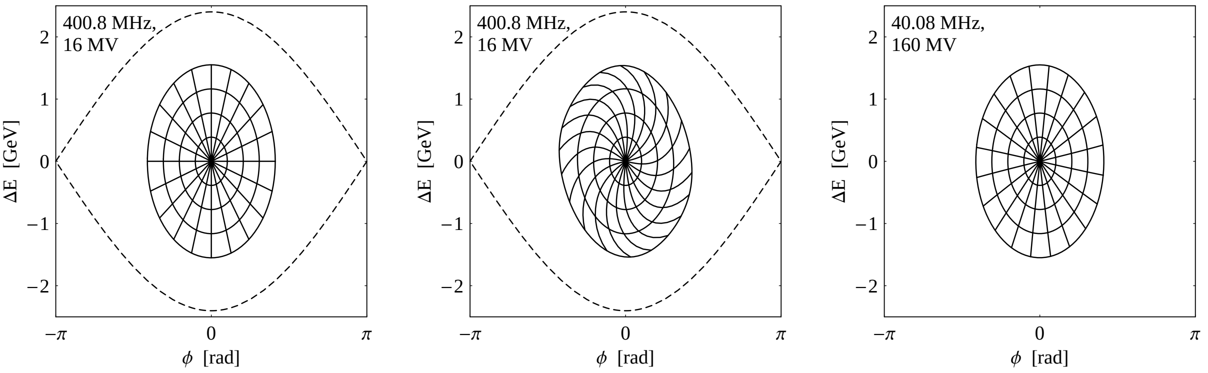

Fig. 6.4: Tracking of particles on a net to illustrate a stationary bunch during one period of the linear synchrotron frequency. The left phase space shows the initial bunch. After one synchrotron period in a 400.8 MHz bucket with an RF voltage of 16 MHz (center) it becomes obvious that the synchrotron frequency in the outer regions of the bunch is reduced. The right phase space shows the same bunch in a matched 40.08 MHz bucket. The separatrix is not visible as it is far away from the bunch. The whole bunch can be considered to be within the linear region of the bucket so that no dispersion is visible. It is important to point out that the RF amplitude of 160 MV has only been chosen as an example to obtain matched bunches under the same conditions as for the 400.8 MHz system.

The average dipole motion of the whole ensemble of oscillators is expressed by

$$<\phi(\omega)>=\left[\int_{-\infty}^{\infty}\frac{G(\omega_s)}{\omega_s^2-\omega^2}\,d\omega_s\right]e^{-i\omega t}\,, \tag{6.17}$$

where the integration over negative frequencies is included for convenience. Part of the integrand can be expanded according to [200, 201]

$$\frac{1}{\omega_s^2-\omega^2}=\frac{1}{2\omega}\left(\frac{1}{\omega_s-\omega}-\frac{1}{\omega_s+\omega}\right)$$

so that the average bunch motion Eq. (6.17) reduces to

$$<\phi(\omega)>=\frac{1}{2\omega}\left[\int_{-\infty}^{\infty}\frac{G(\omega_s)}{\omega_s-\omega}\,d\omega_s-\int_{-\infty}^{\infty}\frac{G(\omega_s)}{\omega_s+\omega}\,d\omega_s\right]e^{-i\omega t}=\left[\frac{1}{\omega}\int_{-\infty}^{\infty}\frac{G(\omega_s)}{\omega_s-\omega}\,d\omega_s\right]e^{-i\omega t}\,. \tag{6.18}$$

The singularity of the integrand at $\omega=\omega_s$ leads to a complex solution of the integral in Eq. 6.18 which can be split into real and imaginary part according to

$$<\phi(\omega)>=\frac{1}{\omega}\left[\mathrm{PV}\int_{-\infty}^{\infty}\frac{G(\omega_s)}{\omega_s-\omega}\pm i\pi G(\omega)\right]e^{-i\omega t}\,, \tag{6.19}$$

where PV is again the principal value excluding the singularity. From the velocity variation of the bunch center, namely

$$\frac{d}{dt}<\phi(\omega)>=-i\omega<\phi(\omega)>=\left[\pi G(\omega)-i\mathrm{PV}\int_{-\infty}^{\infty}\frac{G(\omega_s)}{\omega_s-\omega}\,d\omega_s\right]e^{-i\omega t}\,, \tag{6.20}$$

it becomes clear that the first term is in phase with the initially applied driving term (see Eq. 6.17), whereas the second term always has a phase deviation of $\pi/2$. Therefore, the in phase contribution absorbs energy from the driving force and leads to a virtual damping of the average dipole motion of the bunch. However, only the average motion of the ensemble of oscillating particles is damped and individual particles may be excited enormously. It is interesting to note that the damping term is proportional to the value of the density function at the excitation frequency and that it vanishes once the excitation frequency is outside of the synchrotron frequency spread so that $G(\omega) = 0$. The preservation of Landau damping is therefore mandatory to prevent particle beams from exciting themselves due to self-induced perturbations. Comparing Eq. (6.20) with the dispersion integral Eq. (6.8) for coasting beams reveals that coasting beam stability is based on Landau damping.

6.3 Longitudinal bunched beam stability in the LHC

There are two different classes of longitudinal bunched beam instabilities. On the one hand, single bunch instabilities are based on the excitation of longitudinal oscillations of the particle distribution within the bunch. On the other hand, multi-bunch instabilities arise because of a coupling between different bunches within a batch so that different bunches oscillate in phase with respect to each other. The order of the single bunch oscillation mode is identified by the mode number m whereas the mode along the bunch train of M equal bunches in the accelerator is denoted as $n = 1 \ldots M$ [202]. The phase advance between two bunches is described by $2\pi\, n/M$. Considering that the bunch shape oscillation is in fact a rotation of the perturbed longitudinal distribution with the synchrotron frequency and that the coupled bunches circulate with the revolution frequency, the excitation frequency for all possible modes can be written as

$$\omega = h\omega_0 \pm m\omega_s \pm n\omega_0 = \omega_{\mathrm{RF}} \pm m\omega_s \pm n\omega_0 \,. \tag{6.21}$$

The following analysis of bunched beam stability is limited to equidistant bunches held by single harmonic RF system and is not applicable to the bunches during RF gymnastics, where more RF systems act on the bunches simultaneously.

6.3.1 Bunch shape oscillations

The first six single bunch modes are illustrated in Fig. 6.5. One can observe that the number of nodes in the line density plots corresponds to the mode number. The oscillation frequencies of the modes are directly given by $\omega = m\omega_s$, which becomes obvious considering that a distorted distribution of the mode m just needs to be rotated by $2\pi/m$ to reproduce itself.

6.3.2 Coupled bunch oscillation modes

The second kind of possible oscillations of a bunch train in a circular accelerator are coupled bunch modes. These modes are mostly excited by resonators with a high quality factor, and therefore a narrow bandwidth, which are coupled to the beam. The long time constant of the field decay in the resonators bridges the time distance between two or even more bunches. In fact, the cavity is excited by a bunch passing through and the excited electromagnetic fields act back on the subsequent bunch train. The number of possible oscillation modes is identical to the number of bunches in the accelerator. An illustration of the four longitudinal coupled bunch modes of a bunch train consisting of four bunches is given in Fig. 6.6. For the mode number n the phase position of the M bunches is calculated according to [203]

$$\Delta\phi_i(t) = \Delta\phi_0 \cos\left(\omega t - 2\pi \frac{n}{M} i\right) \,, \tag{6.22}$$

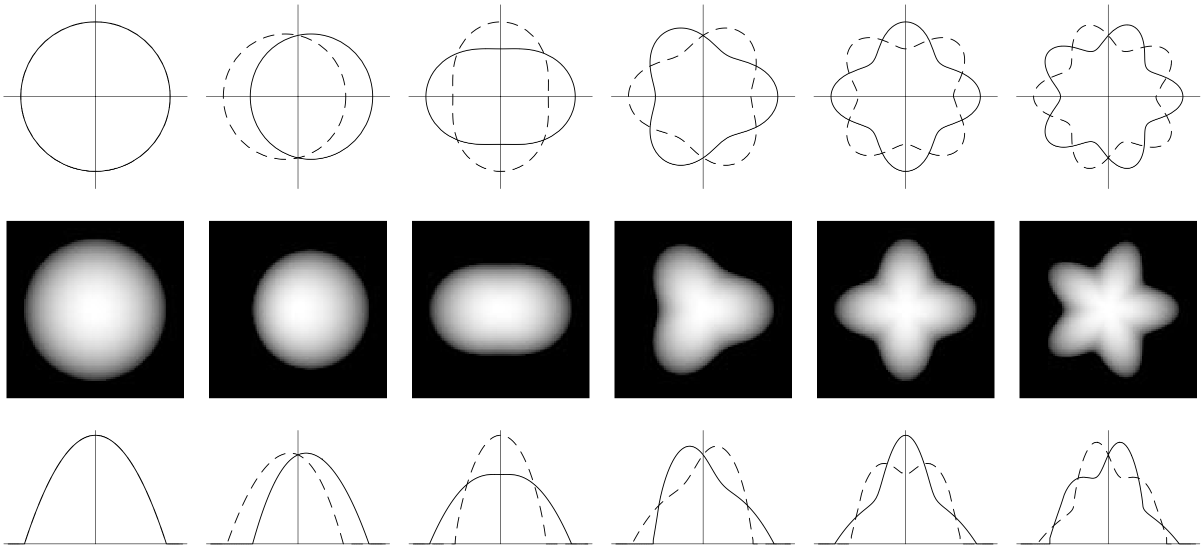

m = 0 m = 1 m = 2 m = 3 m = 4 m = 5

Fig. 6.5: Illustration of the single bunch oscillation modes $m = 0 \dots 5$. Whereas the upper row shows the bunch outline for two different phases of the oscillation, the center row presents the longitudinal distribution assuming parabolic bunches. The resulting line density is sketched in the bottom row. The zeroth mode just results in a stationary parabolic bunch.

where i is the number of the bunch and $\Delta\phi_0$ its maximum phase excursion. The Landau damping time constant of single bunch higher order oscillation modes as well as coupled bunch modes can be larger or smaller as their inverse growth rate resulting in stable, damped or exponentially growing oscillations.

6.3.3 Narrow band resonator impedances

The complex synchrotron tune shift for bunched beams and finally a criterion for the longitudinal stability of bunched beam can be derived similarly to the calculation of the Keil-Schnell criterion for coasting beams as shown in Sec. 6.1. However, adding the synchrotron motion introduces considerable complexity to the calculation so that only the basic ideas shall be given in this report. The full derivations and the underlying theory can be found in [204, 205, 206, 207]. The procedure to derive longitudinal bunched beam instabilities is summarized as follows [208]:

As shown for the case of a coasting beam, a reasonable unperturbed beam distribution is chosen firstly and a small perturbation is added to it. Secondly, the local density $f(\tau, E, z)$ is derived and inserted into the Vlasov equation, wherein the external force due to the synchrotron motion is also taken into account. The ansatz for the perturbed local density function, namely

$$f(\tau, \Delta E, z) = f_0(\tau, \Delta E) + f_1(\tau, \Delta E, z)\,, \tag{6.23}$$

is chosen in such a way that only the perturbed part depends on the longitudinal position z. The unperturbed part is not influenced by the excitation caused by preceding beam particles, however is contributes to the excitation of subsequent beam. It is worth noting that the coordinate system can be defined so that the unperturbed synchrotron motion of the single particles is transformed to circles in a normalized longitudinal phase space. This allows an easy separation

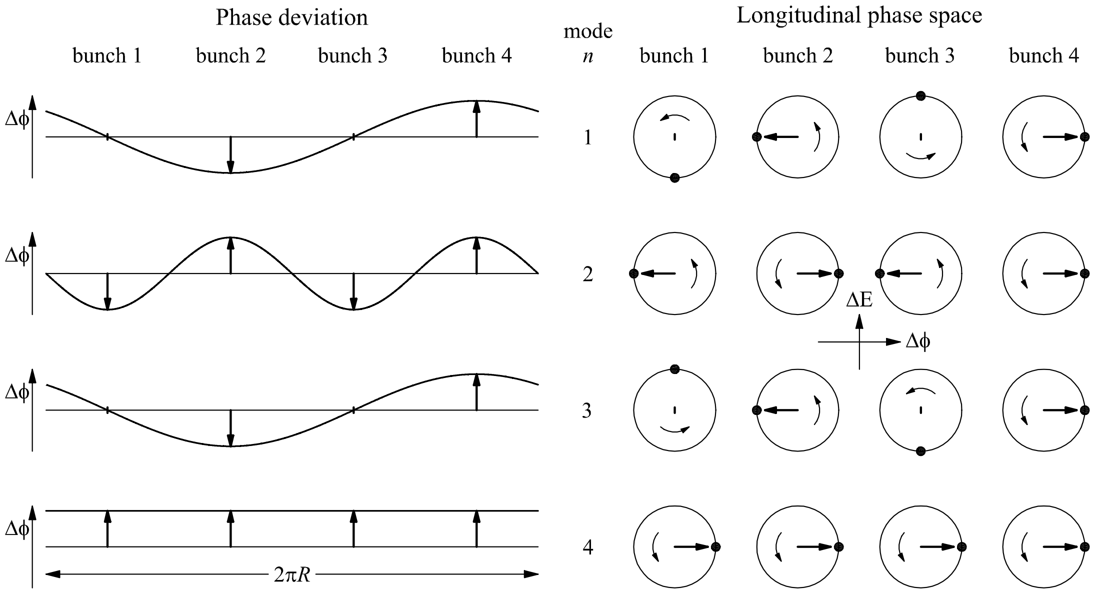

Fig. 6.6: Illustration of the possible coupled bunch modes of four bunches in a circular accelerator. Besides of a phase difference of π, the first and the third mode are identical in this case.

of the radial modes (illustrated in Fig. 6.5), and the local density can be written as

$$f_0(r)\,d\tau\,dE = Ng_0(r)r\,dr\,d\phi \tag{6.24}$$

where $g_0(r)$ is the radial distribution normalized according to

$$\int_0^{2\pi}\int_0^{\infty} g_0(r)r\,dr\,d\phi = 1\,. \tag{6.25}$$

It should be pointed out that the radius is defined in time units $[r] = [\text{time}] = \text{s}$. Finally one ends up with a dispersion relation similar to the dispersion relation of coasting beams but including a general longitudinal force. This force must be expressed in such a way that the influence of preceding on subsequent particles passing through the accelerator is incorporated.

The dispersion relation for a perturbation excited by a narrow band cavity with the shunt impedance R_s at the resonance frequency ω_r can be written as [207]

$$1 = -i\frac{e^2NR_s mM\eta\omega_0^2}{2\pi E\beta^2\omega_s\omega_r}D(\alpha\tau_{\text{sep}})\int_0^{\infty}\frac{dg_0(r)}{dr}\frac{J_m^2(\omega_r r)}{\omega - m\omega_s(r)}\,dr\,, \tag{6.26}$$

where J_m denotes the m-th Bessel function of the first kind. The parameter α represents the inverse filling time $\omega_r/(2Q)$ of the cavity and the function

$$D(\alpha\tau_{\text{sep}}) = -i2\alpha\tau_{\text{sep}}\sum_{k=0}^{\infty}e^{2\pi ikn/M-k(\alpha-i\omega)\tau_{\text{sep}}}\sin(k\omega_r\tau_{\text{sep}})$$

describes the coupling between the bunches and the resonator, taking the bunch spacing field decay within the bunch spacing into account [202]. In case of a small relative synchrotron frequency spread $[\omega_s(r) - \omega_s]/\omega_s \ll 1$, the complex synchrotron frequency shift is expressed by

$$\Delta\omega = \omega - m\omega_s = i\frac{e^2NMR_s\eta\omega_0^2}{8\pi^2E\beta^2\omega_s\hat{\tau}}D(\alpha\tau_{\text{sep}})F_m(2\omega_r\hat{\tau}) \tag{6.27}$$

with

$$F_m(2\omega_r\hat{\tau}) = -\frac{4\pi m\hat{\tau}}{\omega_r}\int_0^\infty \frac{dg_0(r)}{dr} J_m^2(\omega_r r)\,dr\,.$$

The form factor F_m is plotted for a parabolic (left) and quartic (right) distribution in Fig. 6.7. The bunches have a total length of $2\hat{\tau}$. It is worth noting that Eq. (6.27) is consistent with the synchrotron tune shift given in [202].

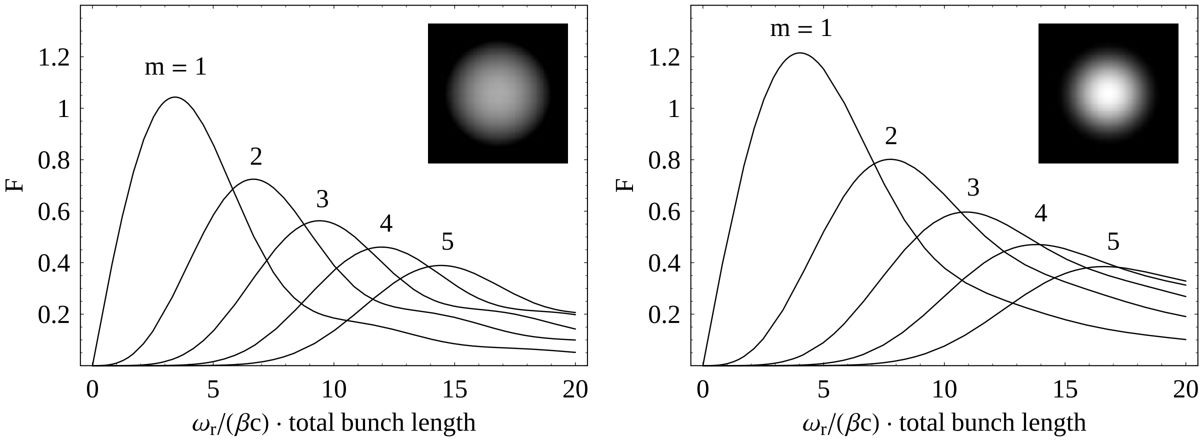

Fig. 6.7: Form factor $F(2\omega_r\hat{\tau})$ for parabolic (left) and quartic (right) radial distribution function $g_0(r)$.

In analogy to the calculations for coasting beam stability a simple stability criterion based on circles in the complex stability diagram can be given from the analysis of the dispersion integral in Eq. (6.26). Landau damping is preserved as long as [202]

$$\frac{1}{\tau} < \frac{\sqrt{m}}{4}\Delta\omega\,, \qquad (6.28)$$

and the excited mode of coupled bunch oscillations remains stable. This means for dipole oscillations that the tune spread in synchrotron frequency should be four times wider than the tune shift due to the narrow band resonance.

For a first estimation of longitudinal stability considering the most sensitive mode, the coupling function $D(\alpha\tau_{\text{sep}})$ can be replaced by its maximum value as illustrated in Fig. 6.8. Clearly, the coupling function becomes small for driving impedances having small field decay durations compared to the bunch frequency. Consequently, a preceding bunch has almost no

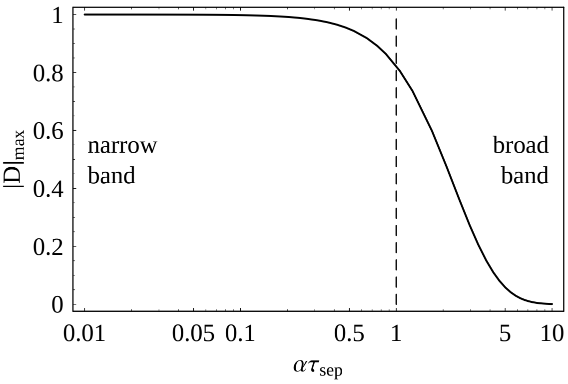

Fig. 6.8: Maximum of the coupling function versus $\alpha\tau_{\text{sep}} = \pi\omega_r/(QM\omega_0)$. The number of equally distributed bunches is defined by M.

influence on the subsequent particles. However, for resonators with a large quality factor, as it is mostly the case for higher order mode resonances of RF cavities or parasitic resonance in metallic objects within the accelerator like pumping slots, the coupling function $D(\alpha\tau_{\mathrm{sep}})$ can be approximated to unity.

Following the stability criterion imposed by Landau damping from Eq. (6.28), the maximum tolerable narrow band impedance is derived considering that the growth rate is defined as the inverse imaginary frequency shift (see Sec. 6.1.2). Landau damping is thus preserved as long as the shunt impedance of the driving resonance fulfills the relation

$$R_s \lesssim \sqrt{m}\frac{U_0 \cos\phi_0 \omega_0}{2I_0}\frac{\hat{\tau}h}{M}\frac{\Delta\omega_s}{\omega_s} \Bigg/ \left[D\left(\frac{\pi\omega_r}{QM\omega_0}\right)F(2\omega_r\hat{\tau})\right] , \tag{6.29}$$

where $I = NMe\omega_0/(2\pi)$ denotes the total beam current, and where M equidistant bunches are assumed. The total bunch length is given by $2\beta c\hat{\tau}$. The azimuthal dipole mode $m = 1$ is most prone to a coupled bunch instability due to a narrow band excitation as the tolerable threshold impedance increases proportionally to $\sqrt{m}$, and also the maximum height of the bunch form factor $F_m(2\omega_r\hat{\tau})$ as shown in Fig. 6.7 decreases with the mode number.

6.3.4 Broad band impedance

In the preceding section, the narrow band resistive impedance driving the coupled bunch instability is assumed to be the only impedance present in the accelerator. However, in real machines a so-called broad band impedance, which is in fact the contribution of all components, like bellows, monitors or kicker magnets seen by the beam, is modeled as broad band resonance. This broad band resonator directly has a negligible effect on the coupled bunch instabilities, as the fields in this virtual resonator decay much faster than the bunch spacing (see Fig. 6.8). However, it contributes to the synchrotron tune shifts, displacing them in such a way that Landau damping can be lost for coupled bunch modes which would be well damped according to Eq. (6.28) neglecting the broad band impedance.

Following the analysis in [205, 206], the absolute tune shift due to the longitudinal broad band impedance can be written as

$$\Delta\omega = -i\frac{\pi^3 I_0}{3\hat{\tau}^3\omega_0^3 U_0\cos\phi_0}\frac{1}{Mh}\frac{m\omega_s}{m+1}\underbrace{\sum_{p=-\infty}^{\infty}\frac{Z(p)}{p}h_{\mathrm{mm}}(p)\Bigg/\sum_{p=-\infty}^{\infty}h_{\mathrm{mm}}(p)}_{(Z_{\|}/n)_{\mathrm{eff}}} , \tag{6.30}$$

where the coefficients $h_{\mathrm{mm}}(p)$ denote the relative spectral power of the bunches at the frequency $p\omega_0$. It is convenient to define an effective longitudinal impedance $(Z_{\|}/n)_{\mathrm{eff}}$ including the spectral distribution [209]. Landau damping for the m-th mode is preserved as long as

$$\frac{1}{\tau} = -\mathrm{Im}\{\Delta\omega\} < \frac{1}{2}\frac{m}{m+1}\Delta\omega_s .$$

It is worth noting that longitudinal coupled bunch modes are driven by the imaginary part of the effective impedance only. The threshold impedance can be derived by inserting Eq. (6.30) into the criterion for Landau damping, namely[2]

$$\left(\frac{\mathrm{Im}\{Z_{\|}\}}{n}\right)_{\mathrm{eff}} \lesssim \frac{3}{2\pi^2}\frac{Mh^3U_0\cos\phi_0}{I_0}\frac{\Delta\omega_s}{\omega_s}\hat{\tau}^3\omega_0^3 . \tag{6.31}$$

---

[2] A different derivation of the criterion finally ends up with the same result as Eq. (6.31) for $\pi \simeq 3$ [210].

It should be pointed out that the instability threshold criteria for longitudinal narrow as well as broad band impedances are, due to the formulation of the Landau damping criterion, proportional to the synchrotron frequency spread of the bunch. An artificial increase of the spread normally results in improved bunched beam stability.

6.3.5 Stability of the LHC beam during long and flat bunch scheme

The longitudinal stability of the nominal LHC beam during injection flat-bottom, acceleration and collision mode held by the superconducting RF system operated at 400.8 MHz has been analyzed in detail by several authors [209, 211, 212, 213, 214, 215, 216]. Basically, the stability criteria introduced above have been applied to the relevant beam parameters. However, during the RF manipulation at injection and collision energy, multiple RF harmonics act on the beam simultaneously and the criteria are not strictly valid anymore. They may only give a first estimation of stability as the bunches are held by a single harmonic RF in between the substeps of the batch combination scheme.

The longitudinal stability during the long and flat bunch generation scheme presented in Chapter 5, as well as during acceleration of partly combined bunches with a 40.08 MHz RF system, is estimated in this section.

The longitudinal beam parameters during acceleration in the LHC are derived on the basis of the realistic magnetic cycle [217] of the LHC dipole magnets, which is assumed to remain unchanged with respect to the nominal scheme. The magnetic dipole induction corresponding to the particle energy and its first derivative are sketched in Fig. 6.9. The ramp rate is varied smoothly at the beginning as well as at the end of the acceleration. The maximum ramp rate of 7.3 mT/s is limited by the voltage capabilities of the main power converters. It is important to point out that the average energy gain of the particles during acceleration does not exceed 485 keV/turn.

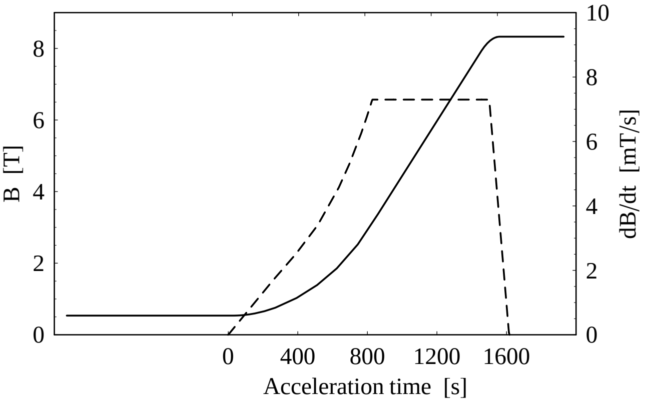

Fig. 6.9: Magnetic cycle of the LHC dipole magnets during acceleration (continuous). The first derivative is shown as a dashed line.

Fig. 6.10 shows the longitudinal emittance development during the cycle according to Tab. 5.6 as well as the available bucket area. The bucket area during acceleration is presented for a constant RF amplitude of 3 MV throughout the cycle. In fact, $2 \cdot 1.5$ MV would be available in a scheme where 16 bunches are combined to one long and flat bunch. At the injection flat-bottom, a linear increase from about 1 eVs to the emittance of the combined bunches of 12.9 eVs is assumed for simplicity. During this linear increase, the time scale in Fig. 6.10 has no validity, as the combination scheme is performed within one minute, too fast to be visible in the plot. Furthermore, the longitudinal emittance does not increase linearly due to the re-combination of bunches but rather stepwise with each bunch pair merging.

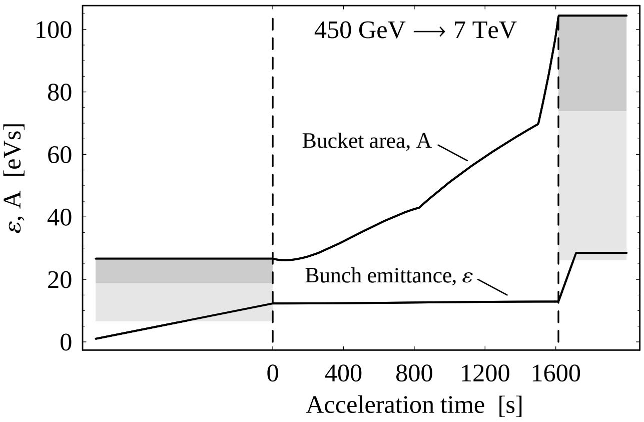

Fig. 6.10: Bucket area (upper curve) and bunch emittance (lower curve) during the LHC acceleration cycle including the combination scheme of 16 initial bunches to a long and flat bunch. The area shaded in dark gray represents possible bucket areas at 40.08 MHz ($h = 3564$) for an RF amplitude between 1.5 and 3 MV. The light gray shaded area below shows the bucket area for 1.5 MV RF voltage in the frequency range from 40.08 to 80.16 MHz that means during the combination RF gymnastics (see also Fig. 5.10).

The qualitative behaviour of bucket area and beam emittance of the second long and flat bunch option combining 32 bunches is equivalent to the graphs shown in Fig. 6.10. The quadrupled RF voltage of 2·6 MV results in twice the bucket area, and the longitudinal beam emittance is assumed to grow to some 26 eVs; twice the bunch emittance of the 16 bunch scheme due to the further bunch merging at flat-bottom. At collision energy one also finally ends up with twice the bunch emittance. It is however worth mentioning that the filling factor, the ratio between bunch emittance and bucket area, remains constant for the 16 and the 32 bunch combination option.

Tolerable narrow band impedance

For a worst-case estimation of the tolerable resonator impedances to preserve Landau damping of coupled bunches bunch modes in the LHC, the form factors in Eq. (6.29) can be substituted by their maximum values: according to Figs. 6.8 and 6.7 the coupling function $D(\pi\omega_r/[QM\omega_0])$ is set to unity and the form factor $F(2\omega_r\hat{\tau})$ is approximated to 1.05 for the dipole mode $m = 1$.

Evaluating Eq. (6.29) according to these simplifications, and with respect to the set of beam parameters introduced above, results in the development of the impedance threshold during the LHC cycle as plotted in Fig. 6.11. Even though the bunch intensity was assumed to be only $1.15 \cdot 10^{11}$ ppb, the minimum threshold impedance is more than an order of magnitude below the threshold for operation with the 400.8 MHz RF system [212]. In fact, two problematic regions can be determined: firstly, during injection, when the bunches with a small emittance are injected to the huge buckets at 40.08 MHz. Secondly, when approaching the collision energy

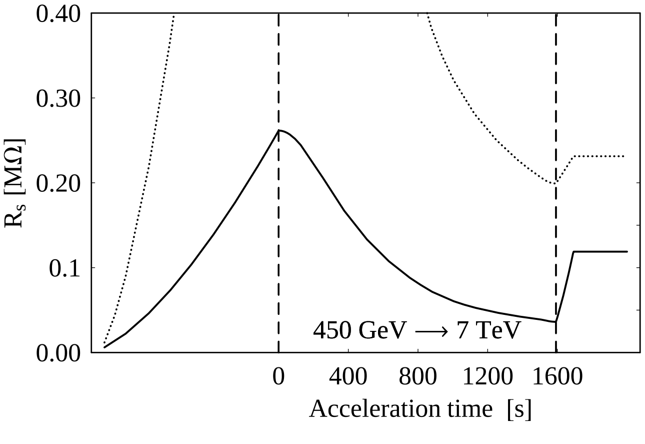

Fig. 6.11: Worst case estimation of the tolerable narrow band impedance along the LHC cycle for a constant RF amplitude of 3 MV at 40.08 MHz (16 bunch scheme, continuous) and $4 \cdot 3$ MV (32 bunch scheme, dotted). The initial bunch intensity is assumed to be nominal in both cases: $1.15 \cdot 10^{11}$ ppb. The stability criteria can be only applied rigorously during acceleration, as multiple harmonic RF systems act on the beam otherwise.

due to the energy dependence of the threshold impedance. A potential cure for the former is proposed in Sec. 6.3.6. Analyzing the scaling of the threshold impedance indicates the main reason for the severe stability limitations of the beam held by a 40.08 MHz RF system. For energies well above transition, so that the phase slip factor η remains constant and for ultra-relativistic beams, it scales according to

$$R_s \propto \frac{\varepsilon_l^{3/2} h^{9/4} U_0^{1/4}}{E^{3/4}} \propto U_0 \left(\frac{\varepsilon_l}{A}\right)^2 ,$$

where ε_l/A denotes the bucket filling factor. Consequently the bunches are prone to become unstable if the buckets are sparsely filled. This is the case for the tiny bunches at injection and at the end of the acceleration, when the bucket area increases proportional to $\sqrt{E}$ times the area reduction factor due to the non-zero synchronous phase (see 2.2.5). Furthermore, the threshold scales as $h^{9/4}U^{1/4}$ so that higher harmonics of the revolution frequency are preferable to hold and accelerate low longitudinal emittance bunches.

Tolerable broad band impedance

A similar analysis can be performed to estimate the threshold of the longitudinal broad band impedance as derived in Eq. (6.31). Fig. 6.12 shows this threshold $(\mathrm{Im}\{Z_\parallel\}/n)_{\mathrm{eff}}$ along the acceleration cycle. The graph looks qualitatively similar to the narrow band impedance limitation as illustrated in Fig. 6.11. The problematic phases can again be identified during injection and at the end of the injection cycle. The former region during injection would impose a severe limitation of $(\mathrm{Im}\{Z_\parallel\}/n)_{\mathrm{eff}} \simeq 0.0058\,\Omega$ for the nominal bunch intensity to the tolerable broad band impedance so that bunches would certainly become unstable without counter measures. As soon as the longitudinal emittance increases during the combination procedure, the threshold stays well above the estimated broad band impedance of $0.076\,\Omega$ in the LHC. The scaling of the threshold impedance can be written as

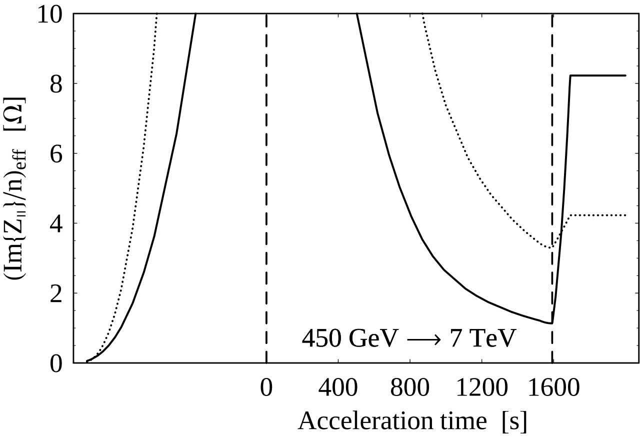

Fig. 6.12: Worst case estimation of the tolerable broad band impedance along the LHC cycle for a constant RF amplitude of 3 MV at 40.08 MHz (16 bunch scheme, continuous) and 4 · 3 MV (32 bunch scheme, dotted). The bunch intensity is assumed to be nominal.

$$\left(\frac{\mathrm{Im}\{Z_\parallel\}}{n}\right)_{\mathrm{eff}} \propto \frac{\varepsilon_l^{5/2} h^{7/4}}{E^{5/4} U_0^{1/4}} \propto \frac{U_0}{h^2} \left(\frac{\varepsilon_l}{A}\right)^{5/2} ,$$

wherein the strong dependence on the bucket filling factor becomes apparent. Furthermore, the threshold decreases rapidly with growing beam energy.

The reduced threshold is partly attributed to the small synchrotron frequency spread of low emittance bunches in large RF buckets. Applying means to increase the synchrotron frequency spread avoiding unreasonable blow-up, the longitudinal emittance improves the stability threshold for broad band as well as for narrow band impedances directly proportionally (see Eqs. 6.29 and 6.31). This counter measure is discussed in the subsequent section.

The installation of an additional RF system to capture and hold the beam during the filling procedure of the LHC rings could be envisaged as a second counter measure; e.g. a capture RF system operated at 200.4 MHz in the LHC has already been considered and designed [218] up to the construction of the required normal conducting cavities, but has been finally postponed [219, 220]. This system would be potentially available for the upgrade. Filling the two LHC rings by injecting into 200.4 MHz bucket would provide stable beams until the hand-over to the 40.08 MHz RF system. The bunch combination scheme to generate long and flat bunches could commence immediately and the sojourn time of the small emittance bunches in the large buckets could be reduced to the order of a few seconds. This might be sufficient if the instability cannot grow fast enough during this period.

6.3.6 Increase of the synchrotron frequency spread

Both narrow band and broad threshold impedances for longitudinal bunched beam stability are directly proportional to the relative spread of the synchrotron frequencies within the bunch. In the case of bunches in stationary buckets (see Eq. 2.43), the relative synchrotron frequency spread in the single harmonic RF system is expressed in terms of the longitudinal emittance ϵ_l as

$$\frac{\Delta\omega_s}{\omega_s} = \frac{1}{16}\sqrt{\frac{2|\eta|\omega_0^2 h^3}{\pi E\beta^2 eU_0}} \cdot \varepsilon_l \,, \tag{6.32}$$

where the emittance is given in units of $\mathrm{eV} \cdot s$. In fact, decreasing the RF harmonic by one order of magnitude from $h = 35640$ to 3564, as proposed for the long and flat bunch generation scheme, and decreasing the RF voltage by a factor of approximately another order of magnitude, reduces the synchrotron frequency spread by a factor of ten. This results in an unstable beam during the generation of long and flat bunches. Inserting the stationary bucket area into Eq. (6.32) reduces it to $\Delta\omega_s/\omega_s = 1/\sqrt{\pi} \cdot \varepsilon_l/A_{\mathrm{eVs}}$ so that the spread is actually proportional to the relative filling factor of the bucket. Consequently, the synchrotron frequency spread of bunches in 40.08 MHz buckets is lowest during the injection of the small bunches from the SPS, where the bucket area is large compared to the tiny bunch emittance in the range of 1 eVs. After the combination of several of these bunches, the situation becomes less critical. Adding some higher harmonic RF amplitude is a well known technique to increase the synchrotron frequency spread of a bunch [168, 169], which shall be analyzed in what follows.

Synchrotron frequency spread including a higher harmonic RF system

For an arbitrary RF amplitude function, the synchrotron frequency of a particle oscillating on a closed trajectory can be written in integral form according to Eq. (2.41), and analytic approximations for a stationary as well as for an accelerating harmonic bucket are given in Sec. 2.2.6 and App. D.

The influence of increasing the synchrotron frequency spread of the low emittance bunches to the large RF buckets at 40.08 MHz can be analyzed numerically. The following assumptions for the higher harmonic RF system have been made: firstly, the synchrotron frequency spread of a 1 eVs bunch should be increased by at least one order of magnitude. Secondly, the higher harmonic RF systems should be compatible with the RF manipulations so that it can stay active also during the first combination steps of the long and flat bunch generation procedure. This implies that the increase in synchrotron frequency must be sufficient for any phase relation between main RF focusing. The longitudinal emittance dilution due to the additional RF system should be below 25 % to keep the degradation of the longitudinal beam quality within reasonable limits.

The frequency of the higher harmonic has be chosen so that it results in a significant slope variation of the effective RF focusing along the bunch. Considering that the initial bunch length in the LHC is of the order of 4 ns, the use of 200.4 MHz and 400.8 MHz is investigated. The relative synchrotron frequency versus single particle emittance is plotted in Figs. 6.13 and 6.14. It is interesting to note that the influence on particles with a certain emittance is compensated so that they oscillate with the single harmonic synchrotron frequency, unaffected by the phase of the higher harmonic RF.

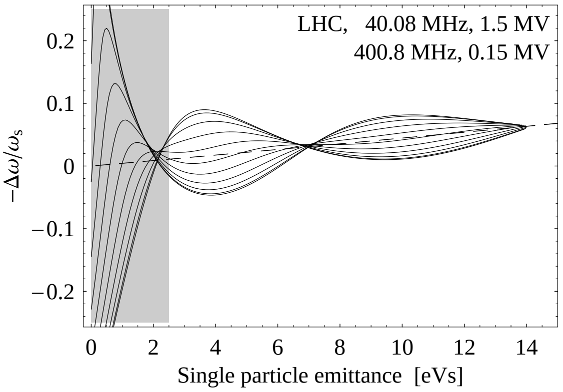

Fig. 6.13: Relative synchrotron frequency deviation versus single particle emittance for a combination of 40.08 and 400.8 MHz RF amplitude in the LHC at injection flat-bottom. The ensemble of continuous curves is calculated for phase relations between the two RF systems, varying from 0 to π in steps of $\pi/10$. The dashed line shows the unperturbed relative synchrotron frequency of the 40.08 MHz RF system alone.

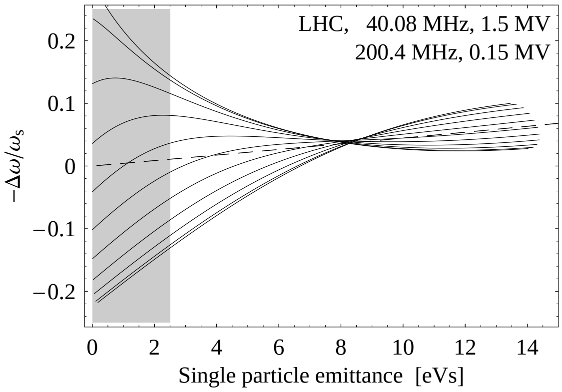

Fig. 6.14: Same representation as in Fig. 6.13 but for the combination of 40.08 and 200.4 MHz. The relative spread for bunches with an emittance smaller than 1.5 eVs is significantly reduced compared to the higher harmonic RF system operated at twice 200.4 MHz. The gray shaded area represents the nominal bunch emittance.

As shown in Fig. 6.13, only some 150 kV at 400.8 MHz would suffice to restore a relative synchrotron frequency spread comparable to $\Delta\omega_s/\omega_s = 0.1$ of the nominal LHC bunch. However, the large frequency ratio between the main and the higher harmonic system is mandatory to obtain large synchrotron frequency spreads within small bunches, independent from the phase relationship of the two RF amplitudes (see Fig. 6.13). It is important to point out that the superconducting 400.8 MHz RF installations cannot be employed directly as higher harmonic RF system. Due to their large shunt impedance, the beam induces too much voltage in the eight cavities to control the RF amplitude down the level of 150 kV (see Sec. 6.5).

Emittance blow-up

Following the analysis in the preceding section, the synchrotron frequency spread of small bunches in large buckets can be increased significantly by adding some higher harmonic RF voltage to the main bucket. However, bunches with in elliptic boundary injected to such a double harmonic RF system are not perfectly matched anymore, resulting in emittance blow-up depending on the frequency and the amplitude of the higher harmonic system. After some initial emittance dilution, the bunch matches itself to the perturbed trajectories of the bunch so that virtually no further emittance increase is expected after a few periods of the synchrotron frequency.

The emittance blow-up of a bunch held in a 40.08 MHz bucket caused by some RF voltage at 400.8 MHz is presented in Fig. 6.15. It can be obtained by tracking a parabolic bunch with an initial elliptic contour under the influence of the two RF systems. The emittance dilution increases proportionally to voltage at 400.8 MHz and up to some 0.5 MV it remains well below 25 %. Under these conditions, it is therefore justified to assume an increase of the synchrotron frequency spread by one order of magnitude for the longitudinal stabilization at the cost of some 25 % in emittance (see Tab. 5.6).

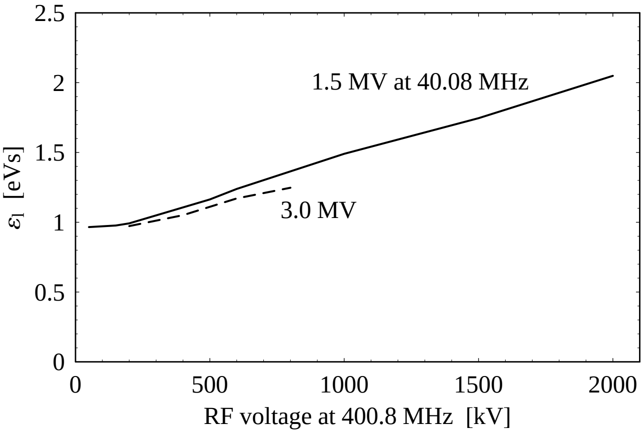

Fig. 6.15: Blow-up after full dilution of a parabolic bunch injected into a double harmonic RF system 40.08/400.8 MHz, where the higher harmonic RF amplitude increases the spread of synchrotron frequencies within the bunch. The main RF voltage is set to 1.5 and 3 MV.

Non-harmonic RF system

Up to now the ratio of fundamental and higher harmonic RF system has been assumed to be whole numbered so that both contributions to the RF buckets are symmetric to the reference energy. Setting the higher harmonic system to a non-integer harmonic shifts the energy of the sub-buckets with respect to the average beam energy in the main RF buckets. In fact, the frequency offset causes a phase slippage of main and sub-bucket, leading to a continuous variation of the local synchrotron frequency within the bunch.

However, as can be seen in Fig. 6.16, the application of such a scheme can introduce parametric resonances due to the phase slippage of the higher harmonic RF system, which moves in the same direction as individual particles in spheres of influence of the off-energy sub-buckets.

Tracking calculations like the example above show that the development of the effective longitudinal emittance is very sensitive to energy offset and amplitude of the higher harmonic. During batch compression, the RF focusing of the individual bunches varies along the batch so that also the coupling between main and higher harmonic RF system changes continuously. Therefore, such a scheme cannot be applied straightforward in combination with the long and flat bunch generation scheme in the LHC.

6.4 Synchrotron frequency distribution with respect to RF phase stability in long bunch collision mode

The synchrotron frequency distribution during storage of the final long bunches in bucket generated by multiple RF harmonics is of special interest as the bunches are stored in this mode for

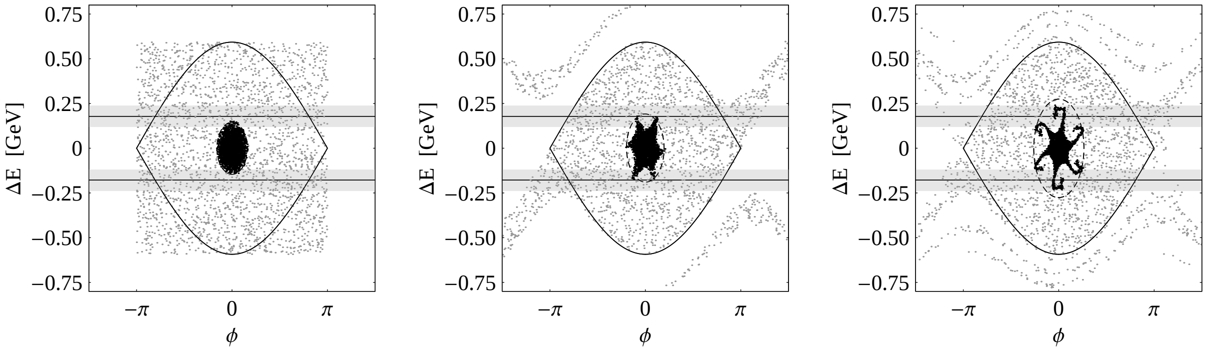

Fig. 6.16: Development of a 1 eVs bunch held by an RF voltage of 1.5 MV at 40.08 MHz under the influence of two additional higher harmonic RF systems at 400.8 MHz. The higher harmonic RF systems have an amplitude of some 150 kV. They are operated symmetrically slightly below and above the integer harmonic. Their center energy is indicated by the continuous horizontal lines, and their bucket height is illustrated as gray stripes. The gray shaded macro-particles are tracked for reference only. The dashed emittance ellipse contains 99 % of the particles. The phase space on the left shows the initial phase space while center and right plot illustrate the bunch after 0.64 and 2.1 periods of the synchrotron frequency.

several hours. Studies in the SPS with bunches held by a double harmonic RF bucket generated by the 200 and 800 MHz have shown that the phase stability between both RF systems must be kept within tight tolerances if the bunches should be stretched [168].

The synchrotron frequency distribution for the final long bunches held by two, three and four multiples of 40.08 MHz is illustrated in Fig. 6.17. The synchrotron frequencies of particles with

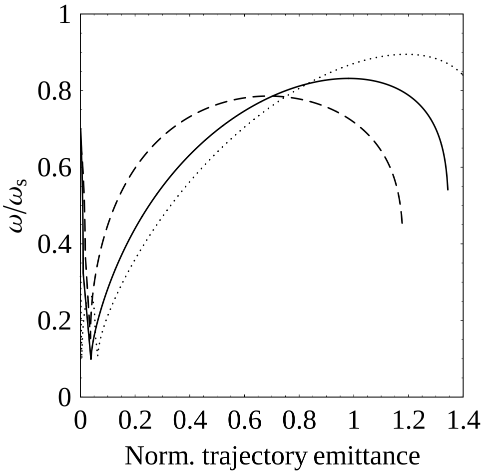

Fig. 6.17: Relative synchrotron frequency versus single particle emittance normalized to bucket area of the single harmonic bucket for the voltage ratios given in Tab. 4.3. The distribution for three RF harmonics is represented by the continuous line while dashed and dotted lines show the case for two and four RF harmonics. The phase relation between the different harmonics is assumed to be ideal.

large oscillation amplitudes are very similar to those of an ideal barrier bucket (see Fig. 2.12, graph for $\phi_0 = 0$). However, few particles in the bunch center may be captured in the sub-buckets so that their synchrotron frequency increases. This effect causes the increase of the synchrotron frequency distribution for small single particle emittances.

The phase relation between different RF systems is not perfectly defined in a real accelerator environment. Transient beam loading due to gaps in the bunch pattern of the LHC may cause small phase variations from bucket to bucket. The effect of such phase variations on the synchrotron frequency distribution for a bunch held by three RF harmonics is presented in Figs. 6.18 and 6.19. The lowest curves are consistent with the continuous line shown

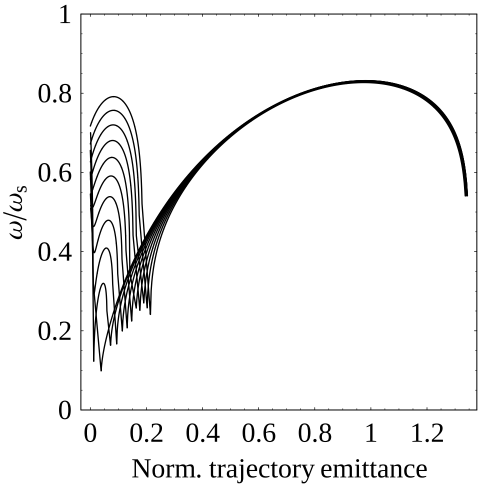

Fig. 6.18: Ensemble of frequency distributions versus single particle emittance normalized to the single harmonic bucket area in a three harmonic RF system according to Tab. 4.3. The phase of the two RF systems at $h = 3564$ and $h = 10692$ is kept constant, while the phase of the harmonic $h = 7128$ is varied up to 20^0 from its ideal value in steps of 2^0.

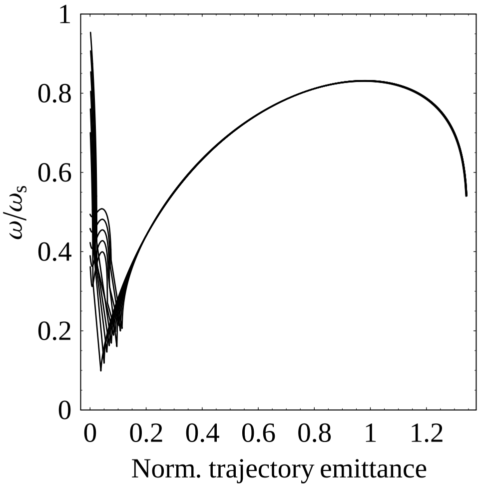

Fig. 6.19: Same representation as in Fig. 6.18 but for the variation of the third harmonic at $h = 10692$ while the phase relation between $h = 3564$ and $h = 7128$ is kept constant. The distributions are calculated for the phase of largest bucket height. The phase units are defined with respect to the RF harmonic whose phase is varied.

in Fig. 6.17. For the phase shift under consideration the synchrotron frequency distribution changes significantly for particles in the center of the bunch. For particles in the outer regions with a normalized single particle emittance above 0.2, the phase deviations between the different RF harmonics are not critical in this case.

6.5 Beam loading

As discussed above, the bunches in an accelerator can communicate via narrow band impedances, which may cause excitation of coupled bunch modes. Not only the succeeding bunches suffer from the field induced by particles before them, but also the element representing the impedance, mostly a cavity, is obviously influenced and this phenomenon is called beam loading. As the RF cavities couple the beam to an RF power source, their impedance is intentionally made as large as possible and they are thus most prone to beam induced voltage.

In fact, there are two resulting effects: firstly, the cavity is detuned by a long chain of equal bunches and secondly, transient RF voltages may be induced by an asymmetric bunch pattern including gaps or intensity variations from bunch to bunch. After comparing the effect of stationary beam loading in the LHC for the 400.8 MHz and a 40.08 MHz RF system under basic assumptions, calculations on transient beam loading during generation and storage of long and flat bunches in the LHC shall be presented. It is shown that the transient voltages in the superconducting 400.8 MHz cavities cannot be suppressed effectively enough so that the RF manipulation to generate long and flat bunches would be severely deteriorated. Consequently, the superconducting RF system must be removed for the LHC operation with long bunches.

6.5.1 Stationary beam loading: steady state

Neglecting transients due to gaps in the bunch pattern or intensity variations of the individual bunches, a simple RF system, consisting of an RF amplifier as power generator and the cavity to couple the RF power to the beam (Fig. 6.20), can be represented as sketched in Fig. 6.21 by a circuit of lumped elements to model its behaviour. As the large stored energy of a high intensity beam can create enormous instantaneous RF power compared to the capabilities of the power amplifier, it is approximated as a pure current generator. The cavity is replaced by its parallel resonant circuit and the power generator by a current source having a finite internal resistance. It is important to point out that its internal resistance is already converted by the transformation ratio of the coupling system in the lumped element circuit in Fig. 6.21 .

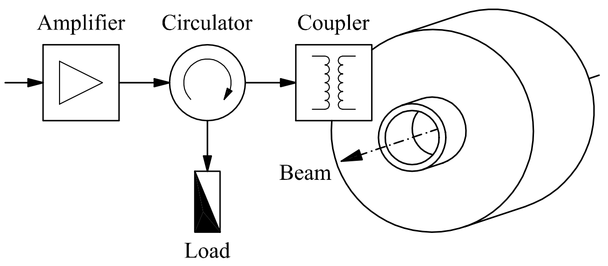

Fig. 6.20: Simple RF system consisting of an RF amplifier protected by a circulator and an RF cavity. The coupler matches the high impedance of the cavity to the low impedance of the amplifier.

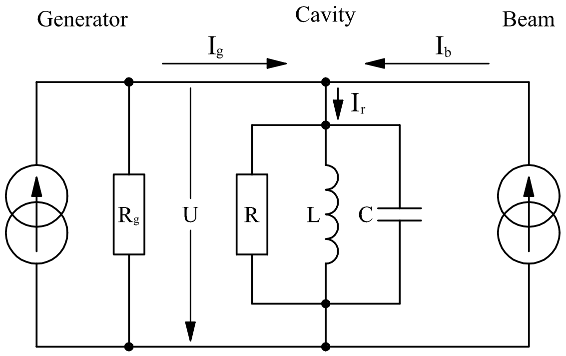

Fig. 6.21: The right part of Fig. 6.20 sketched as a lumped element circuit. The coupler is already included in the generator impedance R_g [221].

To optimize the effective generator power needed to drive the beam, the generator current must be decomposed into a forward component I_g^+, flowing from the generator to the cavity, and a reflected component I_g^- in the opposite direction. Minimizing the reflected power $P_g^- = 1/2R|I_g^-|$ back to generator assures that most of its power drives the combination of cavity and beam.

In the following analysis all voltages and currents are assumed to oscillate with the excitation frequency ω defined by the generator. According to Fig. 6.21 the relation between currents is expressed by

$$I_g + I_b - I_r = 0 \qquad \text{or} \qquad I_g^+ - I_g^- + I_b - I_r = 0\,.$$

Application of Ohm's law to the generator as well as to the resonant circuit, assuming that its resonant frequency is given by $\omega_0^2 = 1/(LC)$ and the loss resistor is large so that the resonant circuit has a small bandwidth compared to ω_0, the current relation can be written as [222]

$$2I_g^+ + I_b = \left[\left(\frac{1}{R} + \frac{1}{R_g}\right) + 2i\Delta\omega\, C\right] U\,, \tag{6.33}$$

where $\Delta\omega = \omega - \omega_0$ denotes the frequency difference between generator and resonant frequency of the lumped element resonator. The lumped elements L and C still have to be exchanged by their equivalent cavity parameters, the resonant frequency ω_0 and the so-called R/Q, a geometrical parameter of the cavity, namely

$$C = \frac{1}{\omega_0 (R/Q)} \qquad \text{and} \qquad L = \frac{(R/Q)}{\omega_0}\,.$$

Eq. (6.33) is thus transformed to

$$2I_g^+ + I_b = \left[\left(\frac{1}{Q_0} + \frac{1}{Q_g}\right) + 2i\frac{\Delta\omega}{\omega_0}\right]\frac{U}{(R/Q)}\,, \tag{6.34}$$

where Q_0 and Q_g are defined to give the resonator shunt impedance R and the internal resistance of the generator R_g respectively, when multiplied by the geometry parameter R/Q.

Keeping in mind that all current and voltage vectors rotate in the complex plane, the current phase ψ is chosen so that the center phase of the bunch coincides with a real voltage at the synchronous phase ϕ_0:

$$Ue^{i\omega t} \quad \longleftrightarrow \quad I_b e^{i\omega t} e^{i\psi} \tag{6.35}$$

$$Ue^{i\omega t}\sin\phi_0 = Ue^{i\omega t}(\cos\psi - i\sin\psi) \quad \longleftrightarrow \quad I_b e^{i\omega t}\,. \tag{6.36}$$

The current phase is determined by the relation $\sin\phi_0 = \cos\psi$ so that the current can be written as $I_b = |I_b|(\sin\phi_0 + i\cos\phi_0)$. It is worth noting that the synchronous phase at constant energy is defined as $\phi_0 = 0$ below and $\phi_0 = \pi$ above transition. Additionally, I_b denotes the Fourier component of the beam current at the RF frequency as this spectral line represents the only component which can excite the narrow band impedance. Its absolute value may be replaced by $2I_0 f_b$, where the form factor f_b becomes unity for infinitely short bunches and decreases with increasing bunch length.

Finally, the forward and reflected generator currents are expressed by [223]

$$I_g^+ = \left\{\left[\frac{1}{Q_g} + \frac{1}{Q_0}\right]\frac{U}{2(R/Q)} - I_0 f_b \sin\phi_0\right\} + i\left[\frac{\Delta\omega}{\omega_0}\frac{U}{(R/Q)} - I_0 f_b\cos\phi_0\right]\,, \tag{6.37}$$

$$I_g^- = \left\{\left[\frac{1}{Q_g} - \frac{1}{Q_0}\right]\frac{U}{2(R/Q)} + I_0 f_b \sin\phi_0\right\} - i\left[\frac{\Delta\omega}{\omega_0}\frac{U}{(R/Q)} - I_0 f_b\cos\phi_0\right]\,, \tag{6.38}$$

and the RF power reflected back to the generator is now derivated easily according to $P_g^- = 1/2(R/Q)Q_g|I_r^-|^2$. In fact, there are two parameters to reduce the reflected power: the detuning $\Delta\omega$ of the cavity and the external load Q_g of the generator. The former acts on the imaginary part of the generator current and the latter on its real one so that the conditions for minimum RF power requirements can be written as

$$\frac{\Delta\omega}{\omega} = -\frac{I_0 f_b\cos\phi_0(R/Q)}{U} \qquad \text{and} \qquad \frac{1}{Q_g} = \frac{2(R/Q)I_0 f_b\sin\phi_0}{U} - \frac{1}{Q_0}\,. \tag{6.39}$$

It is interesting to note that both the optimum detuning as well as the optimum generator Q_g depend on beam current and RF voltage. It is thus desirable to operate the RF system with variable power couplers as foreseen for the superconducting RF system in the LHC [224].

As the superconducting resonators have an unloaded Q_0 in the order of 10^9 being much larger than the external generator Q_g, the second condition reduces to

$$Q_g = \frac{U}{2(R/Q)I_0 f_b\sin\phi_0}\,.$$

In case of constant particle energy so that the synchronous phase is either 0 or π, the optimum external Q_g should be infinite so that there is negligible coupling between generator and cavity. However, this represents only an idealized solution if no transient beam loading is present because virtually small changes of the RF amplitude in the cavity would take infinitely long.

Therefore, superconducting cavities are generally coupled much stronger so that the power amplifier can act against transient effects within reasonable time.

The situation changes for a normal conducting RF system, operated at 40.08 MHz foreseen for the long and flat bunch scheme in the LHC. At constant beam energy, the cavity must be theoretically coupled critically to the power generator by choosing $Q_0 = Q_g$ so that the generator just compensates the resistive losses in the resonator. However, as in the case of the superconducting RF system, more power must be installed coupled more strongly to compensate for transient effects, whose influence is discussed in the subsequent section.

The steady state beam loading parameters neglecting all gaps in the LHC bunch pattern is summarized in Tab. 6.1 to illustrate their order of magnitude. Even though the superconducting cavities are compared to a completely normal conducting RF system, the detuning by the beam is rather similar as the total quality factor of the former RF system is determined by the external quality factor contributed by power amplifier and coupler.

RF frequency, $\omega/(2\pi)$	[MHz]	400.8	40.08	
RF amplitude, U	[MV]	16	1.5	6
Characteristic impedance, R/Q	[Ω]	$8 \cdot 44.5$	$2 \cdot 5 \cdot 30$	$2 \cdot 20 \cdot 30$
Unloaded quality factor, Q_0		$> 10^9$	$2 \cdot 10^4$	$2 \cdot 10^4$
External quality factor, Q_g		10^5	$2 \cdot 10^4$	
Beam induced voltage per bunch (short bunch limit, $f_b = 1$)	[kV]	-16.5	-1.4	-5.6
Cavity detuning, $\Delta\omega/(2\pi)$	[kHz]	6.6	6	

Tab. 6.1: Comparison of the steady state beam loading parameters of the superconducting 400.8 MHz and a normal conducting 40.08 MHz. Gaps in the bunch train are neglected. The assumptions for the cavity parameters of the RF system at 40.08 MHz, twice 5 or 20 cavities per beam, is based on simple extrapolation of similar RF systems operational the PS [180, 182]. The estimations assume the nominal bunch intensity, but can be scaled proportionally to a higher beam current.

6.5.2 Transient beam loading

It is shown above that in the absence of transient effects, corresponding to a machine filled by a uniform chain of equal bunches, the generator would just have to compensate losses in the normal conducting RF cavities. As the suggested long and flat bunch scheme is based on batches of 16 or 32 bunches with gaps in between, transient effects cannot be avoided.

A charge passing through an RF cavity induces a certain amount of voltage and thus deposits energy inside the cavity. According to the so-called fundamental theorem of beam loading, it can be proven in general [225] that the deposited energy is given by

$$\Delta W = \frac{1}{2} q U_b \,.$$

Consequently, the charge q experiences half of the RF voltage induced by itself. Due to the finite quality factor of the combination of cavity and power amplifier, the induced energy decays exponentially. For the case of short bunches compared to the RF wavelength, it is justified to replace the cavity by its lumped element capacity (see Sec. 6.5.1) so that the induced amplitude becomes $U_b = R\omega_0 q/Q$.

The simple analysis is not restricted to a single charge passing through the resonator but can be generalized easily to a complete chain of point-like bunches with arbitrary distances in between the bunches. The resulting RF amplitude is composed of the contribution from the power generator plus the summed up contributions of all bunches having passed the cavity until that instant.

This can be formulated by a tracking like algorithm [177, 226], where the bunches are consecutively moved through the cavity, while calculating the voltage for the subsequent bunch, starting at the passage of the previous one. Additionally, the generator counteracts the induced beam induced voltages. The total voltage at the gap of the RF cavity is derived starting from the real part of

$$U(t) = U_g e^{i\omega t} + \text{const.} \cdot e^{i(\omega-\Delta\omega)t} e^{-(t-t_0)/\tau} , \tag{6.40}$$

where $\tau = 2Q/\omega_0$ denotes the characteristic field decay time in the cavity, and the constant represents a parameter defined by the initial condition given by the instantaneous gap voltage U_0 at the previous bunch passage t_0. Replacing the constant in Eq. (6.40) results in the general bunch-to-bunch tracking equation:

$$U(t) = \underbrace{U_0 \left[e^{i(\omega-\Delta\omega)(t-t_0)} e^{-(t-t_0)/\tau} \right]}_{\text{beam and generator}} + \underbrace{U_0 e^{i\omega t} \left[1 - e^{-i\Delta\omega(t-t_0)} e^{-(t-t_0)/\tau} \right]}_{\text{generator}} . \tag{6.41}$$

The free parameters, generator voltage U_g, generator frequency ω and cavity detuning $\Delta\omega$, are chosen as input variables including a set of initial conditions for bunch positions and energies.

It is important to point out that the extension of the algorithm to multiple RF system can be performed straightforward: the chain of bunches is tracked sequentially through the ensemble of RF systems.

Some examples of the time variation of the gap voltage $U(t)$ are sketched in Fig. 6.22. The right plot shows a periodic solution, where the beam induced jump of the voltage vector is compensated by a cavity detuning so that the absolute value of the vector remains constant. For small beam induced voltages compared to the contribution of the generator, this result reproduces in fact the steady state solution for beam loading compensation by cavity detuning as introduced by the first relation of Eq. (6.39).

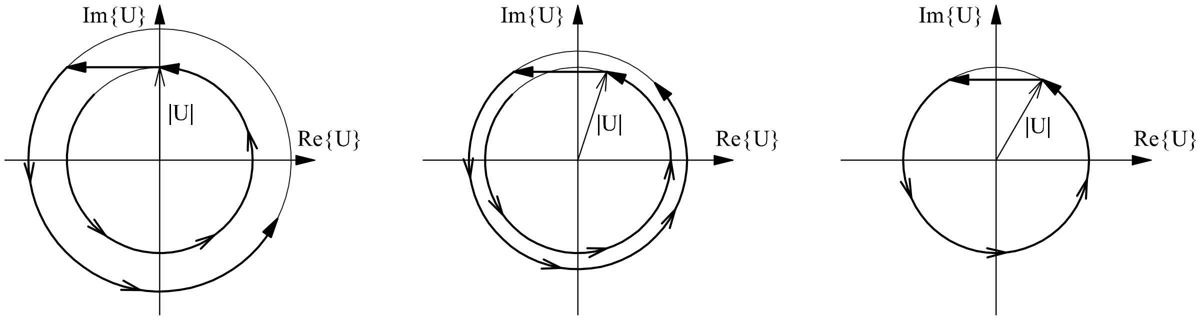

Fig. 6.22: Illustration of the effective voltage vector in the cavity. On the left, the cavity is exactly tuned to the harmonic of the revolution frequency, causing a jump in the absolute RF voltage during each bunch passage [227]. The center diagram represents a partly compensated situation, where the absolute beam induced jump is already reduced. The completely compensated and thus steady state case is shown on the right. The cavity is detuned so that the passing bunch causes a phase jump but the absolute voltage remains constant. Above transition, the unperturbed synchronous phase is located at the positive to negative zero crossing of the U, respectively at $\text{Re}\{U\} = 0$ and $\text{Im}\{U\} = |U|$.

Furthermore it becomes obvious from Fig. 6.22 (right) why small RF amplitudes in order of magnitude of the beam induced voltage can be hardly produced with a reasonable amount of RF power. An enormous detuning is required even in the steady state case, which is mostly outside the tuning range of the cavities. Although the steady state beam-loading can be compensated theoretically, this becomes unfeasible in the presence of beam gaps causing large transients as in the case of the LHC. The maximum tolerable residual voltage at 400.8 MHz during the long and flat bunch generation is limited to some 50 . . . 100 kV, which would lead to a cavity detuning of 6.4 . . . 3.2 MHz to compensate for steady state beam loading, by far out of the tuning range of the superconducting cavities. Furthermore, any beam gap induces huge transients which cannot be compensated. As presently no technique to compensate the transients is available, the 400.8 MHz RF cavities have to be removed or short-circuited for the operation for the creation and storage of long bunches. Transients induced by beam gaps also represent an important issue for the 40.08 MHz alone, however stable periodic solutions can be found for realistic bunch patterns:

An averaged cavity detuning as from Eq. (6.39) can be taken as a starting point for the numerical calculation. Then, the full bunch train is shifted sequentially through the RF system and the influence of the combination between generator and beam induced voltage is applied to the passing bunch according to Eq. (6.41). The average bunch energy is adjusted according to its energy loss or gain while traversing the cavity. Finally, this tracking scheme is repeated multiple times and the bunch positions are memorized for each turn. Actually, the bunches perform synchrotron oscillations around their optimum positions, which can be reconstructed from the synchrotron oscillations seen on the simulated bunch position data.

The optimum bunch phase deviation with respect to its nominal position is shown in Fig. 6.23, for a bunch train having nominal LHC filling pattern (see Sec. 5.1.1) held by the superconducting RF system at 16 MV. The result of the analogous simulation, for the same bunch pattern held by a 1.5 MHz RF system at 40.08 MHz, is found in Fig. 6.24. The parameters of the 40.08 MHz system have been set according to Tab. 6.1. The operation of the LHC with such an RF system results in almost ten times larger phase deviations of the bunches. If this causes too large jitter of the collision point of a pair of bunches, it could be compensated by stronger coupling of the generator to the cavity at the expense of an increase in instantaneous RF power [227].

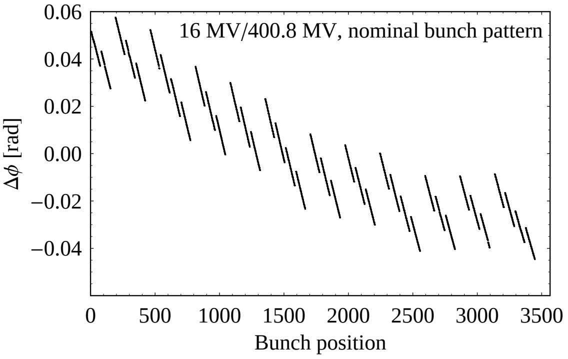

Fig. 6.23: Periodic solution of the steady state phase position for the nominal LHC bunch pattern held by the superconducting RF system with 16 MV. The external quality factor Q_g is assumed to be 10^5.

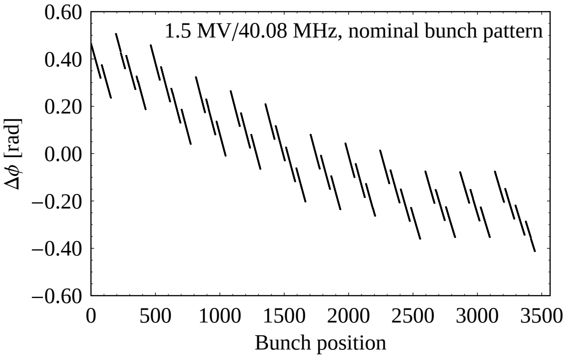

Fig. 6.24: Periodic solution of the steady state phase position for the nominal LHC bunch pattern as in Fig. 6.23 but for a normal conducting 40.08 MHz RF system with 1.5 MV. The phase deviation is given in radians with respect to 400.8 MHz.

The corresponding RF amplitude is, for the 400.8 as well as for the 40.08 MHz system, nearly constant and the residual variation together with the bunch pattern is plotted in Figs. 6.25 and 6.26. It should be pointed out that both RF systems show a very similar time dependence concerning beam loading. This can be attributed to the fact that both RF systems have an almost identical filling time of some 50 μs. This time constant is of the order of half the revolution time which explains in fact the periodicity of the RF voltage illustrated in Figs. 6.25 and 6.26.

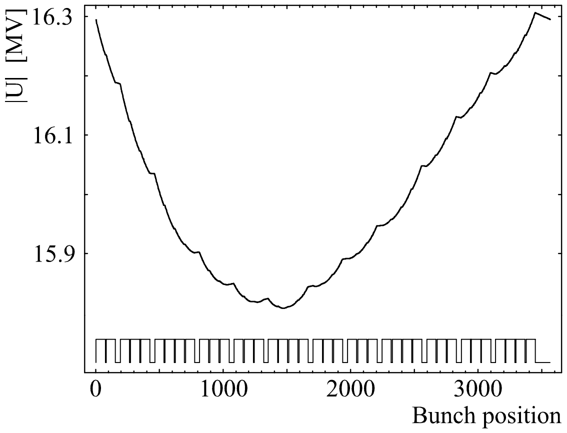

Fig. 6.25: Residual RF amplitude variation at 400.8 MHz along one turn due to beam loading according to the bunch position deviations shown in Fig. 6.23.

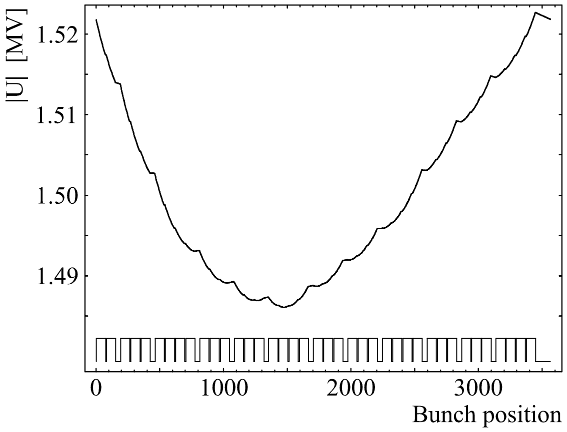

Fig. 6.26: Same representation as in Fig. 6.25 but for the normal conducting RF system at 40.08 MHz. The beam dump kicker gap is located from bunch position 3446 to 3564.

The analysis of transient beam loading effects therefore shows that the behaviour of an LHC operated with normal conducting 40.08 MHz cavities would be similar to the nominal situation. The requirements for beam loading compensation are comparable and no special problems are expected. However, the operation of the superconducting 400.8 MHz during the RF manipulations to create and store long and flat bunches causes intolerable transient RF voltages, which cannot be compensated with present technology, and the superconducting cavities will have to be removed from the ring. Although it is clear that the cavities will be of coaxial type, no detailed design is available so far and the beam loading parameters certainly have to be revised according to more elaborated cavity parameters.

Chapter 7

Summary and Outlook

The choice of the longitudinal beam parameters, such as bunch length or bunch form, has a considerable influence on the final performance of the high energy proton-proton collider LHC. Various upgrade options to improve the luminosity of the LHC have been considered so far. This study presents an analysis of the possibilities to operate the collider with long and flat bunches.

After an introduction of the fundamentals of longitudinal beam dynamics, a survey of the large variety of longitudinal beam manipulations is made. This overview includes classical, well established beam manipulation techniques, but also RF gymnastics with barrier buckets, short RF pulses commonly generated in broadband cavities. The conditions for longitudinal matching at beam transfer between two synchrotrons are described.

In the following section, the possibilities of luminosity improvements using long and flat bunches are explored, with respect to the strong beam-beam limit. Three different options are compared. Firstly, short rectangular bunches with a length comparable to nominal LHC bunches intersecting at large crossing angles of some 5 mrad could partially remove the beam-beam limitation far away from any realistic average beam current. However, for a given number of protons per bunch, a large crossing angle is associated with a significant reduction of the luminosity so that the intensity already has to be increased by a large factor to simply recover the nominal and ultimate luminosities. Secondly, long and flat bunches of intermediate length, about an order of magnitude longer than nominal bunches and containing either 16 or 32 nearly nominal bunches each, could push the beam-beam limit by fractional tune spread compensation in the crossing plane. These bunches are held in collision mode by multiples of 40.08 MHz to reproduce a flat line density. Finally, the scenario of operating the LHC with a single superbunch per beam, held by barrier buckets, is investigated for comparison.

The result of these comparisons is that, in terms of beam dynamics, the scheme with bunches of intermediate length has quite competitive performance to the single superbunch case. Additionally, the technical implementation of the former scenario is much more realistic, because of the numerous inherent disadvantages of superbunches, like the need for synchrotron radiation compensation and for broadband cavities.

Based on the final long and flat bunch parameters, a realistic RF manipulation to create them, starting from a nearly nominal bunch pattern, is described and optimized in detail. This manipulation consists of a series of batch compression and bunch pair merging RF gymnastics. Both of these basic ingredients have been amply demonstrated in a real accelerator environment.

Finally, the influence of longitudinal collective effects and beam loading is analyzed. The bunches held by the 40.08 MHz RF system are prone to coupled bunch instabilities, especially during the period of LHC filling, as their longitudinal emittance is much smaller than the bucket area. The tolerable impedance limitations are at least an order of magnitude more tight than for the storage of the nominal LHC beam. Two cures can be envisaged to suppress longitudinal instabilities: firstly, Landau damping can be improved by superimposing some RF amplitude at a higher harmonic and thus increasing the synchrotron frequency spread within the bunches. The induced emittance growth by such an additional RF system could be kept within reasonable limits. Secondly, a longitudinal coupled bunch feedback, as has been initially considered for the LHC [228, 229], could stabilize the beam. This feedback would have to cover a bandwidth of some 20 MHz since the bunch frequency remains 40.08 MHz during injection.

It is important to point out that the challenge for the detectors of the physics experiments is as large as for the accelerator. However, from the point of view of the experiments, the different scenarios do not have equal interest, even if they can theoretically deliver the same luminosity. Extrapolating from today's detector and data handling technologies, more numerous bunches are clearly preferable in the framework of a first stage LHC upgrade.

In any case, this report shows that long and flat bunches offer potentially valuable solutions for upgrading the LHC luminosity and proposes a challenging but feasible method for creating them.

Appendix A

Experimental Results with Thick Barrier Buckets in the SPS

As has been shown in the preceding chapters, the application of the barrier bucket technique in a circular accelerator requires a special broadband RF installation, being capable to transfer nearly arbitrary RF amplitude to the beam. None of the CERN accelerators is however equipped with such an RF system.

The Super Proton Synchrotron (SPS) is a synchrotron to accelerate protons from some 14 GeV up to 450 GeV located at CERN. It has a circumference of 6911.5 m [230]. Originally the SPS was constructed for experiments with fixed targets. In the near future its main role will be to serve as proton and heavy ion injector for the LHC [148, 231, 232].

For beam acceleration, the SPS is equipped with a so called traveling wave RF system working at 200 MHz, the 4620th harmonic of the revolution. This system is operated as a waveguide coupled to the beam and has the advantage that its filling time is well below the revolution period. The RF amplitude can be controlled on a turn-to-turn basis which offers new possibilities for RF manipulations. In fact, thick barrier buckets can be generated by filling and depleting the traveling wave cavities several times per revolution. Thick means that these barriers have a sub-structure given by the resonance frequency at which the RF system is operated, namely 200 MHz. The potential barrier itself evolves from the amplitude modulation of the fast RF oscillation at the resonance frequency of the cavities.

This thick barrier bucket technique has already been tested successfully with low beam currents at 14 GeV (below transition) in the SPS at CERN in 1999 to check its prospects for a future upgrade [233, 234] in the framework of the CERN Neutrino to Grand Sasso project (CNGS). At that time the performance was limited by intensity effects. However, since the SPS has undergone a major impedance improvement program during the last few years [235], it was suggested to repeat the machine development experiment above the transition energy and with increased beam intensity. The chapter is based on the results of the machine development experiment as reported in [236, 237].

After an introduction to the beam dynamics of thick barrier buckets, their generation in the SPS is described. The experimental results are presented and commented afterwards. Finally, beam loading issues are discussed in the last part of this chapter.

A.1 Hamilton beam dynamics of thick barrier buckets

Pulsing the TW structures in the SPS with a constant power delivered by their power amplifiers means that the total cavity voltage rises nearly linearly with time, because the group velocity along the cavity length is constant. The normalized potential $W(\phi)$ as defined in Chapter 2 generated by the RF system can then be described by

$$W(\phi) = \begin{cases} \frac{1}{\phi_p}[\sin(\phi_q + \phi) + (\phi_p - \phi_q - \phi)\cos(\phi_q + \phi) - \sin\phi_p]\,, & -\phi_q \le \phi < -\phi_q + \phi_p \\ 0\,, & -\phi_q + \phi_p < \phi < \phi_q - \phi_p \\ \frac{1}{\phi_p}[\sin(\phi_q - \phi) + (\phi_p - \phi_q + \phi)\cos(\phi_q - \phi) - \sin\phi_p]\,, & \phi_q - \phi_p \le \phi \le \phi_q \end{cases}, \tag{A.1}$$

where the phase definitions ϕ_p and ϕ_q were chose according to Fig. A.1. Using the Hamiltonian from Eq. (2.24) with $(\phi, \dot{\phi})$ as the canonical conjugate pair of variables leads to phase space trajectories which are given by

$$\dot{\phi}(\phi) = \sqrt{2\omega_s^2[W_0 - W(\phi)]} \quad \text{with} \quad W_0 = W(\phi_l) \quad \text{or} \quad W_0 = W(\phi_u)\,, \tag{A.2}$$

where ϕ_l and ϕ_u are the limits of the trajectory in ϕ. A typical normalized longitudinal phase space is shown in Fig. A.1.

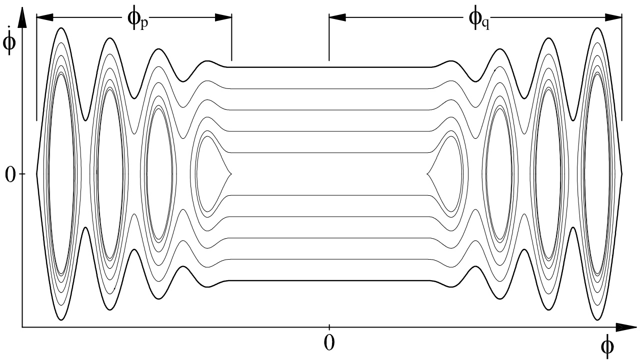

Fig. A.1: Sketch of the longitudinal phase space for a thick barrier bucket with $\phi_q = 12\pi$ and $\phi_p = 8\pi$. It can be seen that the energy acceptance is largest at the bucket ends. The inner trajectories show that separated sub-buckets exist inside the barrier.

A.1.1 Bucket height

Over most of its length the energy acceptance of a thick barrier bucket with a given RF voltage U_0 is reduced by a factor of $\sqrt{2}$ with respect to the energy acceptance of a single sinusoidal barrier bucket ($\Delta\hat{E}_{\text{harmonic}}$). This can be understood by observing that the potential created by the thick barriers is symmetric around the potential during the coasting beam section of the long bucket. Only half of the RF voltage can therefore contribute to the potential and the energy acceptance is lowered. It can be written as

$$\Delta\hat{E} \simeq \sqrt{\frac{pR\,eU_0\omega_0}{\pi h|\eta|}}\,, \tag{A.3}$$

where p is the beam momentum, R is the mean machine radius, ω_0 is the revolution frequency, $h = \omega_{\text{rf}}/\omega_0$ the harmonic number and $\eta = 1/\gamma_{\text{tr}}^2 - 1/\gamma^2 = 6.2 \cdot 10^{-4}$ is the phase slip factor. At the edges of the bucket, the energy acceptance gradually grows by the missing factor $\sqrt{2}$ to the same energy acceptance as in a harmonic RF system.

A.1.2 Bucket area

The exact bucket area of a thick barrier bucket can be calculated by numerical integration over the separatrix. For barriers which were generated in the SPS, the RF frequency is much higher than the frequency of the amplitude modulation, and it takes about 120 RF periods to fill the RF cavities. In this case a simple analytical approximation for the bucket area of a barrier bunch can be found by averaging over the bucket substructure.

The principle of such an approximation is shown in Fig. A.2. As the voltage in the cavities is rising linearly during filling and depletion, the minimum and maximum functions in the right picture of Fig. A.2 that define the areas of which approximately one half is inside the bucket, can be calculated analytically and are of $\sqrt{1 \pm a(\phi - b)}$ type, where a and b are parameters depending on ϕ_p and ϕ_q.

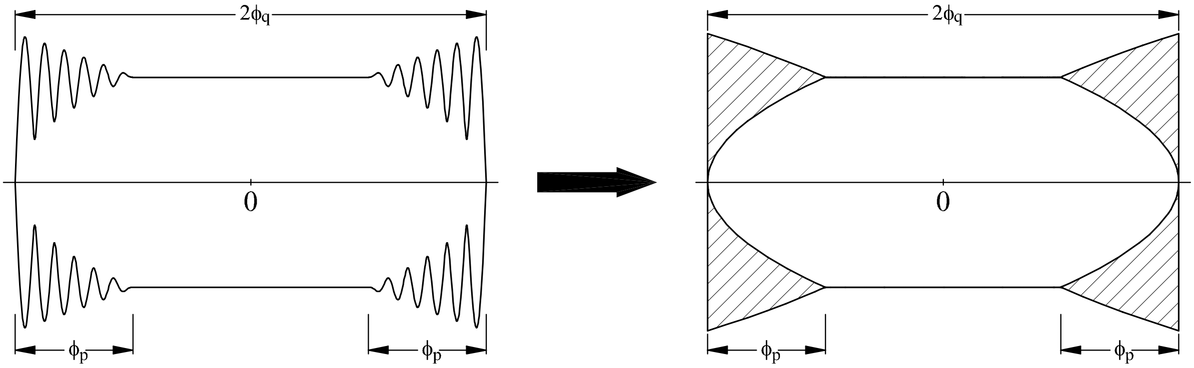

Fig. A.2: Sketch of phase space and approximated phase space for the bucket area estimation. Only half of the hatched areas are taken into account for the bucket area.

From the approximation presented in Fig. A.2 (right) the bucket area in units of $[\phi \cdot \dot{\phi}] =$ rad^2/s can be written as

$$\begin{aligned} A &= 4\sqrt{2}\omega_s \left[(\phi_q - \phi_p) + \frac{2}{3}\phi_p \right] + \frac{1}{2} \cdot 4\sqrt{2}\omega_s \left[\frac{4}{3}(\sqrt{2} - 1)\phi_q \right] \\ &= 4\sqrt{2}\omega_s \left[\phi_q + \left(\frac{2\sqrt{2}}{3} - 1 \right) \phi_p \right] \end{aligned} \tag{A.4}$$

and as

$$A = 4\sqrt{2}\, \frac{E\beta^2\omega_s}{h^2\omega_0^2|\eta|} \left[\phi_q + \left(\frac{2\sqrt{2}}{3} - 1 \right) \phi_p \right] \tag{A.5}$$

in conventional units of [time · energy] = eV · s.

A.2 Generation of thick barrier buckets

Unlike other circular accelerators where special broad band cavities had to be installed for barrier bucket operation, a special form of these longitudinal potential wells can be generated in the SPS thanks to the short filling time of the RF cavities with respect to the revolution period. The standard acceleration system in the SPS consists of four accelerating cavities each of which is composed of either 43 or 54 cells. As these cavities are operated in traveling wave

(TW) mode, the filling time, which is 567 ns for the two structures with 43 cells and 712 ns for the two 54 cell cavities, is much shorter than the revolution time of 23.1 μs.

By switching the amplifiers of the TW cavities on and off twice during each revolution period for some 800 ns, RF wave packages with about 1.4 μs length and a 200 MHz substructure are formed, actually a simple fast amplitude modulation of the 200 MHz RF signal. The RF voltage in the cavity is increasing and decreasing linearly as the group velocity (cf. Tab. A.3) along the TW cavities is constant. An overview of the special pulse generation electronics and the amplitude switching of the TW cavities is given in Fig. A.3. Switching the drive voltage on and off for about one filling time generates amplitude functions which are nearly linear. It is worth noting that because of this special kind of barrier bucket generation, the phase of the 200 MHz stays constant with respect to the revolution frequency and only the amplitude of the cavity voltage is modulated. This becomes important when the phase position of the RF barrier is varied (cf. Sec. A.6).

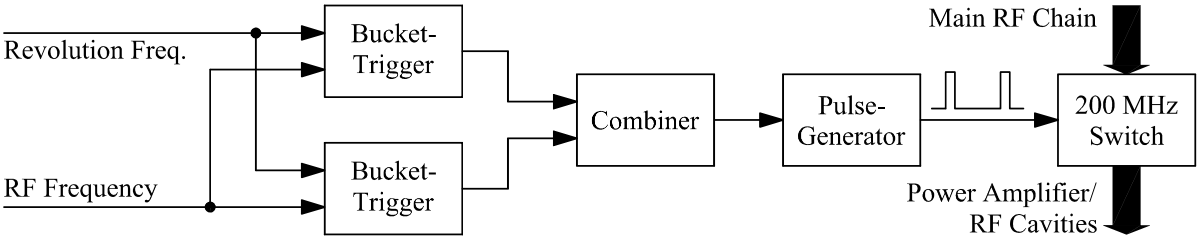

Fig. A.3: Sketch of the thick barrier bucket generation in the SPS. The 200 MHz RF signal is modulated by a switch which is triggered twice per revolution. The main RF power chain passes through the 200 MHz switch on the right of the diagram. The linearly increasing and decreasing voltage ramps in the RF structures are caused by the finite filling time.

The typical RF voltage function composed of the vector sum of all four TW cavities at zero beam current is shown in Fig. A.4. The driving pulses and the beam signal of a stationary long bunch measured with an electrostatic broadband pick-up are presented in Fig. A.5. It is clear that the RF power amplifiers cannot be switched on instantaneously and the measured voltage profile shows that the RF amplitude in the cavities does not raise perfectly linearly. Because of different cable lengths, the two traces are shifted by an arbitrary phase against each other. In fact, both barrier pulses are arranged symmetrically around the beam pulse. The distance between the two pulses, which is approximately equal to the bunch length, was set to about 3.4 μs. It was chosen to be about twice as long as the injected batch of 72 bunches (1.8 μs) from the PS. The slope on the beam pulse in Fig. A.5 arises due to the baseline drift of the broad band pick-up with its amplifier. The low frequency cut-off is at a few kHz.

A.3 Beam parameters

All barrier bucket experiments were carried out with one batch of the standard LHC beam injected in the SPS at an energy of 26 GeV. Since beam with the nominal LHC intensity was observed not to be held inside the barrier bucket, the injected intensity was decreased to about one third of the nominal number of particles. All relevant beam and machine parameters during the barrier bucket experiment are summarized in Table A.1.

The RF frequency was matched to the injected beam energy but was slightly varied during the experiment to compensate for energy mismatch. Compared to the first measurements

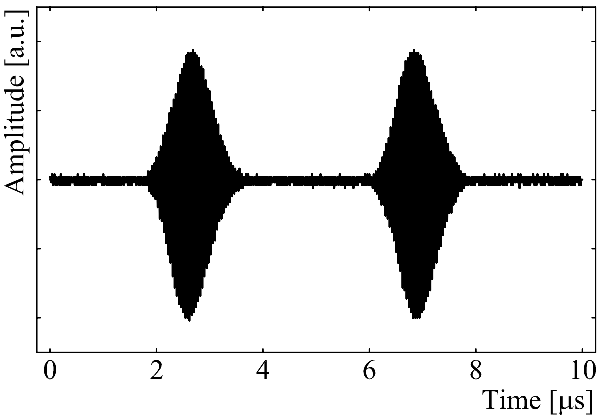

Fig. A.4: Vector sum of the cavity voltage produced by two TW cavities in barrier bucket mode. The peak voltage of the barriers is approximately 2 MV.

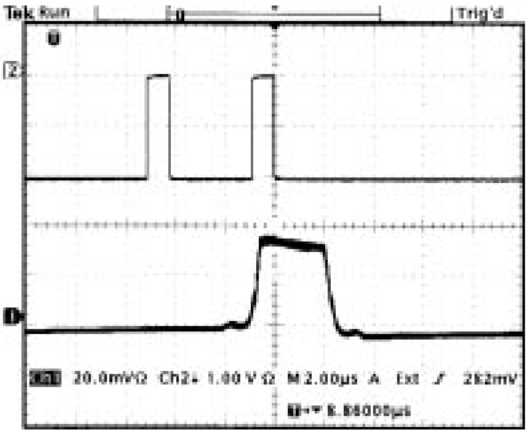

Fig. A.5: Driving pulses for the RF switch to trigger generate the barriers in Fig. A.4 (upper trace). In between the two barriers a long bunch with homogeneous line density is kept (lower trace).

Injected beam parameters:		
Momentum, p	[GeV/c]	26
Intensity per bunch (total), N		$\lesssim 0.4 \cdot 10^{11}$ ($\lesssim 2.9 \cdot 10^{12}$)
Bunch length, τ	[ns]	4
Momentum spread, $\Delta p/p$		$\pm 2 \cdot 10^{-3}$
Longitudinal bunch emittance, ε_l	[eVs]	0.35
Batch length	[μs]	1.8
	[$2\pi R_{\mathrm{SPS}}$]	1/12.8
Barrier bucket parameters:		
Harmonic number, h		4620
Frequency of RF systems, $f = h\omega_0/(2\pi)$	[MHz]	200.265
Driving pulse length of barrier excitation	[μs]	0.9
Total RF pulse length	[μs]	1.5
Total cavity voltage of two/four TW cavities, U_0	[MV]	2/4
Distance between barrier pulses	[μs]	3.3 – 4.3

Tab. A.1: Beam and machine parameters during the barrier bucket experiment. The number of injected protons corresponds to approximately one third of the nominal LHC beam intensity.

described in [233, 234], the new measurements mainly differ in the intensity per bunch ($4 \cdot 10^{10}$ instead of at the utmost $2.5 \cdot 10^{10}$ resp. $5 \cdot 10^{9}$ particles per 200 MHz bucket) and in the particle energy (26 GeV instead of 14 GeV) chosen for the experiments.

It is worthwhile noting that the earlier barrier bucket tests [233] have been performed below transition at 14 GeV, whereas the injection flat bottom for the LHC beam at 26 GeV is above the transition energy. The feedback and feed-forward loops around the cavity amplifier chains, which normally reduce the impedance of the RF systems, had to be switched off during barrier operation.

A.4 Properties of stationary barrier bunches

As a first experiment the behavior of a stationary long bunch kept by thick RF barriers over a long timescale in the SPS was studied. A single LHC beam batch was injected in between two barriers. The SPS was then set to coast mode, meaning that the magnetic field and the RF parameters remain constant for a timescale from minutes up to hours). In our case the longest coast was kept for about 100 minutes.

A.4.1 Stationary long bunch in the SPS

During the first few seconds after injection longitudinal particle density waves swashing back and forth between the two potential barriers generated by the cavities have been observed. This and its transient character are analyzed in detail in the subsequent section. About 10 s after injection, due to dilution in the longitudinal phase space, the beam becomes stable.

During the storage of the barrier bunch, the longitudinal beam profile, again measured with the electrostatic broadband pick-up and the 200 MHz component, detected by a cavity tuned to 200 MHz, have been recorded. Two such measurements are shown in Fig. A.6 and A.7.

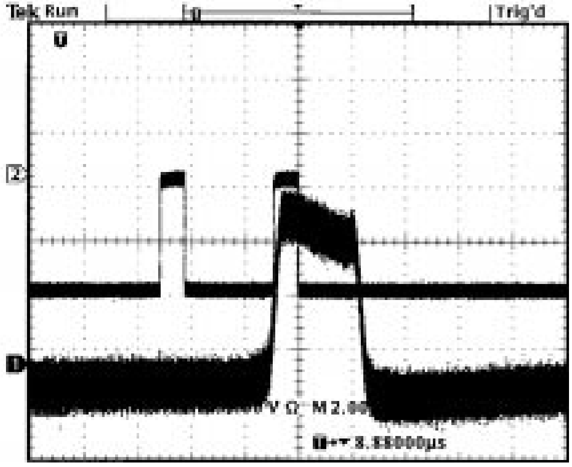

Fig. A.6: Bunch signal (lower trace) and barrier pulses (upper trace) about one minute after injection. As can be seen, the current density along the bunch is constant as expected for such a band. The slope of the line density is introduced by the low frequency limit of the broadband pick-up. The horizontal scale is 2 μs per division.

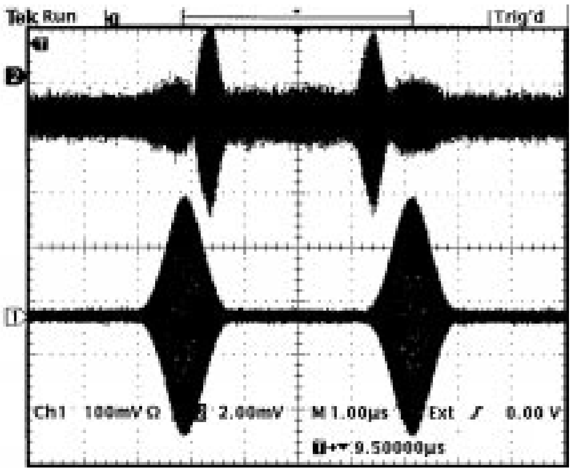

Fig. A.7: 200 MHz component of the bunch signal (upper trace) and RF voltage (lower trace) during the passage of the intentionally generated long bunch 3.5 minutes after injection. The absolute phase of the signals is not exactly the same. The horizontal scale is 1 μs per division. The beam signal should be modulated only at the bunch edges by the 200 MHz RF waveform.

The intensity at about one minute after injection was about $2 \cdot 10^{12}$ p corresponding to $2.8 \cdot 10^{10}$ p/bunch. It should be noted that the measurements by the beam current transformer include all particles circulating in the accelerator and thus the coasting beam background also contributes to the measured beam currents. The long bunch was perfectly stable at this intensity and no instability was observed during the beam storage. The beam lifetime calculated from intensity readings based on the current transformer during one of the coasts is $\tau = 1202\,\mathrm{s} \pm 80\,\mathrm{s}$.

As can be seen on the measured 200 MHz component of the beam, there are also particles outside the intentionally populated bucket. A small fraction of them are captured inside the complementary bucket situated in the rest of the circumference (see Fig. A.8) shortly after the unmatched injection. As the line density in this bucket is also stretched around the ring, it can be estimated that the corresponding beam current is in any case below a few percent of the current in the main bucket.

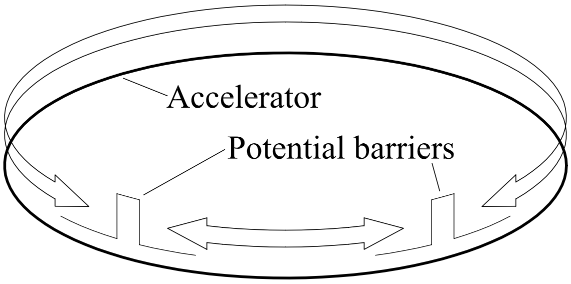

Fig. A.8: The two barrier pulses in the SPS actually generate two barrier buckets. The first bucket is intentionally built up between the two barrier pulses. The second occupies the rest of the ring.

A third group of particles drifts around the ring, not captured inside either of the two buckets. They were kicked onto such trajectories in the longitudinal phase plane during the first hundred turns after injection. Their large energy deviation is due to the voltage induced by the beam in the RF cavities themselves. Although situated outside buckets, their density is still modulated by the RF barriers and the particles show up as small peaks in the 200 MHz component, with maxima close to the barriers.

Theoretical parameters of barrier buckets with two and four SPS RF cavities of 1 MV each delivering bursts separated by 3.3 μs are summarized in Table A.2. In any case the bucket area is much larger than the longitudinal emittance of the injected batch which adds up to only $72 \cdot 0.35 = 25.2$ eVs. As the bunched beam debunches after the injection in the long bucket, it is obvious that the phase space density of the final bunch is at least one order of magnitude below the longitudinal particle density in nominal LHC bunches.

RF voltage, U_0	$\Delta\hat{E}$ ($\Delta\hat{E}_{\text{harmonic}}$)	$\Delta\hat{p}/p$ ($\Delta\hat{p}_{\text{harmonic}}/p$)	A_{bucket}
1 MV	53.6 (75.8) MeV	$2.14\ (3.02) \cdot 10^{-3}$	346 eVs
2 MV	75.8 (107.2) MeV	$3.02\ (4.13) \cdot 10^{-3}$	489 eVs
4 MV	107.2 (151.6) MeV	$4.13\ (5.83) \cdot 10^{-3}$	692 eVs

Tab. A.2: Barrier bucket parameters for different RF amplitudes. The total bucket length is 3.3 μs and the filling time is assumed to be approximately 600 ns. The values in brackets given for the bucket height correspond to an harmonic RF system.

A.4.2 Stationary beam loading of a long bunch

The line density in a long bunch kept between two thick barriers in the SPS is much smaller than the line density of nominal LHC bunches injected from the PS. Nevertheless beam loading in the 200 MHz RF system may still influence the effective voltage delivered to the beam.

The four 200 MHz TW structures in the SPS are of backward wave type, which means that the RF power fed to the structure at its downstream end, travels in the opposite direction to the beam and is dissipated in a resistive load at the upstream end [238, 239].

The beam transfer impedance of such a structure is given by

$$Z_b = \frac{L^2 R_2}{8} \left[\left(\frac{\sin \frac{\tau}{2}}{\frac{\tau}{2}} \right)^2 - 2j\, \frac{\tau - \sin\tau}{\tau^2} \right] , \tag{A.6}$$

wherein L is the interaction length and R_2 is the series impedance of the structure. The total phase slip τ is due to the velocity difference between accelerating wave and the beam:

$$\tau = \frac{L}{v_g}\left(1 - \frac{v_g}{v}\right) \cdot (\omega - \omega_r)\,. \tag{A.7}$$

The center frequency of the cavities operated in $\pi/2$ mode is defined as $\omega_r = 2\pi \cdot 200.222\,\text{MHz}$, $v = \beta/c$ and v_g are beam velocity and the group velocity of the cavity structure. Some properties relevant for beam loading estimates are condensed in Table A.3. Illustrations of the beam transfer impedance can be found in e.g. [240]. As the frequency of operation at 26 GeV beam momentum is quite close to the center frequency, the cavity impedance is mainly resistive. The line density $\lambda(\phi)$ can be calculated according to Eq. (2.60) by assuming a distribution being parabolic in energy $f(\phi = \text{const.}, \dot{\phi}) \propto (1 - \dot{\phi}^2/\dot{\phi}^2_{\text{max}})^{1/2}$. It is directly proportional to the square of the energy deviation of the limiting trajectory in phase space.

Center frequency of $\pi/2$ mode, $\omega_r/(2\pi)$	[MHz]	200.222
Interaction length 4/5 section cavity, L	[m]	16.082/20.196
Group velocity, v_g	[m/s]	$0.0946c$
Operating frequency at $p = 26\,\text{GeV}$, $\omega/(2\pi)$	[MHz]	200.265
Beam transfer impedance 4 section cavity, Z_b	[MΩ]	$0.874 - j0.048$
Beam transfer impedance 5 section cavity, Z_b	[MΩ]	$1.38 - j0.096$
Total beam transfer impedance	[MΩ]	$4.502 - j0.288$
(two 4 section and two 5 section cavities)		$4.51\,\text{M}\Omega \angle -3.67^0$

Tab. A.3: Relevant parameters of the 200 MHz TW RF system at 26 GeV/c.

The beam current along the bunch with such a distribution for an intensity of $0.35 \cdot 10^{10}$ p/bunch is shown in Fig. A.9. The voltage induced at 200 MHz by this current (averaged on a time scale of a few RF cycles) is plotted in Fig. A.10.

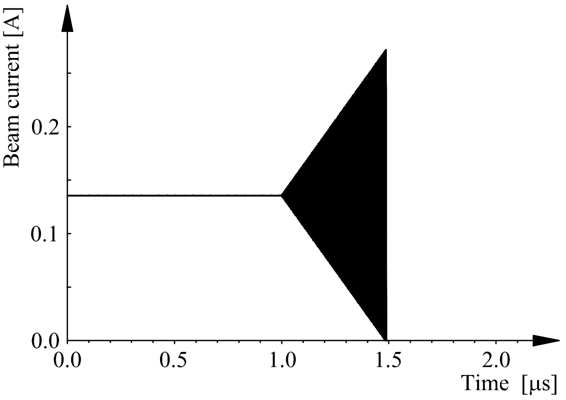

Fig. A.9: Calculated beam current versus time for a line density distribution as assumed in Eq. (2.60). The center of the bunch is at $t = 0$. In the measurements, the particle density at the edges is lower than expected because of separated islands inside the barriers which are less populated than the assumed in the model.

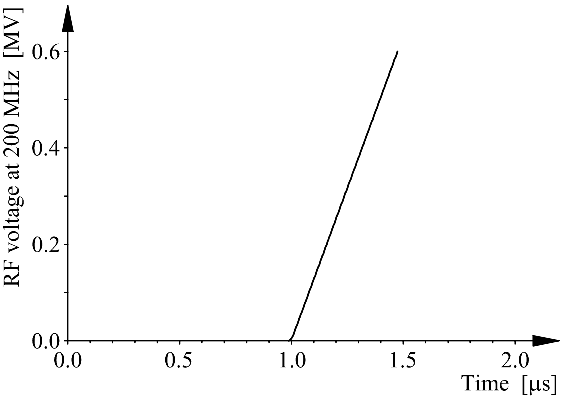

Fig. A.10: Calculated absolute beam induced voltage versus time for the distribution shown in Fig. A.9. This is only an upper estimation of the induced voltage which reduces the external cavity voltage. The measured beam induced voltage does not have the maximum at the edge of the long bunch.

If only the absolute value of the cavity impedance is been taken into account, the maximum voltage reduction induced by beam loading can be estimated to be around 0.6 MV. Compared to the external cavity voltage of 2 MV this is not negligible. It is worth noting that part of this induced voltage is compensated by the amplitude control loop which is acting on the vector sum of all cells of one TW cavity.

The simple model mentioned above would predict a 200 MHz beam component which increases linearly along the barrier and has its maximum at the largest RF voltage. This is in fact not true because the bunch has a more complex structure of separated sub-buckets and outer trajectories (see Fig. A.1) which cover only a fraction of the whole bunch. As the outer regions of the bunch are naturally less populated, the bunch edges will be also less populated than the inner regions. Additionally, there are separated islands in phase space inside the barriers which are also less populated than assumed in the simple model. The 200 MHz beam component therefore shrinks again towards the end of the bucket.

Fig. A.7 shows that the RF component increases nearly linearly where the beam reaches the barrier and decreases again after 380 ns. The analysis of the 200 MHz beam component can give an estimation for the effective voltage seen by the beam in the RF cavities. It should be mentioned that only the DC and the 200 MHz components are the two dominant current contributions to the beam structure. All other frequency components are strongly suppressed.

The beam current distribution along the final bunch kept by the two barriers is much more homogeneous than the injected bunch structure. This causes a peak current along the coasting beam fraction of the final bunch which is about an order of magnitude lower than the peak current of the injected LHC bunches.

A.5 Transient beam behaviour after injection

As shown in the previous section, the behaviour of the long bunch held by thick barriers is as expected; a few seconds after injection equilibrium is attained. It is stable and the line density along the central part of the bunch is constant. However, the most critical process is the formation of the long bunch itself. As it is impossible to prepare a single long bunch in the PS with its present RF systems and to transfer it to a matched bucket in the SPS, an LHC-type batch is injected between the two potential wells. It consists of 72 bunches spaced by 25 ns with a bunch length of 4 ns each (see Table A.1). These bunches have a strong 200 MHz Fourier component during the first turns after injection which decays before the first particles are reflected at the barriers. As an unexpected large fraction of the injected particles was not reflected by the barriers a detailed analysis of the possible mechanism is presented below.

A.5.1 Measured profiles

To analyze the beam dynamics during the injection of a LHC batch into a long bucket, the evolution of the line density was recorded on the broadband pick-up during the first second after injection. One trace is recorded every 300 turns and the full display corresponds to the first $4.5 \cdot 10^4$ turns. Two typical measurements for 2 MV (left) and 4 MV (right) voltage are shown in Fig. A.11.

The first observation is that the injected beam spreads very asymmetrically in azimuth, most particles drifting to the left which means that their energy is below the reference energy. Moreover, only a fraction of the particles is reflected by the barriers. A non-negligible fraction of the injected beam passes through the left barrier and becomes coasting or is captured in the second, extremely long barrier bucket (assuming that the energy of some particles is above the reference energy, see Section A.4.1). Only particles with positive energy deviation can be

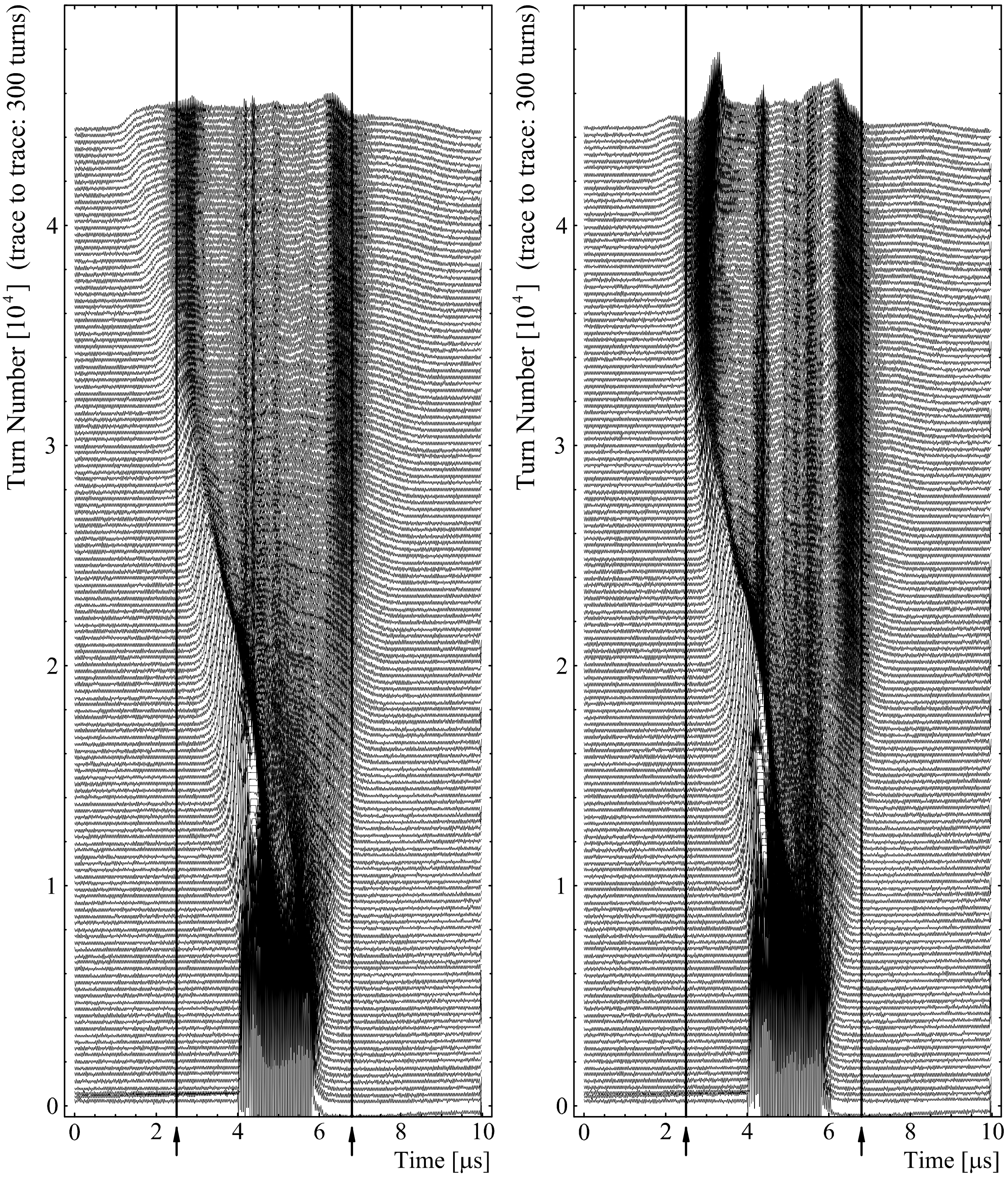

Fig. A.11: Mountain range plot of the pick-up signal during first $4.5 \cdot 10^4$ turns in the SPS. One trace was recorded every 300 turns. The left plot shows a measurement with 2 MV whereas the right plot was taken with 4 MV RF voltage. The barriers (maximum cavity voltage) are located at 2.5 and 6.8 μs (marked by thick lines). The bunches around 4.3 μs do not debunch because of a parasitic 200 MHz RF voltage burst following each barrier pulse.

captured in the second barrier bucket because they need to pass one barrier first and lose energy so that they cannot cross a further barrier.

From the momentum spread of the injected beam given in Table A.1 and the energy acceptance in Table A.2 an RF voltage of 1 MV theoretically should have been sufficient to capture all particles of the injected beam. In this case, an effective RF voltage reduction caused by beam loading should have been compensated, but even without feedback and feed-forward loops, the total beam should have been easily captured with 2 MV RF amplitude.

The fraction of the beam crossing the left barrier is estimated by integrating over the beam profile (Fig. A.11). For an RF voltage of 2 MV, approximately 50–65 % of the injected beam has been captured in between the barrier bucket, whereas still 20 % of the particles drifting away in the 4 MV case. Furthermore, it is possible to estimate the maximum energy deviation of particles crossing the barriers by measuring the drift velocity $\dot{\phi}$ relative to the synchronous particle. In the $U_0 = 2\,\mathrm{MV}$ case, the drift velocity is about $\dot{\phi} = 4.2 \cdot 10^3\,\mathrm{rad/s}$ which corresponds to an energy deviation of 139 MeV. This deviation is indeed larger than the energy acceptance of the bucket (see Table A.2). The situation changes in the $U_0 = 4\,\mathrm{MV}$ case as particles with an energy deviation of up to $\Delta E \simeq 108\,\mathrm{MeV}$ should normally be kept inside the bucket. However, the results are intensity dependent and the precision with which the drift speed can be extracted from the measured profile is rather limited.

Energy loss by transient beam loading in the cavities is thus suspected to be the process which might explain the beam behaviour. On the one hand, particles may lose energy quickly due to the RF cavities during the debunching in the first 200 turns after injection because of transient beam loading. On the other hand, the effective amplitude in the cavities might also be lowered by an RF voltage induced by the 200 MHz component of a stationary long bunch (see Section A.4.2) in equilibrium because of transient and stationary beam loading. The first effect will be analyzed in detail in the next section.

A.5.2 Debunching process after injection

To understand the time scale on which the beam can lose energy after injection in the SPS with its uncompensated cavity impedances, it is necessary to have a closer look at the debunching procedure and especially the decay of the 200 MHz beam component.

The decay of the injected batch structure with 4 ns long bunches spaced by 25 ns caused by the dependence of the revolution period of the individual particle in the SPS is very fast. According to the equations given in Sec. 3.3.2 the debunching time at injection flat-bottom is about 1.8 ms which corresponds to 80 turns. Measurements of the beam induced voltage during the first 150 turns confirm calculations which predict that the 200 MHz beam component should decrease to below 20 % of its initial value within approximately 100 turns. The time needed for the 40 MHz and 200 MHz beam structure to decay is approximately five times longer than the debunching time t_d, because of the 25 ns bunch spacing, where every fifth bucket is populated at 200 MHz.

This decay is nevertheless much shorter than the time needed for particles from the batch to reach the barrier and thus further calculations can be assumed to be independent of any barrier RF voltages. The assumption is confirmed by the fact that, as can be seen from Fig. A.11, no further significant energy loss on a time scale of a few thousand turns is observered.

A.5.3 Estimation of the average energy loss by beam loading

The average rate of energy loss per particle can be estimated by application of energy conservation law. As mentioned before, the filling time of the 200 MHz TW structures in the SPS is much shorter than the revolution time and the cavities have thus no memory from turn to turn. Each time the batch arrives, the cavities are completely empty. Therefore, the total energy delivered by the beam to the cavity can be derived from the measured induced voltage profiles during the beam passage.

The total vector sum measured over all four TW structures in the SPS during the first turn is plotted in Fig. A.12. The voltage profiles of the beam induced voltage in between the barriers are alike on subsequent turns, but their amplitude decreases from turn to turn [236]. Filling the TW structures with power from the beam looks similar to filling them with power amplifiers as the rate of rise of the RF voltage is the same in both cases.

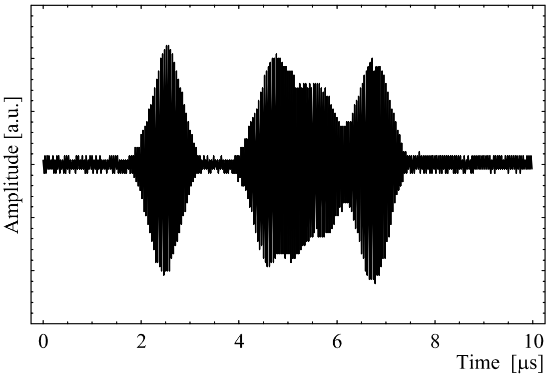

Fig. A.12: Vector sum of all four TW cavity voltages during the first passage of the LHC batch injected from the PS. It can be clearly seen that the beam induced voltage (centre) is nearly as large as the two barrier waveforms generated by the RF power amplifiers.

To compute the average power and also the average beam energy delivered to the cavities one first has to calculate the effective voltage by integrating over the voltage function in Fig. A.12. Only the region where the cavity voltage is induced by the proton beam (between $\tau_i \simeq 4\,\mu$s and $\tau_f \simeq 6.2\,\mu$s) has to be taken into account. The effective power delivered to the cavity is then defined by

$$P_{\mathrm{avg}} = \frac{U_{\mathrm{eff}}^2}{|Z_b|} \simeq \frac{\frac{1}{\tau_f - \tau_i}\displaystyle\int_{\tau_i}^{\tau_f} U(t)^2\,dt}{|Z_b|}\,. \tag{A.8}$$

Multiplying the effective power P_{avg} by the time interval of integration $\tau_f - \tau_i$ gives the total energy which was delivered to the RF system and which was thus lost by the beam at every turn.

For conversion to more convenient units, this can be normalized per proton. The result is given in Fig. A.13. The decay of the beam induced power was fitted by a second order polynomial. The energy losses after the first 200 turns are negligible.

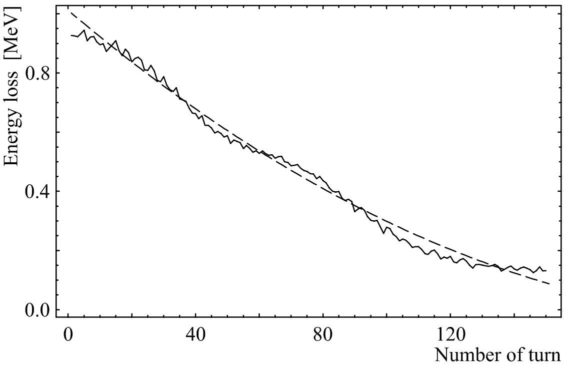

Fig. A.13: Average energy loss per proton per turn versus number of turns normalized to an intensity of $0.4 \cdot 10^{11}$ particles per bunch. The dashed line is a fit to the measured curve and is used for the total energy loss estimate.

Integration over the fitted function therefore gives a good approximation of the total energy. For one injected LHC-type batch with $0.4 \cdot 10^{11}$ protons per bunch this assumption gives

$$\Delta E_{\mathrm{avg}} \simeq 72\,\mathrm{MeV/p}\,. \tag{A.9}$$

This mean energy loss per particle is below the energy deviation of the particles crossing the potential barrier as observed in Fig. A.11 which is above 100 MeV. However, some particles receive a much larger energy kick whereas others experience no significant net energy loss. Moreover, the bunches are not only shifted by a certain amount of energy but also blown up enormously. A simulation of an LHC-type bunch with parabolic distribution in phase and energy was made to check the blow up in energy spread. One bunch of 2000 particles was placed at the crest of the RF voltage and tracked for 200 turns (Fig. A.14) while the RF amplitude was reduced. As the RF amplitude decreases linearly to zero within these 200 turns this situation should give a good estimation for the blow-up in energy spread. If a further energy shift of the center of gravity of the bunch by ΔE_{avg} is assumed which is not included in the tracking, the energy deviation of particles crossing the barriers in the range of some 140 MeV observed from the mountain range plots (Fig. A.11) becomes explicable.

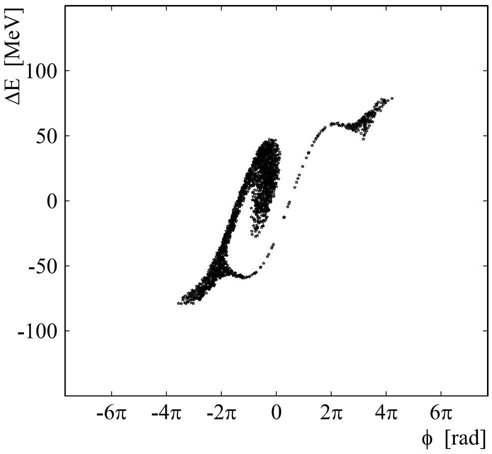

Fig. A.14: Distribution of an LHC bunch placed at the crest of the RF voltage which linearly decreases to zero within 200 turns. In this example, 2000 particles are tracked. The initial bunch distribution was parabolic in phase and energy.

Knowing the total average energy lost by the beam, it is possible to roughly estimate which fraction of the injected batch can be captured in the barrier bucket and which fraction becomes coasting. It is assumed for simplicity that the whole batch is shifted by the average energy loss ΔE_{avg}. It is clear that in reality not all bunches are shifted equally (see Fig. A.14). Some of them receive much larger kicks in energy whereas others stay close to their initial energy. Averaging over the whole batch should however lead to the correct order of magnitude. The barrier bucket in which the batch is injected simply defines a certain, allowed energy range $\pm\Delta\hat{E}$. As long as particles stay inside this energy range they are assumed to be captured.

With a total average energy loss of 72 MeV per particle and an external barrier RF voltage of 2 MV one computes with this method that 39 % of the injected particles should be captured in between the two barriers. In the case of 4 MV RF voltage about 83 % of the injected particles should have been captured. Stationary beam loading has been taken into account. Even though this should be only regarded as a rough estimation because of many assumptions, the results agree quite well with measured values (defined in Section A.5.1).

A.6 Moving the barriers inside the long bunch

As a further experiment, it was also tried to vary the thickness of the barriers to simulate a barrier which moves in phase. Considering the hardware set-up it was however predicted that batch compression by the moving barrier should not take place.

An overview sketch of the barrier bucket generation in the SPS has been given in Fig. A.3. The RF barriers are generated by switching on and off the main 200 MHz RF chain. By doing so, only the amplitude of the 200 MHz RF structure is modulated whereas the phase of the RF signal itself always stays constant in phase with respect to beam at reference energy. If the barrier size is made variable by changing the drive pulse length, only the phase of the amplitude modulation is changed, and not the 200 MHz phase (Fig. A.16). On the contrary, for a real moving barrier the 200 MHz phase should also be shifted synchronously with the amplitude modulation phase shift (Fig A.15).

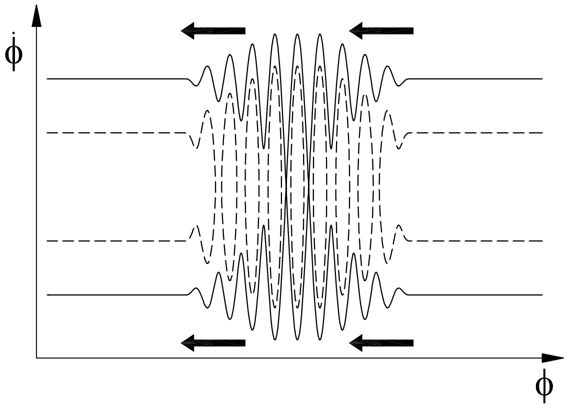

Fig. A.15: Longitudinal phase space for a moving barrier. The phase of the barrier is shifted to the left. If the phase of the amplitude modulation and also the phase at 200 MHz is shifted synchronously, the thick barrier is moved smoothly. Virtually no particles penetrate the barrier and batch compression is possible.

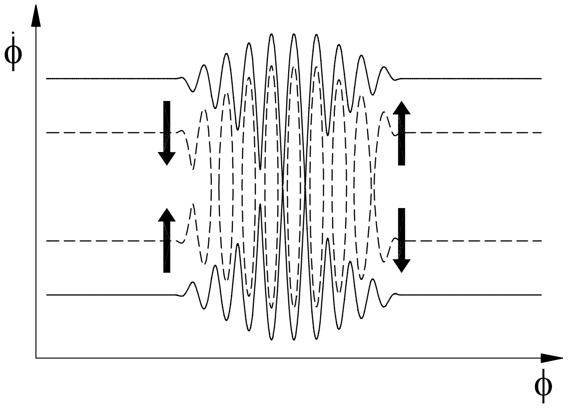

Fig. A.16: Scheme applied in the SPS: same longitudinal phase space as in Fig. A.15 but only the phase of the amplitude modulation is moved now while the 200 MHz phase stays constant. Moving the amplitude modulation to the left, some populated phase space is separated from the main bunch and penetrates into the barrier.

Changing only the phase of the RF amplitude modulation as was done in SPS is not sufficient to achieve batch compression. Increasing the length of the barrier simply leads to capture of some part of the bunch into the barriers. This is exactly what has been measured. Fig. A.17 shows a long bunch which is still unbunched for about half of its length whereas half of the bunch has penetrated inside the barriers and is simply a bunched beam in stationary 200 MHz buckets. Observations in the SPS are thus in agreement with this model.

A.7 Conclusions from the barrier bucket experiment

As the barrier bucket technique is regarded to be a promising scheme to increase the luminosity in LHC, the SPS was used as test bed to study the behaviour of long bunches kept by RF barriers. A first beam experiment on barrier buckets was carried out below transition at 14 GeV, with low beam intensities and fixed target beam. During the second experiment all tests have been performed with one standard LHC batch injected from the PS above transition at an energy of 26 GeV and an intensity of $2.9 \cdot 10^{12}$ p/batch.

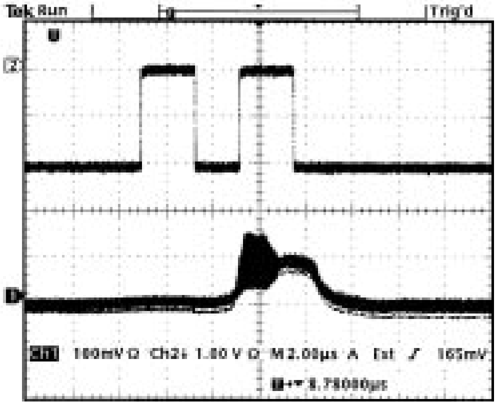

Fig. A.17: Moving only the modulation amplitude does not compress the bunch. About half of the long bunch is rather captured inside the barrier (lower trace). Initial point for this measurement was a stationary long bunch similar to Fig. A.5.

The maximum intensity, which corresponds to one third of the nominal intensity for the LHC, was limited by strong beam loading effects in the 200 MHz TW cavities. On the one hand, the large 200 MHz component of the injected batch caused transient beam loading and on the other hand, stationary beam loading reduced the effective voltage, which was available for the RF barrier. Due to the absence of feedback and feed-forward loops, the beam loading was not compensated. This can be avoided in future experiments by two possible counter measures: firstly, the transient effects during the capture process could be suppressed by capture of the LHC batch by two TW cavities with servo loops switched on, while the other two TW cavities are operated in barrier mode. After capture, the batch could be debunched adiabatically to the barrier bucket. Secondly, the injection of a debunched beam from the PS with a line density modulation as low as possible would decrease the 200 MHz component and lower the transient beam loading.

The effect of the transient beam loading during the first 200 turns after injection leads to an energy loss due to energy transferred from the beam to the 200 MHz TW cavities. Calculations for the average energy loss of the beam, which is in the range of 72 MeV per proton, are found to be in good agreement with the measured number of captured particles.

It is be shown that in the stationary case, when the transient effects had decayed a few seconds after injection, no significant longitudinal density modulation along the bunch was detected and the bunch could be kept stable for more than 80 min at the injection flat bottom. As the beam energy was widely spread by the large beam loading at injection, the particle density in the longitudinal phase space was reduced by more than one order of magnitude so that no instabilities could be observed.

The barrier bucket experiment has shown that if barrier buckets will be used in LHC, special attention has to be paid to RF gymnastics in the presence of strong beam loading. In the SPS the implementation of counter measures against the beam loading effects should allow higher particle densities to be stored in between the barriers and to observe possible instabilities in the long bunch.

Appendix B

Creation of Special Bunch Patterns in the PS Complex

The bunch combination scheme to create long and flat bunches in the LHC is based on trains of either 16 or 32 bunches with spacing of 25 ns. In between these trains, gaps of two or four non-populated bunch positions are required. Preferably, such bunch patterns should be generated directly in the PS complex so that the beam can pass the SPS without further RF manipulations. It is important to point out that the PS complex at the time of a long bunch LHC upgrade might also have undergone significant upgrades itself like the construction of a new injector linac with an energy above 2 GeV or the replacement of the PS Booster by a new rapid cycling or multi-ring synchrotron [175]. Therefore, only some basic ideas shall be given in this appendix on the means to generate the required bunch patterns required by the long bunch combination scheme.

B.1 Bunch pattern for the combination of 16 bunches

The sub-bunch pattern at the beginning of the combination can be written as $16 \otimes b \oplus 2 \otimes e$ and it fits four times into the circumference of the ring so that the full PS bunch pattern at the harmonic number $h = 84$ becomes

$$4 \otimes (16 \otimes b \oplus 2 \otimes e) \oplus 12 \otimes e \, .$$

Assuming at least one conventional bunch pair splitting on the PS flat-top this could be reduced to

$$4 \otimes (8 \otimes b \oplus 1 \otimes e) \oplus 6 \otimes e \, , \tag{B.1}$$

but afterwards no further symmetry remains. Either options can be found to intentionally remove bucket without disturbing the rest of the bunch or train or the PS must be equipped with an additional acceleration system to accelerate the protons from 1.4 GeV to 26 GeV on $h = 42$. Such an RF system must cover the frequency range from 18.4 to 20.0 MHz so that ferrite tuned coaxial resonators could be used to keep the power consumption within reasonable limits [241]. Moreover, the PSB RF systems cannot provide eight bunches per ring and the transition times of the kickers in the transfer line to the PS are too long to allow such a bunch pattern.

The high energy injector linac, the Superconducting Proton Linac (SPL), would be the ideal solution for this problem and the bunch pattern (see Eq. B.1) could be generated from the source without special difficulties.

B.2 Bunch pattern for the combination of 32 bunches

A simpler solution can be found for the case of 32 bunches. It resembles a scheme presented in [242]. The final bunch pattern in the PS in this case is given by

$$2 \otimes (32 \otimes b \oplus 4 \otimes e) \oplus 12 \otimes e \tag{B.2}$$

and a possible way to generate such a pattern can be sketched as follows (Fig. B.1): Firstly, four times four bunches are injected from the booster working at $h = 5$ into matched buckets of the corresponding harmonic in the PS ($h = 20$) in such a way the bunches from two booster rings are stringed up without any gap followed by a gap of one bunch position. Secondly, the harmonic number is adiabatically increased by batch compression to $h = 21$ so that the corresponding bunch pattern becomes

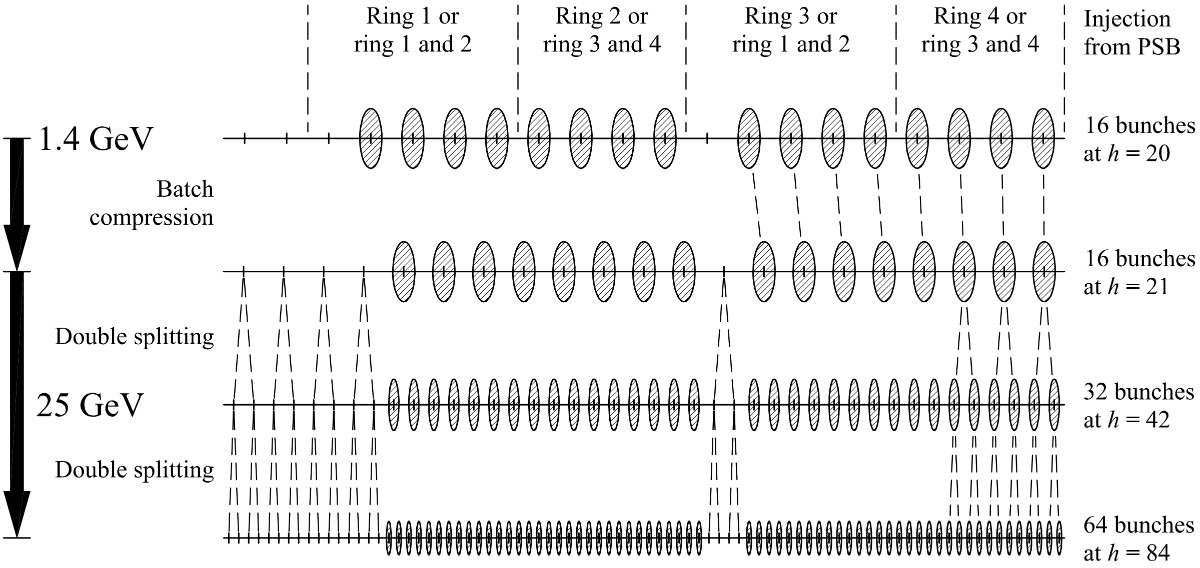

Fig. B.1: Beam preparation scheme to generate trains of 32 bunches with gaps of four empty bucket positions in the PS.

$$2 \otimes (8 \otimes b \oplus 1 \otimes e) \oplus 3 \otimes e\,.$$

Such a pattern can be accelerated with the present 10 MHz main RF system installed in the RF to 26 GeV. Similar to the production of the nominal LHC bunch train, the bunches are finally split twice at the flat-top with existing RF equipment and the resulting bunch pattern corresponds to Eq. (B.2). It is worth noting that the re-combination scheme from the booster also demands shorter kicker rise times than presently available and about 30 ns switching time should be reached between at least two pairs of booster rings. Again in that case, a new injector linac could provide the bunch pattern Eq. (B.2) directly on $h = 21$ without needing the harmonic hand-over from $h = 20$ to 21.

Appendix C

Fast Batch Compression RF Gymnastics in the SIS100

A similar RF manipulation for the combination of bunches as discussed for the long bunch option in the LHC is proposed to be applied in the planned SIS100 of the FAIR project at GSI.

C.1 Introduction

For the physics with radioactive ion beams as well as the plasma physics programme at the GSI future facility (FAIR) it is essential to generate extremely short and intensive ion bunches in the energy range of some 400 MeV/u to 2.7 GeV/u. The largest acceptable bunch length is given by the thermodynamic expansion time of the targets, which is in the order of 50 ns. The accelerator foreseen to produce these bunches is the SIS100 (Schwere-Ionen-Synchrotron) that will have a magnetic rigidity of 100 Tm and a circumference of 1083.6 m which is five times the circumference of its injector, the existing SIS12/18.

In the present stage of planning the SIS12 will deliver four times two bunches to the SIS100. The main RF system of the SIS12 will be operated at the second harmonic of the revolution frequency while the SIS100 will be equipped with an RF system working at the tenth harmonic. Thus, eight bunches will be injected into the SIS100 and accelerated to the desired flat-top energy.

In the design report of the FAIR facility a sophisticated barrier bucket RF gymnastics was suggested to confine these eight bunches to one single bunch and to compress it to its final bunch length in the range of 50 ns by means of fast bunch rotation in the longitudinal phase space [243, 244]. On the one hand, this solution requires a complex and costly barrier bucket RF system. On the other hand, the bunch compression by adiabatically moving barriers in longitudinal phase space takes too long compared to the acceleration time assumed that the emittance blow-up is kept within reasonable limits. Therefore, a new scheme of subsequent batch compression and bunch merging avoiding the disadvantages mentioned above is proposed which is based on the same bunch combination RF gymnastics as the long and flat bunch upgrade option in the LHC. It will be possible to make extensive use of the RF system with which the synchrotron will be equipped for acceleration.

C.2 The batch combination procedure for the SIS100

The heavy ion synchrotron SIS100 will be equipped with an acceleration system based on magnetic alloy or ferrite loaded RF systems covering a frequency range of at least 1.1 to 2.4 MHz (considering that acceleration will take place at harmonic $h = 10$). Such an RF frequency range allows RF manipulations at flat-top energy, e.g. an Uranium U^{28+} beam at 400 GeV/u, between the harmonic numbers $h = 5$ to 10. Furthermore, the RF acceleration system is planned to work at rather high synchronous phase of up to 30 - 40^0 so that at fixed energy even part of its voltage is sufficient to produce bucket areas much larger than the bunch emittances.

Therefore, the following scenario is suggested for the pre-compression of a single intense ion bunch: firstly, four cycles of two bunches each are injected to SIS100 at a kinetic energy of 100 MeV/u. As the SIS100 has five times the circumference of its injector SIS18, there will be two empty buckets, thus only 80 % of the machine is occupied. These bunches are accelerated to flat-top energy and secondly merged to four bunches at $h = 5$. Thirdly, the four bunches are confined to one single bunch using subsequent batch compression and bunch pair merging. Finally one ends up with a single bunch at $h = 5$ which may then be compressed by fast bunch rotation to its desired length of about 50 ns. It is important to point out that additional amplitude modulation during the batch compression as introduced Sec. 5.2.4 is required to preserve sufficient bucket areas along the batch. An overview of bunch patterns and harmonic numbers used during the scheme is given in Tab. C.1. The movement and merging of the buckets during the RF gymnastics is shown in Fig. C.1.

	Bunch pattern	Harmonic numbers
1. Bunch merging	$8 \otimes b \oplus 2 \otimes e \rightarrow 4 \otimes b \oplus 1 \otimes e$	$10 \rightarrow 5$
1. Batch compression	$4 \otimes b \oplus 1 \otimes e \rightarrow 4 \otimes b \oplus 6 \otimes e$	$5 \rightarrow 6 \rightarrow 7 \rightarrow 8 \rightarrow 9 \rightarrow 10$
2. Bunch merging	$4 \otimes b \oplus 6 \otimes e \rightarrow 2 \otimes b \oplus 3 \otimes e$	$10 \rightarrow 5$
2. Batch compression	$2 \otimes b \oplus 3 \otimes e \rightarrow 2 \otimes b \oplus 8 \otimes e$	$5 \rightarrow 6 \rightarrow 7 \rightarrow 8 \rightarrow 9 \rightarrow 10$
3. Bunch merging	$2 \otimes b \oplus 8 \otimes e \rightarrow 1 \otimes b \oplus 5 \otimes e$	$10 \rightarrow 5$
Fast Bunch rotation		2

Tab. C.1: Bunch patterns and harmonic numbers for the proposed batch compression scheme in the SIS100.

C.2.1 Adiabaticity and emittance development

The RF gymnastics to compress and merge the initial bunches to a single dense bunch should be as fast as possible, whereas longitudinal blow-up should be kept within acceptable limits. Several tracking calculations were done to estimated the expected emittance increase for various time lengths. Figs. C.2 to C.5 show the emittance development for different velocities of the batch compression RF gymnastics.

The initial emittance was assumed to be 8×12.5 eVs (total of all charges, U^{28+}) corresponding to a coasting beam with a momentum spread of $\Delta p/p \simeq 5 \times 10^{-4}$ in the SIS12. The emittance given is calculated by summing up the areas of optimized ellipses containing 99 % of the particles of each bunch. This explains why the calculated emittance may be slightly below the initial assumption. The calculation for the 6 s long procedure is for reference only but demonstrates that the RF gymnastic is indeed very clean when the adiabaticity is well respected. The short emittance growths during the bunch mergings arises because ellipses give insufficient approximations of the bunch distribution; but this is only a numerical effect. The bunch boundary is totally non-elliptic during merging.

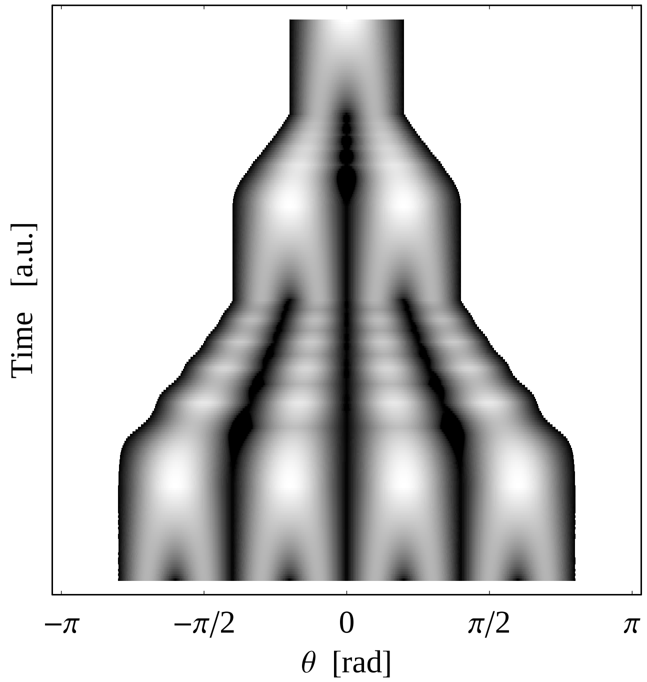

Fig. C.1: Movement and merging of the RF buckets during batch compression in the SIS100. The gray level is proportional to the square root of the energy height of the separatrix at a given θ. White areas signify that there is no occupied bucket.

From these calculation it is visible that even for a batch compression as short as 0.12 s, the emittance blow-up is still acceptable with some 40 %. However, the emittance is much more diluted by an even faster RF gymnastics and the optimum is a trade-off between dilution and time. It is worth noting that beam induced effects, which are neglected so far, may lead to further blow-up especially when the batch compression takes a rather long time. Taking these effects into account may lead to a well defined emittance blow-up minimum.

C.3 Hardware requirements

A main advantage of the proposed RF gymnastics is that only little additional high power RF hardware will be required. The scheme relies heavily on the flexibility of the acceleration system in the SIS100. As mentioned, it will cover the harmonics from 5 to 10 at flat-top and delivering some 400 kV. Thus it matches very well to the requirements of the batch compression procedure.

The RF voltage needed for the main carriers during batch compression is about 100 kV. Therefore, the cavities of the acceleration are split in groups: the first two groups generate both main carriers for the batch hand-over to the next higher harmonic number. A third group contains the same number of cavities but produces no RF voltages as it is tuned and prepared for the next harmonic number. The cavities left will be used to generate the two amplitude modulation carriers. The cyclic operation of the cavity groups is sketched in Fig. C.6, whereas the complete voltage program is shown in Fig. C.7. The grouping of the cavities is proposed such that always one spare group capable of delivering some 100 kV is tuned without amplitude and thus no time is lost due to limitations of the cavity tuning speed.

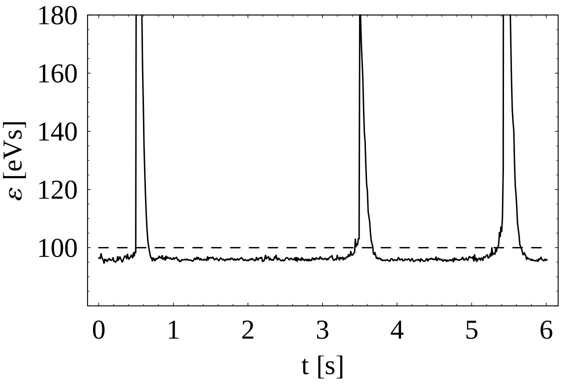

Fig. C.2: Emittance development during the batch compression lasting 6 s.

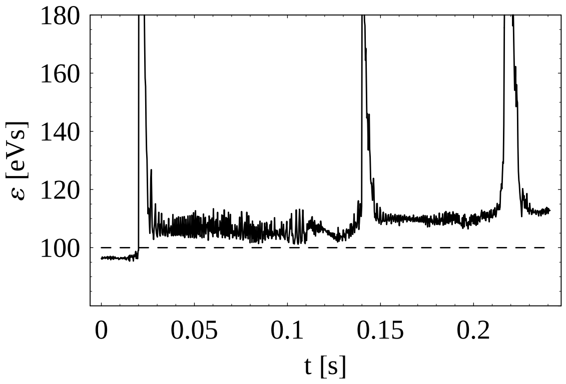

Fig. C.3: Emittance development during the batch compression lasting 240 ms.

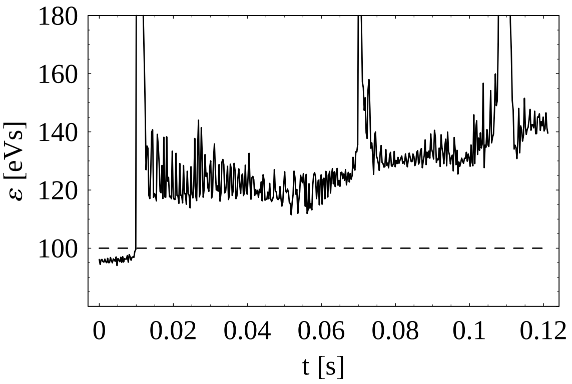

Fig. C.4: Emittance development during the batch compression lasting 120 ms.

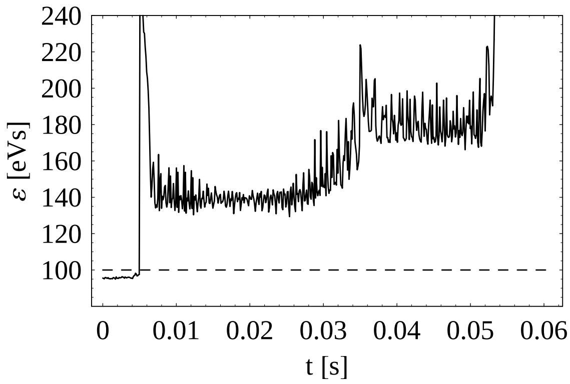

Fig. C.5: Emittance development during the batch compression lasting 60 ms. The vertical scale is different from the other plots.

However, two additional RF systems will be necessary as the equilibrated batch compression needs some 20 kV at $h = 4$ and $h = 11$ during the beginning and the end of the two batch compressions. These two frequencies might not be covered by the main acceleration system. As their voltage is quite moderate and they are only operated at fixed frequencies, the additional costs are much less compared to other schemes [243].

C.4 Conclusions

An RF gymnastics scheme to confine all bunches of an eight bunch batch in the SIS100 by repetitive use of batch compression and bunch merging to a single, dense bunch is proposed and analyzed. This scenario makes extensive use of the acceleration RF system which has to be installed by definition. In addition to the low level RF equipment required to provide flexibility of the acceleration system, only two fixed frequency RF systems at moderate amplitudes have to be installed additionally.

Furthermore, the scheme has several inherent advantages. Firstly, it consists of a chain of conventional RF gymnastics which have been proven at different accelerators to work well up to largest particle intensities. Secondly, the beam is always kept at large RF voltages meaning that RF focusing is strong and the beam can be kept under control of feedback loops if necessary.

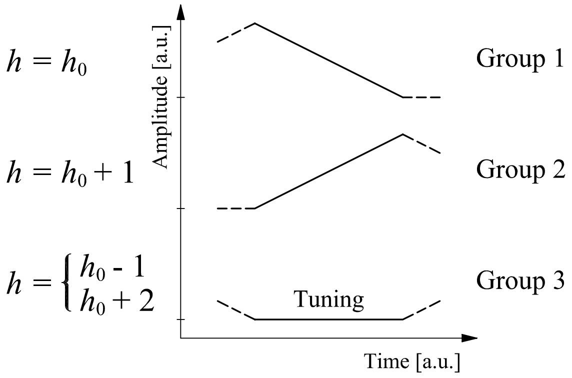

Fig. C.6: Amplitudes of the first three groups of RF cavities. For simplicity the amplitude variations are assumed to be linear. Furthermore, the modulation cavities are not shown.

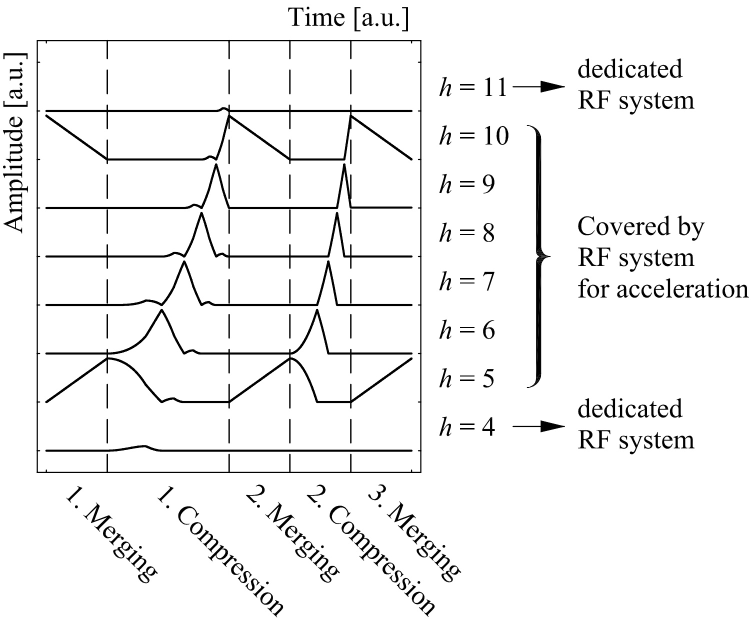

Fig. C.7: Voltage programme for the complete compression RF gymnastics in the SIS100. The amplitudes are normalized to 100 kV. It should be mentioned that no more than four RF systems act on the beam simultaneously. This can be easily achieved by the described grouping of RF cavities. The RF phases are generally fixed but have to be switched by 180^0 for the third bunch merging. The bucket configuration of the voltage programme has been illustrated in Fig. C.1.

Finally, as a consequence of the large RF amplitudes, the proposed scenario can be executed within 0.12 s, while the longitudinal emittance blow-up caused by dilution stays reasonable. This amount of time required at flat-top energy is not negligible but at least comparable to the duration of the acceleration (0.1–0.2 s, [245]).

It should be mentioned that collective effects caused high beam current are not covered here and should be investigated elsewhere. Especially direct space charge is supposed to limit the performance at low extraction energies. Flat-topping [246] or hollow bunch techniques [247] could be added for improvement. However, a good candidate for a scheme to perform the bunch pre-compression in the SIS100 is found and should be analyzed in more detail. In the case of an RF acceleration system working at the 20th harmonic, a similar scheme could be applied, but the bucket area of such a system would not be sufficient to end up with a single bunch. Additional RF installations would be necessary.

The investigation of different scenarios for the final bunch compression indicates that the RF acceleration system can be utilized to optimize the synchrotron frequency distribution for linearization during bunch rotation. Approximately 1.5 times more particles, some 80 % of the bunch, are transported to the desired target emittance ellipse ($\tau = 50\,\mathrm{ns}$, $\Delta p/p = 0.01$). Finally, the possibility of a staged installation of the RF systems in SIS100 should be considered. Even without the very costly bunch rotation system bunches with some 150 ns length can be obtained.

Appendix D

Synchrotron Frequency in an Accelerating Bucket

The synchrotron frequency distribution of particles oscillating in the longitudinal phase space of a stationary bucket has been derived in Sec. 2.2.6. The calculation is extended to the general case of particles in a single harmonic accelerating bucket in what follows. The order of the approximations is chosen so that the first term which is dependent on ϕ_0 is kept.

The Hamiltonian of motion for the interaction of particles with one RF system is given by Eq. (2.20)

$$H(\Delta\phi, \dot{\phi}) = \frac{1}{2}\dot{\phi}^2 + \frac{\omega_s^2}{\cos\phi_0}[\cos\phi_0 - \Delta\phi\sin\phi_0 - \cos(\phi_0 + \Delta\phi)]\,. \tag{D.1}$$

Replacing the trigonometric expressions by their Taylor expansion up to fourth order in $\Delta\phi$ and division by the constant factor $h\eta\omega_0$ leads to [248]

$$H\left(\Delta\phi, \frac{\Delta p}{p}\right) = \frac{1}{2}h\omega_0\eta\left(\frac{\Delta p}{p}\right)^2 + \frac{1}{2}\frac{\omega_0}{h\eta}Q_s^2\left[\Delta\phi^2 - \frac{1}{6}\Delta\phi^3\tan\phi_0 - \frac{1}{12}\Delta\phi^4 + \ldots\right], \tag{D.2}$$

where $Q_s = \omega_s/\omega_0$ denotes the synchrotron tune.

The Hamiltonian can be converted to a new set of so-called action-angle variables by applying the transformation function (see e.g. [249])

$$F_1(\Delta\phi, \psi) = -\frac{Q_s}{2h|\eta|}\Delta\phi^2\tan\psi\,.$$

According to the transformation equations

$$J = -\frac{\partial F_1}{\partial\psi} = \frac{Q_s}{2h|\eta|}\Delta\phi^2\frac{1}{\cos^2\psi} \qquad \text{and} \qquad \frac{\Delta p}{p} = -\frac{Q_s}{h|\eta|}\Delta\phi\tan\psi \tag{D.3}$$

the old set of variables is expressed by

$$\Delta\phi = \sqrt{\frac{2h|\eta|J}{Q_s}}\cos\psi \qquad \text{and} \qquad \frac{\Delta p}{p} = -\sqrt{\frac{2Q_sJ}{h|\eta|}}\sin\psi\,.$$

After some algebraic transformations the Hamiltonian can be rewritten as

$$H(\psi, J) = \omega_0 Q_s J - \frac{1}{12}\omega_0\sqrt{h|\eta|Q_s}\tan\phi_0 J^{3/2}(\cos 3\psi + 3\cos\psi) - \frac{1}{6}\omega_0 h|\eta|J^2\cos^4\psi\,, \tag{D.4}$$

where the relation $\cos^3\psi = (\cos 3\psi + 3\cos\psi)/4$ has been used. The next step is the removal of the terms proportional to $J^{3/2}$ by application of the canonical perturbation theory [250]. Choosing

$$F_2(\psi, I) = \psi I + G_3(I)\sin 3\psi + G_1(I)\sin\psi \tag{D.5}$$

as general attempt for a generating function to convert the action J into a new action-angle variable I [248], the transformation equation simply becomes

$$J = \frac{\partial F_2}{\partial\psi} = I + 3G_3(I)\cos 3\psi + G_1(I)\cos\psi\,.$$

This expression is inserted into the Hamiltonian and the functions $G_1(I)$ as well as $G_3(I)$ are calculated so that terms proportional to $I^{3/2}$ vanish. To get the conditional equations it is thus sufficient to keep only orders below I^2:

$$\begin{aligned} H(\psi, I) = {} & \omega_0 Q_s I + 3\omega_0 Q_s G_3(I)\cos 3\psi + \omega_0 Q_s G_1(I)\cos\psi \\ & - \frac{1}{12}\omega_0\sqrt{2h|\eta|Q_s}\tan\phi_0 I^{3/2}(\cos 3\psi + 3\cos\psi) + \mathcal{O}(I^2)\,. \end{aligned} \tag{D.6}$$

Now it becomes clear that the choice of the generating function Eq. (D.5) is reasonable and the conditional equations for $G_1(I)$ and $G_3(I)$ become

$$\begin{aligned} \left(\omega_0 Q_s G_1(I) - \frac{1}{4}\sqrt{2h|\eta|Q_s}\tan\phi_0 I^{3/2}\right)\cos\psi &= 0 \\ \text{and}\quad \left(3\omega_0 Q_s G_3(I) - \frac{1}{12}\sqrt{2h|\eta|Q_s}\tan\phi_0 I^{3/2}\right)\cos 3\psi &= 0 \end{aligned}$$

so that the functions can be written as

$$G_1(I) = \frac{1}{4}\sqrt{\frac{2h|\eta|}{Q_s}}\tan\phi_0 I^{3/2} \quad \text{and} \quad G_3(I) = \frac{1}{36}\sqrt{\frac{2h|\eta|}{Q_s}}\tan\phi_0 I^{3/2}\,. \tag{D.7}$$

The general transformation equation (D.5) reduces to

$$J = I + \frac{1}{12}\sqrt{\frac{2h|\eta|}{Q_s}}\tan\phi_0 I^{3/2}(\cos 3\psi + 3\cos\psi)\,. \tag{D.8}$$

To insert this result into the Hamiltonian Eq. (D.4) powers of J with a precision up to an order of I^2 have to be derived according to

$$\begin{aligned} J &= I(1 + aI^{1/2}) \\ J^{3/2} &= I^{3/2}\left(1 + \frac{3}{2}aI^{1/2}\right) + \mathcal{O}(I^{5/2}) \\ J^2 &= I^2(1 + aI^{1/2} + a^2 I) = I^2 + \mathcal{O}(I^{5/2}) \end{aligned}$$

so that the Hamiltonian including perturbation orders up to $\mathcal{O}(I^2)$ can be rewritten as

$$H(\psi, I) = \omega_0 Q_s I - \frac{1}{6}\omega_0 h|\eta| I^2\cos^4\psi - \frac{1}{3}\omega_0 h|\eta| I^2\tan\phi_0\cos^6\psi\,. \tag{D.9}$$

For the calculation of the oscillating frequency the knowledge of the averaged Hamiltonian over one oscillation period in ψ is sufficient and according to

$$< \cos^4 \psi >= \frac{3}{8} \qquad \text{and} < \cos^6 \psi >= \frac{5}{16}$$

the averaged Hamiltonian

$$<H(I,\psi)> = <H> = \omega_0 Q_s I - \frac{1}{16}\omega_0 h|\eta| \left(1 + \frac{5}{3}\tan^2\phi_0\right) I^2 \tag{D.10}$$

is obtained.

As introduced in Sec. 2.2.6 the synchrotron frequency can be derived directly from the Hamiltonian in action-angle variables, namely

$$\omega(I) = \frac{\partial <H>}{\partial I} = \omega_0 Q_s \left[1 - \frac{h|\eta|}{8Q_s}\left(1 + \frac{5}{3}\tan^2\phi_0\right) I\right] . \tag{D.11}$$

Now the action-angle variable I remains to be converted back to phase space coordinates. With respect to the set of canonical transformations Eq. (D.3) applied to the Hamiltonian, the action-angle variable ψ vanishes in case of an oscillating test particle reaching its maximum phase excursion at $\Delta\phi_m = \sqrt{2h|\eta|J/Q_s}$. Up to the first leading order the second transformation just gives $J \simeq I$ so that

$$I \simeq \frac{Q_s}{2h|\eta|}\Delta\phi_m^2 .$$

Finally, the dependence of the synchrotron frequency on the maximum phase excursion $\Delta\phi_m$ can be written as [33, 251]

$$\frac{\omega(\Delta\phi_m)}{\omega_s} \simeq 1 - \frac{1}{16}\left(1 + \frac{5}{3}\tan^2\phi_0\right)\Delta\phi_m^2 , \tag{D.12}$$

which is identical to Eq. (2.44).

It is worth noting that some authors use slightly different relations which might be based on other approximations of the Hamiltonian, see e.g. [206, 252].

Appendix E

Derivation of Betatron Tune Shifts

Forces acting focusing or defocusing can be generally approximated as an additional element in the machine lattice which shifts the betatron frequencies of a circular accelerator. This interpretation is independent of whether the forces have their origin in real quadrupole magnets, in self-field of the beam, like in the case of space-charge, or in field generated by a counter-rotating beam. In what follows, it is assumed that both transverse phase space planes are well decoupled so that the derivation can be simplified to one transverse direction only.

It can be shown from the general solution of the transverse particle motion in connection with the condition for periodicity from one turn to the next that the transformation matrix for the a particle with the initial offset x at its local derivation $x' = dx/dz$ can be written as [253]

$$\begin{aligned} \begin{pmatrix} x \\ x' \end{pmatrix}_{z_0+2\pi R} &= M_{z_0\to z_0+2\pi R} \begin{pmatrix} x \\ x' \end{pmatrix}_{z_0} \qquad \text{with} \\ M_{z_0\to z_0+2\pi R} &= \begin{pmatrix} \cos 2\pi Q + \alpha_0 \sin 2\pi Q & \beta_0 \sin 2\pi Q \\ -\gamma_0 \sin 2\pi Q & \cos 2\pi Q - \alpha_0 \sin 2\pi Q \end{pmatrix} , \end{aligned} \tag{E.1}$$

where Q is the number of betatron oscillations per revolution and β_0, $\alpha_0 = -\beta'|_{z=z_0}/2$ as well as $\gamma_0 = (1+\alpha_0^2)/\beta_0$ are the optical functions at the position z_0 of the perturbation. The transverse beam dimension is proportional to $\sqrt{\beta(z)}$. The transformation matrix of a quadrupole acts only on the beam divergence and is given by

$$M_\mathrm{Q} = \begin{pmatrix} 1 & 0 \\ -kl & 1 \end{pmatrix} . \tag{E.2}$$

The length of the quadrupole in z-direction is defined by l and its so-called strength[1] is k in units of $[k] = 1/\mathrm{m}^2$. The quadrupole strength is defined for a magnetic field that vanishes at the beam center and that grows linearly with the distance (see Sec. 4.2.2):

$$k_x = \frac{e}{p}\frac{dB_y^\mathrm{quad}}{dx} = -\frac{1}{m_0\gamma\beta^2c^2}\frac{dF_x}{dx} \quad \text{and} \quad k_y = -\frac{1}{m_0\gamma\beta^2c^2}\frac{dF_y}{dy} . \tag{E.3}$$

It is worth noting that k_x and k_y are coupled for a quadrupole magnet [255] so that $k_x = -k_y = k$, which e.g. is not the case for beam-beam forces. The definitions above show that focusing or defocusing forces acting on the beam can be expressed by a short quadrupole at $z = z_0$ with

---

[1] The sign of the quadrupole strength is not unique in the literature, e.g. compare [253, 254].

length dz and Δk as its quadrupole strength. This additional element has to be added to the transformation matrix Eq. (E.1) so that the perturbed transformation for one turn becomes

$$M^{\text{pertub}}_{z_0+2\pi R} = \begin{pmatrix} 1 & 0 \\ -\Delta k\, ds & 1 \end{pmatrix} M_{z_0+2\pi R} \tag{E.4}$$

$$= \begin{pmatrix} \cos 2\pi Q + \alpha_0 \sin 2\pi Q & \beta_0 \sin 2\pi Q \\ \begin{matrix} -\Delta k\, dz\, (\cos 2\pi Q + \alpha_0 \sin 2\pi Q) \\ -\gamma_0 \sin 2\pi Q \end{matrix} & \begin{matrix} -\Delta k\, dz\, \beta_0 \sin 2\pi Q \\ + \cos 2\pi Q - \alpha_0 \sin 2\pi Q \end{matrix} \end{pmatrix} \tag{E.5}$$

which can be expressed in the form of an unperturbed transformation matrix with modified betatron tune:

$$M_{z_0+2\pi R}(Q + dQ) = \begin{pmatrix} \begin{matrix} \cos 2\pi(Q + dQ) \\ +\alpha_1 \sin 2\pi(Q + dQ) \end{matrix} & \beta_1 \sin 2\pi(Q + dQ) \\ -\gamma_1 \sin 2\pi(Q + dQ) & \begin{matrix} \cos 2\pi(Q + dQ) \\ -\alpha_1 \sin 2\pi(Q + dQ) \end{matrix} \end{pmatrix} . \tag{E.6}$$

The new optical functions α_1, β_1 and γ_1 also vary due to the perturbing quadrupole as an additional optical element.

Comparing Eq. (E.5) and (E.6) all matrix elements must be equal in general. For the derivation of the betatron tune only, it is however sufficient to compare the traces of the matrices [256, 257] so that relation between the perturbing quadrupole element parameters $\Delta k\, dz$ and the tune shift can be written as

$$2 \cos 2\pi Q - \Delta k\, dz\, \beta_0 \sin 2\pi Q = 2 \cos 2\pi(Q + dQ) \,,$$

and for $dQ \ll 1$ it reduces to

$$\Delta k\, dz\, \beta_0 = 4\pi\, dQ \,. \tag{E.7}$$

Finally, the finite tune shift is calculated by integration of Eq. (E.7) with respect to a beta function $\beta(z)$ that may vary along the quadrupolar perturbation:

$$\Delta Q = \frac{1}{4\pi} \int \Delta k(z) \beta(z)\, dz \,. \tag{E.8}$$

This result corresponds to Eq. (4.39).

Appendix F

The Direct Space Charge Tune Spread

The direct space charge tune spread which is regarded as an ultimate intensity limit for low and intermediate energy accelerators can be derived similarly to the calculation of the beam-beam tune spread as shown in Sec. 4.2. Firstly, the focusing or defocusing electromagnetic force is calculated, which is secondly transformed to a transverse tune shift[1] (see App. E).

In the most simple case of a long and round beam the transverse electric field and the magnetic induction outside the beam can be expressed by

$$E_x = \frac{I}{\pi \epsilon_0 \beta c} \cdot \frac{x}{a_x(a_x + a_y)}\,, \qquad E_y = \frac{I}{\pi \epsilon_0 \beta c} \cdot \frac{y}{a_y(a_x + a_y)}$$

and

$$B_x = -\frac{\mu_0 I}{\pi} \cdot \frac{y}{a_y(a_x + a_y)}\,, \qquad B_y = \frac{\mu_0 I}{\pi} \cdot \frac{x}{a_x(a_x + a_y)}\,,$$

where a_x and a_y denote the transverse radii of the elliptic beam. The transverse components of the Lorentz force for a round beam with $a = a_x = a_y$ thus become

$$F_x = \frac{eE_x}{\gamma^2} = \frac{eI}{2\pi \epsilon_0 \beta \gamma^2 c} \cdot \frac{x}{a}^2 \qquad \text{and} \qquad F_y = \frac{eE_y}{\gamma^2} = \frac{eI}{2\pi \epsilon_0 \beta \gamma^2 c} \cdot \frac{y}{a}^2\,. \tag{F.1}$$

Transforming these forces to tune shifts according to Eq. (E.8), reduces the direct space charge tune shift to

$$\Delta Q = \frac{eI}{8\pi^2 m_0 \beta^3 \gamma^3 c^3 \epsilon_0} \oint \frac{\beta(z)}{a(z)^2}\, dz\,. \tag{F.2}$$

It should be mentioned that the tune shift also can be calculated directly from Hill's equation of betatron motion [259]. As the beam radius $a(z)$ is proportional to the square root of the beta function numerator and denominator of the integrand have an identical dependence on z so that the integral may be expressed in terms of an averaged beta function: $2\pi R <\beta> /a^2$. Furthermore, the betatron function in the tune integral is replaced by average value over one turn according to

$$Q = \frac{1}{2\pi} \oint \frac{1}{\beta(z)}\, dz = \frac{R}{<\beta>}$$

---

[1] According to the analysis in [258] the incoherent space charge tune shift is also known as Laslett tune shift.

so that the tune shift can be written as

$$\Delta Q = \frac{eIR^2}{4\pi m_0 \beta^3 \gamma^3 c^3 \epsilon_0 Q a^2} \, . \tag{F.3}$$

Introducing the normalized transverse beam emittance $\varepsilon_n = a^2 Q/R$ and converting the current to the particle intensity $I = Ne\beta c/(2\pi R)$, which both remain constant throughout the acceleration, the tune spread finally reduces to

$$\Delta Q = \frac{Ne^2}{8\pi^2 \epsilon_0 \beta \gamma^2 m_0 c^2 \varepsilon_n} \, , \tag{F.4}$$

where its energy dependence proportional to $1/(\beta\gamma^2)$ becomes directly obvious.

It is worth noting that Eq. (F.4) is only the most simple case of the incoherent space charge tune shift. As the beam normally travels inside a metallic beam pipe, field corrections due to multiple image currents must be taken into account [260]. Additional geometrical corrections to different shapes of vacuum chamber and beam have to be added to Eq. (F.4) in the case of elliptic beams in a non-circular beam pipe [258].

List of Symbols

Symbol	Quantity	Unit
α	adiabaticity	–
α	inverse cavity filling time $\omega_r/(2Q)$	[1/s]
α	normalized energy separation for slip-stacking	–
α_c	momentum compaction factor, $1/\gamma_{\mathrm{tr}}$	–
$\alpha(\phi_0)$	bucket area reduction function	–
β	velocity relative to the speed of light, v/c	–
β	moving barrier bucket adiabaticity coefficient	–
β^*	betatron amplitude function at the interaction point	[m]
$\beta(z)$	betatron amplitude function	[m]
γ	ratio of total and rest mass	–
γ_{tr}	γ at transition energy	–
ϵ_0	vacuum permittivity, $8.854187817 \cdot 10^{-12}\,\mathrm{A\,s/(V\,m)}$	[A s/(V m)]
ε_0	initial longitudinal emittance	[eV s]
ε_l, $\varepsilon_{\mathrm{RMS}}$	longitudinal (RMS) emittance	[eV s]
ε_n	normalized transverse emittance	[m rad]
ζ	normalized longitudinal distribution	–
η	phase slip factor, $\alpha - 1/\gamma^2$	–
θ	particle phase with respect to the accelerator	[rad]
θ	full crossing angle	[rad]
$\lambda(\phi)$, $\lambda(z)$	normalized line density	[1/rad], [1/m]
μ_0	vacuum permeability, $4\pi \cdot 10^{-7}\,\mathrm{V\,s/(A\,m)}$	[V s/(A m)]
σ_x, σ_y, σ_z	beam dimensions	[m]
σ^*	transverse RMS beam dimension at the interaction point	[m]
ς	cross section	[m^2]
τ, $2\hat{\tau}$	total bunch duration	[s]
τ_{bc}, τ_{bm}	duration of batch compression, bunch merging	[s]
τ_{sep}	bunch spacing	[s]
$1/\tau$	instability growth rate	[1/s]
ϕ	particle phase with respect to RF phase	[rad]
ϕ_0	synchronous phase	[rad]
ϕ_l, ϕ_u	phase limits of a trajectory	[rad]
$\Delta\phi_l$, $\Delta\phi_u$	phase limits with respect to synchronous phase	[rad]
$\Delta\phi_m$	phase limits of a symmetric trajectory	[rad]
$\chi_{\mathcal{L}}$	luminosity form factor	–
ω	$2\pi \cdot$ frequency	[rad/s]
ω_0	$2\pi \cdot$ revolution frequency	[rad/s]

ω_r	$2\pi \cdot$ resonance frequency	[rad/s]
ω_s	$2\pi \cdot$ synchrotron frequency	[rad/s]
A, A_{eVs}	bucket area	[J s], [e Vs]
B	magnetic induction	[T]
c	speed of light in vacuum, 299792458 m/s	[m/s]
c_{sf}	space charge parameter	–
$D(\alpha\tau_{\mathrm{sep}})$	beam cavity coupling form factor	–
E	energy	[J], [eV]
E_x, E_r	electric field	[V/m]
E_0	energy of the reference particle	[J], [eV]
$\Delta\hat{E}$	bucket height	[J], [eV]
e	electron charge, $1.602177 \cdot 10^{-19}$ C	[C]
F	form factor of the order of unity	–
$\vec{F}_L$	Lorentz force, $e(\vec{E} + \vec{v} \times \vec{B})$	[N]
$F_0(x)$	fully normalized energy distribution	–
$F_m(2\omega_r\hat{\tau})$	bunch distribution form factor	–
f_0	revolution frequency	[Hz]
$f(\phi, \dot{\phi})$	normalized longitudinal distribution	[1/J]
$f(\theta, E)$	longitudinal beam distribution	[1/J]
$f_0(E)$	unperturbed beam energy distribution	[1/J]
$f_1(E)$	perturbation of the energy distribution	[1/J]
$f_0(\tau, \Delta E, z)$	longitudinal bunch distribution	[1/(J s)]
$f_0(\tau, \Delta E)$	unperturbed bunch distribution	[1/(J s)]
$f_1(\tau, \Delta E, z)$	perturbation of the bunch distribution	[1/(J s)]
f_b	harmonic weight form factor, two for short bunches	–
$\mathrm{fs}_{\mathrm{PS}}$, $\mathrm{fs}_{\mathrm{LHC}}$	filling scheme in the PS, LHC	–
$g(\phi)$	normalized RF amplitude function	–
$g(\theta, \Delta E/\omega)$	longitudinal beam distribution	[1/(rad J s)]
$g_0(r)$	normalized radial distribution	[1/s^2]
H	Hamiltonian, unit depends on normalization	(various)
h	harmonic number of the RF system	–
h_b	local harmonic number of barrier RF pulse	–
I, I_0	beam current	[A]
I	normalized action-angle variable	–
I_g, I_r, I_b	generator, resonator, harmonic beam current	[A]
$J(H)$	action-angle variable, unit depends on normalization	–
$J_m(x)$	Bessel function of the first kind	–
$K(x)$	complete elliptic integral of the first kind	–
k, k_x, k_y	quadrupole strength	[m]
$\mathcal{L}$	bunch crossing luminosity	[cm^{-2}s^{-1}]
$\mathcal{L}_{\mathrm{tot}}$	total luminosity	[cm^{-2}s^{-1}]
L	circumference of an orbit trajectory	[m]
l_b	total bunch length of a rectangular bunch	[m]
l_{det}	detector length	[m]
M	number of possible coupled bunch modes	–
$M_{z_1 \to z_2}$	beam optics transformation matrix	(matrix)
m	particle rest mass	[kg]

m	coupled bunch mode number	–
m_p	proton rest mass, $938.272\,\mathrm{MeV}/c^2 = 1.67262 \cdot 10^{-27}\,\mathrm{kg}$	[kg]
n	single bunch mode number	–
n_1, n_2	particle density	[1/m^3]
n_b	number of bunches	–
N	particle number	–
dN/dt	interaction rate	[1/s]
p	particle momentum	[kg m/s], [eV/c^2]
Q, Q_0, Q_g	quality factor, unloaded and external	–
Q_x, Q_y	horizontal, vertical betatron tune	–
ΔQ_x, ΔQ_y	betatron tune shift, spread	–
ΔQ_{tot}	total tune shift of two alternate crossings	–
R_{mag}	bending radius of the dipole magnets	[m]
R_{mean}, R	average radius, circumference/(2π)	[m]
R_s	shunt impedance of a resonator	[Ω]
R/Q	characteristic cavity impedance	[Ω]
r_p	classical proton radius, $1/(4\pi\epsilon_0 c^2)e^2/m_p \simeq 1.535 \cdot 10^{-18}\,\mathrm{m}$	[m]
t	time	[s]
$t_1(t)$	time equilibration function	[s]
S	half relative momentum spread at half height	[1/s]
U	RF voltage	[V]
v	velocity	[m/s]
W_0	energy loss or gain of the synchronous particle	[J], [eV]
$W(\phi)$	normalized RF potential function	–
Z	impedance	[Ω]
Z_0	vacuum impedance, $\sqrt{\mu_0/\epsilon_0} \simeq 377\,\Omega$	[Ω]
$Z_\parallel$	longitudinal broad band coupling impedance	[Ω]
$(Z_\parallel/n)_{\mathrm{eff}}$	effective longitudinal broad band impedance	[Ω]
z	longitudinal coordinate	[m]

The physical units in the figures and tables throughout this report are given in square brackets.

Bibliography

[1] V. E. Barnes, P. L. Connolly, D. J. Crennell, B. B. Culwick et al., *Observation of a Hyperon with Strangeness Minus Three*. Phys. Rev. Lett., Vol. 12, 1964, p. 204-206

[2] G. Arnison, A. Astbury, B. Aubert, C. Bacci et al., *Experimental Observation of Isolated Large Transverse Energy Electrons with Associated Missing Energy at* $\sqrt{s} = 540\,GeV$. Phys. Lett., Vol. 122B, 1983, pp. 103-116

[3] F. Abe, M. G. Albrow, S. R. Amendolia, D. Amidei et al., *Evidence for Top Quark Production in* $p\bar{p}$ *Collisions at* $\sqrt{s} = 1.8\,TeV$. FERMILAB-PUB-94/097-E, CDF/PUB/-TOP/PUBLIC/2561, Phys. Rev. D, Vol. 50, 1994, pp. 2966-3026

[4] J. Ellis, *The 115 GeV Higgs Odyssey*. CERN-TH/2003-307, CERN, Geneva, Switzerland, 2000

[5] V. Ruhlmann-Kleider, *Review of Higgs Boson Searches at LEP*. DAPNIA-04-81, Advanced Studies Inst. - Phys. at LHC, Prague, Tcheque Republic, 2003, in: Czechoslovak Journal of Phys., Vol. 54, Suppl. A, 2004, pp. A23-A34

[6] M. Jacob, K. Johnsen, *A Review of Accelerator and Particle Physics at the CERN Intersecting Storage Rings*. CERN 84-13, CERN, Geneva, Switzerland, 1984

[7] V. Hatton, *Operational History of the SPS Collider 1981-1990*. Part. Acc. Conf., San Francisco, California, 1991, pp. 2952-2954

[8] V. Shiltsev for the Collider Run II Team, *Status of Tevatron Collider Run II and Novel Technologies for Luminosity Upgrades*. Europ. Part. Acc. Conf., Lucerne, Switzerland, 2004, pp. 239-243

[9] R. Johnson, *Initial Operation of the Tevatron Collider*. Part. Acc. Conf., Washington, D.C., 1987, pp. 8-12

[10] M. Curch, *Tevatron Run II Performance and Plans*. Europ. Part. Acc. Conf., Paris, France, 2002, pp. 11-14

[11] E. Ciapala, *Stacking and Phase Displacement Acceleration*. CERN 85-19, CERN Acc. School on General Acc. Phys., Gif-sur-Yvette, France, 1984, pp. 195-225

[12] G. Brianti (ed.), Kurt Hübner (ed.), *The Large Hadron Collider in the LEP Tunnel*. CERN 87-05, CERN, Geneva, Switzerland, 1987

[13] The LHC Study Group, *Design Study of the Large Hadron Collider (LHC)*. CERN 91-03, CERN, Geneva, Switzerland, 1991

[14] P. Lefèvre (ed.), T. Petterson (ed.), D. Boussard, L. Evans et al., *LHC, The Large Hadron Collider.* CERN/AC/95-05 (LHC), CERN, Geneva, Switzerland, 1995

[15] O. Brüning, P. Collier, P. Lebrun, S. Myers et al., *LHC Design Report, Volume I, The LHC Main Ring.* CERN-2004-003, CERN, Geneva, Switzerland, 2004

[16] K. Takayama, J. Kishiro, M. Sakuda, Y. Shimosaki et al., *Superbunch Hadron Colliders.* Phys. Rev. Lett., Vol. 88, pp. 144801, 2002

[17] T. Suzuki, *Equations of Motion and Hamiltonian for Synchrotron Oscillations and Synchro-Betatron Coupling.* KEK Report 96-10, KEK, Tsukuba, Japan, 1996

[18] T. Suzuki, *Orbit Theory for Accelerators.* Asian Part. Acc. Conf., Beijing, China, 2001, pp. 463-465

[19] H. Bruck, *Accélérateurs Circulaires de Particules.* Institut National des Sciences et Techniques Nucléaires, Saclay, Presses Universitaires de France, Paris, 1966, p. 165

[20] H. Bruck, *Circular Particle Accelerators.* LA-TR-72-10 Rev., Los Alamos Scientific Laboratory, Los Alamos, New Mexico, 1972, English translation of [19], p. 173

[21] B. W. Montague, *Single-Particle Dynamics - RF Acceleration.* CERN 77-13, 1st Course of the Int. School on Part. Acc. Phys., Erice, Italy, 1976, pp. 63-81

[22] W. Pirkl, *Longitudinal Beam Dynamics.* CERN 95-06, CERN Acc. School on Advanced Acc. Phys., Rhodes, Greece, 1993, pp. 233-257

[23] K. Johnsen, *Effects of Non-Linearities on the Phase Transition.* CERN Symposium on High Energy Acc., CERN, Geneva, Switzerland, 1956, pp. 106-109

[24] H. G. Hereward, *What are the Equations for the Phase Oscillations in a Synchrotron?* CERN 66-6, CERN, Geneva, Switzerland, 1966

[25] V. E. Veksler, *A New Method of Accelerating Relativistic Particles.* Comptes Rendus (Dokaldy) de l'Academie Sciences de l'URSS, Vol. 43, 1944, pp. 329-331

[26] E. M. McMillan, *The Synchrotron - A Proposed High Energy Accelerator.* Phys. Rev., Vol. 68, 1945, pp. 143-144

[27] K. R. Symon, A. M. Sessler, *Methods of Radio Frequency Acceleration in Fixed Field Accelerators with Applications to High Current and Intersecting Beam Accelerators.* CERN Symposium on High Energy Acc., CERN, Geneva, Switzerland, 1956, pp. 44-58

[28] E. Ciapala, S. Myers, C. Wyss, *Phase Displacement Acceleration of High Intensity Stacks in the CERN ISR.* Part. Acc. Conf., Chicago, Illinois, 1977, pp. 1431-1433

[29] H. Damerau, M. Kirk, Y. Liu, *Maschinenexperimente zum longitudinalen Strahlverhalten während des Hochfrequenzeinfangs.* SIS28062.HF, GSI Darmstadt, Germany, 2002

[30] A. A. Andronow, C. E. Chaikin, *Theory of Oscillations.* Princeton, New Jersey, 1949, pp. 75-78

[31] H. Goldstein, *Classical Mechanics.* Addison-Wesley, Reading, Massachusetts, 2nd ed., 1985, pp. 457-461

[32] see [31], pp. 506-509

[33] B. Zotter, *Longitudinal Stability of Bunched Beams, Part II: Synchrotron Frequency Spread.* CERN SPS 81/19 (DI), CERN, Geneva, Switzerland, 1981

[34] B. Zotter, *Sacherer Formulae.* In: A. W. Chao (ed.), M. Tigner (ed.), *Handbook of Accelerator Physics and Engineering.* World Scientific, Singapore, Singapore, 1998, pp. 122-124

[35] A. G. Ruggiero, *Beam Stacking with Suppressed Buckets in the ISR.* CERN 68-22, CERN, Geneva, Switzerland, 1968

[36] K. Takayama, J. Kishiro, K. Koseki, E. Nakamura et al., *Superbunch Acceleration and its Applications.* Europ. Part. Acc. Conf., Paris, France, 2002, pp. 998-1000

[37] C. M. Bhat, *Barrier RF Systems in Synchrotrons.* Europ. Part. Acc. Conf., Lucerne, Switzerland, 2004, pp. 236-238

[38] J. E. Griffin, C. Ankenbrandt, J. A. MacLachlan, A. Moretti, *Isolated Bucket RF Systems in the Fermilab Anitproton Facility.* IEEE Trans. Nucl. Sci., Vol. NS-30, 1983, pp. 3502-3504

[39] A. M. Farson, *The Missing Bucket System.* CERN-ISR-RF-70-27, CERN, Geneva, Switzerland, 1970

[40] L. L. Foldy, *A Method for Expanding the Phase-Stable Regime in Synchronous Accelerators.* Il Nuovo Cimento, Vol. 19, 1961, pp. 1116-1120

[41] J. Claus, M. Month, *Exotic RF Systems for High Intensity High Energy Proton Storage Rings.* BNL 50469, ISA 75-12, Brookhaven Nat. Lab., Upton, New York, 1975

[42] S. Y. Lee, K. Y. Ng, *Particle Dynamics with Barrier RF Systems.* FERMILAB-Pub-96/403, Phys. Rev. E, Vol. 55, 1997, pp. 5992-6001

[43] C. M. Bhat, K. Y. Ng, *Potential-Well Distortion in Barrier RF.* FERMILAB-Conf-03/395-T, e^+e^- Factories 2003, Stanford, California, 2003, pp. WGB02

[44] J. A. MacLachlan, *Longitudinal Tracking With Space Charge and Inductive Wall Coupling Impedance.* FERMILAB-FN-446, Fermi National Accelerator Lab., Batavia, Illinois, 1987

[45] J. A. MacLachlan, J.-F. Ostiguy, *User's Guide to ESME2003.* Fermi National Accelerator Lab., Batavia, Illinois, 2003

[46] S. R. Koscielniak, *LONG1D User's Guide.* TRI-DN-97-12 v3.2, TRIUMF Vancouver, Canada, 2003

[47] A. Ando, K. Takayama, *$\bar{P}$ Bunch RF Rotation in the Debuncher Ring with Very Small η.* FERMILAB-TM-1073, Fermi National Accelerator Lab., Batavia, Illinois, 1981

[48] P. Lucas, J. A. MacLachlan, *Simulation of Space Charge Effects and Transition Crossing in the Fermilab Booster.* Part. Acc. Conf., Washington, D.C., 1987, pp. 1114-1116

[49] W. H. Press (ed.), Saul A. Teukolsky (ed.), W. T. Vetterling, B. P. Flannery, *Numerical Recipes in C++*. Camebridge University Press, Cambridge, U.K., 2nd ed., 2002, pp. 290-291

[50] P. M. Lapostolle, *Possible Emittance Increase through Filamentation due to Space Charge in Continous Beams*. IEEE Trans. Nucl. Sci., NS-18, 1971, pp. 1101-1104

[51] F. J. Sacherer, *RMS Envelope Equations with Space Charge*. IEEE Trans. Nucl. Sci., NS-18, 1971, pp. 1105-1107

[52] M. Weiss, *A Short Demonstration of Liouville's Theorem*. CERN 87-10, CERN Acc. School on Advanced Acc. Phys., Aarhus, Denmark, 1986, pp. 162-163

[53] S. van der Meer, *Stochastic Cooling of Betatron Oscillations in the ISR*. CERN/ISR-PO/72-31, CERN, Geneva, Switzerland, 1972

[54] S. van der Meer, *Stochastic Cooling and the Accumulation of Antiprotons*. In: Gösta Ekspong (ed.), *Nobel Lectures in Physics 1981-1990*. World Scientific, Singapore, Singapore, 1993, pp. 291-308

[55] G. I. Budker, *Status Report of Works on the Storage Rings at Novosibirsk*. Int. Symposium on Electron and Positron Storage Rings, Saclay, France, 1966, pp. II-1

[56] G. I. Budker, N. S. Dikansky, V. I. Kudelainen, I. N. Meshkov et al., *Experimental Studies of Electron Cooling*. Part. Acc., Vol. 7, 1976, pp. 197-211

[57] D. Neuffer, *Stability of Longitudinal Motion in Intense Ion Beams*. FERMILAB-FN-320, Fermi National Accelerator Lab., Batavia, Illinois, 1979

[58] A. Hofmann, F. Pedersen, *Bunches with Local Elliptic Energy Distributions*. IEEE Trans. Nucl. Sci., Vol. NS-26, 1979, pp. 3526-3528

[59] S. Hansen, H. G. Hereward, A. Hofmann, K. Hübner et al., *Effects of Space Charge and Reactive Wall Impedance on Bunched Beams*. IEEE Trans. Nucl. Sci., Vol. NS-22, 1975, pp. 1381-1384

[60] C. E. Nielsen, A. M. Sessler, *Longitudinal Space Charge Effects in Particle Accelerators*. Rev. Sci. Instr., Vol. 30, 1959, pp. 80-89

[61] V. K. Neil, A. N. Sessler, *Longitudinal Resistive Instabilities of Intense Coasting Beams in Particle Accelerators*. Rev. Sci. Instr., Vol. 36, 1965, pp. 429-436

[62] A. M. Sessler, V. G. Vaccaro, *Passive Compensation of Longitudinal Space Charge Effects in Circular Accelerators: The Helical Insert*. CERN 68-1, CERN, Geneva, Switzerland, 1968

[63] M. A. Plum, D. H. Fitzgerald, J. Langenbrunner, R. J. Macek et al., *Experimental Study of Passive Compensation of Space Charge at the Los Alamos National Laboratory Proton Storage Ring*. Phys. Rev. Special Topics - Acc. and Beams, Vol. 2, 1999, pp. 064201

[64] J.R. Maidment, E.A. Karantzoulis, *Longitudinal Space Charge via Multi Particle Simulation*. DESY HERA 88-09, Europ. Part. Acc. Conf., Rome, Italy, 1988, pp. 782-784

[65] R. Bossart, J. Bosser, L. Burnod, R. Coïsson et al., *Observation of Visible Synchrotron Radiation Emitted by a High-Energy Proton Beam at the Edge of a Magnetic Field*. Nucl. Instr. Meth., Vol. 164, 1979, pp. 375-380

[66] M. Sands, *The Physics of Electron Storage Rings*. SLAC-121, SLAC, Stanford, California, 1970, pp. 98-103

[67] C. G. Lilliequist, K. R. Symon, *Deviations from Adiabatic Behaviour during Capture of Particles into an R. F. Bucket*. MURA-491, Midwestern Universities Research Association, Madison, Wisconsin, 1959.

[68] R. Garoby, *RF Gymnastics in a Synchrotron*. In: A. W. Chao (ed.), M. Tigner (ed.), *Handbook of Accelerator Physics and Engineering*. World Scientific, Singapore, Singapore, 1998, pp. 287-292

[69] M. Bouthéon, J. Gareyte, *Adiabatic Trapping in the CERN PS*. Conf. High Energy Acc., Geneva, Switzerland, 1971, pp. 94-97

[70] H. Damerau, M. Emmerling, *Emittanzoptimierter Hochfrequenz-Einfang bei niedriger Strahlintensität*. SIS08012.HF, GSI Darmstadt, Germany, 2002

[71] D. G. Edwards, *Theoretical RF Trapping Behaviour for Various Time Functions of RF Voltage and Stable Phase Angle Without and With Space Charge Forces*. MPS/BR Note/73-17, CERN, Geneva, Switzerland, 1973

[72] I. Bozsik, I. Hofmann, A. Jahnke, R. W. Müller, *Numerical Investigation of Bunch-Merging in a Heavy-Ion-Synchrotron*. Proc. of Computing in Acc. Design and Operation, Berlin, 1983, pp. 128-133

[73] R. Garoby, *New RF Exercises Envisaged in the CERN-PS for the Antiprotrons Production Beam of the ACOL Machine*. IEEE Trans. Nucl. Sci., Vol. NS-32, 1985, pp. 2332-2334

[74] R. Garoby, *Bunch Merging and Splitting Techniques in the Injectors for High Energy Hadron Colliders*. CERN/PS 98-048(RF), Int. Conf. High Energy Acc., Dubna, Russia, 1998, pp. 172-174

[75] R. Garoby, *LHC Proton Beams in the PS: Status of Preparation and Capabilities*. CERN-AB-2003-008-ADM, LHC Performance Workshop, Chamonix XII, Chamonix, France, 2003, pp. 34-37

[76] R. Garoby, *Multiple Splitting in the PS: Results and Plans*. CERN-SL-2001-003 DI, LHC Workshop Chamonix, Chamonix XI, Chamonix, France 2001, pp. 32-36

[77] H. Damerau, *Vorschlag einer 20→1-Bunchmerging-Prozedur für die Vorbereitung des Strahls zur Bunchkompression im SIS100*. SIS25102.HF, GSI Darmstadt, Germany, 2002

[78] M. Benedikt, S. Hancock, J.-L. Vallet, *A Proof of Principle of Asymmteric Bunch Pair Merging*. AB-Note-2003-080 MD, CERN, Geneva, Switzerland, 2002

[79] C. Carli, *Creation of Hollow Bunches using a Double Harmonic RF System*. CERN/PS 2001-73 (AE), CERN Geneva, Switzerland, 2003

[80] C. Carli, M. Channel, *Creation of Hollow Bunches by Redistribution of Phase Space Surfaces.* CERN/PS 2002-19 (AE), Europ. Part. Acc. Conf., Vienna, Austria, 2000, pp. 233-235

[81] R. Garoby, *Proposal for a new Process Realizing Longitudinal Merging of Bunches in the CPS, while Conserving the Total Longitudinal Emittance of the Beam.* PS/RF/Note 83-15, CERN, Geneva, Switzerland, 1983

[82] R. Cappi, B. J. Evans, R. Garoby, *Status of the Anti-Proton Production Beam in the CERN PS.* Part. Acc., 1990, Vol. 26, pp. 217-222

[83] B. Autin, B. Bianchi, R. Billinge, D. Blechschmidt et al., *Design Study for a Proton-Antiproton Colliding Beam Facility.* CERN/PS/AA 78-3, CERN, Geneva, Switzerland, 1978, pp. 84-86

[84] G. Wiesenfeldt, *Untersuchungen zur longitudinalen Strahlanpassung beim Protonentransfer von PETRA nach HERA.* Diploma thesis, University of Hamburg, Germany, 1995

[85] E. J. N. Wilson (ed.), *Design Study of an Antiproton Collector for the Antiproton Accumulator (ACOL).* CERN 83-10, CERN, Geneva, Switzerland, 1983, pp. 14-16

[86] P. J. Bryant, K. Johnsen, *The Principles of Circular Accelerators and Storage Rings.* Cambridge University Press, Cambridge, U.K., 1993, pp. 281-284

[87] K. M. Fung, M. Ball, C. M. Chu, B. Hamilton et al., *Bunch Length Compression Manipulations.* Phys. Rev. Special Topics - Acc. and Beams, Vol. 3, 2000, pp. 100101

[88] R. Garoby, *Une Procédure de Fabrication de Paquets Courts dans le PS.* PS/LR/Note 79-16, CERN, Geneva, Switzerland, 1979

[89] G. Franchetti, I. Hofmann, G. Rumolo, *Effect of Space Charge on Bunch Compression near Transition.* Phys. Rev. Special Topics - Acc. and Beams, Vol. 3, 2000, pp. 084201

[90] K. Y. Ng, *Space-Charge Effects on the Bunch Rotation in the Longitudinal Phase Space.* Part. Acc. Conf., Chicago, Illinois, 2001, pp. 2893-2895

[91] K. Y. Ng, *Space-Charge Effects on Bunch Compression.* FERMILAB-FN-702, Fermi National Accelerator Lab., Batavia, Illinois, 2001

[92] E. Shaposhnikova, *Time Scales for the Motion of Uncaptured Particles With RF Off and RF On in LHC.* LHC Project Note 281, CERN, Geneva, Switzerland, 2002

[93] D. Boussard, *RF for $p\bar{p}$ (Part II).* CERN/SPS/84-2 ARF, CERN, Geneva, Switzerland, 1984

[94] M. Tigner, *Improved Method for Filling an Electron Storage Ring from a Synchrotron.* Part. Acc., Vol. 6, 1975, pp. 211-212

[95] J. E. Griffin, J. MacLachlan, A. G. Ruggiero, K. Takayama, *Time and Momentum Exchange for Production and Collection of Intense Antiproton Beams at Fermilab.* IEEE Trans. Nucl. Sci., Vol. NS-30, 1983, pp. 2630-2632

[96] J. E. Griffin, J. A. MacLachlan, G. N. Nicholls, Z. B. Qian, *Bunch Coalescing in the Main Ring to Form Intense Proton and Antiproton Bunches Without RF Counterphasing.* FERMILAB-TM-1280, Fermi National Accelerator Lab., Batavia, Illinois, 1984

[97] D. Wildman, P. Martin, K. Meisner, H. W. Miller, *Bunch Coalescing in the Fermilab Main Ring.* Part. Acc. Conf., Washington, D.C., 1987, pp. 1028-1030

[98] D. Boussard, J. Gareyte, P. Lefèvre, D. Möhl, *Une Procédure d'Accélération des Antiprotons via le PS.* PS/DL/Note 78-2, CERN, Geneva, Switzerland, 1978

[99] R. Garoby, *La Recombinaison Longitudinale dans le PS, Principe et Mise en Œvre Pratique.* CERN/PS/LR/Note 80-9, CERN, Geneva, Switzerland, 1980

[100] C. Ankenbrandt, *"Slip-Stacking": A New Method of Momentum-Stacking.* FERMILAB-FN-352, Fermi National Accelerator Lab., Batavia, Illinois, 1981

[101] D. Boussard, Y. Mizumachi, *Production of Beams with High Line-Density by Azimuthal Combination of Bunches in a Synchrotron.* CERN-SPS/ARF/79-11, IEEE Trans. Nucl. Sci., Vol. NS-26, 1979, pp. 3623-3625

[102] D. Boussard, Y. Mizumachi, *Numerical Computation of the Behaviour of Bunches in the Azimuthal Combination Processes.* SPS/ARF/YM/gs/Int. Note/79-12, CERN, Geneva, Switzerland, 1979

[103] K. Koba, J. Steimel, *Slip Stacking.* FERMILAB-Conf-02/205, 20th ICFA Advanced Beam Dynamics Workshop on High Intensity and High Brightness Hadron Beams, Fermi National Accelerator Lab., Batavia, Illinois, 2002, in: AIP Conf. Proc. 642, 2003, pp. 223-225

[104] K. Takayama, J. Kishiro, *Induction Synchrotron.* Nucl. Instr. Meth. A, Vol. 451, 2000, pp. 304-317

[105] U. Oeftiger, I. Hofmann, R. W. Müller, W. Pirkl, *Longitudinal Particle Dynamics in the HIDIF Driver Accelerator.* Nucl. Instr. Meth. A, Vol. 415, 1998, pp. 444-449

[106] G. W. Foster, C. M. Bhat, B. Chase, K. Seiya et al., *Beam Manipulation and Compression Using Broadband RF Systems in the Fermilab Main Injector and Recycler.* Europ. Part. Acc. Conf., Lucerne, Switzerland, 2004, pp. 1479-1481

[107] J. A. MacLachlan, *RF Stacking Without Emittance Dilution.* FERMILAB-Conf-00/117, American Physical Society April Meeting, Long Beach, California, 2000, in: Bull. Am. Phys. Soc., Vol. 45, 2000, p. 84

[108] W. Chou, J. Griffin, K. Y. Ng, D. Wildman et al., *Barrier RF Stacking at Fermilab.* Part. Acc. Conf., Portland, Orgegon, 2003, pp. 2922-2924

[109] C. M. Bhat, *A New Scheme for Momentum Mining of Beam Particles in a Storage Ring.* FERMILAB-FN-0746, Fermi National Accelerator Lab., Batavia, Illinois, 2004

[110] C. M. Bhat, *Longitudinal Momentum Mining in of Beam Particles in a Storage Ring.* FERMILAB-Pub-04/077-AD, Fermi National Accelerator Lab., Batavia, Illinois, 2004

[111] D. Broemmelsiek, M. Hu, S. Nagaitsev, *Stochastic Cooling in Barrier Buckets at the Fermilab Recycler.* Europ. Part. Acc. Conf., Lucerne, Switzerland, 2004, pp. 794-796

[112] J. Griffin, *Momentum Stacking in the Main Injector Using Longitudinal Barriers.* Fermi National Accelerator Lab., Batavia, Illinois, 2002, unpublished

[113] K. Y. Ng, *Continous Multiple Injection at the Main Injector.* Phys. Rev. Special Topics - Acc. and Beams, Vol. 5, 2002, pp. 061002

[114] K. Y. Ng, *Continous Multiple Injection at the Main Injector.* FERMILAB-FN-0715, Fermi National Accelerator Lab., Batavia, Illinois, 2002

[115] K. Y. Ng, *Doubling Main Injector Beam Intensity using RF Barriers.* FERMILAB-Conf-02/222, 20th ICFA Advanced Beam Dynamics Workshop on High Intensity and High Brightness Hadron Beams, Fermi National Accelerator Lab., Batavia, Illinois, 2002, in: AIP Conf. Proc. 642, 2003, pp. 226-228

[116] K. Y. Ng, *Double Intensity Injection for Antiproton Production.* FERMILAB-TM-2183, Fermi National Accelerator Lab., Batavia, Illinois, 2002

[117] see [15], p. 132

[118] J. Tückmantel, *The SPS/LHC Longitudinal Interface.* CERN-SL-99-007-DI, 9th LEP-SPS Performance Workshop, Chamonix IX, Chamonix, France, 1999, pp. 61-68

[119] O. Brüning, R. Cappi, R. Garoby, O. Gröbner et al., *LHC Luminosity and Energy Upgrade: A Feasibility Study.* LHC Project Report 626, CERN, Geneva, Switzerland, 2002

[120] F. Ruggiero, *LHC Accelerator R&D and Upgrade Scenarios.* LHC Project Report 666, Int. Symp. on LHC Physics and Detectors, Fermi National Accelerator Lab., Batavia, Illinois, 2003, in: Europ. Phys. Journal C - Particles and Fields, Vol. 34, 2004, pp. 433-442

[121] W. C. Middelkoop, A. Schoch, *Interaction Rate in Colliding Beam Systems.* AR/Int. SG/63-40, CERN, Geneva, Switzerland, 1963

[122] T. Suzuki, *General Formulae of Luminosity for Various Types of Colliding Beam Machines.* KEK-76-3, KEK, Tsukuba, Japan, 1976

[123] E. Keil, *Luminosity Optimisation for Storage Rings with Low-β Sections and Small Crossing Angles.* Nucl. Instr. Meth., Vol. 113, 1973, pp. 333-339

[124] L. Smith, *On the Calculation of Luminosity for Electron-Proton Colliding Beam.* PEP Note-20, Lawrence Berkeley Lab., Berkeley, California, 1972

[125] F. Ruggiero, G. Rumolo, F. Zimmermann, Y. Papaphilippou, *Beam Dynamics Studies for Uniform (Hollow) Bunches or Superbunches in the LHC: Beam-Beam Effects, Electron Cloud, Longitudinal Dynamics and Intrabeam Scattering.* LHC Project Report 627, Int. Workshop on Recent Progress in Induction Accelerators, Tsukuba, Ibaraki, Japan, 2002, pp. 131-147

[126] F. Ruggiero, F. Zimmermann, *Luminosity Optimization near the Beam-Beam Limit by Increasing Bunch Length or Crossing Angle.* Phys. Rev. Special Topics - Acc. and Beams, Vol. 5, 2002, pp. 061001

[127] see [119], p. 9

[128] E. Keil, *Beam-Beam Dynamics*. CERN 95-06, CERN Acc. School on Advanced Acc. Phys., Rhodes, Greece, 1993, pp. 539-555

[129] G. Guignard, *Review of the Investigation of the Beam-Beam Interactions at the ISR*. CERN ISR-BOM/79-28, Symposium on Nonlinear Orbit Dynamics and the Beam-Beam Interaction, Brookhaven Nat. Lab., Upton, New York, in: AIP Conf. Proc. 57, 1979, pp. 69-83

[130] L. R. Evans, J. Gareyte, *Beam-Beam Effects*. CERN 87-03, CERN Acc. School on Advanced Acc. Phys., Oxford, England, 1985, pp. 159-186

[131] K. Cornelis, L. Evans, A. Faugier, R. Schmidt, *Beam-Beam Effects and High Luminosity Operation in the SPS Proton Antiproton Collider*. CERN SPS/86-14 (MS), CERN, Geneva, Switzerland, 1986

[132] R. Schmidt, *Beam-Beam Observation in the SPS Proton Antiproton Collider*. Part. Acc., Vol. 50, 1995, pp. 47-60

[133] X. Zhang, T. Sen, V. Shiltsev, M. Xiao et al., *Experimental Studies of Beam-Beam Effects in the Tevatron*. Part. Acc. Conf., Portland, Orgegon, 2003, pp. 1757-1759

[134] T. Sen, B. Erdelyi, M. Xiao, V. Boocha, *Beam-beam effects at the Fermilab Tevatron: Theory*. Phys. Rev. Special Topics - Acc. and Beams, Vol. 27, 2004, pp. 041001

[135] W. Herr, *Tune Shifts and Spreads due to Short and Long Range Beam-Beam Interactions in the LHC*. CERN SL/90-06 (AP), LHC Note 119, CERN, Geneva, Switzerland, 1990

[136] F. Ruggiero, F. Zimmermann, G. Rumolo, Y. Papaphilippou, *Beam-Beam Interaction, Electron Cloud and Intrabeam Scattering for Proton Super-Bunches*. CERN-AB-2003-037 ABP, Part. Acc. Conf., Portland, Orgegon, 2003, pp. 123-125

[137] W. Herr, *Beam-Beam Effects in the LHC*. Part. Acc., Vol. 50, 1995, pp. 69-81

[138] K. Cornelis, W. Herr, M. Meddahi, *Proton Antiproton Collisions at a Finite Crossing Angle in the SPS*. Part. Acc. Conf., San Francisco, California, 1991, pp. 153-155

[139] K. Eggert, K. Honkavaara, A. Morsch, *Luminosity Considerations for the LHC*. CERN AT/94-04 (DI), LHC Note 263, CERN, Geneva, Switzerland, 1994

[140] H. Grote, W. Herr, *Nominal and Ultimate Luminosity Performance of the LHC*. LHC Project Note 275, CERN, Geneva, Switzerland, 2002

[141] A. Piwinski, *Abhängigkeit der Speicherring-Luminosität von der Taillenweite und vom Kreuzungswinkel*. DESY 67/7, DESY, Hamburg, Germany, 1967

[142] A. Piwinski, *Limitation of the Luminosity by Satellite Resonances*. DESY 77/18, DESY, Hamburg, Germany, 1977

[143] J. Strait, M. Lamm, P. Limon, M. V. Mokhov et al., *Towards a New LHC Interaction Region Design for a Luminosity Upgrade*. LHC Project Report 643, Part. Acc. Conf., Portland, Orgegon, 2003, pp. 42-44

[144] K. Takayama, *Super-bunch Hadron Colliders*. Int. Workshop on Recent Progress in Induction Accelerators, Tsukuba, Ibaraki, Japan, 2002, pp. 39-46

[145] R. Cappi, R. Garoby, S. Hancock, M. Martini et al., *The PS Complex as Part of the LHC Injector Chain.* CERN PS/91-07 (PA), CERN, Geneva, Switzerland, 1991

[146] M. Benedikt, A. Blas, J. Borburgh, R. Cappi et al., *The PS Complex as Proton Pre-Injector for the LHC - Design and Implementation Report.* CERN 2000-03, CERN, Geneva, Switzerland, 2000

[147] G. Arduini, *Beam Quality Preservation in the CERN PS-SPS Complex.* Europ. Part. Acc. Conf., Lucerne, Switzerland, 2004, pp. 78-82

[148] P. Collier (ed.), B. Goddard, R. Jung, K. H. Kissler, *The SPS as Injector for LHC, Conceptual Design.* CERN-SL-97-07 DI, CERN, Geneva, Switzerland, 1997

[149] E. Boltezar, H. Haseroth, W. Pirkl, G. Plass et al., *The New CERN* 50 *MeV Linac.* BNL-51134, Lin. Acc. Conf, Montauk, New York, 1979, pp. 66-77

[150] Study Group for CPS Improvements, *The Second Stage CPS Improvement Study* 800 *MeV Booster Synchrotron.* MPS/Int. DL/B 67-19, CERN, Geneva, Switzerland, 1967

[151] K. Schindl, *The PS Booster as Pre-Injector for LHC.* Part. Acc., Vol. 58, 1997, pp. 63-78

[152] J. M. Baillod, M. Corcelle, P. Gourcy, A. Krusche et al., *The Low Frequency Fundamental RF System for the LHC Beam Tests in the PSB.* PS/RF/Note 94-09, CERN, Geneva, Switzerland, 1994

[153] J. M. Baillod, M. Corcelle, P. Gourcy, A. Krusche et al., *The Second Harmonic RF System for the LHC Beam Tests in the PSB.* PS/RF/Note 94-10, CERN, Geneva, Switzerland, 1994

[154] A. Krusche, M. Paoluzzi, *The New Low Frequency Accelerating Systems for the CERN PS Booster.* CERN/PS 98-026 (RF), Europ. Part. Acc. Conf., Stockholm, Sweden, 1998, pp. 1782-1783

[155] A. Hofmann, S. Myers, *Calculation of the RF and Beam Parameters for the Double RF System.* LEP Note 158, CERN, Geneva, Switzerland, 1979

[156] A. Hofmann, S. Myers, *Beam Dynamics in a Double RF System.* CERN ISR-TH-RF/80-26, Conf. High Energy Acc., CERN, Geneva, 1980, pp. 610-614

[157] E. Regenstreif, *Le Synchrotron à Protons du CERN (1ère Partie).* CERN 58-6 a, CERN, Geneva, Switzerland, 1958

[158] E. Regenstreif, *Le Synchrotron à Protons du CERN (2ème Partie).* CERN 59-26, CERN, Geneva, Switzerland, 1959

[159] E. Regenstreif, *Le Synchrotron à Protons du CERN (3ème Partie).* CERN 61-9, CERN, Geneva, Switzerland, 1961

[160] R. Cappi, *The PS in the LHC Injector Chain.* Part. Acc., Vol. 58, 1997, pp. 79-89

[161] R. Garoby, J. Jamsek, P. Konrad, G. Lobeau et al., *RF System for High Beam Intensity Acceleration in the CERN PS.* CERN/PS 89-28(HF), Part. Acc. Conf., Chicago, Illinois, 1989, pp. 135-137

[162] D. Grier, *The PS 10 MHz Cavity and Power Amplifier.* PS/RF Note 2002-073, CERN, Geneva, Switzerland, 2002

[163] R. Garoby, S. Hancock, J.-L. Vallet, *Demonstration of Bunch Triple Splitting in the CERN PS.* Europ. Part. Acc. Conf., Vienna, Austria, 2000, pp. 304-306

[164] R. Garoby, *Requirements to the PS RF System for Filling the LHC with* 25 *ns Spacing between Bunches.* PS/RF/Note 93-04, CERN, Geneva, Switzerland, 1993

[165] R. Garoby, *A Non-Adiabatic Procedure in the PS to Supply the Nominal Proton Bunches for LHC into* 200 *MHz RF Buckets in SPS.* PS/RF/Note 93-17, CERN, Geneva, Switzerland, 1993

[166] M. Benedikt, R. Cappi, M. Chanel, R. Garoby et al., *Performance of the LHC Pre-Injectors.* CERN-PS-2001-011 (DR), High Energy Acc. Conf., Tsukuba, Japan, 2001, pp. MO-09

[167] CERN, *The* 300 *GeV Programme.* CERN/1050, CERN, Geneva, Switzerland, 1971

[168] T. Bohl, T. Linnecar, E. Shaposhnikova, *Study of Different Operating Modes of the 4th RF Harmonic Landau Damping System in the CERN SPS.* CERN-SL-98-026 RF, Europ. Part. Acc. Conf., Stockholm, Sweden, 1998, pp. 978-980

[169] P. Baudrenghien, T. Bohl, T. Linnecar, E. Shaposhnikova et al., *Nominal Longitudinal Parameters for the LHC Beam in the CERN SPS.* Part. Acc. Conf., Portland, Orgegon, 2003, pp. 3050-3052

[170] D. Boussard, T. Linnecar, *The LHC Superconducting RF System.* LHC Project Report 316, Cryogening Engineering and Int. Cryogenic Materials Conf., Montreal, Canada, 1999, in: Advances in Cryogenic Engineering, Vol. 45 A, pp. 835-844

[171] R. Bailey, P. Collier, *Standard Filling Schemes for Various LHC Operation Modes (Revised).* LHC-Project Note 323_Revised, CERN, Geneva, Switzerland, 2003

[172] P. Collier, *Baseline Proton Filling Schemes.* CERN-AB-2004-014 ADM, LHC Performance Workshop, Chamonix XIII, Chamonix, France, 2004, pp. 30-33

[173] see [14], p. 46

[174] J. M. Jowett, *Collision Schedules for the LHC.* Beam Physics Note 21, CERN, Geneva, Switzerland, 1999

[175] M. Benedikt, K. Cornelis, R. Garoby, E. Métral et al., *Report of the High Intensity Protons Working Group.* CERN-AB-2004-022 OP/RF, CERN, Geneva, Switzerland, 2004

[176] H. Damerau, R. Garoby, *Reference Scheme for Barrier Bucket RF Gymnastics in the LHC.* Internal note, in preparation

[177] J. Tückmantel, *Simulation of LHC with a Realistic RF System.* CERN-SL-2001-003 DI, LHC Workshop Chamonix, Chamonix XI, Chamonix, France 2001, pp. 306-311

[178] T. Bohl, *A Superconducting RF Cavity for Bunch Compression of the High Intensity SPS Proton Beam at Transfer to LHC.* Europ. Part. Acc. Conf., Sitges, Spain, 1996, pp. 2094-2096

[179] S. Wolfram, *Mathematica: A System for Doing Mathematics by Computer*. Addison-Wesley, Redwood City, California, 1988

[180] R. Garoby, D. Grier, E. Jensen, A. Mitra et al., *The PS 40 MHz Bunching Cavity*. Part. Acc. Conf., Vancouver, Canada, 1997, pp. 2953-2955

[181] E. Jensen, R. Hohbach, A. K. Mitra, R. L. Poirier, *Higher Order Mode Damping of the CERN PS 40 MHz Cavity*. Europ. Part. Acc. Conf., Sitges, Spain, 1996, pp. 2068-2070

[182] D. Grier, E. Jensen, R. Losito, A. K. Mitra, *The PS 80 MHz Cavities*. Part. Acc. Conf., Stockholm, Sweden, 1998, pp. 1773-1775

[183] The CERN Study Group on New Accelerators, *Report on The Design Study of Intersecting Storage Rings (ISR) for the CERN Proton Synchrotron*. CERN/542, AR/Int. SG/64-9, CERN Geneva, Switzerland, 1964

[184] K. Johnsen, *28 GeV Intersecting Proton Storage Rings at CERN*. Conf. High Energy Acc., Yerevan-Tsahkadzor, Russia, 1969, Vol. II, pp. 131-144

[185] K. Johnsen, *The CERN Intersecting Storage Rings*. Conf. High Energy Acc., Geneva, Switzerland, 1971, pp. 79-84

[186] A. Hofmann, *Single-Beam Collective Phenomena - Longitudinal*. CERN 77-13, 1st Course of the Int. School on Part. Acc. Phys., Erice, Italy, 1976, pp. 139-174

[187] A. Sessler, V. Vaccaro, *Longitudinal Instabilities of Azimuthally Uniform Beams in Circular Vacuum Chambers with Walls of Arbitrary Electrical Properties*. CERN 67-2, CERN, Geneva, 1967

[188] E. Keil, W. Schnell, *Concering Longitudinal Stability in the ISR*. CERN-ISR-TH-RF/69-48, CERN, Geneva, Switzerland, 1969

[189] K. Hübner, V. G. Vaccaro, *Dispersion Relations and Stability of Coasting Particle Beams*. CERN-ISR-TH/70-44, CERN, Geneva, Switzerland, 1970

[190] A. G. Ruggiero, V. G. Vaccaro, *Solution of the Displersion Relation for Longitudinal Stability of an Intense Coasting Beam in a Circular Accelerator (Application to the ISR)*. ISR-TH/68-33, CERN, Geneva, Switzerland, 1968

[191] B. Zotter, *Longitudinal Stability Diagrams for Some Particular Distribution Functions*. CERN/ISR-GS/76-11, CERN, Geneva, Switzerland, 1976

[192] W. Schnell, *Stacking and Acceleration*. BNL 20550, Proc. 1975 Isabelle Summer Study, Brookhaven Nat. Lab., Upton, New York, 1975, pp. 126-132

[193] D. Boussard, *Observation of Microwave Longitudinal Instablilities in the CPS*. CERN LABII/RF/Int./75-2, CERN, Geneva, Switzerland, 1975

[194] K. Hübner, B. Zotter, *Microwave Instability Criteria for Bunches Proton Beams*. CERN/ISR-TH/78-3, CERN, Geneva, Switzerland, 1978

[195] J. M. Wang, C. Pellegrini, *On the Condition for a Single Bunch High Frequency Fast Blow-up*. Conf. High Energy Acc., Geneva, Switzerland, 1980, pp. 554-561

[196] E. Shaposhnikova, *Signatures of the Microwave Instability.* CERN-SL-99-008 HRF, Joint US-CERN-Japan-Russia Particle Accelerators School on Beam Measurement, Montreux, Switzerland, 1998, pp. 351-377

[197] see [15], p. 101

[198] L. D. Landau, *On the Vibrations of the Electronic Plasma.* J. Phys. U.S.S.R, Vol. 10, 1946, pp. 25-34, in: D. Ter Haar (ed.), *Collected Papers of L. D. Landau.* Pergamon Press, Oxford, 1965, pp. 445-460

[199] H. G. Hereward, *The Elementary Theory of Landau Damping.* CERN 65-32, CERN, Geneva, Switzerland, 1965

[200] A. Hofmann, *Landau Damping.* CERN 89-01, CERN Acc. School on Acc. Phys., Berlin, Germany, 1989, pp. 40-56

[201] A. Hofmann, *Landau Damping.* CERN 95-06, CERN Acc. School on Advanced Acc. Phys., Rhodes, Greece, 1993, pp. 275-305

[202] F. J. Sacherer, *A Longitudinal Stability Criterion for Bunched Beams.* CERN/MPS/Int. BR/73-3, IEEE Trans. Nucl. Sci., Vol. NS-20, 1973, pp. 825-829

[203] Y. Baconnier, D. Boussard, J. Gareyte, *Some Preliminary Results on Coherent Longitudinal Instabilities in the CPS.* CERN/MPS/SR 70-6, CERN, Geneva, Switzerland, 1970

[204] F. Sacherer, *Methods for Computing Bunched-Beam Instabilities.* CERN/SI-BR/72-5, CERN, Geneva, Switzerland, 1972

[205] F. Sacherer, *Bunch Lengthening and Microwave Instability.* CERN/PS/BR/77-5, IEEE Trans. Nucl. Sci., Vol. NS-24, 1977, pp. 1393-1395

[206] F. Sacherer, *Bunch Lengthening and Microwave Instability (Part 2).* CERN/PS/BR 77-06, CERN, Geneva, Switzerland, 1977

[207] K. Y. Ng, *Introduction to Collective Instabilities - Longitudinal and Transverse.* FERMILAB-TM-2053, Overseas Chinese Phys. Association Accelerator School, Hsinchu, Taiwan, 1998

[208] J. L. Laclare, *Bunched-Beam Instabilities, Memorial Talk for F. J. Sacherer.* Int. Conf. High Energy Acc., Geneva, Switzerland, 1980, pp. 526-539

[209] F. Ruggiero, *Single-Beam Collective Effects in the LHC.* CERN SL/95-06 (AP), LHC Note 313, Part. Acc., Vol. 50, 1995, pp. 83-104

[210] E. Shaposhnikova, personal communication, 2003, see also: V. I. Balbekov, S. V. Ivanov, *Longitudinal Beam Instabilities in Proton Synchrotrons.* Conf. High Energy Acc., Novosibirsk, Russia, 1983, pp. 124-129

[211] D. Boussard, D. Brandt, L. Vos, *Is a Longitudinal Feedback Required for LHC?* LHC Project Note 205, CERN, Geneva, Switzerland, 1999

[212] E. Shaposhnikova, *Longitudinal Beam Parameters during Acceleration in the LHC.* LHC Project Note 242, CERN, Geneva, Switzerland, 2000

[213] E. Shaposhnikova, *Longitudinal Phenomena during the LHC Cycle*. CERN-SL-2001-003 DI, LHC Workshop Chamonix, Chamonix XI, Chamonix, France 2001, pp. 312-316

[214] D. Angal-Kalinin, L. Vos, *Coupled Bunch Instabilities in the LHC*. LHC Project Report 585, Europ. Part. Acc. Conf., Paris, France, 2002, pp. 290-292

[215] D. Angal-Kalinin, D. Brandt, L. Vos, *Intermediate Review of Single Bunch Collective Effects in the LHC*. LHC Project Report 587, Europ. Part. Acc. Conf., Paris, France, 2002, pp. 305-307

[216] D. Angal-Kalinin, *Review of Coupled Bunch Instabilities in the LHC*. LHC Project Report 595, CERN, Geneva, Switzerland, 2002

[217] L. Bottura, P. Burla, R. Wolf, *LHC Main Dipoles Proposed Baseline Current Ramping*. LHC Project Report 172, CERN, Geneva, Switzerland, 1998

[218] D. Boussard, E. Chiaveri, H. P. Kindermann, T. Linnecar et al., *Design Condiderations for the LHC 200 MHz RF System*. LHC Project Report 368, CERN, Geneva, Switzerland, 2000

[219] R. Losito, E. Chiaveri, R. Hanni, T. Linnecar et al., *Industrial Production of Eight Normal-Conducting 200 MHz ACN Cavities for the LHC*. Europ. Part. Acc. Conf., Lucerne, Switzerland, 2004, pp. 956-958

[220] T. Linnecar, *RF Capture and Synchronization*. CERN-AB-2003-008-ADM, LHC Performance Workshop, Chamonix XII, Chamonix, France, 2003, pp. 234-237

[221] P. B. Wilson, *Theory and Design of Superconducting Electron Linear Accelerators*. In: Septier, A. L. (ed.), P. M. Lapostolle, *Linear Accelerators*. North-Holland Publ. Co., Amsterdam, Netherlands, 1970, pp. 1107-1140

[222] J. Tückmantel, *Operating an LHC RF Station on a Sideband or with Amplitude-Modulation*. AB-Note-2004-045 RF, CERN, Geneva, Switzerland, 2004

[223] J. Tückmantel, *Consequences of an RF Power Trip in LHC*. AB-Note-2004-008, CERN, Geneva, Switzerland, 2004

[224] H. P. Kindermann, M. Stirbet, *The Variable Power Coupler for the LHC Superconducting Cavity*. CERN-SL-99-074 HRF, 9th Worshop on RF Superconductivity, Santa Fe, New Mexico, 1999, pp. 566-569

[225] P. B. Wilson, *Transient Beam Loading in Electron-Positron Storage Rings*. CERN-ISR-TH/78-23 (Rev.), CERN, Geneva, Switzerland, 1978

[226] J. Tückmantel, *Realistic RF System and Beam Simulation in Real Time for a Synchrotron*. CERN-SL-2001-007 HRF, High Energy Acc. Conf., Tsukuba, Japan, 2001, pp. P2hc07

[227] J. Tückmantel, *The LHC Beam with Suppressed RF Transients*. AB-Note-2004-22 RF, CERN, Geneva, Switzerland, 2004

[228] V. Rödel, L. Verolino, *Geometry of a 400 MHz Feedback Cavity for the LHC*. SL/RFS/Note 91-10, CERN, Geneva, Switzerland, 1991

[229] W. Höfle, *RF-Power Requirements for the LHC Bunch to Bunch Longitudinal Feedback-System.* SL/Note 94-60, CERN, Geneva, Switzerland, 1994

[230] J. B. Adams, J. V. Allaby, F. Amman, F. Bonaudi et al., *A Design of the European 300 GeV Research Facilities.* CERN/MC/60, CERN, Geneva, Switzerland, Vol. 1/2, 1970

[231] G. Arduini, P. Baudrenghien, T. Bohl, P. Collier et al., *Status of the LHC Proton Beam in the CERN SPS.* Europ. Part. Acc. Conf., Paris, France, 2002, pp. 206-208

[232] G. Arduini, P. Baudrenghien, T. Bohl, P. Collier et al., *The LHC Proton Beam in the CERN SPS: An Update.* Part. Acc. Conf., Portland, Oregon, 2003, pp. 1718-1720

[233] T. Bohl, T. Linnecar, E. Shaposhnikova, *Barrier buckets in the CERN SPS.* CERN-SL-2000-020 HRF, Europ. Part. Acc. Conf., Vienna, Austria, 2000, pp. 1220-1222

[234] T. Bohl, T. Linnecar, E. Shaposhnikova, *Thick barrier buckets using the SPS travelling wave structures.* CERN SL-Note-2000-032 HRF, CERN Geneva, Switzerland, 2000

[235] T. Bohl, T. Linnecar, E. Shaposhnikova, *Impedance Reduction in the CERN SPS as Seen from Longitudinal Beam Measurements.* CERN-SL-2002-023 (HRF), Part. Acc. Conf., Vienna, Austria, 2000, pp. 1446-1448

[236] T. Bohl, H. Damerau, R. Garoby, T. Linnecar et al., *MD on Barrier Buckets in the SPS.* AB-Note-2003-096 (MD), CERN, Geneva, Switzerland, 2003

[237] T. Bohl, H. Damerau, R. Garoby, T. Linnecar et al., *Barrier Buckets and Transient Beam Loading in the SPS.* CERN-AB-2004-008, CERN Geneva, Switzerland, 2004

[238] G. Dôme, *The SPS Acceleration System Travelling Wave Drift-Tube Structure for the CERN SPS.* CERN-SPS/ARF/77-11, Proton Linear Accelerator Conference, Chalk River, Ontario, Canada, 1976, pp. 138-147

[239] D. Boussard, *Beam loading.* CERN 95-06, CERN Acc. School on Advanced Acc. Physics, Rhodes, Greece, 1993, pp. 415-436

[240] P. Baudrenghien, G. Lambert, *Reducing the impedance of the Travelling Wave Cavities: Feed-forward and one turn delay feed-back.* CERN-SL-2000-007-DI, 10th Workshop on LEP-SPS Performance, Chamonix X, Chamonix, France 2000, pp. 94-101

[241] National Accelerator Laboratory, *Design Report.* National Accelerator Laboratory, Batavia, Illinois, 1968, pp. 9-26 to 9-30

[242] R. Garoby, *Longitudinal Limitations in the PS Complex for the Generation of the LHC Proton Beam.* Part. Acc., Vol. 58, 1997, pp. 121-136

[243] Gesellschaft für Schwerionenforschung mbH, *An International Accelerator Facility for Beams of Ions and Antiprotons.* GSI Conceptual Design Report, 2001, pp. 535-537

[244] P.Spiller, K. Blasche, U. Blell, O. Boine-Frankenheim et al., *SIS100/300 Conceptual Design Studies.* GSI Report 2004-1, GSI, Darmstadt, 2004, pp. 249-250

[245] see [243], pp. 528-531

[246] J. M. Baillod, L. Magnani, G. Nassibian, F. Pedersen et al., *A Second Harmonic (6-16 MHz) RF System with Feedback-Reduced Gap Impedance for Accelerating Flat-Topped Bunches in the CERN PS Booster.* IEEE Trans. Nucl. Sci., Vol. NS-30, 1983, pp. 3499-3501

[247] A. Blas, S. Hancock, M. Lindroos, *Hollow Bunch Distributions at High Intensities in the PS Booster.* Europ. Part. Acc. Conf., Vienna, Austria, 2000, pp. 1528-1530

[248] S. Y. Lee, *Accelerator Physics.* World Scientific, Singapore, 1999, p. 234-235, p. 241

[249] F. Kuypers, *Klassische Mechanik.* Wiley-VCH, Weinheim, 5. ed., 1997, pp. 331-332

[250] H.L. Hagedoorn, J. I. M. Botman, W. J. G. M. Kleeven, *Hamiltonian Theory is a Tool for Accelerator Physics.* CERN 92-01, CERN Acc. School on Advanced Acc. Phys., Noordwijkerhout, Netherlands, 1991, pp. 1-50

[251] B. Zotter, *BBI - A Program to Compute Bunches Beam Instabilities in High Energy Particle Accelerators and Storage Rings.* CERN LEP/TH 89-74, CERN, Geneva, Switzerland, 1989

[252] G. Besnier, *Contribution à la Théorie de la Stabilité des Oscillations Longitudinales d'un Faisceau Accéléré en régime de charge d'espace.* Thèse, Université de Rennes 1, 1978, p. 12

[253] Klaus Wille, *Physik der Teilchenbeschleuniger und Synchrotronstrahlungsquellen.* Teubner Verlag, Stuttgart, Germany, 1996, 2nd ed., pp. 130-132

[254] cf. [86], pp. 100-101

[255] P. Schmüser, *Basic Course on Accelerator Optics.* CERN 94-01, CERN Acc. School on General Acc. Phys., Jykväskylä, Finland, 1992, pp. 17-88

[256] E. Wilson, *Transverse Beam Dynamics.* CERN 94-01, CERN Acc. School on General Acc. Phys., Jykväskylä, Finland, 1992, pp. 131-158

[257] see [248], p. 91-92

[258] L. J. Laslett, *On the Limitations Imposed by Transverse Space-Charge Effects in Circular Particle Accelerators.* BNL 7534, Proc. 1963 Summer Study on Storage Rings, Accelerators and Experimentation at Super-High Energies, 1963, BNL, Upton, New York, pp. 324-367

[259] K. Schindl, *Space Charge.* CERN-PS-99-012-DI, Joint US-CERN-Japan-Russia Particle Accelerators School on Beam Measurement, Montreux, Switzerland, 1998, pp. 127-151

[260] M. Reiser, *Theory and Design of Charged Particle Beams.* Wiley-Interscience, New York, New York, 1994, pp. 260-273

Acknowledgements

This is dedicated to all those who have contributed to make this work possible:

First of all, I would like to acknowledge Prof. Dr. Thomas Weiland (Darmstadt University of Technology) for his advice and support during the studies for this thesis.

I am thankful to Prof. Dr. Klaus Wille (University of Dortmund) for accepting to serve as second examiner.

It is a great pleasure to thank Roland Garoby who supervised the thesis project at CERN. His continuous interest, dedicated ideas and straightforward guidance based on his deep insight into the physics of particle accelerators were invaluable to keep the studies right on track.

I am grateful to Dr. Elena Shaposhnikova for many stimulating discussions on longitudinal beam instabilities, and to Drs. Thomas Bohl, Steven Hancock, Joachim Tückmantel who illuminated innumerous details of the RF systems at CERN and their interaction with the particle beam. I am also indebted to Dr. Frank Zimmermann for helpful explanations of luminosity and beam-beam effects.

I am thankful to Drs. Andreas Jankowiak (University of Mainz), Juris Kaugerts (GSI), Boris Keil (PSI) and Gerald Schreiber (GSI) for the proof-reading of this report.

Finally, I would like to acknowledge GSI, Darmstadt for supporting the studies at CERN.

Curriculum Vitae

Personal data

Name: Heiko Damerau
Born on: 21 December 1974 in Lünen

Education and professional experience

2003 – 2004	Delegated as associate to the radio frequency group at CERN, Geneva, Switzerland
2001	Participant of the CERN Accelerator School, *Intermediate Accelerator Physics Course*, Sevilla, Spain
2001 – 2005	Graduate studies of accelerator physics Darmstadt University of Technology, Darmstadt, Germany and scientific employee in the radio frequency group at GSI, Darmstadt, Germany
2001	Diploma thesis, *Entwicklung eines subharmonischen Bunchkompressionssystems für das Booster-Synchrotron BoDo bei DELTA*, University of Dortmund, Dortmund, Germany
2000	Participant of the CERN Accelerator School, *RF Engineering*, Seeheim, Germany
1999 – 2000	Diploma student in the accelerator group of the Dortmund Electron Test Facility (DELTA), University of Dortmund, Dortmund, Germany
1995 – 2001	Studies of physics University of Dortmund, Dortmund, Germany